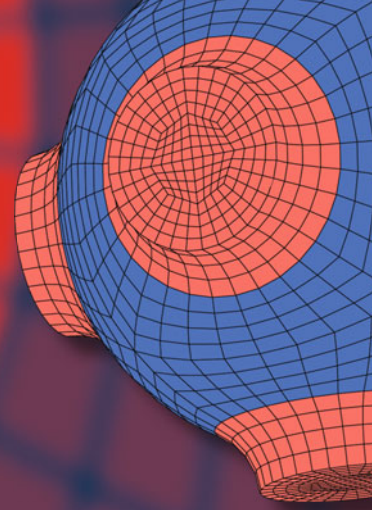


Advanced Structured Materials

Azman Ismail
Muhamad Husaini Abu Bakar
Andreas Öchsner *Editors*



Advanced Engineering for Processes and Technologies

 Springer

Advanced Structured Materials

Volume 102

Series editors

Andreas Öchsner, Faculty of Mechanical Engineering, Esslingen University of Applied Sciences, Esslingen, Germany

Lucas F. M. da Silva, Department of Mechanical Engineering, Faculty of Engineering, University of Porto, Porto, Portugal

Holm Altenbach, Otto-von-Guericke University, Magdeburg, Sachsen-Anhalt, Germany

Common engineering materials reach in many applications their limits and new developments are required to fulfil increasing demands on engineering materials. The performance of materials can be increased by combining different materials to achieve better properties than a single constituent or by shaping the material or constituents in a specific structure. The interaction between material and structure may arise on different length scales, such as micro-, meso- or macroscale, and offers possible applications in quite diverse fields.

This book series addresses the fundamental relationship between materials and their structure on the overall properties (e.g. mechanical, thermal, chemical or magnetic etc.) and applications.

The topics of *Advanced Structured Materials* include but are not limited to

- classical fibre-reinforced composites (e.g. glass, carbon or Aramid reinforced plastics)
- metal matrix composites (MMCs)
- micro porous composites
- micro channel materials
- multilayered materials
- cellular materials (e.g. metallic or polymer foams, sponges, hollow sphere structures)
- porous materials
- truss structures
- nanocomposite materials
- biomaterials
- nano porous metals
- concrete
- coated materials
- smart materials

Advanced Structures Material is indexed in Google Scholar and Scopus.

More information about this series at <http://www.springer.com/series/8611>

Azman Ismail · Muhamad Husaini Abu Bakar
Andreas Öchsner
Editors

Advanced Engineering for Processes and Technologies

 Springer

Editors

Azman Ismail
Malaysian Institute of Marine Engineering
Technology
Universiti Kuala Lumpur
Lumut, Perak, Malaysia

Andreas Öchsner
Faculty of Mechanical Engineering
Esslingen University of Applied Sciences
Esslingen am Neckar, Baden-Württemberg,
Germany

Muhamad Husaini Abu Bakar
Malaysian Spanish Institute
Universiti Kuala Lumpur
Kulim, Kedah, Malaysia

ISSN 1869-8433

ISSN 1869-8441 (electronic)

Advanced Structured Materials

ISBN 978-3-030-05620-9

ISBN 978-3-030-05621-6 (eBook)

<https://doi.org/10.1007/978-3-030-05621-6>

Library of Congress Control Number: 2018964016

© Springer Nature Switzerland AG 2019

This work is subject to copyright. All rights are reserved by the Publisher, whether the whole or part of the material is concerned, specifically the rights of translation, reprinting, reuse of illustrations, recitation, broadcasting, reproduction on microfilms or in any other physical way, and transmission or information storage and retrieval, electronic adaptation, computer software, or by similar or dissimilar methodology now known or hereafter developed.

The use of general descriptive names, registered names, trademarks, service marks, etc. in this publication does not imply, even in the absence of a specific statement, that such names are exempt from the relevant protective laws and regulations and therefore free for general use.

The publisher, the authors, and the editors are safe to assume that the advice and information in this book are believed to be true and accurate at the date of publication. Neither the publisher nor the authors or the editors give a warranty, express or implied, with respect to the material contained herein or for any errors or omissions that may have been made. The publisher remains neutral with regard to jurisdictional claims in published maps and institutional affiliations.

This Springer imprint is published by the registered company Springer Nature Switzerland AG
The registered company address is: Gewerbestrasse 11, 6330 Cham, Switzerland

Preface

We are honored to announce the publication of the book *Advanced Engineering for Processes and Technologies* which is a collection of reviewed international chapters in the Advanced Structured Materials series of Springer. All the chapters published in this book were mostly contributed by the academia of Universiti Kuala Lumpur Malaysia Spanish Institute (UniKL MSI) in Kulim, Malaysia, led by their research and innovation head, Dr. Muhamad Husaini Abu Bakar.

Nowadays, advanced engineering is the key driver for sustainable innovation and productivity. As we engage on this new revolution of technology, it would be beneficial for those involved in Internet of things (IoT), big data, automation, and many more. Thus, expanding the business and technology opportunities access that exists among us is crucial. This book explained a range of advanced processes and technology methods used for the establishment of engineering innovation and productivity through their enlightening/competitive research findings and the exposure of their relative merits and limitations, together with some directions of further researches for sustainability operations and developments in advanced engineering research fields.

Lumut, Malaysia
Kulim, Malaysia
Esslingen am Neckar, Germany

Azman Ismail
Muhamad Husaini Abu Bakar
Andreas Öchsner

Contents

Three Dimensional Simulation of Filling Process for Stacked-Chip Scale Packages	1
Mior Firdaus Mior Abd Majid, Mohamad Sabri Mohamad Sidik, Muhamad Husaini Abu Bakar, Khairul Shahril Shafee, Zainal Nazri Mohd Yusuf, Mohamad Shukri Mohd Zain and Mohd. Zulkifly Abdullah	
Analysis of Temperature Distribution Behavior of Motorcycle Brake Pads	13
Khairul Shahril bin Shafee, Mohd Khairuddin Hj. Ali Musa, Mohamad Sabri Mohamad Sidik, Mior Firdaus Mior Abd. Majid and Muhamad Husaini Abu Bakar	
Application of a Portable Coordinate Measuring Machine onto Automotive Door Panel for Quality Inspection Activity	25
Tajul Adli bin Abdul Razak, B. T. Hang Tuah bin Baharudin, Khairul Shahril bin Shafee and Khairul Akmal bin Shamsuddin	
Study on Implementation of Neural Network Controlling Four Quadrants Direct Current Chopper	37
S. Arof, N. H. Diyanah, P. A. Mawby and H. Arof	
Processor in the Loop for Testing Series Motor Four Quadrants Drive Direct Current Chopper for Series Motor Driven Electric Car	59
S. Arof, N. H. Diyanah, N. M. Yaakop, P. A. Mawby and H. Arof	
Comparative Study of Fuel Consumption, Acceleration and Emission for Road Vehicle Using LPG or Gasoline	77
Loke Kean Koay, Muhammad Jasni Md Sah and Rusli bin Othman	

Design and Construction of a Micro-hydro Turbine for Additional Home Power to Use a Conventional Water Pipeline	89
Tajul Adli bin Abdul Razak, Shahril Nizam bin Mohamed Soid, Khairil Shahril bin Shafee, Mohd Riduan bin Ibrahim and Aznizam bin Abdullah	
Design and Fabrication of a Magneto-rheological Fluid Based Torque Sensor for Automotive Application	101
Muhamad Husaini Abu Bakar and Amirul Qusyaini Alwi	
Development of a 2-Dof Parallel Kinematics Machine for Macro Scale Products	115
Nor Liyana Maskuri, Muhamad Husaini Abu Bakar and Ahmad Razlee Ab Kadir	
Development of a Capacitor Using a Rubber Based Magneto Rheological Elastomer	125
Muhamad Husaini Abu Bakar, Mohd Nor Hazwan Hadzir and Muhamad Termizi Muhamad	
Effect of the Magnetic Field on Magnetic Particles in Magnetorheological Elastomer Layers	135
Mohd Nor Hazwan Hadzir, Muhamad Husaini Abu Bakar and Ishak Abdul Azid	
Effects of the Coconut Pulp Fiber on the Mechanical Properties and Water Absorption of Reinforced Ethylene Propylene Diene Monomer	145
Mohamad Sabri Mohamad Sidik, Mohamad Taufiq and Nurulhuda Amri	
Flow Analysis Inside Coated Porous Media	153
Ahmad Kamal Ismail, Mohd. Zulkifly Abdullah, Abdul Rashid Jamaludin, Mohammed Zubair and Nor Haslina Ibrahim	
Francis Turbine Analysis Between Computational Fluid Dynamics (CFD) and Experimental Methods	161
Muhammad Naim bin Md. Kamal, Khairul Shahril bin Shaffee, Mohamad Sabri bin Mohamad Sidik, Ahmad Razlee Ab. Kadir and Johan Ihsan bin Mahmood	
Refining 5S Awareness Through an Interactive Game Board	173
Jumázulhisham Abdul Shukor, Rahim Jamian and Mohd Nizam Ab Rahman	
Kinetic Modelling of a Particle Grinding Process in a Planetary Ball Mill Jar	183
Muhamad Husaini Abu Bakar, Ahmad-Fazireen Ahmad-Fauzi and Nor Liyana Maskuri	

Large Eddy Simulation of Vehicle Aerodynamics Using Parallel Computational Fluids Dynamics 199
 Abd-Munim Abd-Halim and Muhamad Husaini Abu Bakar

Performance Characteristics of a Small Engine Fueled by Liquefied Petroleum Gas 207
 Mohamad Shukri bin Mohd Zain, Shahril Nizam bin Mohamed Soid, Mior Firdaus bin Mior Abd Majid and Mohd Nurhidayat bin Zaelem

Machining Performance of AISi/10% AlN Metal Matrix Composite Material in Milling Process Using Uncoated Insert 215
 Nurul Na’imy Wan, Mohamad Sazali Said, Norzalina Othman, Ahmad Razlee Ab Kadir and Baizura Zubir

Numerical Investigation of Magneto-hydrodynamics in a Magnetic Peristaltic Pump 225
 Faizah Osman and Muhamad Husaini Abu Bakar

Parametric Study of the Two-Stage Pyrolysis Process for Activated Carbon Preparation from *Pithecellobium Jiringa* 241
 Muhamad Husaini Abu Bakar, Mohamad-Syafiq Mohd-Kamal and Mohd-Nazri Che-Adnan

Performance of a Small Engine Fueled by Methane Using a Simulation Tool 253
 Shahril Nizam Mohamed Soid, Muhammad Najib Abdul Hamid, Mohd Suyerdi Omar and Muhammad Iqbal Ahmad

Simulation Analysis on the Performance of a Hydrogen Port Fuel Injection Engine 261
 Shahril Nizam Mohamed Soid, Surenthar Magalinggam and Muhammad Iqbal Ahmad

Simulation of Flange Modeling by Using the Finite Element Method 269
 Khairul Shahril Shaffee, Khairulanwar Haris, Khairul Akmal Shamsuddin, Mohamad Sabri Mohamad Sidik and Megat Mohd Amzari Megat Mohd Aris

Material Removal Rate and Cutting Force of AISi/10% AlN Metal Matrix Composite Material in Milling Process Using Uncoated Inserts 279
 Mohamad Sazali Said, Nurul Na’imy Wan, Norzalina Othman, Ahmad Razlee Ab Kadir and Baizura Zubir

Synthesis of Polypropylene Solid State Electrolytes for Batteries Using a Polymerization Heat Chamber 289
 Muhamad Husaini Abu Bakar and Kartina Farah Hana

The Effect of Cutting Fluid Condition on Surface Roughness in Turning of Alloy Steel	297
Baizura Zubir, Mohd Zaki Abdul Razak, Ahmad Fauzie Abd Rahman and Mohamad Sazali Said	
Thermal Analysis of a Cylindrical Sintered Wick Heat Pipe	307
Faiza Mohamed Nasir, Mohd. Zulkify Abdullah and Fairosidi Idrus	
Three Point Bending Analysis on the Side Impact Beam of a Perodua Kancil	321
Fazidah Saad, Zainal Nazri Mohd Yusuf, Zulkarnain Abdul Latiff and Norhisham Ismail	
Time Optimization Implementation in Conventional Lathe Machining Operations	329
Jumázulhisham Abdul Shukor, Syed Ahmad Faiz Syed Mohd and Mozaimi Mohamad	

Three Dimensional Simulation of Filling Process for Stacked-Chip Scale Packages



Mior Firdaus Mior Abd Majid, Mohamad Sabri Mohamad Sidik, Muhamad Husaini Abu Bakar, Khairul Shahril Shafee, Zainal Nazri Mohd Yusuf, Mohamad Shukri Mohd Zain and Mohd. Zulkify Abdullah

Abstract Encapsulation is one of the key processes in electronic packaging in order to protect the integrated circuit chips from environmental and mechanical damages. The most obvious choice for the encapsulation process is transfer moulding due to its capability to mould small parts with complex features. An electronic package that employs transfer moulding is Stacked-Chip Scale Package (S-CSP). However, a computer simulation is one of the tools that could be used to simulate and predict the mould process. It is highly desirable in order to avoid the typical time-consuming procedure of mould design and process optimization by trial and error. In this paper, a fully three-dimensional analysis to predict the transfer moulding process of S-CSP encapsulation using a finite volume method (FVM) based software, FLUENT is presented. The proposed FVM simulation model is built and meshed using GAMBIT. Some simplification is done for the

M. F. Mior Abd Majid (✉) · M. S. Mohamad Sidik · M. H. Abu Bakar
K. S. Shafee · Z. N. M. Yusuf · M. S. M. Zain
Universiti Kuala Lumpur, Malaysan Spanish Institute, Kulim Hi-Tech Park,
09000 Kulim, Kedah, Malaysia
e-mail: miorfirdaus@unikl.edu.my

M. S. Mohamad Sidik
e-mail: msabri@unikl.edu.my

M. H. Abu Bakar
e-mail: muhamadhusaini@unikl.edu.my

K. S. Shafee
e-mail: khairuls@unikl.edu.my

Z. N. M. Yusuf
e-mail: zainalnazri@unikl.edu.my

M. S. M. Zain
e-mail: mshukrimz@unikl.edu.my

Mohd.Zulkify Abdullah
School of Mechanical and Aerospace Engineering, Universiti Sains Malaysia,
Engineering Campus, Seri Ampangan, 14300 Nibong Tebal,
Seberang Perai Selatan, Pulau Pinang, Malaysia
e-mail: mezul@eng.usm.my

simulation model due to time consumption and the complicated geometry of the actual S-CSP model. In the analysis, the volume of fluid (VOF) technique was used to track the flow front of the encapsulation. The viscosity versus shear rate is plotted and the void formation problem is also discussed. The numerical results are compared with the previous experimental results and are in good agreement.

Keywords Stacked-Chip Scale Package (S-CSP) · Finite volume method (FVM) Volume of fluid (VOF) · Front tracking · Void

1 Introduction

Electronic packaging is defined as a package to house a silicon chip in an electronic system. The main functions of an electronic package are to protect the electronic components from adverse environmental and mechanical effects and to act as a structural support and electrical insulation [1]. It also provides heat dissipation, signal timing and power distribution [2]. In electronic packaging, one of the key processes is encapsulation. Generally, transfer moulding and liquid encapsulation are the most common encapsulation techniques. In transfer moulding, an epoxy moulding compound (EMC) is preheated before loading into the transfer port. By applying certain pressure, the heated moulding compound is transferred from the transfer port through the runners and then into the mould cavities which may consist of a single or many dies [3].

An example of electronic package using the transfer moulding process is Chip Scale Package (CSP) which is a package whose area is less than 1.2 times the area of the Integrated Chip (IC). CSP has smaller, thinner and lighter characteristics and has been developed to address the demands of modern electronics. The pace of CSP technology development is accelerating rapidly. The semiconductor industry is driven by the broad adoption of CSP in wireless handsets and handheld electronic devices. Looking into the modern life today, the market demand for thin, small, light and user friendly electronic packaging that can provide wider variety of functions is still on the increase in recent years [4–6]. The Stacked-Chip Scale Packages (S-CSP) can be the best option to meet the aforesaid demands to a remarkable extend. It integrates Application Specific Integrated Circuit (ASIC) and memories such as flash, Static Random Access Memory (SRAM), and Double Data Rate (DDR) into one package by stacking dies, interconnecting them with wire bonding and moulding all into one package based on the Joint Electronic Device Engineering Council (JEDEC) standard [7, 8]. S-CSP is adopted widely in portable multimedia devices such as cellular telephones, digital cameras, PDAs and audio players [9].

There are several factors that can affect the mould filling yields, such as die thickness (gap clearance), size and array arrangement of complicated stacking dies.

They are defined as critical factors at the initial stage of the product quality planning [10]. As the S-SCP mould is the matrix array type with thin space and wide filling area, the quality concern of the filling process becomes very significant. It involves complex non-Newtonian fluid flow, coupling heat transfer and chemical reaction. As a result, the problems like incomplete mould, void formation, unbalanced flow and wire sweeping are common. Moreover, these phenomena in the complex mould geometry make it difficult to analyze the process and further optimize the design [11].

Although transfer moulding is a mature technology, it is still difficult to optimize and the mould design is a costly and lengthy process. Prototyping often requires numerous modifications and revisions. To minimize the impact of these problems and for better mould design and optimization, numerical flow analysis during the encapsulation process is needed [12]. Turng and Wang [13], Han and Wang [14], and Nguyen et al. [15–18] are the pioneers in numerical simulation of the flow during encapsulation. Their numerical formulation was mostly based on the finite element method (FEM) coupled with the volume of fluid (VOF) technique. The Generalized Hele Shaw approximation was made for the fluid field. Basically, the Hele-Shaw cell consists of two flat plates that are parallel to each other and separated by a small distance. The Hele Shaw approximation uses gap wise-averaged mass and momentum-conservation equations ignoring the gap wise component of the flow. Moreover, the thickness of the model is relatively small as compared to its width and length, and the viscous effect dominates the flow. Thus, the inertia effect is negligible [19]. Abdullah et al. [20, 21] presented flow visualization and EMC rheology on S-CSP encapsulation studies using the finite difference method. An alternative FVM-based three-dimensional mould filling analysis using the incompressible Navier-Stokes equation is introduced in the current study. The Epoxy Moulding Compound (EMC) is modelled as a non-Newtonian fluid and the EMC is treated as a generalized Newtonian fluid (GNF). Accordingly, in our previous work [22], 3D simulation of pressurized under-filling of flip chip package has been presented. The Simulations were done with the computational fluid dynamics code FLUENT 6.3. The Volume of fluid (VOF) Technique is used to track the flow front during calculation. In the present study, we adopt the technique to investigate the flow visualization and encapsulate filling microchip encapsulation process. Numerical results of flow front profiles are compared with previous experimental results. In addition, the void formation is observed.

2 Numerical Model

The three-dimensional incompressible flow equation, namely the conservation of mass, Navier-Stokes equation and conservation of energy for non-isothermal, generalized Newtonian fluids (GNF) are given below:

(i) *Continuity equation:*

$$\frac{\partial u}{\partial x} + \frac{\partial v}{\partial y} + \frac{\partial w}{\partial z} = 0 \quad (1)$$

(ii) *Navier-Stokes Equation:*

x-direction

$$\frac{\partial u}{\partial t} + u \frac{\partial u}{\partial x} + v \frac{\partial u}{\partial y} + w \frac{\partial u}{\partial z} = -\frac{1}{\rho} \frac{\partial p}{\partial x} + \eta \left(\frac{\partial^2 u}{\partial x^2} + \frac{\partial^2 u}{\partial y^2} + \frac{\partial^2 u}{\partial z^2} \right) \quad (2)$$

y-direction

$$\frac{\partial v}{\partial t} + u \frac{\partial v}{\partial x} + v \frac{\partial v}{\partial y} + w \frac{\partial v}{\partial z} = -\frac{1}{\rho} \frac{\partial p}{\partial y} + \eta \left(\frac{\partial^2 v}{\partial x^2} + \frac{\partial^2 v}{\partial y^2} + \frac{\partial^2 v}{\partial z^2} \right) \quad (3)$$

z-direction

$$\frac{\partial w}{\partial t} + u \frac{\partial w}{\partial x} + v \frac{\partial w}{\partial y} + w \frac{\partial w}{\partial z} = -\frac{1}{\rho} \frac{\partial p}{\partial z} + \eta \left(\frac{\partial^2 w}{\partial x^2} + \frac{\partial^2 w}{\partial y^2} + \frac{\partial^2 w}{\partial z^2} \right) \quad (4)$$

(iii) *Energy equation:*

$$\rho C_p \left(\frac{\partial T}{\partial t} + u \cdot \nabla T \right) = \nabla \cdot (k \nabla T) + \Phi \quad (5)$$

However, a modification in the conservation of energy has been made by inserting an energy source term. The energy source term is as follows:

$$\Phi = \eta \dot{\gamma} \quad (6)$$

For predicting the relationship between viscosity and the degree of polymerization that are given accordingly as:

The Cross rheology model:

$$\eta(T, \dot{\gamma}) = \frac{\eta_0(T)}{1 + \left(\frac{\eta_0 \dot{\gamma}}{\tau^*} \right)}, \quad (7)$$

where

$$\eta_0(T) = B \exp\left(\frac{T_b}{T}\right) \quad (8)$$

n is the power law index, η_0 is the zero shear rate viscosity, τ^* is the parameter that describes the transition region between zero shear rates and the power law region of the viscosity curve, $\dot{\gamma}$ is the shear rate, B is an exponential-fitted constant and T_b is a temperature fitted-constant, and T is the absolute temperature.

In a three-dimensional filling simulation, accurate tracking of the melt fronts as well as the representation and evolution of the complex topology are very important. In the VOF method the melt front can be tracked by solving the transport equation of the fractional volume function. The transport equation can be solved by either in the geometrical approach or the algebraic approach. The VOF equation is given as:

$$\frac{dF}{dt} = \frac{\partial F}{\partial t} + u \frac{\partial F}{\partial x} + v \frac{\partial F}{\partial y} + w \frac{\partial F}{\partial z} - \left\{ \frac{\partial^2 F}{\partial x^2} + \frac{\partial^2 F}{\partial y^2} + \frac{\partial^2 F}{\partial z^2} \right\} = 0, \quad (9)$$

where F is defined either as equal to one ($F = 1$) for the fluid region or equal to zero ($F = 0$) for the empty region and partially full if F has value in between one and zero at the melt front ($0 < F < 1$).

3 Simulation Setup

The volume of fluid (VOF) model in FLUENT 6.3.26 is utilized to simulate the S-CSP mold filling process. In the VOF model, a single set of momentum equations is shared by the fluids, and the volume fraction of each of the fluids in each computational cell is tracked throughout the domain. Air and encapsulant material Hitachi CEL-9200 XU (LF) [23] are defined as the phases in the analysis and the mould temperature is set as 175 °C. Implicit solution and time dependent formulation are applied for the volume fraction in every time step. The volume fraction of the encapsulant material is defined as one and zero value for the air phase. Besides, viscosity cross model and VOF techniques are applied to track the melt front. The model is created by using GAMBIT software and a total 94196 tetrahedral elements are generated for the simulation. The simulation took about seven hours to complete for a single case. The S-CSP package model used in the present study and its simplified model and the meshed model are shown in Figs. 1 and 2, respectively. Some simplifications have been made to the actual model such as replacement of chamfered corners by 90° corners and removal of vents for the simulation model. The material properties [23] for the current study are summarized in Table 1. The boundary and initial conditions used in the calculation are as follows:

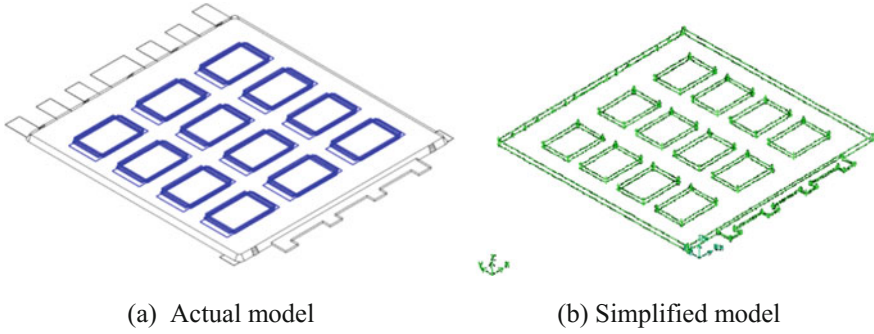


Fig. 1 The actual and simplified S-CSP models. **a** Actual model. **b** Simplified model

Fig. 2 3D meshed model

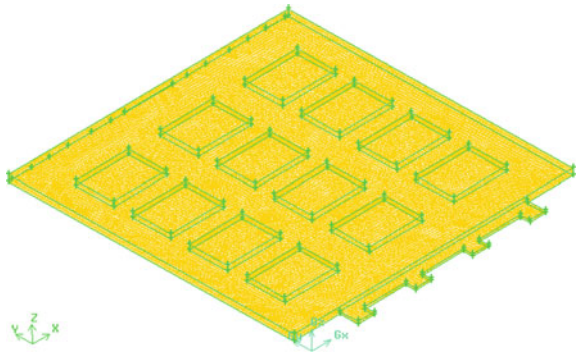


Table 1 Material properties [23]

Parameter	Value
n	0.7938
τ^* (Pa)	7.264E-4
B	5.558E 4
T_b (K)	7.166E3
ρ (kg/cm ³)	2.000E3
c_p (J/kg*K)	1079
k (W/m*K)	0.97

(a) On the mould wall: $u = v = w = 0$; $T = T_w$; $\frac{\partial p}{\partial n} = 0$

(b) On the melt front: $p = 0$

(c) On the inlet: $u = v = w = \text{given}$; $p = p_{in}(x, y, z, t)$; $T = T_{in}$.

4 Results and Discussion

The experiments have been done to investigate the flow behaviour of epoxy moulding compound (EMC) inside the actual mould of Stacked-Chip Scale Package (S-CSP) with twelve arrays of six stacking dies. The EMC used in this investigation is the HITACHI CEL-9200-XU (LF). The mould temperature is set at 175 °C and the package pressure is 70 kg/cm². Short-shot results have been performed to observe the melt front advancement at different times step. The short-shot samples can be obtained by setting certain stroke length of the plunger. The package will be incomplete if the sets less then the stroke length. Thus the front profile can be attained. Figure 3 illustrates the gate, air vents, stacking dies in matrix array of 4 × 3 and the flow direction.

Figure 4 demonstrates respectively the experiment and simulation (short shot) results of melt front advancement with an inlet velocity of 4 mm/s in the S-CSP. Hitachi CEL-9200-XU (LF) is used as an encapsulant in the simulation. The encapsulation process shows a good agreement of flow front profile at 1.5 s and 2 s for experimental and simulation result. The mould compound flows around the dies and moves quickly before it starts to cover the dies. However, the flow above the dies covers more area in the experiments compared to that of the simulation. The effect of dies on the flow fronts is clearly visible. It restricted the flow along the edges and over the dies. As a result, the flow around the dies is accelerated.

However, at 2.5 s the simulation flow front profile is found more slowly in filling compared to experiments. This phenomenon is caused by the simplification of the simulation model. The simplification on the stacked chip may be a factor for affecting the encapsulant during the process. The simplified chips act as a larger obstruction to the flow and caused the encapsulant to fill the free region. At 6 s of

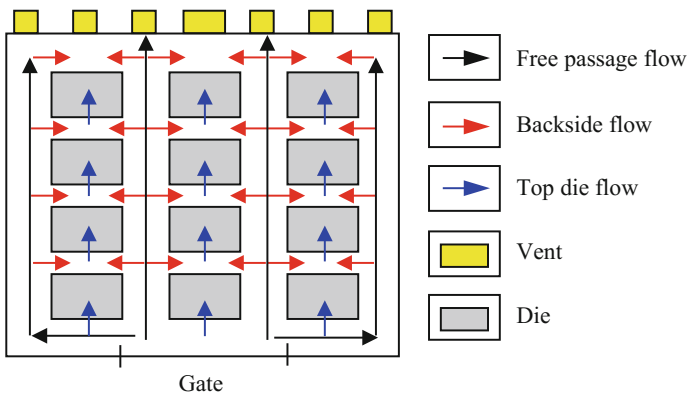


Fig. 3 Schematic of flow in the cavity

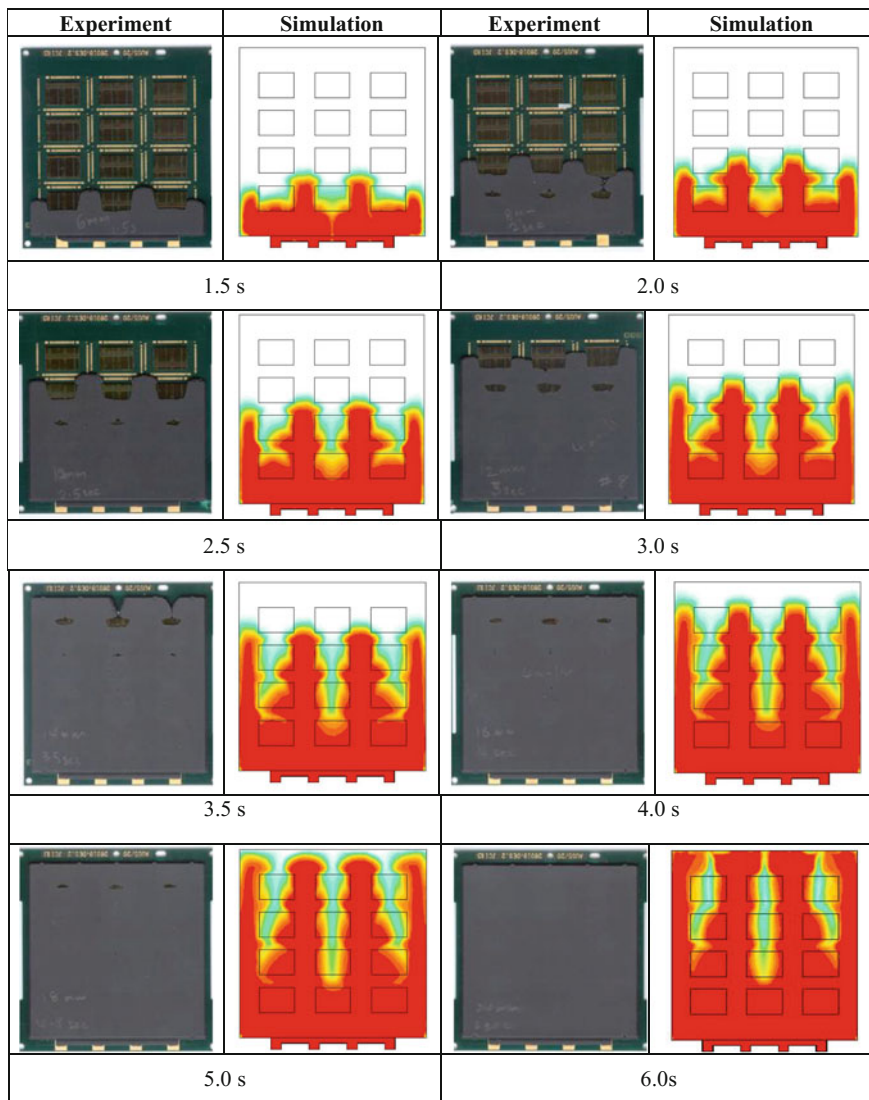


Fig. 4 Short shot results of melt front advancement at distinct time steps with velocity inlet of 4 mm/s

the filling stage, a void is found in the mold filling process. Figure 5 shows the void formation during the S-CSP filling process.

Figure 6 shows viscosity variation versus shear rate. The curves show as a power law viscosity variation where the viscosity reduces with the shear rate.

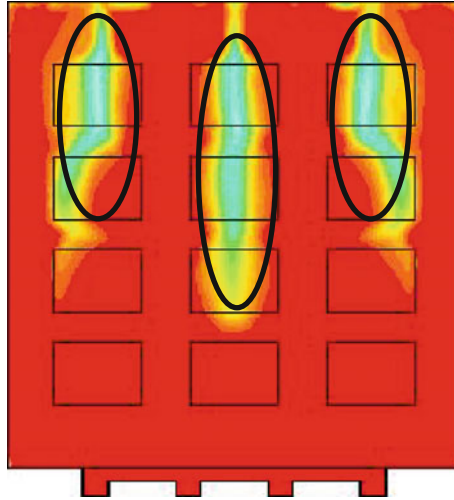


Fig. 5 Void formation at circled region

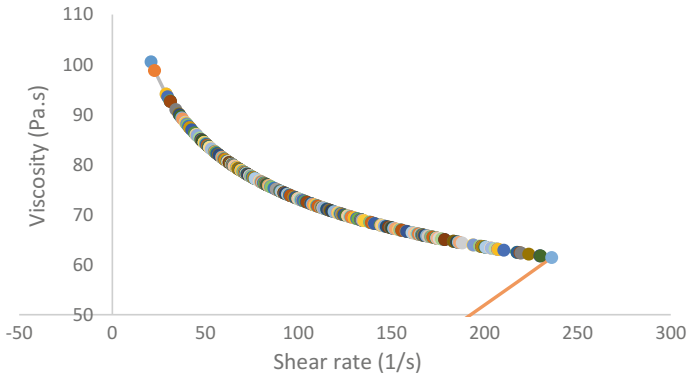


Fig. 6 Viscosity versus Shear rate

5 Conclusion

A three-dimensional non-isothermal incompressible analysis model based on the finite difference method (FVM) for the transfer moulding process is presented and compared with the experimental results. The three-dimensional S-CSP package is simulated to study the flow visualization in the process. The encapsulant material used is the Hitachi Chemical CEL-9200-XU (LF). Cross-viscosity model and volume of fluid (VOF) technique are used to track the flow front in the numerical simulation. Navier-Stokes equations are solved by the finite volume method and SIMPLE segregated algorithm. It is found that simulation results of melt fronts are

in good agreement with the experimental results, thus proving the strength of the model and the fluent software in handling stacked chip encapsulant problems. The present study may be extended further for more actual type of stacked chip and different parameters on different S-CSP packages.

References

1. Tummala, R.R.: *Fundamentals of Microsystems Packaging*, pp. 44–79. McGraw Hill, Singapore (2001)
2. Manzione, L.T.: *Plastic Packaging of Microelectronic Device*, pp. 1–35. Van Nostrand Reinhold, New York (1990)
3. Liang, C.W., Kulakarni, V.M., Aswatha Narayana, P.A., Seetharamu, K.N.: Parametric studies in transfer molding for Newtonian fluids. *J. Phys. Sci.* **16**(2), 103–114 (2005)
4. Kulkarni, V.M., Seetharamu, K.N., Azid, I.A., Aswatha Narayana, P.A., Quadir, G.A.: Numerical simulation of underfill encapsulation process based on characteristic split method. *Int. J. Numer. Meth. Engng.* **66**, 1658–1671 (2006)
5. Kada, M., Smith, L.: Advancements in Stacked Chip Scale Packaging (S-CSP) provides system-in-a-package functionality for wireless and handheld applications. *Future Fab. Intl.* **9**, 246–251 (2000)
6. Sze, M.W.H., Papageorge, M.: Encapsulation selection, characterization and reliability for fine pitch BGA (fpBGA). In: 4th Annual Flip Chip, BGA, Chip Scale Packaging '98, April 28–29, 1998, pp. 1–7 (1998)
7. Pei, C.C., Hwang, S.J.: Three-dimensional paddle shift modelling for IC packaging. *Trans. ASME J. Electron. Packag.* **127**, 324–334 (2005)
8. Nguyen, L., Quentin, C., Lee, W., Bayyuk, S., Bidstrup-Allen, S. A. and Wang, S.T.: Computational modeling and validation of the encapsulation of plastic packages by transfer molding. *Trans. ASME J. Electron. Packag.* **122**, 138–146 (2000)
9. Chang, R.-Y., Yang, W.-S., Chen, E., Lin, C., Hsu, C.-H.: On the dynamic of air trap in the encapsulation process of microelectronics package. In: *Proceedings of ANTEC' 98 Conference* (1998)
10. Zhou, T., Dreiza, M.: *Stacked Die Package Design Guidelines*. In: *Proceedings of IMAPS Conference* (2004)
11. Fukui, Y., Yano, Y., Juso, H., Matsune, Y., Miyata, K., Narai, A., Sota, Y., Takeda, Y., Fujita, K., Kada, M.: *Triple-Chip Stacked CSP*. In: *IEEE 2000 International Electronic Components and Technology Conference*. ISBN 0-7803-5908-9 (2000)
12. Kim, S.W., Turng, L.S.: Developments of three-dimensional computer-aided engineering simulation for injection molding. *Institute of Physics Publishing. Model. Simul. Mater. Sci. Eng.* **12**(2004), S151–S173 (2004)
13. Turng, L.S., Wang, V.W.: On the simulation of microelectronic encapsulation with epoxy molding compound. *J. Reinf. Plastics Compos.* **12**, 506–519 (1993)
14. Han, S., Wang, K.K.: Flow analysis in a cavity with lead frame during semiconductor chip encapsulation. In: *Advance in Electronic Packaging*, ASME EEP, vol. 10–11 (1995)
15. Nguyen, L.T.: Reactive flow simulation in transfer molding of IC Packages. In: *Proceedings 43rd IEEE Electronic Components and Technology Conference 1993*, pp. 375–390 (1993)

Conference Proceeding

16. Nguyen, L.: Flow simulation in IC chip encapsulation. Electronic Components and Technology Conference, Buena Vista (1994)
17. Nguyen, L., Jackson, J., Teo, C.H., Chillara, S., Asanasavest, C., Burke, T., Walberg, R., Lo, R., Weiler, P., Ho, D., Rauhut, H.: Wire Sweep Control with Mold Compound Formulation. In: 1997 Proceedings 47th Electronic Components and Technology, pp. 60–71 (1997)
18. Nguyen, L., Quentín, C.G., Lee, W.W.: Flow modeling and visualization of the transfer molding of plastic ball grid array packages. In: 1999 Electronic Components and Technology Conference, Santa Clara (1999)
19. Lee, M.M., Kim, J.Y., Yoo, M., Chung, J.Y., Lee, C.H.: Rheological characterization and full 3D mold flow simulation in multi-die stack CSP of chip array packaging. In: Electronic Components and Technology Conference, 1-4244-0152-6/06(2006)
20. Khalil Abdullah, M., Abdullah, M.Z., Mujeebu, M.A., Kamaruddin, S.: A study of effect of epoxy molding compound (EMC) rheology during encapsulation on stacked-CHIP scale packages (S-CSP). *J. Reinf. Plast. Compos.* 28, 2527–2538 (2008)
21. Khalil Abdullah, M., Abdullah, M.Z., Kamarudin, S., Ariff, Z.M.: Study of flow visualization in stacked-chip scale packages (S-CSP). *Int. Commun. Heat Mass Transfer* 34(7), 820–828 (2007)
22. Khor, C.Y., Mujeebu, M.A., Abdullah, M.Z., Che Ani, F.: Finite volume based CFD Simulation of pressurized flip chip underfill encapsulation process, microelectronics reliability. *Microelectron. Reliab.* 50(1), 98–105 (2010)

Book Chapter

23. Modeling multiphase flow, FLUENT Documentation, Chapter 23

Analysis of Temperature Distribution Behavior of Motorcycle Brake Pads



Khairul Shahril bin Shaffee, Mohd Khairuddin Hj. Ali Musa, Mohamad Sabri Mohamad Sidik, Mior Firdaus Mior Abd. Majid and Muhamad Husaini Abu Bakar

Abstract The gradual phasing-out of asbestos in motorcycles brake friction materials in many parts of the world has sparked the onset of extensive research and development into safer alternatives. As a result, the brake friction industry has seen the birth of different brake pads and shoes in the past decade, each with their own unique composition, yet performing the very same task and claiming to be better than others. This suggests that the selection of the brake pad design geometry surface is based more on original shape and simulation trial and error rather than fundamental understanding. This analysis strives to eliminate the cloud of uncertainty by providing an insight into the pros and cons of the geometry surface shape of motorcycle brake pad and make-up used in contemporary temperature behavior distribution on pads and shoes. In this analysis brake pad designs are reviewed and their advantages and disadvantages in contemporary brake applications are discussed.

Keywords Different brake pads geometry surfaces · New design Temperature distribution · Brake friction · Advantages and disadvantages brake pads

K. S. bin Shaffee (✉) · M. K. Hj.A. Musa · M. S. Mohamad Sidik
M. F. M. Abd.Majid
Mechanical Section, Universiti Kuala Lumpur Malaysian Spanish Institute,
Kulim Hi-Tech Park, 09000 Kulim, Kedah, Malaysia
e-mail: khairuls@unikl.edu.my

M. K. Hj.A. Musa
e-mail: khairuddin.jpm@gmail.com

M. S. Mohamad Sidik
e-mail: msabri@unikl.edu.my

M. F. M. Abd.Majid
e-mail: miorfirdaus@unikl.edu.my

M. H. A. Bakar
Manufacturing Section, Universiti Kuala Lumpur Malaysian Spanish Institute, Kulim
Hi-Tech Park, 09000 Kulim, Kedah, Malaysia
e-mail: muhamadhusaini@unikl.edu.my

1 Introduction

Brake pads are a component of disk brakes used in automotive and other applications. Brake pads are steel backing plates with friction material bound to the surface that faces the disk brake rotor. Brake pads convert the kinetic energy of the car to thermal energy by friction. Two brake pads are contained in the brake caliper with their friction surfaces facing the rotor. When the brakes are hydraulically applied, the caliper clamps or squeezes the two pads together into the spinning rotor to slow/stop the vehicle. When a brake pad is heated by contact with a rotor, it transfers small amounts of friction material to the disc, turning it dull gray. The brake pad and disc both now with friction material, then “stick” to each other, providing the friction that stops the vehicle.

Brake pad materials range from asbestos to organic or semi-metallic formulations. Each of these materials has proven to have advantages and disadvantages regarding environmental friendliness, wear, noise, and stopping capability. Semi-metallic pads provide strength and conduct heat away from rotors but also generate noise and are abrasive enough to increase rotor wear.

Asbestos was widely used in pads for its heat resistance but, due to health risks, has been replaced with alternative materials, such as mineral fibers, cellulose, aramid, chopped glass, steel, and copper fibers as shown in Fig. 1. Depending on material properties, disc wear rates vary. The properties that determine the material’s wear, involve trade-offs between performance and longevity. Newer pads can be made of exotic materials like ceramics, aramid fibres, and other plastics. Vehicles have different braking requirements. Friction materials offer application-specific formulas and designs. Brake pads with a higher coefficient of friction provide good braking performance with less brake pedal pressure requirement, but tend to lose efficiency at higher temperatures which increases the stopping distance. Brake pads with a smaller and constant coefficient of friction do not lose efficiency at higher temperatures and are stable, but require higher brake pedal pressure.

Fig. 1 Brake pads



1.1 Problem Statement

The disc brake is a device for slowing or stopping the rotation of a wheel of vehicles. To stop the wheel, the friction material in the form of brake pads is forced mechanically, hydraulically, pneumatically, or electromagnetically against both sides of the disc and causes the wheel to slow down or stop.

By the First Law of Thermodynamics, when the brake pedal is pressed, the brakes on the vehicle heat up, slowing it down. But if the brakes are used rapidly, the discs and brake pads will stay hot and get no chance to cool off. The brake cannot absorb much more heat because the brake components are already so hot. The braking efficiency is reduced. This malfunction of the brake system is called the brake fade. In every brake pad there is the friction material which is held together with some sort of resin. Once the brake pad starts to get too hot, the resin holding the pad material together starts to vaporize forming gas. This gas cannot stay between the pad and the disc, so it forms a thin layer between the brake pad and rotor trying to escape. The pads lose contact with the disc, thus reducing the amount of friction. The design of the brake pad is important to determine the rate of cooling and uniform wear of disc and brake pad and thus affecting the braking efficiency.

This project will focus on the simulation analysis of the temperature distribution behavior of motorcycle brake pads during operation when forces and moments generated from the braking are applied. The temperature distribution of the brake pad from the simulation result can be analyzed. To study about the effect of motorcycle brake pads performance includes the following variables:

- Contribution on heat transfer coefficient (h),
- Temperature (T),
- Total heat (q),
- Brake pads geometry (surface, area) and provide result of area.

There is never a right analysis data about motorcycles brake pads.

High temperature distributions at disc brake components may cause undesirable effects, leading to brake failure.

1.2 Objective

The aim of this project is to determine the temperature distribution and to study the temperature behavior from the new design geometry shape of motorcycle brake pad. To achieve this project, the objectives are set as below:

1. To analyze the temperature distribution as well as the maximum temperature attained.
2. To design a new model of motorcycle brake pads.
3. To compare the datum design with the new design to determine the best design of motorcycle brake pads.

1.3 Scope and Limitation

The scopes and limitation of this project are:

1. Literature review on the working principles, component, standard and theories about the brake system.
2. To analyze the temperature distribution behavior of the best geometry shape design for the motorcycle brake pad.
3. Develop a new design geometry surface of brake pads.
4. Simulation of the thermal transient behavior using ANSYS software.
5. Construction of 3D modeling for motorcycle brake pad design.

2 Literature Review

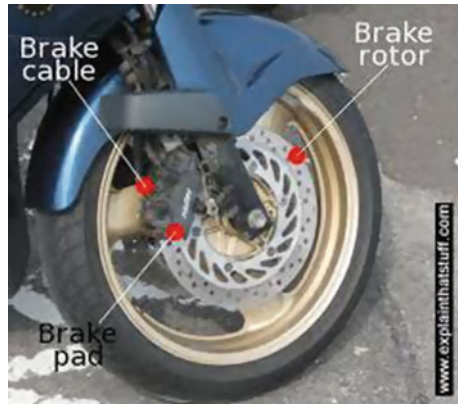
The braking system used in the car is used primarily to help the driver to control the vehicle deceleration. It is one of the major systems and specifically designed to reduce the speed of a fast-moving vehicle. An ordinary car braking system consists of a brake device having different components, which are used to slow down or stop the vehicle. More precisely, the tools to reduce or stop the speed of a moving or rotating body by absorbing kinetic energy mechanically or electrically. The system automatically controls the wheel slip and prevents the wheels from spinning. They are widely used in motor vehicles, buses, trucks, trains, airplanes, motorcycles and other types of vehicles. The braking system used in cars has come a long way in recent years. The use of anti-lock braking system along with the introduction of different brake components made of carbon fiber, steel, aluminum and others have completely stopped giving better performance compared to traditional brake system.

Sliding contact member brake discs result in the conversion of kinetic energy into heat at the pad and disc interface. Increase in friction is a limited quantity and depends on the coefficient of friction, rubbing the radius of the road, and the forces acting on the pad. The slip process leads to a rise in temperature, while the peak is one of the most important factors in the action to occur. The temperature at the contact surfaces during the quarter emergency brake system is intensified by a significant heat load caused by the friction force and high velocity of this process [1].

Temperature and thermal constriction resistance as a function of the parameters of the velocity is determined. Temperature and thermal stresses pad (band) with retarded continuous sliding on the surface of the disk (a half) both during and after the heating studied [2].

However these geometric configurations can study with the actual engineering applications, where there is no perfect solution, particularly the application of finite frictional heating system needs to be recognized. Simplification of the actual

Fig. 2 Motorcycle brake pads system



modeling techniques from three-dimensional to two-dimensionality associated with the rate of heat uniformly distributed circumferentially were so far achieved [3].

Disc brakes consist of a cast iron disc that rotates with the wheel, caliper fixed to the steering knuckle and the friction material (brake pads) as shown in Fig. 2. When the braking process occurs, the hydraulic pressure forces the piston and therefore the pad and the disc brakes are in sliding contact. This prepares a resistance movement and the vehicle slows down or eventually stops. The friction between the disc and the pads are always opposes to the motion and the heat generated by the conversion of kinetic energy. Under the influence of temperature, friction elements, the operating conditions become less favorable friction patches and result in decreasing wear and friction coefficient decreases, which can lead to emergency situations. Therefore, experimental, mathematical and numerical modeling of the temperature distribution is a significant problem in the design of the braking system.

The experimental determination of the surface temperature of objects authentic touch in most cases significant technical problems and expenses [4]. Therefore, the analytical or numerical definition of a temperature regime of friction pair elements obtained with the corresponding problem solving frictional heat during braking attracted great interest.

3 Methodology/Experimental Set-Up/Model Set-Up

There is an advantage of brake pads, where most of them are poor to thermal conductivity which protects the hydraulic actuating elements from overheating. It is also ease to manufacture and low cost. However, the pads needs to be inspect frequently due to rapid wear as a result from higher temperatures and contact pressures associated with the operation of a brake disc. Figure 3 shows a typical geometry of the brake pad design.

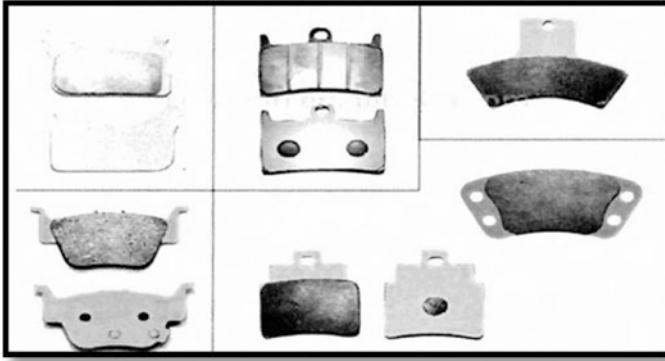


Fig. 3 Motorcycle brake pads geometry shape

3.1 Modeling Software

There are different softwares available for modeling some of them are:

- Solid works
- Pro-E
- Ideas
- Inventor
- Catia v5.

Solidworks a multi-platform CAD/CAM/CAE is used as the modeling tool in this project.

3.2 Solidworks (Part Modeling)

The SolidWorks is a Parasolid-based solid modeler, and utilizes a parametric feature-based approach to create models and assemblies. Parameters refer to constraints whose values determine the shape or geometry of the model or assembly. Parameters can be either numeric parameters, such as line lengths or circle diameters, or geometric parameters, such as tangent, parallel, concentric, horizontal or vertical, etc. Numeric parameters can be associated with each other through the use of relations, which allow them to capture design intent. SolidWorks allows the user to specify that the hole is a feature on the top surface, and will then honor their design intent no matter what height they later assign to the model as shown in Fig. 4.

Building a model in SolidWorks usually starts with a 2D sketch (although 3D sketches are available for power users). The sketch consists of geometry such as points, lines, arcs, conics (except the hyperbola), and splines. Dimensions are added



Fig. 4 Brake pads part design using solidworks

to the sketch to define the size and location of the geometry. Relations are used to define attributes such as tangency, parallelism, perpendicularity, and concentricity. The parametric nature of SolidWorks means that the dimensions and relations drive the geometry, not the other way around. The dimensions in the sketch can be controlled independently, or by relationships to other parameters inside or outside of the sketch.

3.3 Material Properties

Young’s modulus (EX) must be defined for a static analysis. If we plan to apply inertia loads (such as gravity) we define mass properties such as density (DENS). Similarly if we plan to apply thermal loads (temperatures) we define the coefficient of thermal expansion (ALPX) as shown in Table 1.

3.4 Thermal Analysis

A thermal analysis calculates the temperature distribution and related thermal quantities in a system or component. Typical thermal quantities are:

- The temperature distributions
- The amount of heat lost or gained
- Thermal fluxes.

Table 1 Material properties for asbestos

Thermal conductivity	2.06 w/m/k
Density	2798 kg/m ³
Specific heat, c (J/kg k)	691
Poisson’s ratio, ν	0.25
Thermal expansion (×10.5)	1.0
Elastic modulus	14.25 GPa
Coefficient of friction, μ	0.2

Types of Thermal Analysis:

1. A steady state thermal analysis determines the temperature distribution and other thermal quantities under steady state loading conditions. A steady state loading condition is a situation where heat storage effects varying over a period of time can be ignored.
2. A transient thermal analysis determines the temperature distribution and other thermal quantities under conditions that vary over a period of time. The expected result at the end of the research is when the measurement surface geometry changes, the temperature conditions will decrease and produce better results.

3.5 Mesh Generations

In the finite element analysis the basic concept is to analyze the structure, which is an assemblage of discrete pieces called elements, which are connected, together at a finite number of points called nodes. Loading and boundary conditions are then applied to these elements and nodes. A network of these elements is known as the mesh (Fig. 5).

Fig. 5 Meshed model of the brake pads

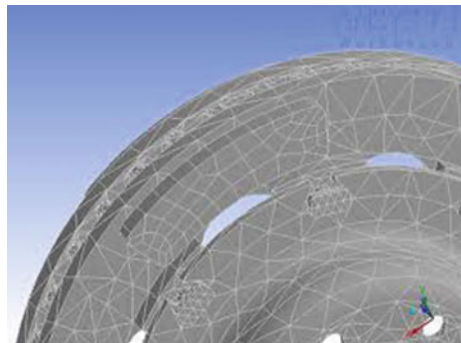
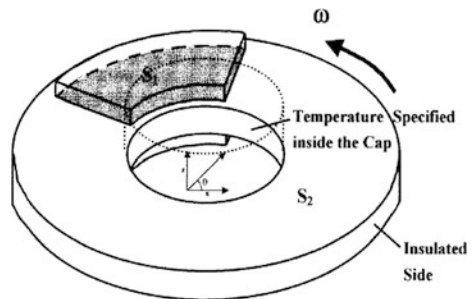


Fig. 6 Boundary condition



3.6 Condition

As shown in Fig. 6 a model presents a three-dimensional solid disk squeezed by two finite-width friction material called pads. The entire surface, S , of the disk has three different regions including $S1$ and $S2$. On $S1$ the heat flux is specified due to the frictional heating between the pads and disk, and $S2$ is defined for the convection boundary. The rest of the region, except $S1$ and $S2$, is either temperature specified or assumed to be insulated: the inner and outer rim area of the disk.

4 Results and Discussion

Design analysis

From the ten design variations, the best design has been chosen which is the design that had a lower maximum temperature distribution. Value of material properties has been added to the new design and then the analysis has been done. The result is shown in Fig. 7.

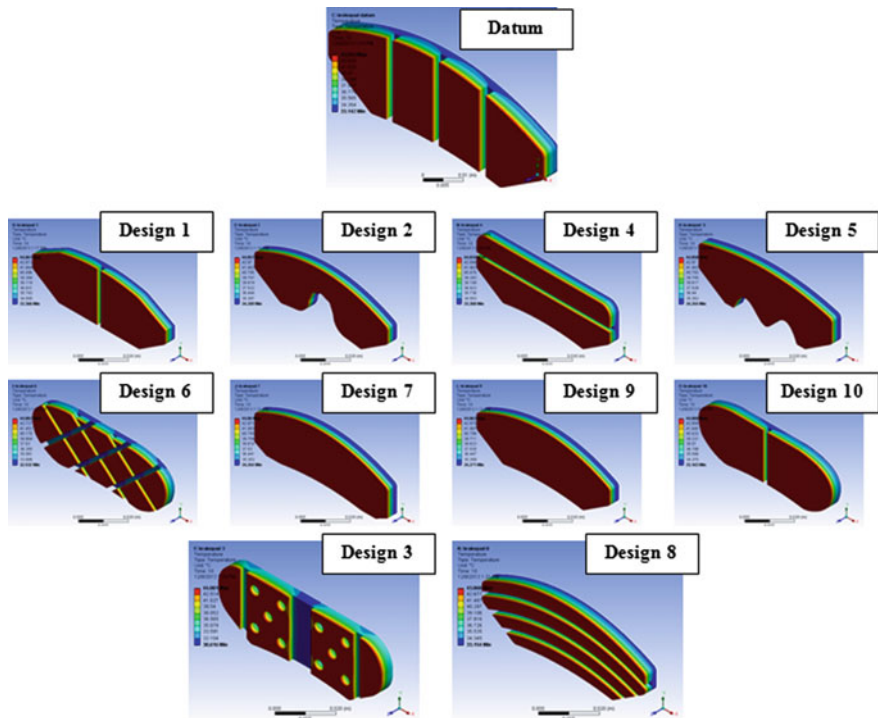


Fig. 7 Design analysis using thermal approach

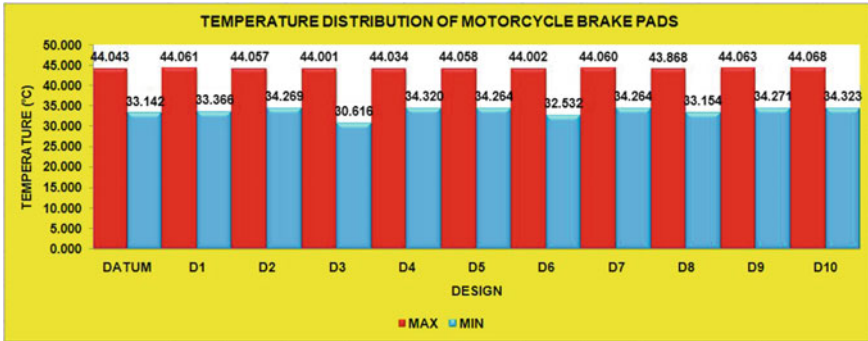


Fig. 8 Temperature distribution

Criteria to determine a good design with datum design

The graph in Fig. 8 shows that the lowest maximum temperature is design 8, compared with the datum design. The results shown in the graph of the temperature distribution, that the actual design 8 is the best compared with the other design. The graph in Fig. 9 shows the total heat flux for all designs compared with the design datum. In this analysis, the determination of the best design is dependent on the highest total heat flux. What can we see in this graph is that the design 3 is the best from the datum design and the design 8 the best design and was selected in the graph of temperature distribution.

Comparison of the new design with the datum design

The pie chart in Fig. 10 shows the difference in percent of each design compare to the design datum. This percentage pie chart shows that the design 8 is the best with 46.54%, while design 3, shows the percentage of 11.17% is moderately good and the percentage of the worst in this analysis is the design 4 which is 2:39% compared to the datum design.

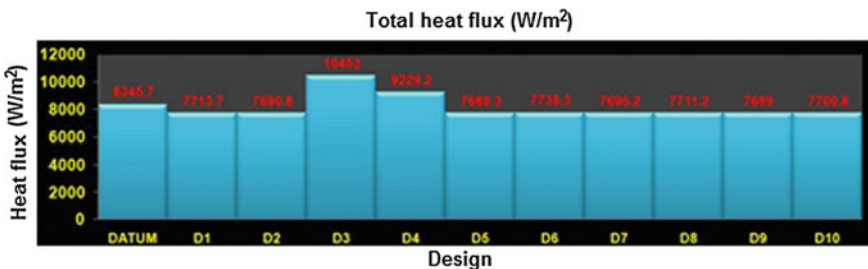


Fig. 9 Total heat flux

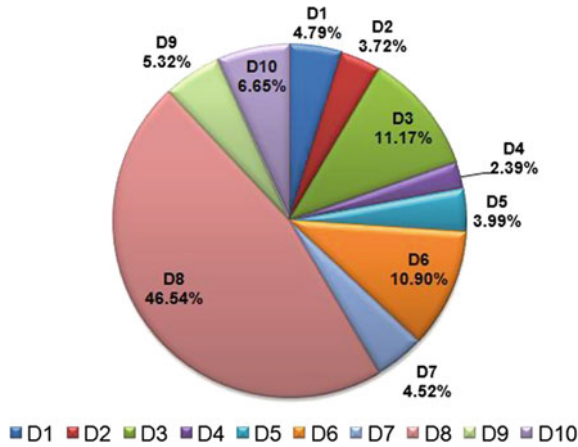


Fig. 10 Percentages new design compared to datum design

5 Discussion

After all the analysis has been completed and the data collection in each analysis, some problems have occurred in the analysis. To find the best design is so difficult because there are two designs, which have their own advantages in the design. First, design 8 (the best lower temperature distribution) and second, design 3 (the best total heat flux), this decision has to be made, with a look at some of the factors that enabled the results to be accurate. Therefore, an additional analysis was made which makes the analysis of the distribution of the temperature, for all design including the datum design to see the movement of the temperature, from the front temperature to the center/grooving surface to the back surface. Among other factors to be considered are analyze the pro & contra between the two designs in Fig. 11 are:

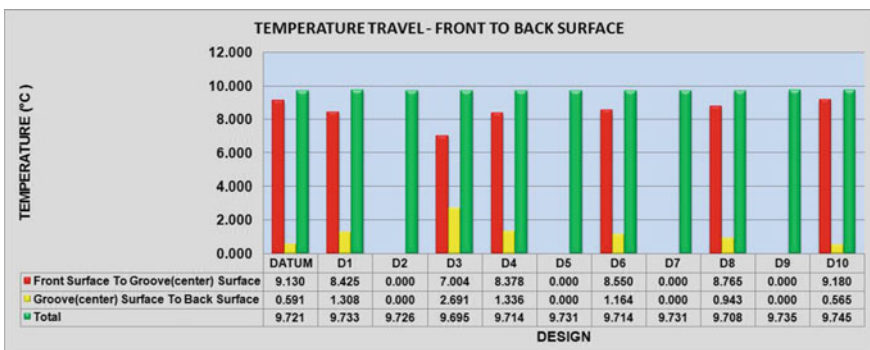


Fig. 11 Percentages of new design compared to datum design

- (Design 3—easy to wear and suitable for superbike racing only)
- (Design 8—can be used for long time and suitable for all standard bikes).

Finally, after consideration of all the mentioned factors, design 8 has been selected to be the best design in the analysis.

6 Conclusion

The conclusion can be made from the result obtained from different forms, the modified model with different surface pads has a better result than the datum design. So the best design option is design 8, after a comparisons made according the criteria required to achieve the objective of the analysis. Finally, it can be concluded that the temperature is slowly expanding by the selected design from design 3, is due to the large surface area and temperature distribution for the selected design is the best design of the datum and nine others.

Acknowledgements First and foremost, all praise be to Allah, the Almighty, the Benevolent for His blessing and guidance for giving us inspiration to embark on this project and instilling in all of us the strength to see this final year project (Analysis of Temperature Distribution Behavior of Motorcycle Brake Pads). Many people have contributed to the creation and completion of this research. We would like to express our gratitude to our supervisor, Mr. Khairul Shahril, because he gives all his effort to conduct us as from the beginning until we finish up our research. He also gives us a lot of guidance and support. We are especially indebted and grateful to the lectures of mechanical department, UniKL MSI. This project gave me an opportunity to participate and learn about the basic and advance skill of handling the great software there are SOLIDWORKS and ANSYS. Special thanks to all my friends for their understanding and support on me in completing this research. Without helps of the particular that mentioned above, i would face many difficulty while doing this.

References

1. Zhu, Z.-C., Peng, Y.-X., Shia, Z.-Y., Chen, G.-A.: Three-dimensional transient temperature field of brake shoe during hoist's emergency braking. *Appl. Therm. Eng.* **29**(5–6), 932–937 (2009)
2. Yevtushenko, A., Kuciej, M.: Temperature and thermal stresses in a pad/disc duringbraking. *Appl. Therm. Eng.* **30**(4), 354–359 (2010)
3. Talati, F., Jalalifar, S.: Investigation of heat transfer phenomena in a ventilated disk brake rotor with straight radial rounded vanes. *J. Appl. Sci.* **8**(20), 3583–3592 (2008)
4. Buyanovskii, I.A., Fuks, I.G.: Physical and chemical aspects of lubricity. *J. Friction Wear* **22**, 227–233 (2001)

Application of a Portable Coordinate Measuring Machine onto Automotive Door Panel for Quality Inspection Activity



Tajul Adli bin Abdul Razak, B. T. Hang Tuah bin Baharudin, Khairul Shahril bin Shafee and Khairul Akmal bin Shamsuddin

Abstract An experimental investigation was conducted to explore the feasibility of replacing the current inspection method by a portable coordinate measuring machine (CMM) for daily quality inspection in automotive industry. The experiment focusses on inspecting stamped body parts due to the significant number of inspection points that could be time consuming for inspection activities. Two inspection methods were performed, i.e. the application of checking fixture (CF) which is the current method and the second method was using a portable CMM. Both inspections were performed onto the same loose freeform surface of an outer door panel. Factors related to inspection duration, economical and data reliability were all compared to understand the practicality of replacing the current inspection method with a portable CMM. It was found that a portable CMM provide a significant shorter inspection duration, more economical and better data reliability but at the same time is unable to match the performance of conventional inspection onto freeform surface. The conclusion was made that a portable CMM alone is not sufficient to replace the current inspection method thus require further study.

T. A. bin Abdul Razak (✉) · K. S. bin Shafee · K. A. bin Shamsuddin
Malaysian Spanish Institute, Universiti Kuala Lumpur, Hi-Tech Park,
09000 Kulim, Kedah, Malaysia
e-mail: tajul.adli@yahoo.com.my

K. S. bin Shafee
e-mail: khairuls@unikl.edu.my

K. A. bin Shamsuddin
e-mail: khairulakmal@unikl.edu.my

B. T. H. T. bin Baharudin
Department of Mechanical and Manufacturing, Universiti Putra Malaysia,
43400 UPM Serdang, Selangor Darul Ehsan, Malaysia
e-mail: hangtuah@upm.edu.my

Keywords Automotive industry · Manufacturing · Portable CMM
Quality inspection

1 Introduction

Quality inspection is part of quality control to detect any defective product and separate it from non-defective products. Inspection is performed at various stages in automotive manufacturing activities starting from incoming material, loose parts, assembled parts and finally to a complete car. In the objective to achieve the highest quality of the product in current mass production business operation, automotive manufacturers have practiced a sampling method in their quality inspection activities.

For obvious reason, it is impossible to perform 100% inspection on mass production due to the massive volume. It will be impractical and time consuming for such commitment. Unlike certain super luxury car makers such as Ferrari and Lamborghini for instance, the volume is small and consider niche that these companies are able to perform 100% inspection on their parts and finished goods. Instead of performing 100% inspection, other car makers that operate in mass production business operation are more interested in inspecting a fraction of samples out of the total volume and produce a mathematical analysis that can indicate the capability of the production process and predict the future trend of quality. Accuracy of this analysis is highly depending on the size of the samples. More samples will produce highly accurate analysis and vice versa.

Sampling has become the practice of many industries especially in mass production business operation in performing reasonable inspection onto a certain number of samples. The randomly picked sample will be measured and evaluated in detail that in the end, will reflect the quality of a production batch. Due to the increasing complexity of engineering parts, standard inspection procedures alone is not always suffice to achieve given quality standards. The higher quality requirement has prompted industries to increase the capabilities of measuring device and with the application of automated coordinate measuring machine (CMM) in automotive industry, it has improved the efficiency of quality inspection. However, automated CMMs are not widely used due to the various limitations of the CMM itself. An automated CMM is more suitable to measure specific pre-programmed assembled products compared to simpler and relatively smaller size parts such as door panels.

Rather than using automated CMMs for measuring, industries are often resolute to checking fixture (CF) and gauge to complete simpler inspection task that can be performed by humans due to its simplicity. The same concept is used in measuring the surface profile, CF that follows the profile of inspected component is introduced as inspection equipment for cheaper, robust and straight forward measurement equipment.

2 Problem Statement

Initial setup of CF will require certain steps for physical geometrical alignment which often could be the major drawback of this method [1]. The problem will start to emerge when there are more parts to inspect. For instance, if a company has 3 different car models to produce, then the company will have 3 different CF for door panel to inspect. In normal practice, a door panel will consist of an inner and an outer door panel. This will require in total 6 CF for door panel inspection. For a single car model, there will be 4 doors as shown in Fig. 1. All 4 doors consist of inner and outer door panel is equivalent to 8 CF. That will be for 1 car model. If a company produce 3 different car models, total CF for door inspection is 24 in total.

The direct effect of the inspection method to this system are:

- Compounding inspection activity is far more time consuming.
- Large area for CF storage.
- Increasing investment for CF development.

The effect is significant towards manufacturing efficiency considering from macro view perspective. A new approach of inspection is required to avoid any future congestion at the inspection area. The objective can be achieved by changing the manufacturing policy regarding new model introduction planning, which requires massive management changes that can be some distance away in the future. Other practical method to increase the manufacturing efficiency could be, re-invent the inspection method using suitable latest technology. This study will look into possibilities of extending the usage of portable CMM in daily quality inspection.

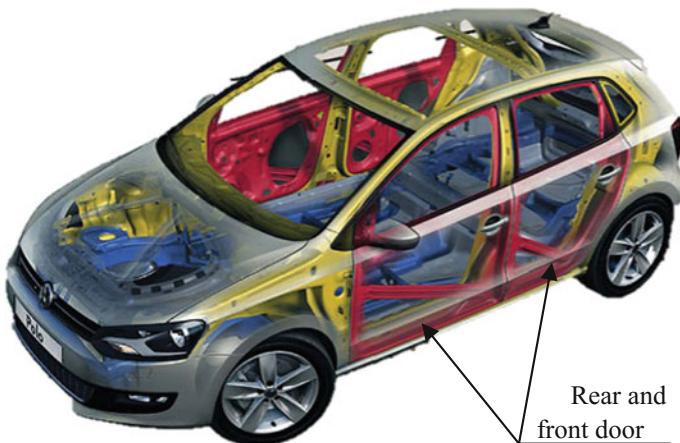


Fig. 1 Sedan model consist of rear and front door assemble

3 Frequent Inspection

Quality in manufacturing can be referred as a state being free from defects, deficiencies and significant variations. It is a practice of consistent commitment to achieve uniform products within permissible tolerance to satisfy certain requirement or specific customers. A basic engineering premise is that a condition is acceptable when “it is close enough for practical purposes” [2].

In order to maintain the close control of production quality, frequent measurement and process parameter adjustments are desirable [3]. Frequent inspection needs to be done to monitor any deviation from the process that can affect the finished good. To inspect is to determine compliance to a specification for such as tolerance by measuring, gauging, or other means of examination [4]. Among other systematic tools used in quality assurance (QA) is statistical process control (SPC). It is an industrial-standard methodology for analyzing process capability in producing quality parts during the manufacturing process. Statistical process control (SPC) is a useful technique of monitoring a production process with the application of control charts. The collected data from random samples or in-process production in various stages can produce an analysis of variations or trends of the processes that may affect the quality of the end product. Since the data is gathered much earlier before the assembly process begins, problems can be detected and eliminated earlier compared to quality control that detects problems at the end of finished goods. Early detection of problems through SPC can reduce wasted time and resources and may detect defects that other methods would not.

SPC is a powerful collection of problem-solving tools useful in achieving manufacturing process stability and improving capability through the reduction of variability [5]. The advantage of SPC for quality assurance (QA) is the application of sampling techniques which require small amount of samples to represent the whole. The sampling strategy is to determine the representative points which are to be measured to approximate the real feature [6]. Application of sampling in quality assurance (QA) can decrease the number of parts to inspect from 100 to 15% or lesser, thus saving time and cost for inspection activity.

3.1 *Coordinate Measuring Machine*

In automotive industry, there has been an increasing requirement of faster measurement of the parts for quality control purposes. This cannot be achieved by using traditional coordinate measurement machines (CMM), due to the time-consuming nature of the point-wise contact measurement [7]. Inspection needs to step up from manual inspection to digital inspection. A digital inspection technique must embody a number of simultaneous characteristics: high speed, high accuracy, large measurement volume, ability to measure features on both simple and complex parts, ability to measure parts with complex surface finishes ranging from freshly

machined to dark paint, operation in ambient factory lighting conditions, real-time data analysis, and operational simplicity [8]. Overall limitation can be classified as below:

- Measuring complex surface profile
- Measuring deformable and fragile parts
- Measuring tube and pipe
- Less portable due to its mechanical build up.

3.2 *The Portable CMM*

A coordinate measuring machine (CMM) is a measuring device that measures the physical geometry of a part. It can be operated both manually and automatically. A CMM is mainly based on mechanical systems designed to move a measuring probe to determine coordinates of points on a workpiece surface. The probe can be mechanical, laser, optical or white light and moved based on the X, Y, Z coordinate. It provides precise measurements of objects for design, testing, assessment, profiling, and reverse engineering of parts. Machines are available in a wide range of sizes and designs depending on the requirements. Based on the requirement also, the interface of software is different from one software to another.

There are mainly 3 main components for CMM: the mechanical machine itself, the measuring probe, and the control or computing system with measuring software. A probe is used to measure different points on the measured part by mapping the X, Y, Z coordinates. The probe operates either manually by an operator or automatically by a control system. The X, Y, Z coordinates are then uploaded to a computer interface where they can be recorded and examined using the specific software integrated in the system.

The main characteristic that differentiates a traditional CMM from a portable CMM is the method to move the probe. A portable CMM uses articulated arms to freely move around the object while for a traditional CMM, the probe is moved on 3 Cartesian axes representing X, Y and Z respectively. As requirements on complexity and accuracy of dimensional metrology increase, multi sensor measurements combining different sensors are implemented to achieve both holistic geometrical measurement and improved reliability of measured data. Because laser scanners and tactile probes have complementary characteristics in capability, systems combining the two are quite common [9]. The accuracy of laser scanning in 3D data acquisition, for a laser scanner mounted on a CMM, is about 25 microns at best, while the accuracy obtained by a CMM equipped with a contact probe is less than a micron [10]. We will use a portable CMM integrated with a 3D laser scanner technology for the study. Measuring instruments that consist of hardware and software from 2 different companies will be used to assist on the measurement.

4 Methodology

The selected mechanical instrument for inspection is a ROMER Absolute Arm that has an integrated laser scanner with portable CMM probing. This hardware has both, i.e. a laser scanner and a probe needle in one single head. The software integrated to this articulated arm is PolyWork Inspector that has the ability to embedded CATIA data and provides a very user-friendly measuring interface. The sample to be used in this study is outer front door panel, right hand (RH) consisting of Outer front door panel as shown in Fig. 2.

Inspection will be performed onto the loose component and comparison among two different inspection techniques will be observed from aspect of duration to inspect, reliability of measured data, cost saving and other related benefits. A cumulative of 51 points of checking need to be performed in this case study. The points are partially taken from the actual inspection practice from OEM. All points are important for various manufacturing reasons such as ease of assembly, wind noise avoidance, surface tangency etc. Table 1 explains the allocation of the 51 points for the outer door panel and show as in Fig. 3 the position of inspection points respectively. There are several steps to follow in completing the task of inspection by using the checking fixture as shown in Fig. 4.

By imitating the same steps for comparison purpose, portable probing also will follow the same set of activities to obtain actual comparison among the 2-inspection method. Figure 5 is the flow chart for the portable probing.

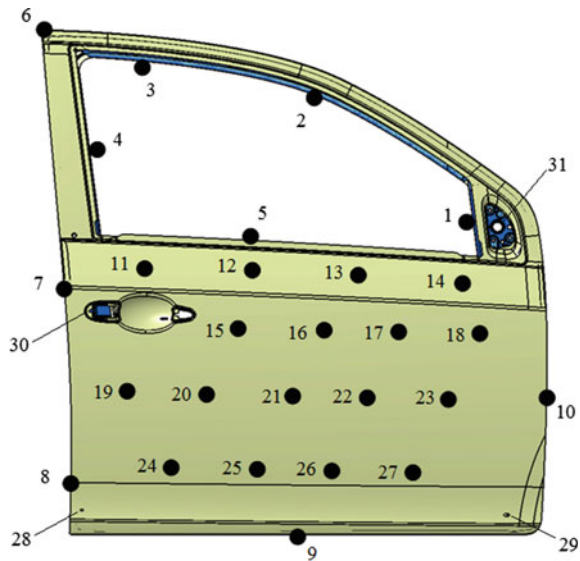
Fig. 2 Inner and outer front door assemble



Table 1 Points allocation of inspection

Point	Inspection area	Inspect item	Total points	Accumulated points
1–5	Window Opening	Surface height	5	5
		Trim edge	5	10
6–10	Edge	Surface height	5	15
		Trim edge	5	20
11–27	Surface area	Surface height	17	37
28–31	Holes and slot location	X	4	41
		Y	4	45
		Z	4	49
	Hole Diameter	Diameter	2	51

Fig. 3 Location of inspection points



5 Results and Discussion

5.1 Inspection Time

The duration taken to inspect outer front door panel has shown a significant time saving when using the Portable CMM probing compared to be checking fixture inspection practice. Figure 6 shows the comparison in every step stated in the previous flowchart.

As proven from Fig. 6, the total duration of inspection using the portable CMM probing is 78 min. A staggering 2.9 h faster than using the checking fixture.

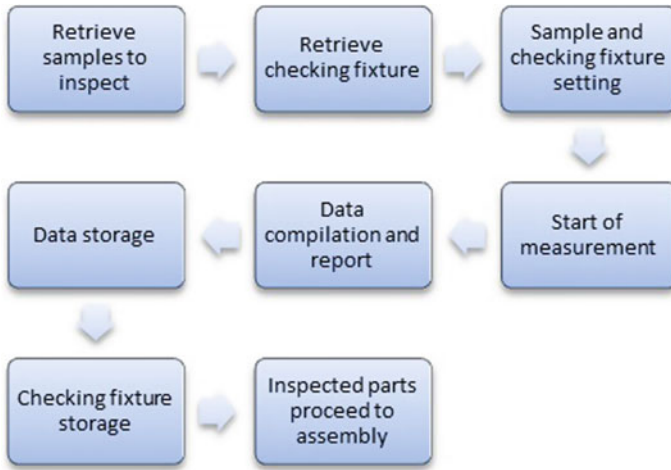


Fig. 4 Flowchart of inspection activity with CF

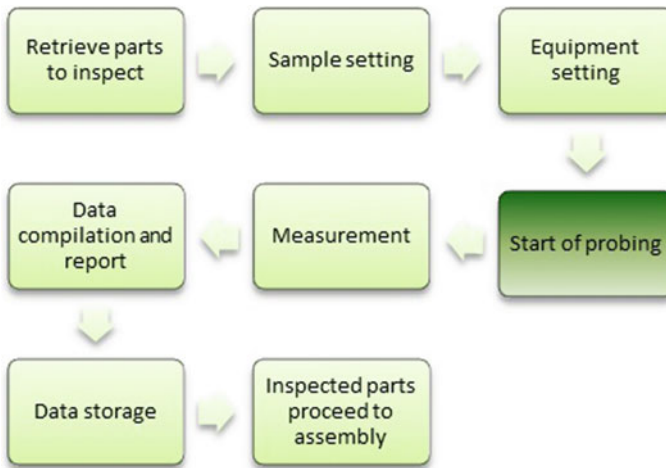


Fig. 5 Flowchart of inspection activity with portable probing

In overall, the major contributors to time reduction in the inspection activity when using the Portable CMM Probing are:

- Measuring equipment setup—Since there is no checking fixture involved, there will be no checking fixture retrieval issue. By using a portable CMM with user friendly inspection software, the troublesome arrangement with another separate department will be eliminated.
- Part setting—Measured parts will be aligned in 3D and embedded with 3D data using Polyworks Inspector. It is a simple and quick process to perform.

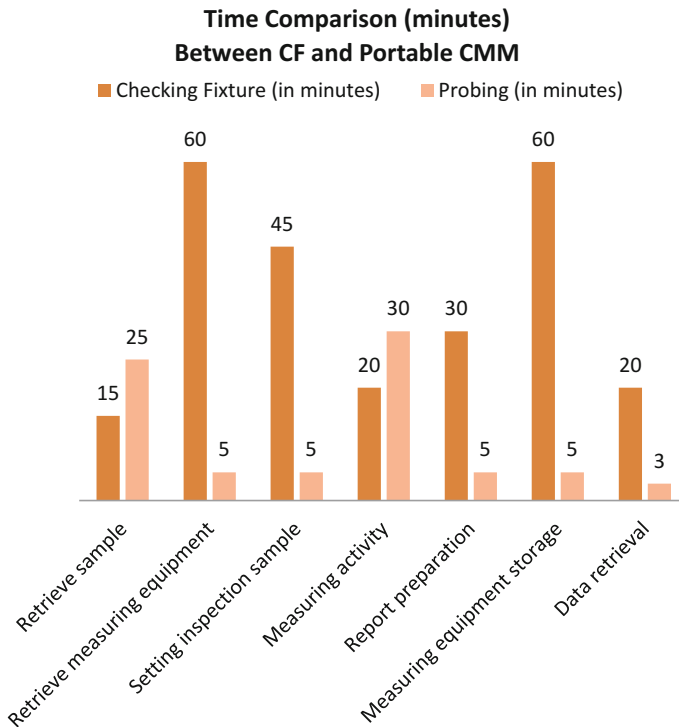


Fig. 6 Time comparison between checking fixture and portable CMM

- Data collection—No more manual writing involves. All dimensions will directly be transferred to the computer.
- Report preparation—Since data is already in softcopy, it can be manipulated to provide different type of document.
- Storage measuring equipment—Multi sensor portable CMM requires a small space for storage and easy to store. It eliminates the need for forklift from another separate department.
- Data retrieval—Since all data are in softcopy and stored on a server, it can be retrieved rapidly within any department.

5.2 Data Reliability

Figure 7 shows the comparison of measurement between the checking fixture and portable CMM probing. From the graph, probing only shows consistency when the measuring area relates to window opening and holes dimension but show great discrepancy when dealing with freeform surface profile.

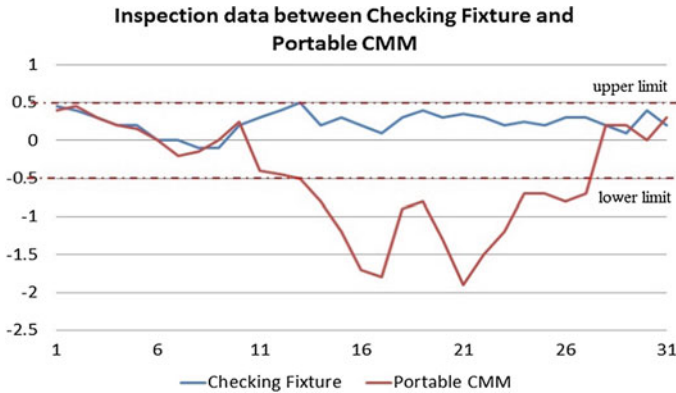


Fig. 7 Measurement consistency between scanning and probing in red circle

The inconsistencies become more obvious when reaching the middle area of the outer door panel in between point 11 till 27. Major contributors to this pattern can be explained as below:

- The outer door panel—The outer door panel is a mild steel formed to be in a required way and will be assembled with other single parts to create a complete door. The outer door panel thickness is just 0.8 mm only. When the loose part was placed on the inspection table, the outer door panel, especially in the middle area will dent due to gravity force. Thus, the panel is already out of tolerance before it was measured.
- Pressure force from CMM Probe—When measuring a surface profile, the probe will require certain pressure onto the profile surface before the sensor can pick up the signal. The pressure force from the activity can deform the surface and provide a wrong measurement. This is because the profile surface is a large area and has no structure to support itself during loose part condition.

5.3 Cost Saving and Other Benefits

Apart from all the technical aspects gained from the application of a portable CMM, it also will help management to save a significant amount of cost by eliminating the usage of checking fixture, reducing duration of inspection, reducing manpower and minimizing storage area. Millions of ringgit can be saved if OEM is able to apply a portable CMM in their daily inspection. For a single checking fixture used in inspecting the outer door panel, the average price is RM75,000 per unit. Usually, the checking fixture will come in a complete car set which consists of 4 separated checking fixtures. The overall price of the checking fixture for a complete car is as expensive as RM300,000 per car set. A Portable CMM on the other hand is quoted

to be around RM198,000 per unit including the mechanical Romer arm and Polyworks software. Unlike the checking fixture which is limited to inspect specific parts only, a multi scanner portable CMM can be used to almost every part within its measuring range making cost saving become more significant when a variety of parts are required to be inspected.

Labor cost also can be reduced in two ways, reducing manpower and reducing duration of man-hour. Fewer workers are required to perform part inspection with a portable CMM application. What once to be the practice of checking fixture where at least 2 peoples are required to perform the measurement activity and recording the measured information are no longer the case when applying a portable CMM for inspection. The simple and easy operation of a portable CMM has reduced the manpower from two inspectors to only one inspector to complete the task.

The cost for direct labor is also reduced when the duration of inspection is decreased significantly compared to the checking fixture. In a typical manufacturing company, direct labor cost is the biggest component of total operating cost. The application of an advanced inspection system is one of the most efficient methods to increase output and reducing annual labor costs. The usage of a portable CMM in inspection will reduce the time needed to perform activities, thereby reducing the total inspection duration. Figure 7 shows the significant amount of time saving of the proposed method compare to checking fixture which can be translated into cost reduction.

The space area in a factory contributes to indirect cost and every space occupied with work-in-progress (WIP) parts, storage area and production activities are as important as the main business itself. With the application of portable a CMM for inspection, it could help eliminating the usage of checking fixture. The dedicated areas in plant for checking fixture storage are now an empty space and can be used for the purpose of increasing production. Further studies should be done to acquire all the information in detail for better management decision.

With the usage of a portable CMM also can provide high level of data integrity compared to checking fixture where there are so many rooms for human errors. Even though the inspection is performed by different inspectors, the chances for human error is minimized and eliminated.

6 Conclusion

The application of advanced technology in daily manufacturing operation can provide a very sound result on the optimization minimize of current inspection activity. Although it is not feasible to fully apply a portable CMM in daily inspection activity due to limitation as discussed, it can act as a complement to fixture and further minimize the inspection duration.

A portable CMM which is not widely used for daily inspection can now be extended to daily inspection manufacturing activity and contributing to maintain high accuracy of components. Instead of performing inspection on a single axis,

inspection is now more accurate with the availability of X, Y, Z measurement distance. Problem analysis and solving can now be improved with all the information gathered.

The application of a portable CMM can reduce the duration of inspection by merely 2.9 h from current practice. The limitation to inspect on freeform surface is the only issue that holding this proposal from materialize. Thus, the solution could be the combination of both methods. By combining portable probing for points and checking fixture for surface inspection, it can further reduce the development cost, inspection time and storage space.

For better inspection in the future, further study on the proposed inspection is required. At this point, we already have a good understanding the disadvantages of a portable CMM towards freeform surface statistical process control and thin sheet metal. We are looking to study on the application of 3D scanning in daily inspection activity in the future. Objective of the study will still be the same, to increase the number of samples for more accurate Statistical Process Control analysis. With more samples used in Statistical Process Control, it can make as much conforming product as possible with a minimum of waste (recall, rework or scrap).

References

1. Kahn, S., Bockholt, U., Kuijper, A., Fellner, D.W.: Towards precise real-time 3D difference detection for industrial applications. *Comput. Ind.* **64**, 1115–1128 (2013)
2. Reedy, R.F., Jones, G.B.: The engineer's role in the assurance of quality. *Nucl. Eng. Des.* **107**, 227–234 (1988)
3. Michaloski, J.L., Zhao, Y.F., Lee, B.E., Rippey, W.G.: Web-enabled, real-time, quality assurance for machining production systems. *Procedia CIRP* **10**, 332–339 (2013)
4. Zhao, Y., Xu, X., Kramer, T., Proctor, F., Horst, J.: Dimensional metrology interoperability and standardization in manufacturing systems. *Comput. Stand. Interfaces* **33**(6), 541–555 (2011)
5. Butala, P., Sluga, A.: Statistical process control as a service: an industrial case study. *Procedia CIRP* **7**, 401–406 (2013)
6. Zhao, H., Kruth, J.P., Van Gestel, N., Boeckmans, B., Bleys, P.: Automated dimensional inspection planning using the combination of laser scanner and tactile probe (2011)
7. Xu, J., Xi, N., Zhang, C., Shi, Q., Gregory, J.: Real-time 3D shape inspection system of automotive parts based on structured light pattern. *Opt. Laser Technol.* **43**(1), 1–8 (2011)
8. Bi, Z.M., Wang, L.: Advances in 3D data acquisition and processing for industrial applications. *Robot. Comput. Integr. Manuf.* **26**(5), 403–413 (2010)
9. Zhao, H., Kruth, J.-P., Van Gestel, N., Boeckmans, B., Bleys, P.: Automated dimensional inspection planning using the combination of laser scanner and tactile probe. *Measurement* **45**(5), 1057–1066 (2012)
10. ElMaraghy, H., YangYang, X.: Computer-aided planning of laser scanning of complex geometries. *CIRP Ann.—Manuf. Technol.* **52**(1), 411–414 (2003)

Study on Implementation of Neural Network Controlling Four Quadrants Direct Current Chopper



Part1: Using Single Neural Network Controller with Binary Data Output

S. Arof, N. H. Diyanah, P. A. Mawby and H. Arof

Abstract This paper describes the implementation of Artificial Neural Network (ANN) as chopper operation controller (COC) that is responsible for selecting the correct mode for a four quadrants direct current Chopper (FQDC) that drives a dc series motor. In turn, the direct current motor propels an electric car (EC). The right mode of chopper operation is necessary for optimum performance and maximum battery power utility. The process starts with preparing the data for training the ANN controller. Then a MATLAB/Simulink model is established to test the performance of the trained ANN. The results show the ANN can perform the tasks of a COC successfully.

Keywords Direct current drive • Artificial neural network • Electric vehicle
Electric car • Series motor • Four quadrants chopper

S. Arof (✉) · N. H. Diyanah
Malaysian Spanish Institute, Universiti Kuala Lumpur,
Kulim Hi-Tech Park, 09000 Kulim, Kedah, Malaysia
e-mail: saharul@unikl.edu.my

N. H. Diyanah
e-mail: diyanahisham94@gmail.com

S. Arof · P. A. Mawby
School of Engineering, University of Warwick, Coventry CV4 7AL, UK
e-mail: P.A.Mawby@warwick.ac.uk

H. Arof
Engineering Department, Universiti Malaya, Jalan Universiti,
50603 Kuala Lumpur, Malaysia
e-mail: ahamzah@um.edu.my

1 Introduction and Review

The advancement of super capacitors as a power storage medium and the introduction of efficient low voltage direct current motors have motivated researchers to develop direct current drive suitable for electric vehicle or hybrid electric vehicle (HEV) application [1–4].

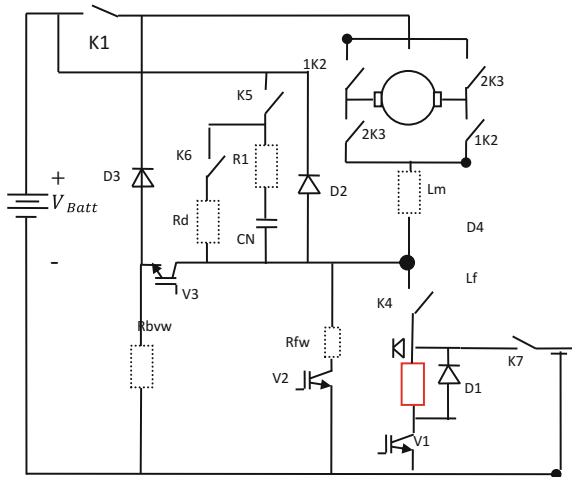
1.1 Four Quadrants Drive DC Chopper and Chopper Operation Controller

The common half-bridge direct current chopper for direct current series motor is not suitable for electric vehicle or hybrid electric vehicle application as it cannot perform reverse driving, field weakening and resistive braking [5–8]. Therefore, a new four quadrants direct current drive chopper (FQDC) that offers a complete set of modes in forward and reverse driving, field weakening, parallel driving, generator, regenerative braking and resistive braking is needed. The FQDC is shown in Fig. 1 [9].

1.2 Chopper Operation Controller

The FQDC uses three controllers to select the right mode of operation, fire IGBTs, and delay the interchange of contactors. The controller that selects the mode of operation is called the chopper operation controller (COC). It contains an expert

Fig. 1 Four quadrants dc chopper



system, fuzzy logic, self tuning fuzzy logic or neural network algorithm that processes the input signals and determines the best operating mode to execute [10–12].

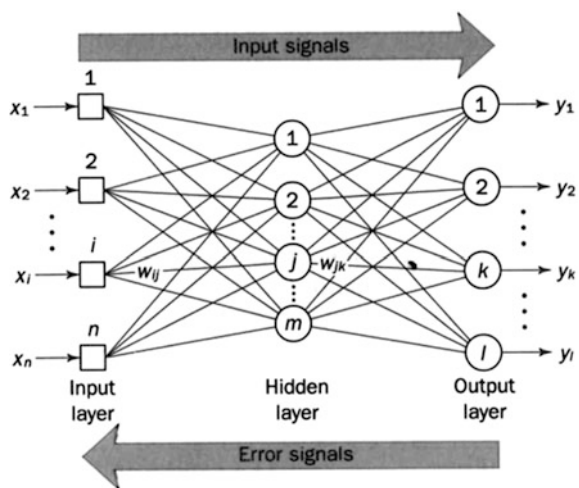
1.3 Neural Network as Chopper Operation Controller

A multilayer perceptron shown in Fig. 2 is a feedforward neural network with one or more hidden layers. It consists of input layer of source neurons, at least one middle or hidden layer and an output layer. The input layer accepts input signals and redistribute them to all neurons in the hidden layers. The output layer accepts output signals from hidden layer and establishes the output pattern. The weight of the neurons represent the features hidden in the input pattern. This multilayer feedforward neural network can be trained with back propagation algorithm such as Lavenberg–Marquardt (LM) technique [13].

2 Methodology

An electric car usually comes with some preset parameters such as maximum torque, speed and expected distance traversed when fully charged. In general, the performance of a particular EC is measured based on these parameters [11, 12, 14]. However, there are other factors that influence its performance like load and the profile of the route such as climbing up a steep hill, negotiating traffic jam, going downhill, etc. If a fully loaded EC climbs up a steep hill its speed will drop and a lot of energy is expended.

Fig. 2 Multilayer perceptron



2.1 Proposed Control Strategy

The FQDC requires three controllers to support its operations and they are the chopper operation controller (COC), subsequent and delay controller (SAD) and IGBT firing controller (IFC) [15–17]. In this study, an ANN algorithm is implemented as the COC of the FQDC to choose the most suitable mode of operation in response to signals from accelerator pedal, brake pedal, speed, error, etc. Failure to choose the right mode is unacceptable and will be downright dangerous. Figure 3 shows the flow of determining the most suitable chopper operation for the EV by the ANN controller. When accelerator or brake pedal signal is received, relevant data such as speed, torque, error, rate of error, load and current mode are passed to the ANN controller and processed based on the inputs. The ANN operator generates an output value for each mode of operation. The output value indicates the fitness of each mode and the one with the highest output will be selected as the most suitable mode to be executed.

2.2 Neural Network Data Training Preparation Process

2.2.1 Neural Network Data Preparation

To train the ANN controller, sufficient data, which include the input and output signal must be available. In preparing the needed data, the first step is to choose the profile of the route also known as the earth profile. Figure 4 shows examples of different earth profiles that can be used to test the EC. Each profile should comprise different driving conditions such as flat driving, going downhill and uphill, so that different modes of the controller are invoked.

Fig. 3 Block diagram of chopper operation controller with NN

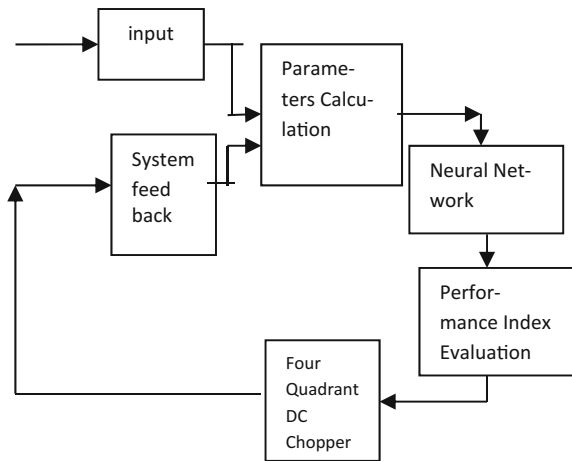
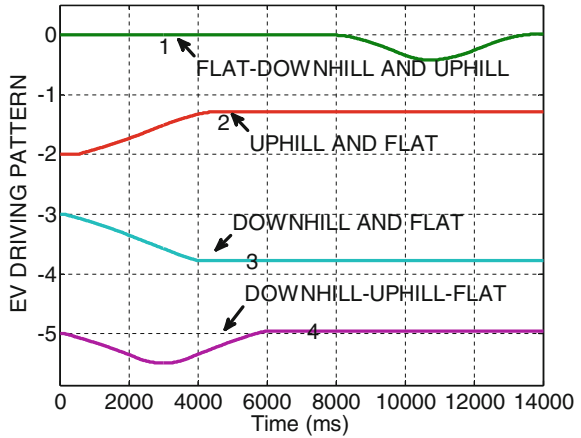


Fig. 4 Samples of earth profiles for training



2.2.2 Accelerator and Brakes Signals

In the second step, the expected accelerator and brake pedal signals that accompany each earth profile are prepared. The accelerator pedal and brake pedal signals for earth profile 1 in Fig. 4, are shown in Figs. 5 and 6 respectively.

2.2.3 Predetermined Chopper Operation

The output data set is the sequence of the chopper operation modes. It must be made available for the ANN training together with the input data. So first, raw input data are estimated logically using simple physics rule based on the earth profile, accelerator and brake pedal signals. Then, using the raw input data, the earth profile and the accelerator and brake signals, the sequence of the operation modes is

Fig. 5 Accelerator pedal signal

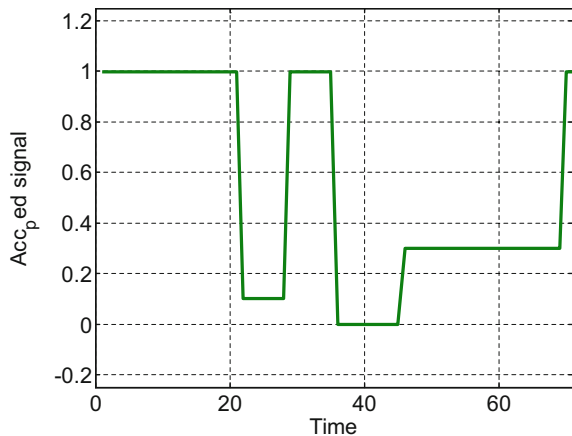
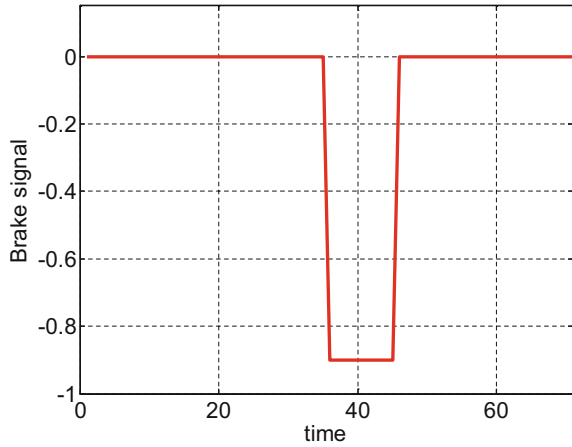
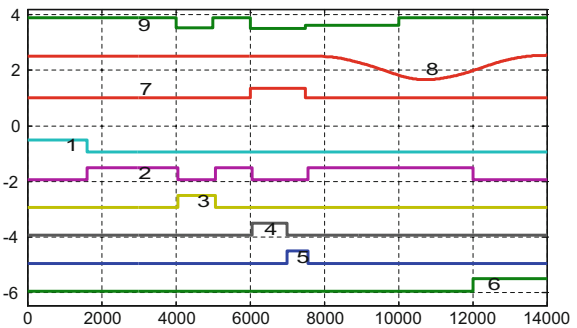


Fig. 6 Brake pedal signal



determined. Figure 7 shows an example of the predetermined chopper mode sequence for a test earth profile. At any instance, only one mode is activated. In the figure, signal 9 is the accelerator pedal, signal 8 is the earth profile, signal 7 is the brake pedal and signals 1–6 are the chopper operation modes. During start up, the driving mode is selected. As the EC reaches a sufficient speed level, the mode switches to the field weakening as more speed is needed due to the high accelerator signal. When the EC attains the desired speed and the accelerator signal turns low, the generator mode is selected to recover the kinetic energy. When a normal brake command is detected at a high speed, the regenerative mode is activated. As the

Fig. 7 Preset FQDC operation results



Legend:

- | | |
|-----------------------|-------------------------|
| 1. Driving | 2. Field Weakening |
| 3. Generator | 4. Regenerative Braking |
| 5. Resistive Braking | 6. Parallel Mode |
| 7. Brake Signal | 8. Earth Profile |
| 9. Accelerator Signal | |

vehicle speed drops to a certain value while the brake signal is still high, the resistive braking mode is triggered. However when brake command is replaced by a low acceleration command at low vehicle speed, the driving mode is activated again. When the vehicle moves downhill while the accelerator signal is low, the generator mode should be selected. However, if the accelerator signal is high, the field weakening mode should be engaged. As the vehicle climbs a steep hill, the speed is expected to drop. Hence, as more torque is required the parallel mode is selected. Finally, as the vehicle gains more speed with the accelerator signal still high, the field weakening mode is selected.

2.2.4 Matlab/Simulink Simulation Model

Once the raw data and the mode sequence are available, a simulation model of the FQDC [12] and the dynamic model of the EC are established using MATLAB/Simulink. Details of the EC vehicle dynamic model are not in the scope of this paper. The simulation model is prepared to obtain more realistic input and output data signals and to correct the data used earlier. Figure 8 below shows the MATLAB/Simulink model for the data collection.

In this step, the data used for the ANN training are adjusted in case they appear illogical or they disregard the influence of intra-variables. As a result, an operation mode can be deleted, delayed or replaced in the mode sequence. Figure 9 shows delay adjustments to a set of modes.

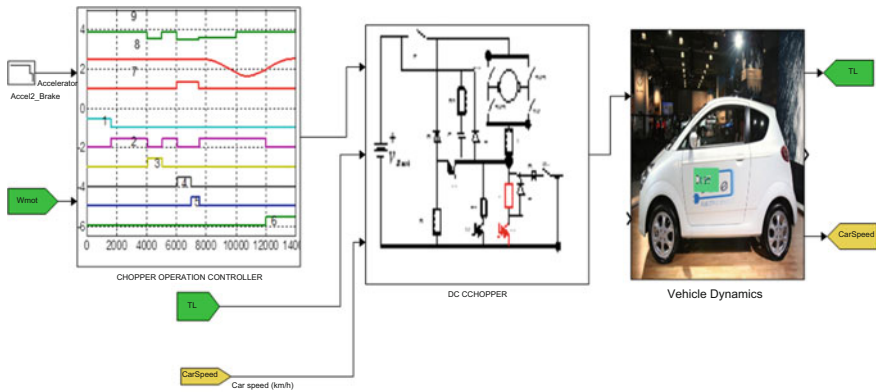
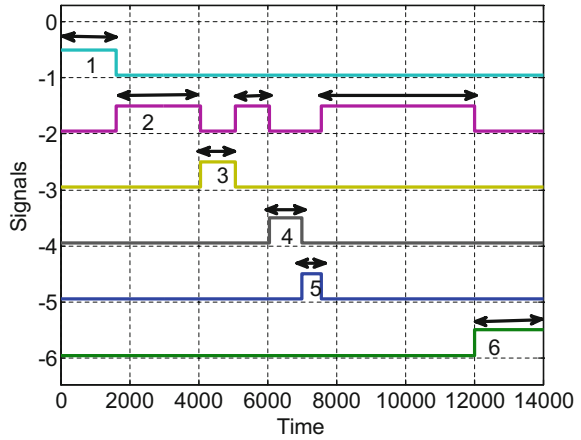


Fig. 8 Simulation model for four quadrants drive test

Fig. 9 Adjust the predetermined chopper operation modes



2.2.5 Gathering Data for NN Training

After the data adjustment step, the MATLAB/Simulink model is run again. This time, the generated data such as speed, error, rate of error, voltage, acceleration signal, brake signal, etc. are recorded. The data will be used as inputs while the chopper modes are used as outputs when training the ANN. Figures 10 and 11 show examples of the signals (normalized) and three different chopper modes.

2.2.6 Target Output Signals for ANN Training

If a single ANN is used, the number of its output nodes can be one or equal to the number of modes. If the number of output node is one, it generates a real value. In this case, each mode is represented by a value within an interval as shown in Table 2.

Fig. 10 Error, load, soc, dt, ROS input signals to ANN

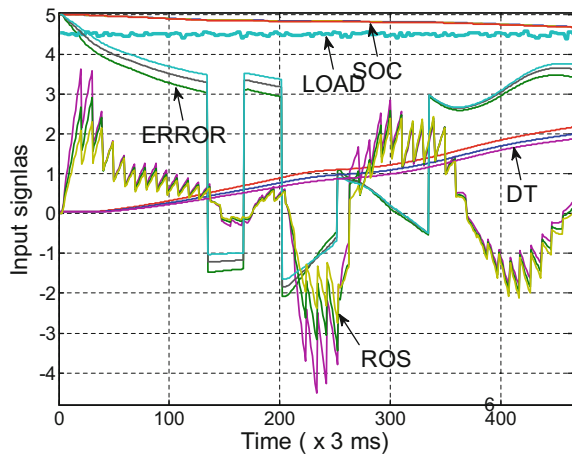
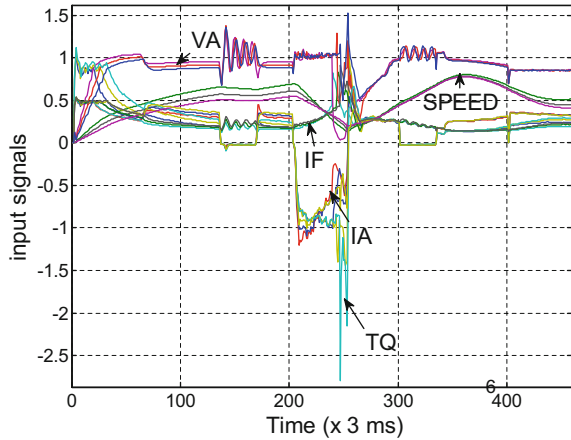


Fig. 11 Armature voltage, armature current, speed, torque



Note that the values representing the modes are equally separated. However, if the output nodes are as many as the modes, each output node can take a binary or real value as shown in Table 1.

Another approach is to use as many ANNs as the number of modes. Thus each ANN has a single output as shown in Fig. 12. In this study, only one ANN is used and it has 6 output nodes as shown in Fig. 13. Each output node has a binary output.

Table 1 Target of NN controller

Neural network output data to represent chopper operation modes in binary						
Selected mode	DRV	FW	PAR	GEN	RGB	RSB
DRIVING	1	0	0	0	0	0
FW	0	1	0	0	0	0
PAR	0	0	1	0	0	0
GEN	0	0	0	1	0	0
RGB	0	0	0	0	1	0
RSB	0	0	0	0	0	1
Neural network output data to represent chopper operation modes in integer						
Selected mode	DRV	FW	PAR	GEN	RGB	RSB
DRIVING	0.15	0	0	0	0	0
FW	0	0.3	0	0	0	0
PAR	0	0	0.4	0	0	0
GEN	0	0	0	0.6	0	0
RGB	0	0	0	0	0.75	0
RSB	0	0	0	0	0	0.9

Table 2 Target of NN controller in single value integer

Neural network output data to represent chopper operation modes one single integer	
Chopper operation	Integer value
Driving	1.5
Field weakening	3.0
Generator	4.5
Regenerative braking	6.0
Resistive braking	7.5
Parallel mode	9.0

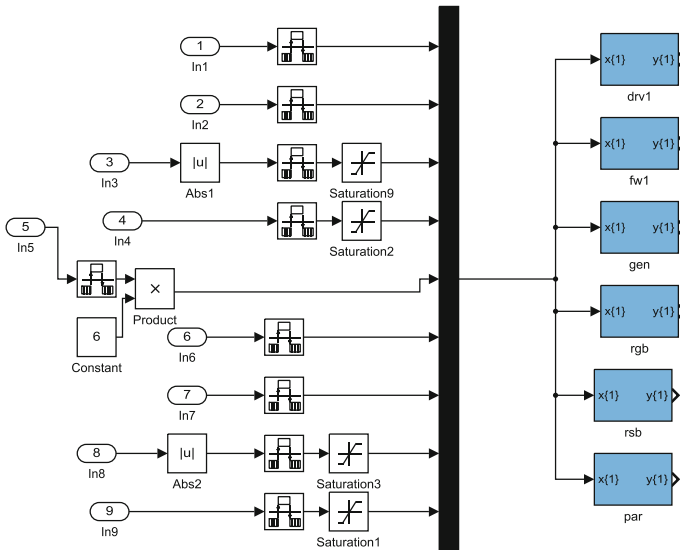


Fig. 12 Six NN controllers with single output

2.3 Neural Network Training

The input and output data sets previously collected, are used to train the ANN controller in a supervised learning. MATLAB/Simulink neural network tool is used for this purpose (Fig. 14).

The number of nodes in the hidden layer and the number of iteration are adjusted during training to get the lowest error rate. Figure 15 shows the flow of training the ANN.

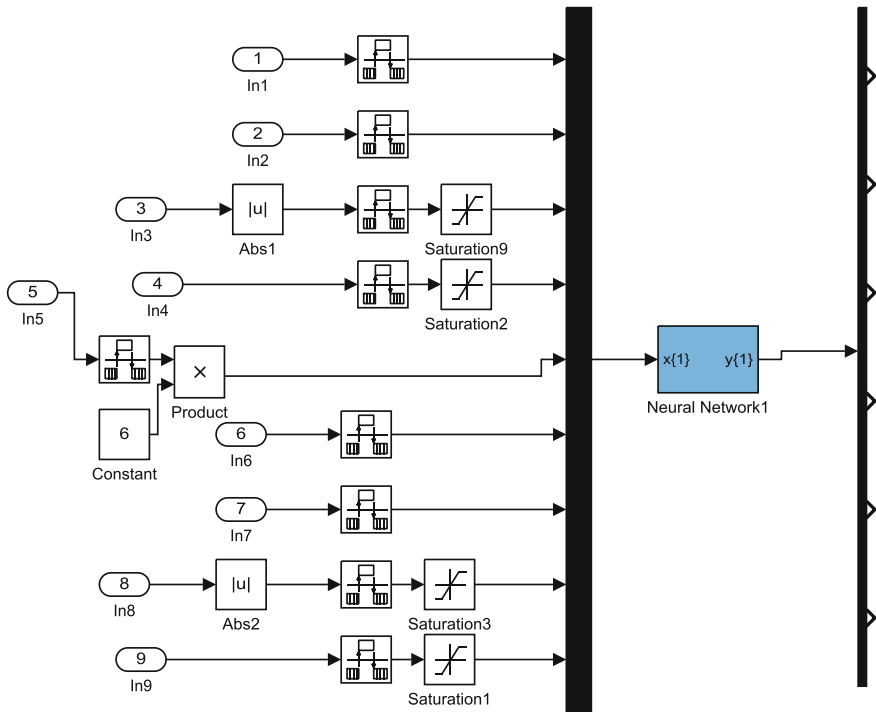


Fig. 13 One single NN controller with six output nodes

2.3.1 NN Training Results

The performance of the ANN controller is tabulated in confusion matrices of Figs. 16, 17, 18 and 19. The training, validation, testing and overall confusion matrices are given in Fig. 16. As seen, the number of incorrect responses for each mode is low, and thus the overall accuracy is high. In Fig. 17, the error histogram indicates that the distribution of errors for training, validation and test phases is almost at -0.033 and this is considered acceptable. Figure 18 shows the relationship between the outputs of the network and the targets. The training, validating and testing curves look similar indicating a good condition. In Fig. 19, the regression result is as expected result due to binary output target and this is acceptable. In Fig. 20, the receiver operating characteristics (ROC) is shown. The colored lines in each axis represent the ROC curves. The ROC curve is a plot of the true positive rate ($1 - \text{sensitivity}$) versus the false negative rate ($1 - \text{specificity}$) as the threshold is varied. A perfect test is shown in the figure in the left upper corner, with 100% sensitivity and 100% specificity [18].

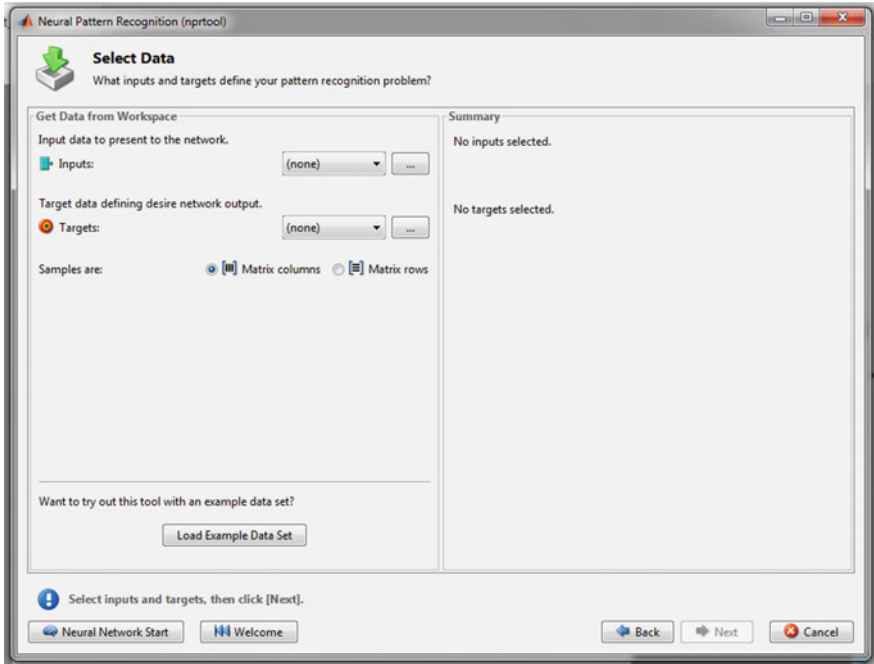


Fig. 14 Matlab/Simulink tool for NN training

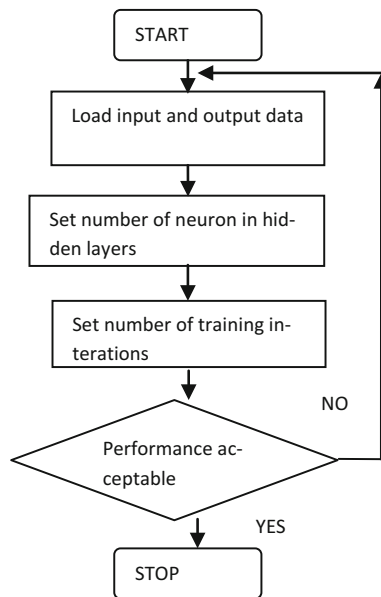


Fig. 15 NN training process flow diagram

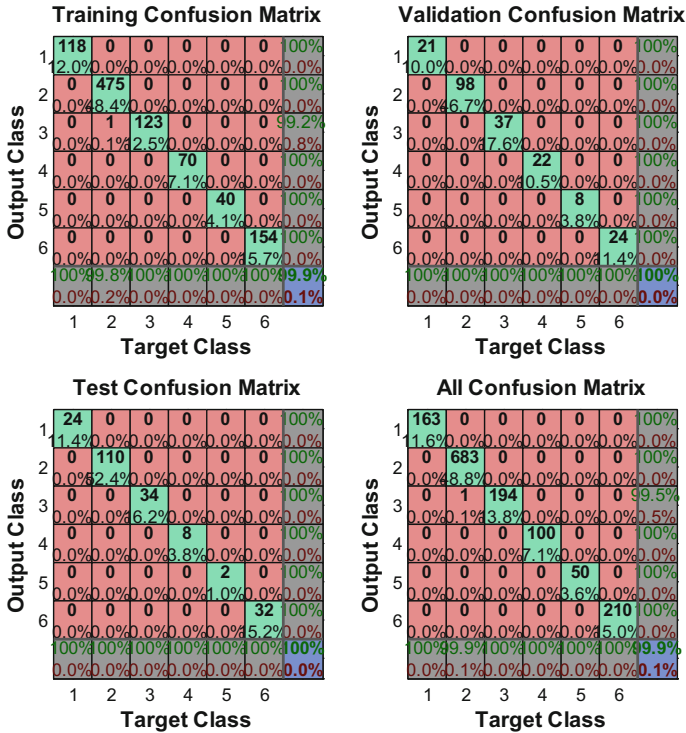


Fig. 16 Training confusion

2.4 Testing the ANN

The ANN controller is tested with a new set of input signals to test its response. Figure 21 shows the simulation model and Fig. 22 shows the chopper operation controller (COC) responses.

3 Neural Network Controller Final Testing and Results

3.1 Development of Complete Simulation Model

Computer simulation using MATLAB/Simulink as shown in Fig. 23 is used to test the Neural Network chopper operation controller (COC) and to study its effectiveness in a complete system that represents an EC. Some parameters value that are required by the simulation software such as car weight, voltage supply, max power, etc. must be provided by the user.

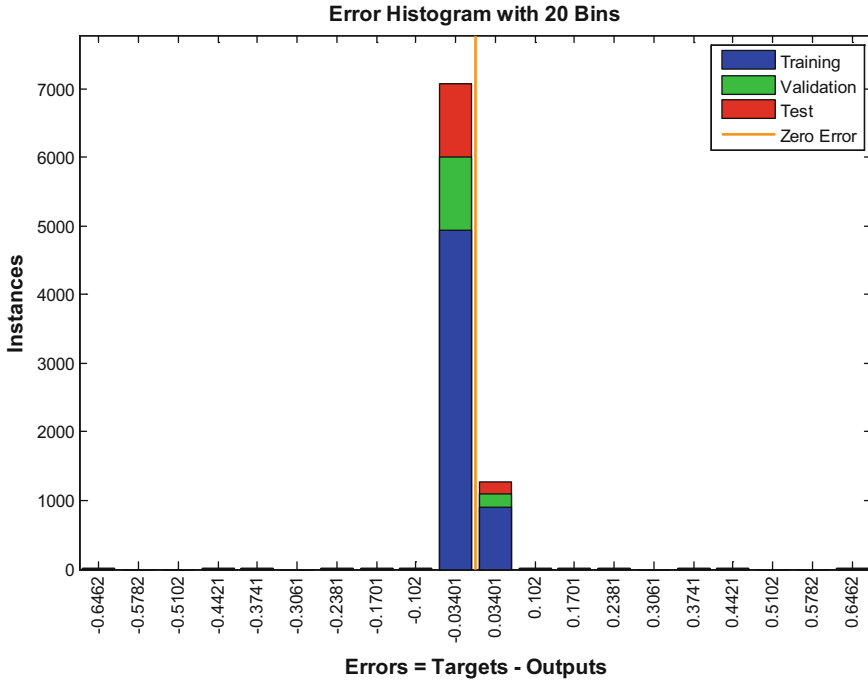


Fig. 17 Error histogram

3.2 Performance Index (PI)

As the ANN controller for this study has six outputs, a performance index(PI) is needed to compare each output of the ANN. The rule to follow is that the output node with the highest value represents the mode to be executed. A PI with “if then rules” is used in this study and in Fig. 24, the associated ANN controller is shown.

Such “if then rules” example is If $O1 > O2$ && $O1 > O3$ && $O1 > O4$ && $O1 > O5$ && $O1 > O6$, then selected mode is O1.

3.3 Results

The results of implementing the MATLAB/Simulink model are shown in Figs. 25, 26, 27, 28 and 29. Figure 25 shows a sequence of FQDC modes chosen by the ANN controller. Overall, the ANN picks the right mode of operation most of the time except where glitches occur at the end of the test. Figure 26 shows an enlarged view of the part where the glitches are. This is due to a slight confusion when the ANN controller is not sure whether to choose the field weakening or parallel mode.

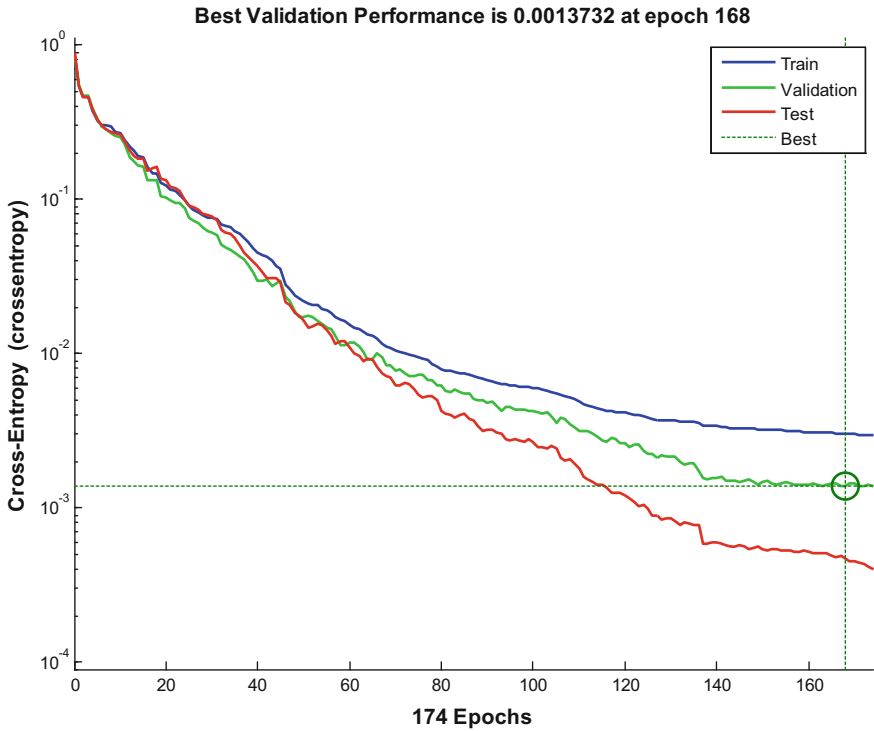


Fig. 18 NN performance

But eventually it picks the parallel mode, which is the correct decision. In Fig. 27 the motor speed is shown. The maximum acceleration and speed are restricted by the state of charge (SOC) of the battery and the remaining distance traverse shown in Fig. 28. The SOC is shown in Fig. 29.

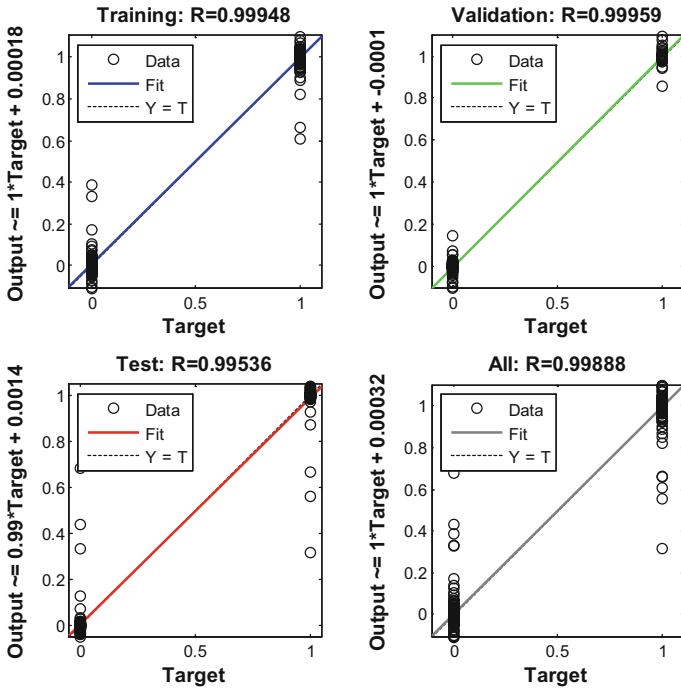


Fig. 19 Regression

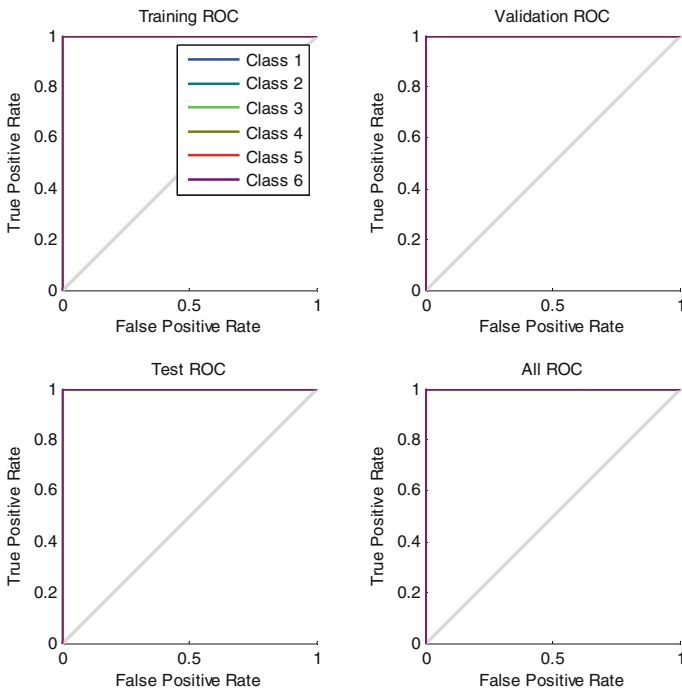


Fig. 20 NN ROC

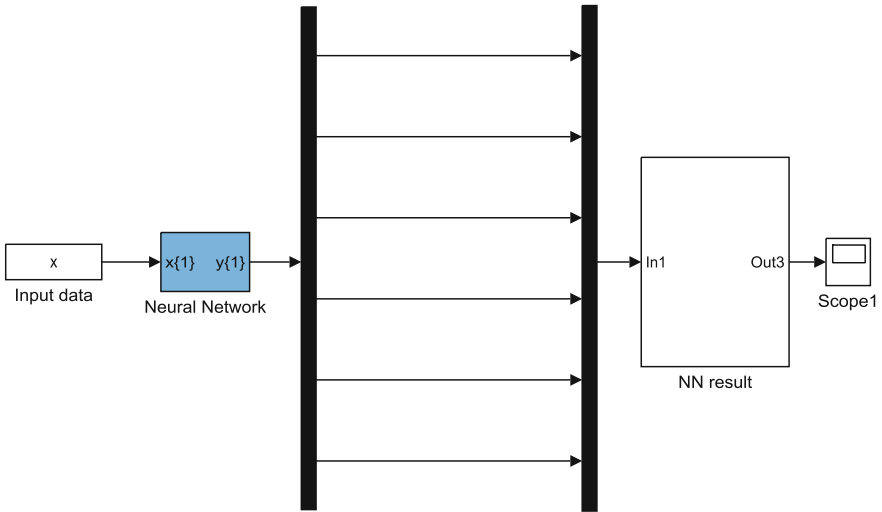


Fig. 21 NN COC testing simulation model

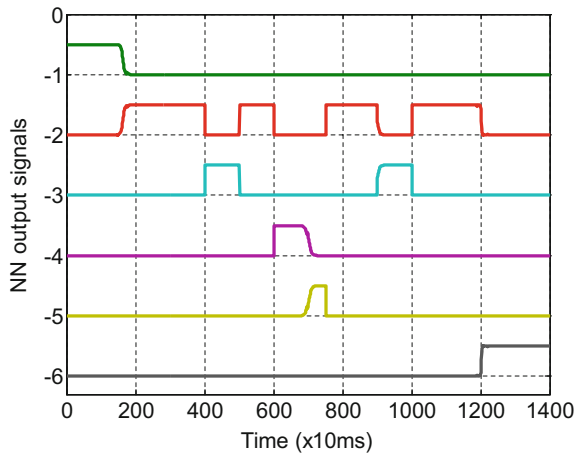


Fig. 22 NN COC responses

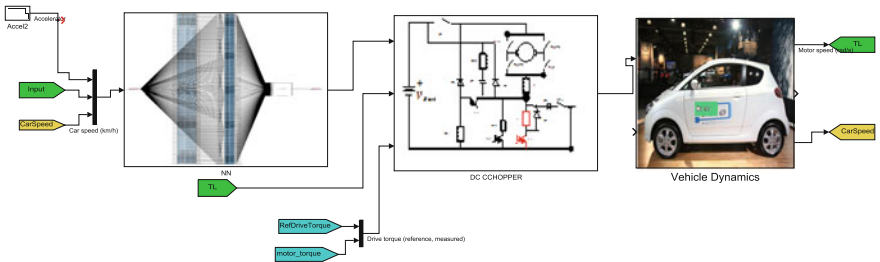


Fig. 23 MATLAB/Simulink model

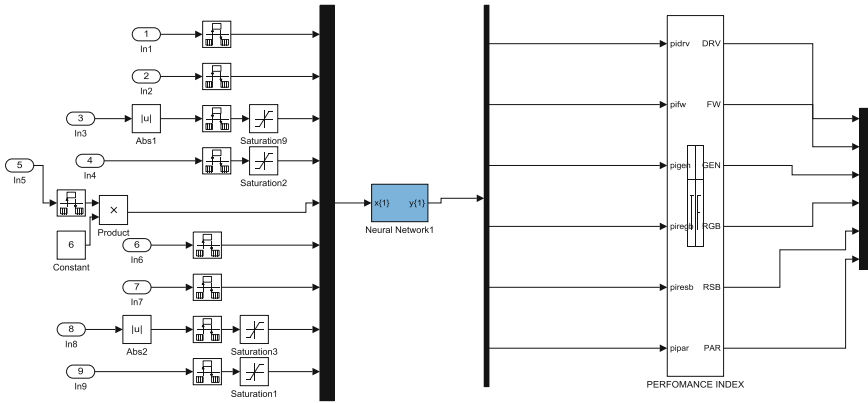


Fig. 24 PI with NN controller

Fig. 25 Results of ANN as FQDC controller

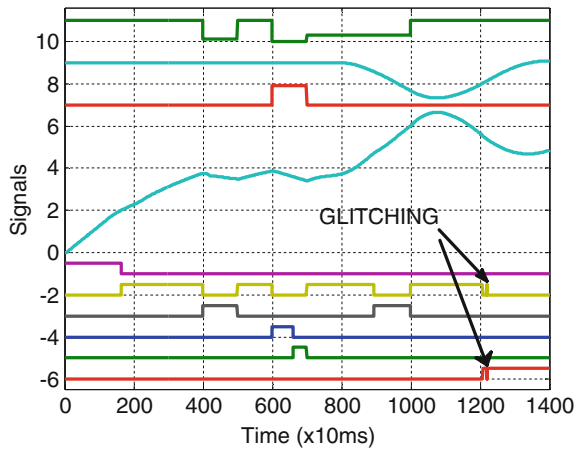


Fig. 26 NN controller output

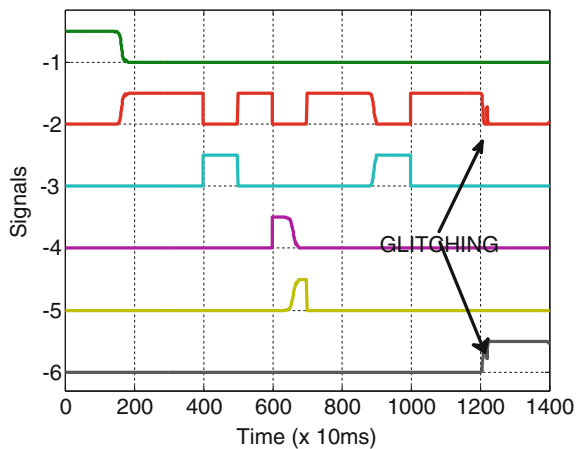


Fig. 27 Vehicle speed

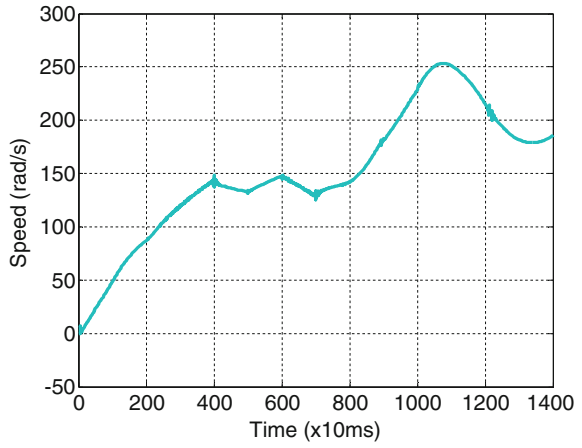


Fig. 28 Distance traverse

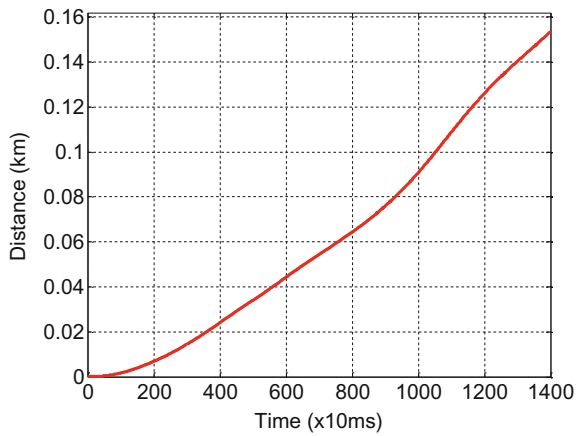
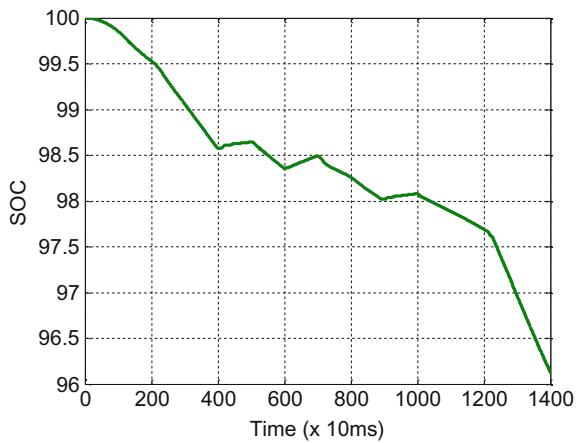


Fig. 29 Battery SOC



4 Conclusion

ANN has a high potential to be utilized as the chopper operation controller (COC) for electric vehicle. In summary, the performance of the ANN, which operates as a COC with six outputs, is satisfactory. The results vindicate that the technique, which starts with preparing the input-output data for training the ANN controller and establishing the MATLAB/Simulink model, is successfully implemented. Retraining the network, increasing the number of hidden neurons, training vectors, input-output data, or trying different training algorithms may improve the performance of the system. The SOC, DT and speed may also influence its performance. The effects of adjusting these parameters will be discussed in another paper.

References

1. Gao, Y., Ehsani, M.: Design and control methodology of plug-in hybrid electric vehicles. *IEEE Trans. Ind. Electron.* **57**(2), 633–640 (2010)
2. Westbrook, M.H.: *The Electric and Hybrid Electric Vehicle*. SAE, USA (2001)
3. Husain, I.: *Electric and Hybrid Electric Vehicles, design fundamentals*. CRC Press, USA (2003)
4. Oak Ridge National Laboratory: *Advanced Brush Technology for DC Motors* (2009). Available: <http://peemrc.ornl.gov/projects/emdc3.jpg>
5. Heinrich, Walter Rentsch, Herbert Dr.-Ing. ABB Industry: “Guide to Variable Speed Drives,” Technical Guide No. 41180 D-68619 LAMPERTHEIM, Germany, 3ADW 000 059 R0201 REV B (02.01), DCS 400/DCS 500/DCS 600: ABB (2003)
6. Bansal, R.C., Birla Institute of Technology and Science, Pilani, India.: *Electric Vehicle, Handbook Of Automotive Power Electronics and Motor Drives*. Taylor & Francis Group, CRC Press, USA (2005)
7. Rashid, M.H.: *Power Electronics, Circuits, Devices and Applications*, 3rd ed. Prentice Hall (2004)
8. Senthil Kumar, N., Sasasivam, V., Muruganandam, M.: A low cost four-quadrant chopper—fed embedded DC drive using fuzzy controller. *J. Electr. Power Compon. Syst.* **35**, 907–920 (2007)
9. Arof, S., Yaakob, N.M. Jalil, J.A., Mawby, P.A., Arof, H.: Series motor four quadrants drive DC chopper, part 1: Overall. In: *International Conference on Power Electronics* (2014)
10. Arof, S., Muhd Khairulzaman, A. K., Jalil, J.A., Arof, H., Mawby, P.A.: Self tuning fuzzy logic controlling chopper operation of four quadrants drive DC chopper for low cost electric vehicle. In: *6th International Conference on Intelligent Systems, Modeling and Simulation*, IEEE computer Society, pp. 40–24 (2015). <https://doi.org/10.1109/isms.2015>
11. Arof, S., Muhd Khairulzaman, A.K., Jalil, J.A., H. Arof, Mawby, P.A.: Artificial intelligence controlling chopper operation of four quadrants drive DC chopper for low cost electric vehicle. *Int. J. Simul. Sci. Technol.* (2015). <https://doi.org/10.5013/ijssst.a.16.04.03.2015.ijssst>
12. Joshi, D., Bansal, R.C.: Performance evaluation of multiquadrant DC drive using fuzzy-genetic approach. *Application of Genetic Algorithm for Optimization of Control Strategy in Parallel HEV*
13. Michael, N.: *Artificial Intelligence, a Guide to Intelligent System*, 3rd edn. (2011)

14. Dazhi, W., Jie, Y., Qing, Y., Dongsheng, W., Hui, J.: Estimation and control of hybrid electric vehicle using artificial neural networks. In: 2nd IEEE Conference on Industrial Electronics and Applications, pp. 35–40 (2007)
15. Arof, S., Hassan, H., Rosyidi, M., Mawby, P.A., Arof, H.: Implementation of series motor four quadrants drive dc chopper for dc drive electric car and LRT. *J. Appl. Environ. Biol. Sci.* 7(3S), 73–82 (2017)
16. Arof, S., Jalil, J.A., Kamaruddin, N.H., Yaakop, N.M., Mawby, P.A., Arof, H.: Series motor four quadrants drive dc chopper part 2: driving and reverse with direct current control. In: International Conference on Power Electronics, pp. 775–780. 978-1-5090-2547-3/16. <https://doi.org/10.1109/pecon2016.7951663>
17. Arof, S., Noor, N.M., Elias, F., Mawby, P.A., Arof, H.: Investigation of chopper operation of series motor four quadrants DC chopper. *J. Appl. Environ. Biol. Sci.* 7(3S), 49–56 (2017)
18. Mathworks: User guide to Neural Network using MATLAB/Simulink Toolbox. <http://www.mathworks.com/help/nnet>

Processor in the Loop for Testing Series Motor Four Quadrants Drive Direct Current Chopper for Series Motor Driven Electric Car



Part1: Chopper Operation Modes Testing

S. Arof, N. H. Diyanah, N. M. Yaakop, P. A. Mawby and H. Arof

Abstract This paper describes the process of testing a four quadrant drive direct current (DC) chopper (FQDC) that controls a DC series motor using the processor in the loop (PIL) technique. The DC motor serves as a propeller to an electric vehicle (EV). The main function of the four quadrant drive chopper is to provide a smooth operation for the electric vehicle (EV) while optimizing battery power consumption and maximizing distance traversed. In the processor in the loop (PIL) test, MATLAB/Simulink environment was used as the platform for the four quadrants drive chopper and electric vehicle, whereas in the hardware part, the FQDC was controlled by three PIC microcontrollers. Serial communication was used as the channel of data transfer between the hardware and software. The simulation results of the ATLAB/Simulink indicate that the FQDC controller was able to control the DC motor that drove the EV. Overall, the PIL technique was suitable for testing and validating the operation of the FQDC, its controllers and the control algorithm.

Keywords Direct current drive · Electric vehicle and hybrid electric vehicle Series motor · Four quadrant drive chopper

S. Arof (✉) · N. H. Diyanah · N. M. Yaakop
Malaysian Spanish Institute, Universiti Kuala Lumpur, 09000 Kulim, Kedah, Malaysia
e-mail: saharul@unikl.edu.my

N. H. Diyanah
e-mail: diyanahisham94@gmail.com

S. Arof · P. A. Mawby
University of Warwick School of Engineering, Coventry CV47AL, UK
e-mail: P.A.Mawby@warwick.ac.uk

H. Arof
Engineering Department, Universiti Malaya, Jalan Universiti, 50603 Kuala Lumpur, Malaysia
e-mail: ahamzah@um.edu.my

1 Introduction and Review

Using electric vehicles (EV) and hybrid electric vehicles (HEV) is one of the solutions to reduce the use of fossil fuel [1]. The present EV/HEV mainly use alternating current(AC) drive but interest in direct current (DC) drive has increased since the introduction of highly efficient brushed direct current motor that operates at low voltage [2]. One of the applications suitable for these direct current(DC) motors is for propelling electric vehicles(EVs) and hybrid electric vehicles(HEVs).

1.1 Proposed Four Quadrant DC Drive Chopper Design

The main purpose of developing a direct current (DC) drive system for EV/HEV using direct current brushed motor is to produce an efficient but cheap hybrid or electric car that is affordable. Brushed direct current motor requires four quadrants chopper to operate in various modes [3–5]. The proposed four quadrants chopper, shown in Fig. 1, has seven modes of operation namely driving, reverse, field weakening, parallel mode, regenerative braking, resistive braking, and generator [6]. This is much better than what the conventional H bridge chopper can offer.

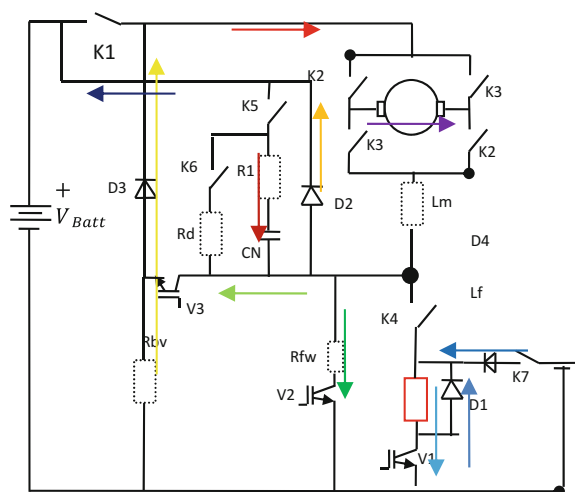
The mathematical model of each mode of the four quadrants drive chopper (FQDC) is given a set of equations below [6].

Driving and reverse mode equations

$$e_g = K_{bemf}i_f\omega \tag{1}$$

$$T_d = K_t i_a i_f \tag{2}$$

Fig. 1 New four quadrants DC Chopper



$$T_d = J \frac{d\omega}{dt} + B\omega + T_L \quad (3)$$

$$\frac{d}{dt} \begin{bmatrix} I_a \\ I_f \\ V_c \end{bmatrix} = \begin{bmatrix} \frac{-(R_a + R_c)}{(L_a)} & \frac{R_c}{(L_a)} & \frac{1}{(L_a)} \\ \frac{R_c}{(L_f)} & \frac{-(R_f + R_c)}{(L_f)} & \frac{1}{(L_f)} \\ \frac{-1}{(C)} & \frac{1}{(C)} & 0 \end{bmatrix} \begin{bmatrix} I_a \\ I_f \\ V_c \end{bmatrix} + \begin{bmatrix} 0 & 0 & 0 \\ \frac{1}{L_f} & \frac{-1}{L_f} & 0 \\ 0 & 0 & 0 \end{bmatrix} \begin{bmatrix} V_{dc} K_{drv} \\ E_g \\ 0 \end{bmatrix} \quad (4)$$

Field weakening

$$\frac{d}{dt} \begin{bmatrix} I_a \\ I_f \\ V_c \end{bmatrix} = \begin{bmatrix} \frac{-(R_a + R_c)}{(L_a)} & \frac{R_c}{(L_a)} & \frac{1}{(L_a)} \\ \frac{R_c}{(L_f)} & \frac{-(R_f + R_c)}{(L_f)} & \frac{1}{(L_f)} \\ \frac{-1}{(C)} & \frac{1}{(C)} & 0 \end{bmatrix} \begin{bmatrix} I_a \\ I_f \\ V_c \end{bmatrix} + \begin{bmatrix} 0 & 0 & \frac{R_c}{R_{fw} * L_a} \\ \frac{1}{L_f} & \frac{-1}{L_f} & \frac{-R_c}{R_{fw} * L_f} \\ 0 & 0 & \frac{1}{(R_{fw} * C)} \end{bmatrix} \begin{bmatrix} V_{dc} K_{drv} \\ E_g \\ V_f K_{fw} \end{bmatrix} \quad (5)$$

Generator

$$\frac{d}{dt} [I_f] = \left[-\left(\frac{R_f}{L_f} \right) \right] [I_f] \left[\frac{1}{(L_f)} \right] [V_{ext} K_{drv}] \quad (6)$$

$$\frac{d}{dt} [I_a] = \left[\frac{-(R_a + R_{bh})}{L_a} \right] [I_a] \left[\frac{1}{L_a} \quad -\frac{1}{L_a} \right] \begin{bmatrix} E_g \\ V_{dc} \end{bmatrix} \quad (7)$$

Parallel

$$\frac{d}{dt} [I_f] = \left[-\left(\frac{R_f}{L_f} \right) \right] [I_f] \left[\frac{1}{(L_f)} \right] [V_{ext} K_{drv}] \quad (8)$$

$$\frac{d}{dt} [I_a] = \left[\frac{-(R_a)}{L_a} \right] [I_a] \left[\frac{1}{L_a} \quad -\frac{1}{L_a} \right] \begin{bmatrix} V_{dc} \\ E_g \end{bmatrix} \quad (9)$$

Regenerative brake pre excitation

$$\frac{d}{dt} [I_f] = \left[-\left(\frac{R_f}{L_f}\right) \right] [I_f] \left[\frac{1}{(L_f)} \right] [V_{ext} K_{drv}] \quad (10)$$

Regenerative brake resonance

$$\frac{d}{dt} \begin{bmatrix} I_f \\ V_c \end{bmatrix} = \begin{bmatrix} -\frac{(R_c + R_f)}{L_f} & \frac{-1}{L_f} \\ \frac{I_f}{C} & 0 \end{bmatrix} \begin{bmatrix} I_f \\ V_c \end{bmatrix} \begin{bmatrix} \frac{1}{L_f} & 0 \\ 0 & 0 \end{bmatrix} \begin{bmatrix} V_{dc} K_{drv} K_{rgb} \\ 0 \end{bmatrix} \quad (11)$$

Regenerative and resistive brake general equations

$$\frac{d}{dt} [I_f] = \left[-\left(\frac{(R_a + R_{bh} + R_f)}{L_a + L_f}\right) \right] [I_f] \left[\frac{1}{(L_f)} \right] [E_g K_{drv} K_{rgb}] \quad (12)$$

$$\frac{d}{dt} [I_{batt}] = \left[-\left(\frac{R_a + R_{batt}}{L_a}\right) \right] [I_{batt}] \left[\frac{1}{(L_a)} \right] [E_g - V_{batt}] \quad (13)$$

$$\frac{d}{dt} [I_{short}] = \left[-\left(\frac{R_a + R_{short}}{L_a}\right) \right] [I_{short}] \left[\frac{1}{(L_a)} \right] [E_g K_{rgb}] \quad (14)$$

$$\frac{d}{dt} [I_{fw}] = \left[-\left(\frac{R_{fw} + R_a}{L_a}\right) \right] [I_{fw}] \left[\frac{1}{(L_a)} \right] [E_g K_{fw}] \quad (15)$$

2 Simulation Model Established from Mathematics Equation

Each set of mathematical equations can be transformed into a simulation model as shown in Fig. 2. The simulation model generated from mathematical model is fast and as a result, a longer simulation is feasible. A similar simulation model can also be created using MATLAB/Simulink toolbox by selecting appropriate components from its library as shown in Fig. 3. This model is easier to establish but is slower in execution. Thus for the same execution time, this model produces a shorter simulation [7].

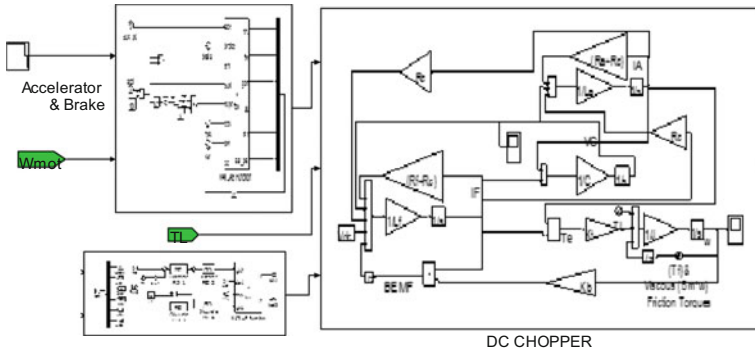


Fig. 2 Complete integrated transfer function of FQDC chopper

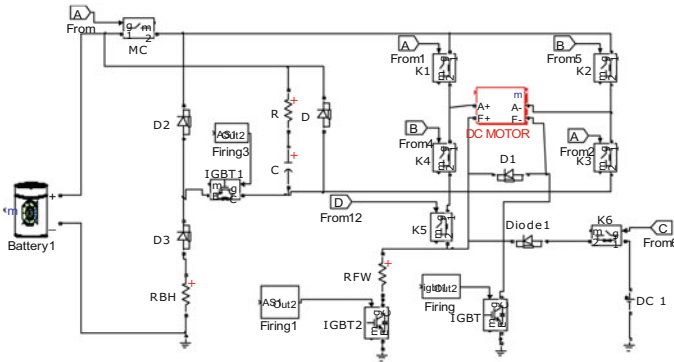


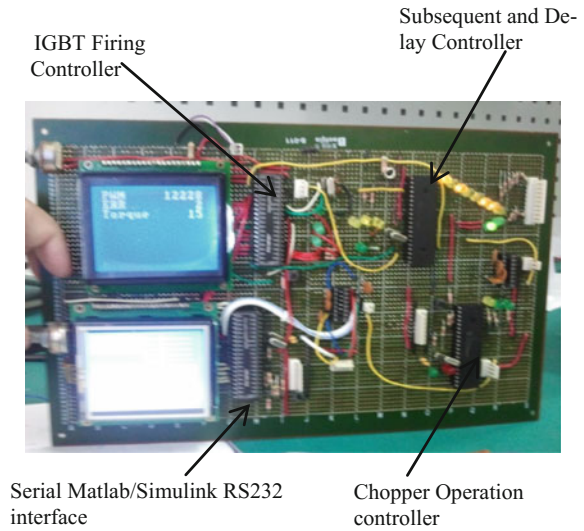
Fig. 3 Overview of proposed four quadrants DC chopper simulation

2.1 Methodology

2.1.1 Processor in the Loop (PIL)

The performance of the proposed FQDC and controllers can be evaluated by simulation or by implementing a real hardware prototype. A real hardware implementation is very desirable as it reveals the true potential and limitations of the system. However, it is very time consuming and expensive. In contrast, simulation is fast and cheap, but the value of its results depends on its ability to emulate the system accurately [8–10]. Hence, simulation also known as virtual experiment, is chosen as a platform to test the four quadrants drive chopper(FQDC) and the algorithm developed for the Electric vehicle or hybrid electric vehicle(EV/HEV) application. Processor in the loop (PIL) is a part of the hardware in the loop (HIL) technique used for verifying hardware in conjunction with simulation software [11–14]. In this study the main objective of applying the PIL is to test the

Fig. 4 Four quadrants chopper controller



FQDC hardware controllers and its control algorithm. Since a four quadrants chopper has many operations, it requires three sub controllers (PIC microcontrollers), which are assigned for chopper operation (COC), subsequent and delay (SAD), and insulated gate bipolar transistor(IGBT) firing controller (IFC) (Fig. 4).

2.1.2 Chopper Operation Controller

MATLAB/Simulink receives data from sensors at the direct current(DC) motor and vehicle. Some important data are field current, armature current, armature voltage, battery voltage, motor speed, accelerator pedal position, brake pedal position, etc. In turn, it sends the data to the chopper operation controller and IGBT firing controller via serial interface. The chopper operation controller selects the suitable mode of operation for the DC motor to run based on the data received [15, 16]. Specifically, the controller runs an expert system(ES) algorithm which processes the input data and determines the best operation mode and passes the decision and other information to the subsequent and delay (SAD) controller via serial communication (UART). Details of the expert system(ES) algorithm is not discussed in this paper.

2.1.3 Subsequent and Delay Controller (SAD)

The subsequent and delay(SAD) controller has four important tasks. The first task is to control the contactors' switching according to the chopper operation. The second is to introduce a delay in the transition from changing one chopper operation to another operation for soft switching [17] transition. The third is to send or remove

ready signal via input or Output(I/O) pin to the igbt firing controller(IFC) in order to start or stop IGBTs firing sequence. The last task is to relay the selected chopper operation mode to the IFC via SPI communication. The delay subroutine algorithm is implemented in this controller but its details are not covered in this paper.

2.1.4 IGBT Firing Controller (IFC)

Besides data from the SAD controller, the IFC also receives several data signals from MATLAB/Simulink such as, accelerator pedal position, brake pedal position, speed, torque, current, voltage, etc. Then the IFC produces the PWM signals for firing the IGBTs and sends information on the chopper operation mode back to MATLAB/Simulink via serial interface. The PWM signals for firing the IGBTs are the output of digital or discrete proportional Integrator derivate (PID) algorithm used to control the direct current(DC) series motor with direct torque control (DTC) implemented in MATLAB Simulink model. Details of the digital PID algorithm and DTC implemented in this controller are also not discussed in this paper [18].

The flow of the data and signals in the Processor in the loop (PIL) from MATLAB/Simulink to FQDC controllers and vice versa is simplified in the block diagram shown in Fig. 5. The signals flow from FQDC controllers to the Matlab/Simulink for communication and data distribution is shown in block diagram as in Fig. 6.

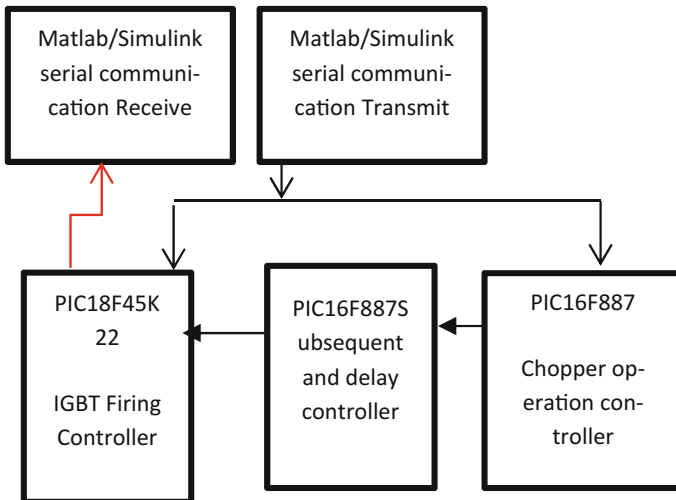


Fig. 5 communication and data distribution between controllers

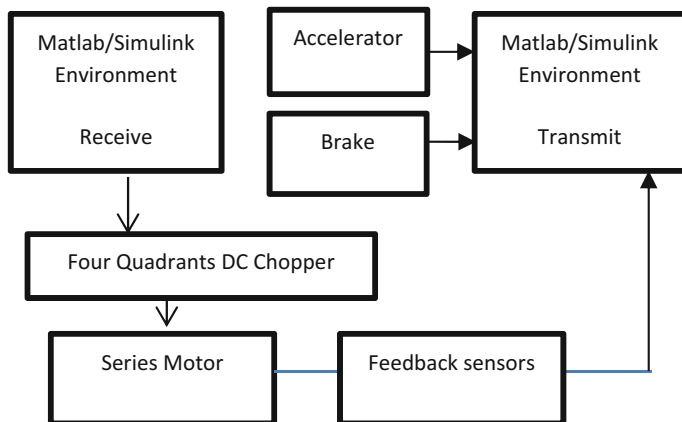


Fig. 6 Block diagram of controller data path

2.1.5 Signal Conversion

MATLAB/Simulink works with data and signals from the FQDC and EV in the form of real, integer, signed integer, double etc. The hardware controllers (PIC microcontrollers) on the other hand, are all running in digital/binary forms. Therefore signal conversion is required. First, all input signals sent to the controllers, such as speed, current, torque, voltage and others, are transformed into voltages. As the microcontrollers run on 5 V direct current (DC) power supply, the voltages are then adjusted using voltage dividers or similar circuits to step down the voltages levels so that their final values are in the range of zero(0)V to five(5)V. Then analog to digital conversion is carried out using analog to digital converter (A/D) with a 10-bit resolution. After the conversion, 5 V is represented by 1024 in decimal and 0 V is represented by zero in decimal. Given a normalized voltage level from zero to five voltage (0 V-5 V), its decimal value is determined by the following equation.

$$\text{The digital representation} = (\text{input voltage}/5\text{v}) * 2^n - 1$$

where $n = 10$, is the A/D resolution in bits.

After A/D conversion, the decimal signals are split into two bytes because at one time only 8 bits of data can be transferred via RS232 or serial port for communication. Since the signals are 10 bits data, they must be divided into two bytes where the two most significant bits (MSB) constitute the first byte and the 8 least significant bits (LSB) comprise the second byte. The action is done using MATLAB/Simulink byte conversion function. In byte utility, the data are converted from decimal numbers into 8 byte ASCII characters. An example of ASCII character table is shown in Fig. 7. This is done automatically before the data signals are sent via UART serial communication.

Fig. 7 ASCII table

ASCII TABLE															
Decimal	Hex	Char		Decimal	Hex	Char		Decimal	Hex	Char		Decimal	Hex	Char	
0	0	(NULL)		32	20	(SPACE)		64	40	@		96	60		
1	1	(START OF HEADING)		33	21	!		65	41	A		97	61	a	
2	2	(START OF TEXT)		34	22	"		66	42	B		98	62	b	
3	3	(END OF TEXT)		35	23	#		67	43	C		99	63	c	
4	4	(END OF TRANSMISSION)		36	24	\$		68	44	D		100	64	d	
5	5	(ENQUIRY)		37	25	%		69	45	E		101	65	e	
6	6	(ACKNOWLEDGE)		38	26	&		70	46	F		102	66	f	
7	7	(BELL)		39	27	'		71	47	G		103	67	g	
8	8	(BACKSPACE)		40	28	(72	48	H		104	68	h	
9	9	(HORIZONTAL TAB)		41	29)		73	49	I		105	69	i	
10	A	(LINE FEED)		42	2A	*		74	4A	J		106	6A	j	
11	B	(VERTICAL TAB)		43	2B	+		75	4B	K		107	6B	k	
12	C	(FORM FEED)		44	2C	,		76	4C	L		108	6C	l	
13	D	(CARRIAGE RETURN)		45	2D	-		77	4D	M		109	6D	m	
14	E	(SHIFT OUT)		46	2E	.		78	4E	N		110	6E	n	
15	F	(SHIFT RE)		47	2F	/		79	4F	O		111	6F	o	
16	10	(DATA LINK ESCAPE)		48	30	0		80	50	P		112	70	p	
17	11	(DEVICE CONTROL 1)		49	31	1		81	51	Q		113	71	q	
18	12	(DEVICE CONTROL 2)		50	32	2		82	52	R		114	72	r	
19	13	(DEVICE CONTROL 3)		51	33	3		83	53	S		115	73	s	
20	14	(DEVICE CONTROL 4)		52	34	4		84	54	T		116	74	t	
21	15	(NEGATIVE ACKNOWLEDGE)		53	35	5		85	55	U		117	75	u	
22	16	(SYNCHRONOUS BULK)		54	36	6		86	56	V		118	76	v	
23	17	(RING OF TRANS BLOCK)		55	37	7		87	57	W		119	77	w	
24	18	(SPACE)		56	38	8		88	58	X		120	78	x	
25	19	(END OF MEDIUM)		57	39	9		89	59	Y		121	79	y	
26	1A	(SUBSTITUTE)		58	3A	:		90	5A	Z		122	7A	z	
27	1B	(ESCAPE)		59	3B	;		91	5B	[123	7B	[
28	1C	(FILE SEPARATOR)		60	3C	<		92	5C	\		124	7C	\	
29	1D	(GROUP SEPARATOR)		61	3D	=		93	5D]		125	7D]	
30	1E	(RECORD SEPARATOR)		62	3E	>		94	5E	^		126	7E	^	
31	1F	(UNIT SEPARATOR)		63	3F	?		95	5F	_		127	7F	_	(DEL)

2.1.6 Signal Serial Transmission and Baud Rate

The baud rate of the RS 232 or serial communication determines the speed of data transmission. It can be set within the range of 9600 bits per seconds (bps) to 115,200 bps. A high baud rate improves communication speed, but a lower baud rate guarantees data integrity. An example of data being transmitted using 11 bits serial data with ASCII is shown in Fig. 8.

2.1.7 Data String Protocol

A data string protocol is implemented to avoid data corruption due to noise. The data string consists of a header, a sequence of data and a terminator. The header is a

Fig. 8 Serial 11 bits binary data transfer

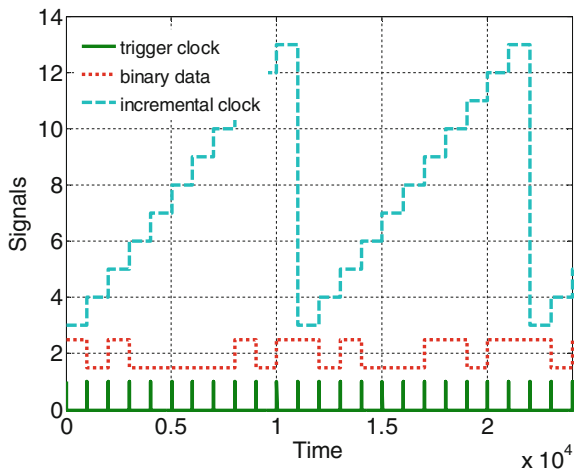
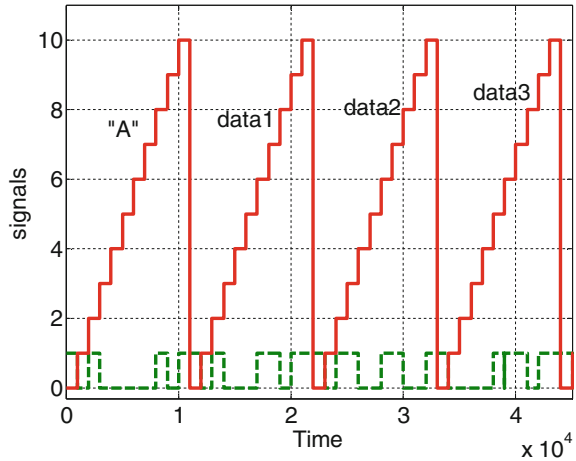


Fig. 9 Data protocol



character “A” and the terminator is a character ('\n'). The overall data sequence will be as follow

A, data1, data2, data3, data4....., /n (Fig. 9).

2.1.8 Hardware in the Loop Processing Time

The processing time is defined as the total time taken to process a batch of data. It starts with the time taken by MATLAB/Simulink to read signals from FQDC and the sensors and then send these signals to COC and IFC to be processed. It also includes the time taken by IFC to transmit output data (IGBT PWM firing and chopper operation mode signals) back to MATLAB/Simulink plus the implementation of the received data on the FQDC and EV. Finally, it adds the delay time before new data are gathered and transmitted again. The sum is called the processing time. In Fig. 10, an example of one cycle of processing time for MATLAB/

Fig. 10 Processing time of MATLAB/Simulink

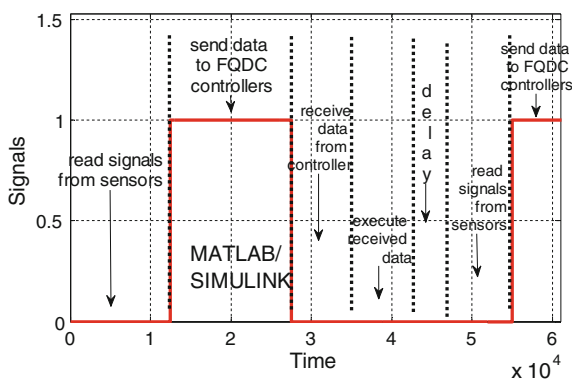


Fig. 11 Data pattern and processing time of each controller

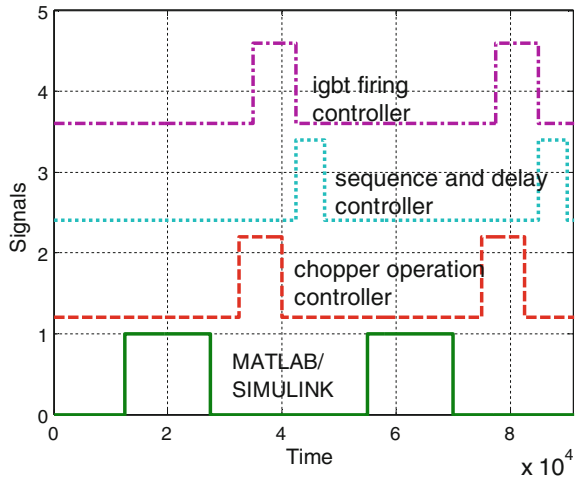
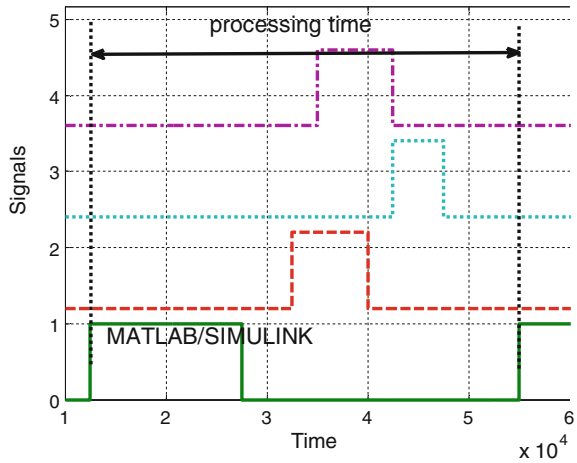


Fig. 12 Processing time in zoom



Simulink with its tasks is shown. In Fig. 11, the processing time of the whole system including Matlab/Simulink and the FQDC controllers is shown.

Figure 12 shows one cycle processing time for MATLAB/Simulink under magnification.

PIC 16F microcontrollers can operate at 20 MHz while PIC 18 microcontrollers can operate at speed of sixty(60) Mhz. The program execution time is calculated by dividing the cycle counts with the clock rate. The results show that the program execution times for the two microcontrollers are 9 and 14 microseconds(μ s) respectively. The processing time also includes the controller’s execution time (run by PIC microcontrollers at 20 MHz) and data transfer time by RS-232 serial communication at 9600 b/s (chosen for low error rate). For data transmission,

all signals require $11 \times 10 \times 3 = 330$ bits, plus a header and terminator of $2 \times 2 \times 11 = 44$ bits. So in total 374 bits are required. If we divide the total bits by the baud rate, $374/9600$, it is equal to 0.038 s (s). This is the time it takes for the serial data to be transmitted and received. If reading an analog channel requires one (1) milliseconds (ms), reading eight (8) A/D channels require eight milliseconds (8 ms). Adding a delay of ten milliseconds (10 ms), the total processing time for MATLAB/Simulink and FQDC controllers which include processing, execution and data transfer can be up to 0.075 s.

2.1.9 Processor in the Loop Test Experiment

The main objective of processor in the loop (PIL) test is to test whether the controllers can handle the data and work as the FQDC. The COC must be able to choose the expected operation mode, the SAD controller can handle the transition from one chopper operation to another without causing torque and current spikes during transition and the IFC can work as DTC and PID controller. For this purpose the system has to pass the preset earth profile test. There are a few different earth profiles that the EV can be tested on such as flat driving, going downhill and uphill as shown in Fig. 13 [19]. The number 1 driving profile is chosen because it can test all FQDC modes of chopper operation.

2.1.10 Accelerator and Brakes Signals

The accelerator pedal and brake pedal signals must be provided so that a full data set is available. In this test, all FQDC chopper modes are tested. The expected accelerator and brake signals are shown in Figs. 14 and 15 respectively.

Fig. 13 Driving profiles

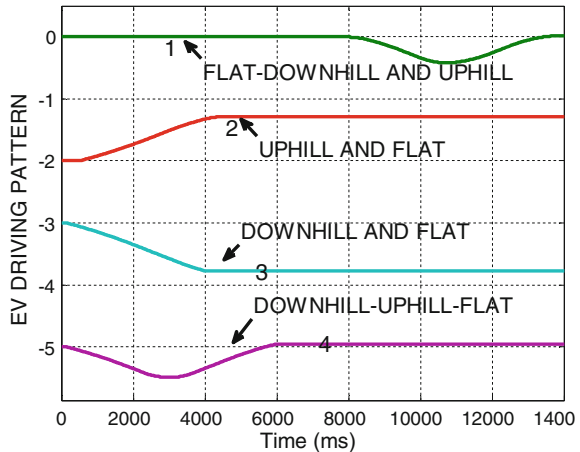


Fig. 14 Accelerator pedal signal

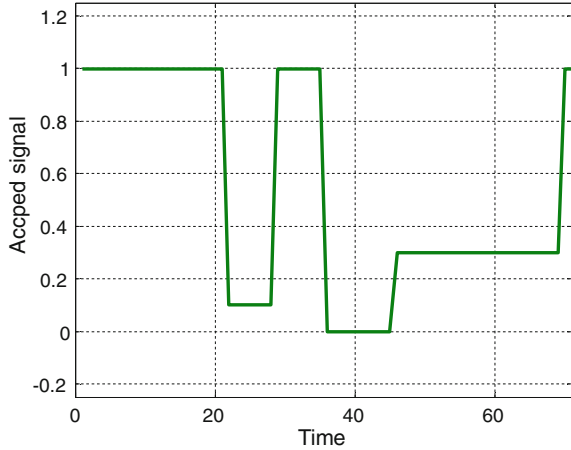
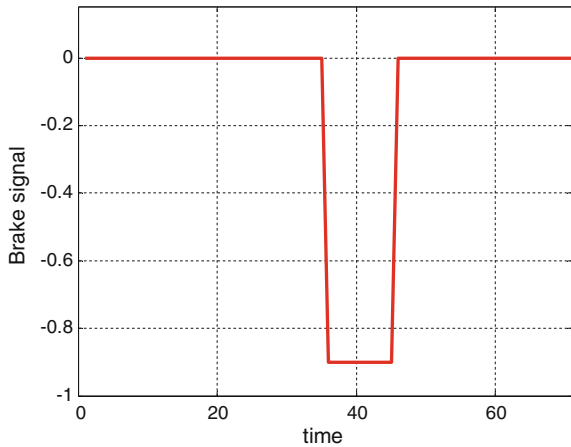


Fig. 15 Brake signal



With the chosen test profile and the accelerator and brake pedal signals, the controller is expected to engage all modes of the FQDC which are driving, field weakening, generator regenerative braking, resistive braking and parallel modes.

Figure 17 shows the block diagram of the processor in the loop(PIL) in MATLAB/Simulink model, and Fig. 16a its hardware setup. In the model, the EV uses a thirty five kilowatt(35 kW) motor operating at the maximum power of twenty kilowatt(22 kW) to drive its total weight of a thousand three hundred and thirty five kilogram (1325 kg). The time interval to update, process, send and receive data signals from MATLAB/Simulink to FQDC controllers and vice versa is in every seventy five milliseconds (75 ms). To speed up MATLAB/Simulink simulation, the model is run in accelerator or rapid accelerator mode.

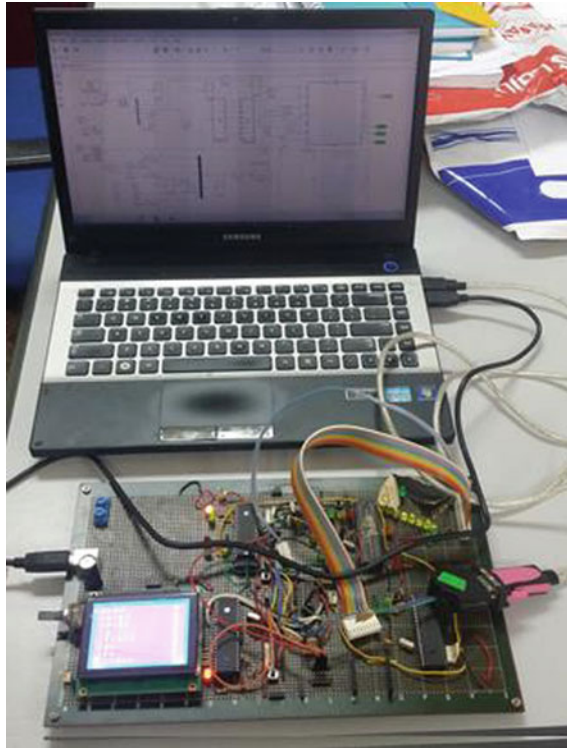


Fig. 16 Processor in the loop hardware setup

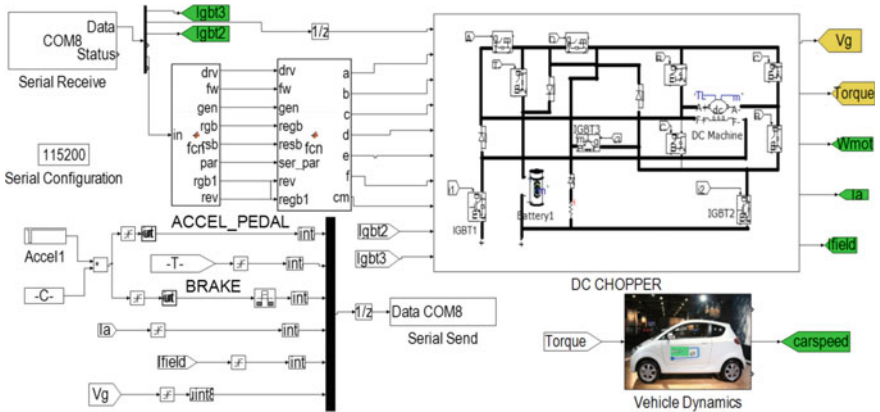
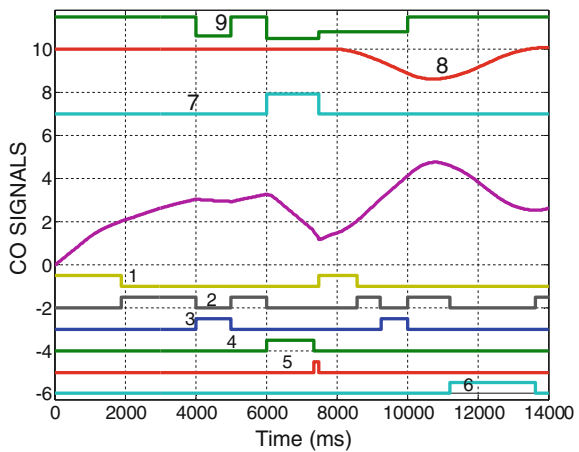


Fig. 17 Matlab/Simulink simulation model for processor in the loop

3 Result

The system is tested according to the signals shown in Fig. 18. At start up, the chopper operation controller(COC) selects driving mode. After building enough speed, the chopper operation controller(COC) selects field weakening mode since the accelerator signal is still high. However, when the accelerator signal decreases, generator mode is selected to save excess energy in the battery. In contrast, when the accelerator signal and the speed are high, field weakening mode is engaged. When brake command is triggered but the vehicle speed is high, regenerative mode is activated. As the vehicle speed drops, resistive braking mode is deployed. When brake command is replaced with low driving command, while the vehicle speed is low, the chopper operation controller(COC) selects driving mode again. As the vehicle moves downhill with a low driving command, the COC selects generator mode to save excess kinetic energy. However, if the driving command is high, the controller selects field weakening mode. As the vehicle climbs a steep hill, the speed is expected to drop. Hence, parallel mode is selected. Finally, as the vehicle regains its speed, field weakening mode is selected.

Fig. 18 Result of FQDC operation modes



chopper operation signals

Legend:

- | | |
|-----------------------|-------------------------|
| 1. Driving | 2. Field Weakening |
| 3. Generator | 4. Regenerative Braking |
| 5. Resistive Braking | 6. Parallel Mode |
| 7. Brake Signal | 8. Earth Profile |
| 9. Accelerator Signal | |

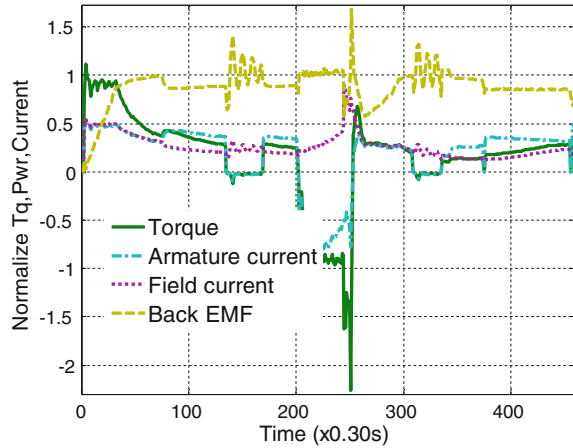
Fig. 19 FQDC performance

Figure 19 shows the output signals of the direct current (DC) series motor, the four quadrants drive chopper (FQDC), and the electric car (EC) in the forms of torque, armature current, field current and back electromagnetic force(EMF). In the figure, two important parameters to be observed are current and torque. They indicate the performance of the subsequent and delay (SAD) and igbt firing (IFC) controllers. The constant currents and torque at the beginning indicates that the IGBT firing controller works well with the PID and DTC control algorithms. No truncated torque and current are detected during chopper mode transition. The smooth transition indicates that the SAD controller and its algorithm functions well. At the beginning, under driving mode, the armature current, field current and torque are almost constant. Then these start to decrease as the back electro magnetive force (emf) increases along with speed. The back electro magnetize force (EMF) increases from zero to its maximum value as the motor reaches its maximum speed. In the field weakening mode there is a slight increase in torque due to the increase in armature current, but the field current decreases and consequently cuts the back electro magnetive force(emf). In generator mode the torque reduces slightly which results in an increase in back electro magnetive force (EMF). In regenerative and resistive braking the torque is negative due to the negative armature current. The back EMF is constant in regenerative braking but reaches its maximum value at the end of resistive braking. This is due to the rise of armature current and demand on braking torque. In parallel mode the torque increases slightly to overcome the steep climbing effect but the back EMF drops to produce a higher armature current.

4 Conclusion

PIL provides a simple method to test the FQDC that controls a series DC motor that propels an EV. It is very suitable when the input and output signals are in digital (binary) form. The capability of the controllers of the FQDC and its control algorithms were demonstrated when the COC managed to select the most appropriate modes of operation smoothly. During mode transition, the SAD was able to provide sufficient delay so the operation mode could change without producing spikes of current or torque. The IFC was able to execute all commands well to achieve the desired speed and torque using DTC and digital PID algorithms. With an appropriate tuning of the controllers, the EV performance can be further optimized. All six modes of FQDC were successfully tested according to the earth profile, and accelerator and brake pedal signals.

References

1. Gao, Y., Ehsani, M.: Design and control methodology of plug-in hybrid electric vehicles. *IEEE Trans. Ind. Electron* **57**(2), 633–640 (2010)
2. Oak Ridge National Laboratory.: Advanced Brush Technology for DC Motors (2009). Available: <http://peemrc.ornl.gov/projects/emdc3.jpg>
3. Heinrich, Walter Rentsch, Herbert Dr.-Ing. ABB Industry: “Guide to Variable Speed Drives,” Technical Guide No. 41180 D-68619 LAMPERTHEIM, Germany, 3ADW 000 059 R0201 REV B (02.01), DCS 400/DCS 500/DCS 600: ABB 2003
4. Bansal, R.C.: Birla Institute of Technology and Science, Pilani, India. *Electric Vehicle, Handbook of Automotive Power Electronics and Motor Drives*, Taylor & Francis Group CRC Press (2005)
5. Rashid, M.H.: *Power Electronics, Circuits, Devices and Applications*, 3rd edn. Prentice Hall (2004)
6. Arof, S., Yaakob, N.M., Jalil, J.A., Mawby, P.A., Arof, H.: Series motor four quadrants drive DC chopper, Part 1: Overall. In: *International Conference on Power Electronics* (2014)
7. Arof, S., Hassan, H., Rosyidi, M., Mawby, P.A., Arof, H.: Implementation of series motor four quadrants drive DC chopper for DC drive electric car and LRT via simulation model. *J. Appl. Environ. Biol. Sci.* **7**(3S), 73–82 (2017)
8. Tipsumanporn, V., Thepsathorn, P., Piyarat, W., Numsomran, A., Bun jungjit, S.: 4—Quadrant DC Motor drive Control By BRM Technique. Warwick University—IEEE. *Proceedings IPEMC 2000. Third International Power Electronics and Motion Control Conference (IEEE Cat. No.00EX435)* (2002)
9. Amjadi, Z., Williamson, S.S.: Power-electronics-based solutions for plug-in hybrid electric vehicle energy storage and management systems. *IEEE Trans. Ind. Electron.* **57**(2), 608–616 (2010)
10. Ghao, D.W., Mi, C., Emadi, A.: Modelling and simulation of electric and hybrid vehicles. *Proc. IEEE* **95**(4), 729–745 (2007)
11. Higashikawa, K., Tajima, M., Urasaki, S., Inoue, M., Fukumoto, Y., Tomita, M., Kiss, T.: Hardware-in-the-loop simulation on fault current limiting operation of RE-123 coated conductors under the influence of spatial inhomogeneity. *IEEE Trans. Appl. Supercond.* **28**(4) (2018)

12. Mina, J., Flores, Z., López, E., Pérez, A., Calleja, J.-H.: Processor-in-the-loop and hardware-in-the-loop simulation of electric systems based in FPGA. In: 2016 13th International Conference on Power Electronics (CIEP) (2016). <https://doi.org/10.1109/CIEP.2016.7530751>
13. Ruba, M., Hunor, N., Hedeshiu, H., Martis, C.: FPGA based processor in the loop analysis of variable reluctance machine with speed control. In: 2016 IEEE International Conference on Automation, Quality and Testing, Robotics (AQTR) (2016). <https://doi.org/10.1109/AQTR.2016.7501375>
14. Lee, S., Bang, H., Lee, D.: Predictive ground collision avoidance system for UAV applications: PGCAS design for fixed-wing UAVs and processor in the loop simulation. In: International Conference on Unmanned Aircraft Systems (ICUAS), IEEE (2016). <https://doi.org/10.1109/ICUAS.2016.7502561>
15. Arof, S., Muhd Khairulzaman, A.K., Jalil, J.A., Arof, H., Mawby, P.A.: Self tuning fuzzy logic controlling chopper operation of four quadrants drive DC chopper for low cost electric vehicle. In: 6th International Conference on Intelligent Systems, Modeling and Simulation, IEEE Computer Society, pp. 40–24 (2015). <https://doi.org/10.1109/isms.2015.34>
16. Arof, S., Muhd Khairulzaman, A.K., Jalil, J.A., Arof, H., Mawby, P.A.: Artificial intelligence controlling chopper operation of four quadrants drive DC Chopper for low cost electric vehicle. *Int. J. Simul. Sci. Technol.* **16**(4), 3.1–3.10 (2015). <https://doi.org/10.5013/ijssst.a.16.04.03>
17. Ching, T.W.: Soft-switching converters for EV propulsion. *J. Asian Electric Veh.* **5**(2) (2007)
18. Arof, S., Jalil, J.A., Kamaruddin, N.H., Yaakop, N.M., Mawby, P.A., Arof, H.: Series motor four quadrants drive DC chopper Part 2: driving and reverse with direct current control, pp. 775–780. In: International Conference on Power Electronics. <https://doi.org/10.1109/pecon.2016.7951663> (978-1-5090-2547-3/16)
19. Arof, S., Noor, N.M., Elias, F., Mawby, P.A., Arof, H.: Investigation of chopper operation of series motor four quadrants DC Chopper. *J. Appl. Environ. Biol. Sci.* **7**(3), 49–56 (2017)

Comparative Study of Fuel Consumption, Acceleration and Emission for Road Vehicle Using LPG or Gasoline



Loke Kean Koay, Muhammad Jasni Md Sah and Rusli bin Othman

Abstract Liquefied petroleum gas (LPG) is also called as butane or propane. LPG is a group of hydrocarbons which exists as vapor under ambient condition and has been widely used in many applications. The objective of this study is to investigate the performance effects of operating a car on LPG. The effects studied included the fuel consumption, acceleration and exhaust emission for road vehicles (cars). The engine had been retrofitted with a bi-fuel LPG kit, thus the engine is able to run with LPG or gasoline. Comparative study of the performance for the engine using gasoline and LPG was conducted. The fuel consumption experiment was conducted based on an on-the road drive cycle. The pick-up performance of the car was measured by the time required to accelerate the vehicle to various speeds. The emission of the vehicle was investigated using a non-dispersive infrared (NDIR) gas analyzer. The result indicated that LPG fuel consumption is slightly higher in comparison with gasoline fuel consumption. However, running on LPG reduces emission such CO, CO₂, O₂ and HC. Finally, fuel cost reduction can be achieved with LPG.

Keywords LPG · Fuel consumption · Performance · Exhaust emission

L. K. Koay (✉) · M. J. M. Sah · R. bin Othman
Mechanical Section, Malaysian Spanish Institute, Universiti Kuala Lumpur,
Kulim Hi-Tech Park, 09000 Kulim, Kedah, Malaysia
e-mail: koaylk@utar.edu.my

M. J. M. Sah
e-mail: jasni_mdsah@rocketmail.com

R. bin Othman
e-mail: rusli@msi.unikl.edu.my

1 Introduction

Liquefied petroleum gas (LPG) is being extracted from 40% crude oil and 60% natural gas, respectively. Basically, LPG contains propane (C_3H_8) and butane (C_4H_{10}). LPG is highly flammable and needs to be stored away from the source of ignition. Therefore, LPG is normally stored in liquid form under pressure in a pressure vessel such as a steel container, cylinder or tank [13]. LPG can also be liquefied and used by others applications by applying moderate pressure [13]. Nowadays, LPG is widely used in many applications such as for commercial business or industries by supplying energy for manufacturing production [10]. LPG is also widely used as alternative fuels for various types of vehicles such as bus, lorry, truck, taxi and car [1].

LPG has a higher octane number (more than RON 105) when compared to gasoline which is in the range of RON 91 to RON 97 [7]. By using LPG as fuel in the internal combustion engines, the thermal efficiency of the engine can be improved and provide better combustion in the engine, thus leading to a better fuel economy compared to unleaded gasoline [7]. Since the LPG is having a high octane number, the fuel can run the engine designed with high compression ratio without engine knocking. The LPG can also be liquefied at low pressure, which is from 0.7 to 0.8 MPa at the atmospheric pressure [9]. LPG provides less harmful emission to the environment. Furthermore, LPG is widely available at reasonable price in comparison to gasoline and diesel. Many investigations have proven that the emission produced by LPG is cleaner compared to the other fuels such as gasoline and diesel which produce high carbon dioxide and other harmful gases. However, the performance of the vehicle running with LPG will drop due to the LPG's low energy density. Cars can be converted to dual fuel type which can run on gasoline and LPG by modifying the engine [9].

1.1 Physical Properties and Characteristics for LPG

Generally, the LPG boiling points that are found from the commercial LPG mixture are very low and usually exist in the vapor phase under the atmospheric condition. LPG exists as heavy gas in the vapor phase, which is approximately 1.5–2.0 times the density of air [11]. LPG is almost odorless when it is in refined state, which is after being extracted from the crude oil and natural gas. However, it is important to have an odor characteristic to detect the leaking from the pipeline. Therefore, stanching agents such as thiophane or ethyl mercaptan have been added to provide odor that can be detected by human sense of smelling [13]. The mixture of air and LPG are highly combustible depending on its concentration [8]. Table 1 shows the properties of the gasoline and LPG used in the study.

Table 1 Comparative properties for different fuel types [11]

Properties/fuels	Gasoline	LPG
Chemical structure	C ₇ H ₁₇ /C ₄ to C ₁₂	C ₄ H ₁₀
Energy density/(kg/m ³)	109,000–125,000	84,000
Octane number	91–97	105+
Lower heating value/(MJ/kg)	43.44	46.60
High heating value/(MJ/kg)	46.53	50.15
Stoichiometric air/fuel ratio	14.7	15.5
Density at 15 °C/kg/m ³	737	525–580
Auto ignition temperature/K	531	724
Specific gravity 60 °F	0.72	0.576
Caloric value/(kJ/kg)	46,100	43,000

1.2 LPG's Fuel Consumption

An investigation on LPG fuel consumption for motorcycles has been conducted. The investigation found out that the fuel consumption increases by 40% when running with LPG. However, the cost for running with LPG is 50% lower than gasoline. The fuel consumption is higher than gasoline because the LPG's energy density is lower than gasoline. Besides, LPG provides clean burning to the engine, reduces clogging on spark plugs and prevents knocking. Thus, the maintenance cost will be lower [3]. Another research used a dynamometer to test the engine with different compression ratios. The result obtained showed that the usage of LPG as fuel is slightly higher than gasoline due to the higher octane rate than gasoline. Besides, the engine that is fueled with LPG can run smoothly at high compression ratio without making the engine knocking [9].

1.3 Performance and Emission of LPG as Alternative Fuel

A performance experiment about the emission characteristics of the LPG-fueled engine by applying variable compression pressures in spark ignition (SI) engine was conducted. The experiment was designed to develop the internal combustion engine that allows the pressure data produced from pressure transducer to process the same data for different types of fuels with different compression pressures. The result obtained shows that the break thermal efficiency is increasing due to the increasing compression pressure. The high octane rating of LPG runs effectively at high compression pressure without making the engine knocking [9]. Another research about the performance of the LPG engine was performed. The result obtained when using LPG's fuel shows the reduction in engine brake power, brake specific fuel consumption, pollutant emission and slightly loss of power [12, 14].

Table 2 Emissions data for LPG and gasoline [11]

No.	Emissions	Gasoline	LPG
1	CO (g/km)	0.87	0.72
2	HC (g/km)	0.14	0.12
3	NO _x (g/km)	0.12	0.16

The exhaust emissions of the four strokes spark ignition (SI) engine that uses the direct injection of LPG system was investigated. The experiment had been carried out using the four stroke SI engine coupled with a dynamometer and gas analyzer. The engine has been applied with different speeds and loads to acquire the emission from the exhaust. The gas emission has been obtained using the gas analyzer. The result showed that LPG produces less amount of harmful gas such as CO, CO₂, HC, O₂ and NO_x compared to gasoline [3, 11]. Table 2 shows the emission data of the LPG and gasoline collected from the previous study.

A test for determining the performance, fuel consumption and emission had been done on the 4 cylinders supercharged direct injection diesel engine. The torque of the engine produced using LPG's fuel is almost equal in comparison to diesel. The reason is due to the reduction in air-fuel ratio. The emission is increased due to the lower quantity of oxygen in the fuel [6]. Then, the cyclic variability at the lean operating system of spark ignition engine was compared. Cylinder pressure, indicated mean effective pressure (Imep), mass fraction burned (MFB) and combustion duration are all taking effect from the cyclic variability. Flame speed and burning rate have been decreased by lean operation. Thus, the overall combustion duration increases [4].

Choi et al. performed a research with minor alterations in the spark ignition (S.I) engine to run on LPG fuel with a shifting volume rate of LPG at 5, 10 and 20% with the assistance of a programmable logic controller (PLC). The engine speed is increased from 4000 rpm and the air-fuel ratio differs from 0.8 to 1.3. The fume gas constituents (CO₂, CO, unburned hydrocarbon (uHC) and NO_x) are measured by using non-dispersive infrared (NDIR) gas analyzer. The ignition of LPG moves towards complete combustion and the emission produced is cleaner. At high air-fuel ratio, the measure of NO_x is higher [5].

2 Methodology

2.1 Experimental Setup

As shown in Fig. 1, the engine modification has been done to run with LPG's and gasoline's fuel. The LPG's injector hose is fitted in the intake manifold to inject the amount of fuel that has been configured in the electronic control unit (ECU) into the

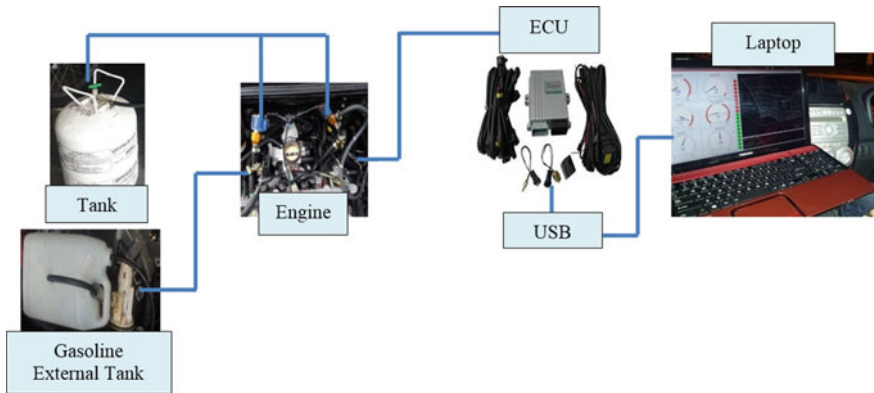


Fig. 1 LPG kits installation schematic diagram

combustion chamber. The ECU has been installed to read the engine sensor according to the information given by the connected sensor to the ECU. However, the LPG system will not work as well as the petrol system because the fuel map for LPG's fuel is not the same as the petrol/gasoline fuel map. In order to ensure the engine is run on LPG, the LPG's fuel map needs to be tuned by using the Tmachi RV2 interface. The software can read and tune the information such as injector opening time, throttle position and the amount of LPG's fuel when it is injected from the ECU. The car is tuned to achieve smooth combustion during driving on the real road. External tank for gasoline has been made to measure the gasoline fuel consumption easily. The car fuel pump casing has been disassembled to pull out the pump in order to design the gasoline external fuel pump.

2.2 Experimental Procedure for Fuel Consumption

The fuel consumption measurement was conducted using the drive cycle method. Drive cycle is a series of data points for a car speed and gear selection for the time given. The drive cycle consists of idling, acceleration, constant speed and deceleration for each session which is 10 laps with the travel distance of 5 km to obtain the same driving speed for both types of fuels. The drive cycle that had been used is the low speed urban cycle as being shown in Fig. 2. The drive cycle was chosen because the experiment was conducted on a university campus.

The usage of fuel that has been used for each experiment session will be measured by weighing the LPG tank and portable gasoline tank [2]. The data that has been obtained will be evaluated to compare the fuel consumption. Then, the engine performance experiments for each type of fuel formed the graph of maximum RPM versus time from the data RV2 software data logger. The car had been accelerated from 5 km/h to the maximum speed at 100 m using the second gear [2]. Lastly, the

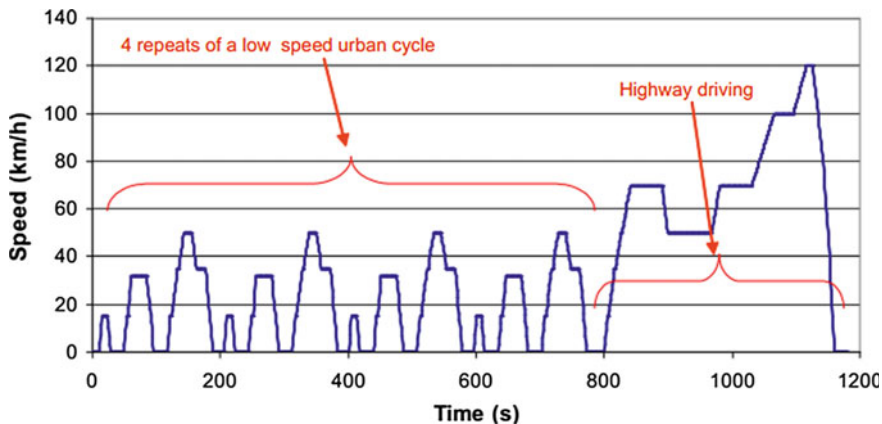


Fig. 2 Drive cycle graph [2]

acceleration performance had been conducted by using the vehicle dynamics experiment which is to accelerate from 0 to 20, 30, 40 m/s for each fuel to compare the fuel with the fastest acceleration. The time data was collected using a stop watch. The distance travelled by the car was recorded at 20, 30, 40 m/s using the vehicle dynamics equation.

3 Results and Discussion

Figure 3 shows the tuned ECU driving data from the data logger. The vehicle was running with a range of engine speed from 0 to 4000 RPM.

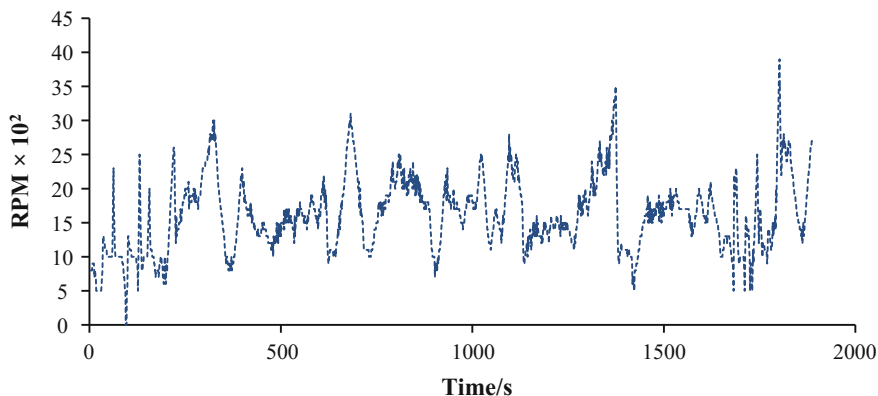


Fig. 3 Engine RPM versus time

3.1 Fuel Consumption Result

The discussion of the results begins with the LPG's fuel consumption. Table 3 shows that the average usage of LPG's fuel for 10 laps (5 km) is about 538 g or 0.195 l/km if the range of the specific gravity (SG) for LPG is 0.525–0.580. The average of the specific density is 0.55 at 15 °C [11].

Table 4 shows that the average gasoline's fuel consumption for 10 laps (5 km) is about 451.3 g or 0.122 l/km if the specific gravity of (SG) for RON 95 gasoline is 0.737. The average of the density is 737 kg/m³ at 15°C [11]. The fuel consumption for LPG is 16% higher than the gasoline fuel consumption. It is because there are many parameters which are affecting the increase of fuel usages such as fuel energy density and fuel heating value.

The higher energy density in fuel results in the less amount of working fluid to produce the desired energy. The other parameter that effects the fuel consumption is the heating value of the fuel. Both lower heating value and higher heating value of gasoline are lower than LPG's heating values which consume less working fluid due to the less heat releases during the combustion process. However, the cost to run with gasoline (0.122 l/km) is higher than LPG (0.195 l/km) even though the engine consumes less gasoline than LPG's fuel which is 0.122 l/km. Therefore, for the fuel cost, LPG is RM 0.27/km while gasoline is RM 0.28/km.

3.2 Acceleration Performance

The experiment for acceleration had been carried out on both fuel types to obtain acceleration time from 0 m/s to reach 20, 30, 40 m/s.

3.3 LPG's Acceleration

Table 5 shows the acceleration data of LPG retrofitted car. Figure 4 indicates the acceleration time for 3 different speeds from 0 to 20, 30 and 40 m/s. The acceleration slope for 40 m/s acceleration shows a drop in the performance compared to gasoline. The car takes more than 5 s to accelerate from 0 to 40 m/s.

Table 3 LPG's fuel consumption data

No. experiment	Initial fuel weight (g)	Final Fuel weight (g)	Fuel usage per 10 laps(g) Initial-final
1	4761	4227	534
2	4227	3715	512
3	3715	3147	568
Average (g)			538

Table 4 Gasoline’s fuel consumption

No. experiment	Initial fuel weight (g)	Final fuel weight (g)	Fuel usage per 10 laps (g) Initial-final
1	3216	2744	472
2	2744	2281	463
3	2281	1862	419
Average (g)			451.3

Table 5 LPG acceleration data

Speed/m/s	Time/s					Average time/s
	Test 1	Test 2	Test 3	Test 4	Test 5	
20	2.59	2.52	2.63	2.78	2.42	2.59
30	3.79	3.20	3.64	3.46	3.70	3.56
40	6.25	4.71	4.95	4.61	5.21	5.14

Fig. 4 LPG’s acceleration graph versus time

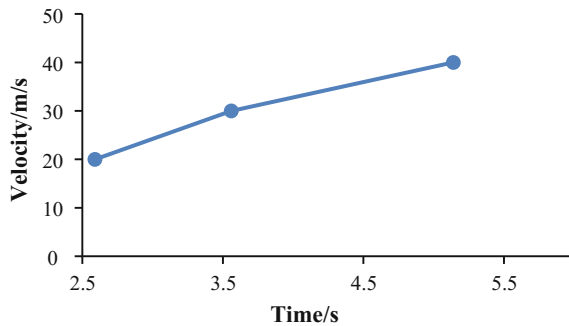


Table 6 shows the acceleration data of the gasoline operated car. Figure 5 indicates the acceleration time for 3 different speeds from 0 to 20, 30 and 40 m/s. The acceleration slope for 40 m/s acceleration shows a drop in the performance compared to gasoline. The car takes more than 5 s to accelerate from 0 m/s. Both fuel acceleration tests have been conducted using the same drive cycle. The acceleration time from 0 to 20 m/s for both fuels do not have much difference that the gasoline’s acceleration time is only shorten about 0.06 s.

3.4 Gas Emission

Tables 7 and 8 indicate the amount of gas emission for LPG fuel and gasoline fuel. The percentage of harmful emission produced by LPG such as CO, CO₂, and HC at

Table 6 Gasoline acceleration data

Speed/m/s	Time/s					Average time/s
	Test 1	Test 2	Test 3	Test 4	Test 5	
20	2.27	2.61	2.71	2.66	2.40	2.53
30	3.32	3.14	3.11	3.26	3.24	3.14
40	4.36	4.07	4.01	4.47	4.35	4.25

Fig. 5 Gasoline acceleration versus time

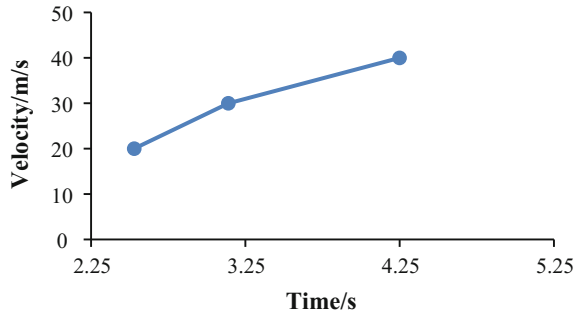


Table 7 LPG gas emission

LPG gas reading				
Type	1000 RPM	2000 RPM	3000 RPM	4000 RPM
CO ₂ (%)	6.67	12.61	12.25	11.75
CO (%)	9.15	11.83	13.37	10.25
HC (ppm)	5847	3562	4511	3325
O ₂ (%)	0.61	0.35	0.39	0.34
Air fuel ratio (AFR)	8.79	10.38	9.94	9.32
Lambda	0.6	0.71	0.68	0.65

Table 8 Gasoline gas emission

Gasoline reading				
Type	1000 RPM	2000 RPM	3000 RPM	4000 RPM
CO ₂ (%)	7.10	13.50	11.70	10.42
CO (%)	13.48	16.12	11.38	8.34
HC (ppm)	4872	5497	4124	3369
O ₂ (%)	0.21	0.19	0.19	0.19
Air fuel ratio (AFR)	12.28	12.17	12.41	12.69
Lambda	0.81	0.83	0.85	0.87

1000 and 2000 RPM are lower than gasoline's emission. However, there is a slightly difference in the amount of HC for both types of fuels at 3000 and 4000 RPM which is in the range of 3000–4000 ppm. On the other hand, the percentage of CO and CO₂ for LPG's are cleaner at 3000 and 4000 RPM compared to gasoline emission due to rich tuning of the engine.

4 Conclusion

The experimental data shows that there is an increase in fuel consumption when LPG is used as fuel compared to gasoline. It is because the energy density of the LPG is lower than gasoline. The fuel consumption for LPG is 16% higher than the gasoline fuel consumption. Besides, the acceleration performance of the car was reduced when using LPG as fuel compared to gasoline. The car takes more than 5 s to accelerate from 0 to 40 m/s when using LPG while only 4.25 s when using gasoline. However, the emission produced by LPG is cleaner than gasoline and that it is better for the environment.

References

1. Agrawal, S.K.: *Internal Combustion Engines*. New Age International, India (2006)
2. Barlow, T.J., Latham, S., Mccrae, I.S., Boulter, P.G.: *A Reference Book of Driving Cycles for Use in The Measurement of Road Vehicle Emissions*, 3rd edn. TRL Limited, Forest Stewardship, Germany (2009)
3. Bisen, H.B., Suple, Y.R.: Experimental investigations of exhaust emissions of four stroke SI engine by using direct injection of LPG and its analysis. *Int. J. Mod. Eng. Res. (IJMER)* **3**, 1600–1605 (2013)
4. Ceviz, M.A., Yüksel, F.: Cyclic variations on LPG and gasoline—fuelled lean burn SI engine. *Renew. Energy* **31**(12), 1950–1960 (2006)
5. Choi, G.H., Kim, J.H., Homeyer, C.: Effects of different LPG fuel systems on performances of variable compression ratio single cylinder engine. In: *Design, Application, Performance and Emissions of Modern Internal Combustion Engine Systems and Components*, pp. 369–375. ASME (2002). <https://doi.org/10.1115/ICEF2002-519>
6. Kumaraswamy, A., Prasad, B.D.: Use of LPG in a dual fuel engine. *Int. J. Mod. Eng. Res.* **2** (6), 4629–4633 (2012)
7. Lanje, A.S., Deshmukh, M.J.: Performance and emission characteristics of SI engine using LPG-ethanol blends: a review. *Int. J. Emerg. Technol. Adv. Eng.* **2**(10), 146–152 (2012)
8. Lucas, K., Blumenberg, E., Weinberger, R.: *Auto Motives Understanding Car Use Behaviours*. Bingley, Emerald (2011)
9. Mamidi, T., Suryawnshi, G.: Investigations on S.I. engine using liquefied petroleum gas (LPG) as an alternative fuel. *Int. J. Eng. Res. Appl. (IJERA)* **2**(1), 362–367 (2012)
10. Mobley, R.K.: *Plant Engineer's Handbook*. Butterworth-Heinemann, Wildwood Avenue (2001)
11. Pundkar, A.H., Lawankar, S.M., Deshmukh, S.: Performance and emissions of LPG fueled internal combustion engine: a review. *Int. J. Sci. Eng. Res.* **3**(3), 1–7 (2012)

12. Salhab, Z., Qawasmi, M.G., Amro, H., Zalloum, M., Qawasmi, S., Sharawi, N.: Ignition outboard engine powered by gasoline and lpg. **5**, 47–52 (2011)
13. Saxon, F.: Tolley's Basic Science and Practice of Gas Service, 4th edn. Elsevier, Jordan Hill (2006)
14. Yousufuddin, S., Mehdi, S.N.: Performance and emission characteristics of LPG-fuelled variable compression ratio SI engine. *Turk. J. Eng. Environ. Sci.* **32**, 7–12 (2008)

Design and Construction of a Micro-hydro Turbine for Additional Home Power to Use a Conventional Water Pipeline



Tajul Adli bin Abdul Razak, Shahril Nizam bin Mohamed Soid, Khairil Shahril bin Shafee, Mohd Riduan bin Ibrahim and Aznizam bin Abdullah

Abstract This paper covers the design and fabrication of a micro-hydro turbine that is using a conventional water pipeline to generate additional home power. The process started with identifying the suitable design and then uses the standard design as reference to develop the micro-hydro turbine. The project included computational fluid dynamics (CFD) simulation test that was run using ANSYS CFX. Data obtained from simulation test was used to verify the actual data that obtain from confirmation test.

Keywords Computational fluid dynamics · ANSYS CFX · Micro-hydro turbine Francis · Energy harvesting

1 Introduction

Since the beginning of civilisation, renewable and sustainable energy sources have been important for humans. For centuries, this type of energy source has been used in many ways such as biomass which has been used for heating, cooking, while for power generation, hydropower and wind energy has been used for mechanical

T. A. bin Abdul Razak (✉) · S. N. bin Mohamed Soid · K. S. bin Shafee
M. R. bin Ibrahim · A. bin Abdullah
Malaysian Spanish Institute, Universiti Kuala Lumpur, Kulim Hi-Tech Park,
09000 Kulim, Kedah, Malaysia
e-mail: tajul.adli@yahoo.com.my

S. N. bin Mohamed Soid
e-mail: shahrilnizam@unikl.edu.my

M. R. bin Ibrahim
e-mail: mohriduan@unikl.edu.my

A. bin Abdullah
e-mail: aznizam@unikl.edu.my

movement. Then, this mechanical movement generated by hydropower and wind energy was used for electricity production. This project focuses more on the hydropower technology and development since it is the second most sustainable renewable energy after wind energy.

2 Problem Statement

A water storage tank will not only be used to save water, but it also has potential energy because it requires gravitational force for the distribution of daily use at home. Unfortunately, this energy is not fully utilized or ignored because the water pressure for household daily use it is not up to the maximum level.

Using micro-hydropower technology as reference, the potential energy of the water storage tank can be used to generate kinetic energy when water is falling into the distribution pipe pushing the turbine blades. Then the kinetic energy or hydropower from the turbine moves a dynamo that is connected to the turbine where the kinetic energy is converted into electrical energy.

3 Significance of the Project

The significance of this project is related to the installation of a micro-hydropower turbine within conventional water pipeline. This does not only offer alternative renewable and sustainable energy sources but it also utilizes all unused energy. Dependency on electricity from on-grid can be reduced and indirectly save money. The results obtained provide a platform for further investigation into our study which aimed at improving the efficiency of the micro-hydro turbine for commercial use of the combination with other renewable and sustainable energy sources such as wind energy and solar energy to create an independent off-grid hybrid power system.

4 Objective of the Project

The objectives of this project are as follows:

- i. Understand the stable turbines runner type, effects of water flow and buildings height to the power output from a micro-hydro turbine.
- ii. Design and construction of a prototype of a micro-hydro turbines that is able to supply additional electricity for standard household usage.
- iii. The output obtained from turbine should be ranged 3–12 V of direct current (VDC).

5 Project Scope and Limitation

This project focused on the design and fabrication of a prototype micro-hydro turbine that is able to supply additional electricity for standard household usage by studying and comparing the type of turbine runner, in terms of performance and head. The design of the prototype is based on design consideration, facilities, cost and performance of the turbine runner and will not cover the electrical or electronic system for the micro-hydropower system. All parts for the electrical or electronic system in this project are commercial products.

6 Literature Review

The history of micro-hydropower started mostly for milling grain with the wooden waterwheel which are for some 2000 years, or waterwheels of various types that had been in use in many parts of Europe and Asia.

6.1 *Micro-hydro Turbine*

To date there is still no internationally agreed definition of term the micro-hydropower where other terms such as mini-, small- and pico- are also used for range diminishing capacity down to a few hundred watts [1].

6.2 *Forms of Energy*

Micro-hydropower is 'fuelled' by water moving in the hydrological cycle or water cycle (see Fig. 1) which is powered by solar energy. It happens when the converted heat from the solar radiation is reaching the surface of earth and evaporates water mostly at the sea. Some of the water vapour is brought over land areas where it later condenses into clouds and rain. Then some of the water flows back towards the sea because of precipitation on the land surface and this generates run-off, under the influence of gravity. Since the water cycle is powered by solar energy, therefore it makes micro-hydropower renewable and sustainable and will continue if the sun continues to shine [2].

As this 'water cycle' concept is applied to conventional piping systems in houses, the stored potential energy in the water storage tank in the house can be harvested to fuel micro-hydropower. Ramage [1] in her book describes that water (or anything else) held at height represents stored energy. To lift one kilogram vertically through one metre against the gravitational force of the earth, about 9.81 J

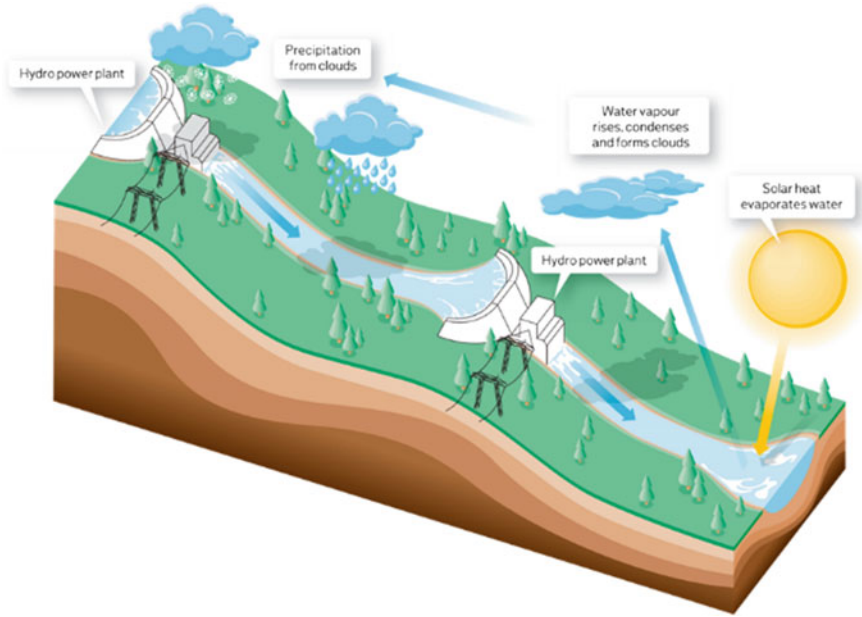


Fig. 1 Natural water cycle

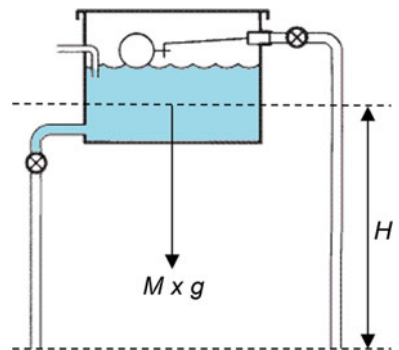
of energy input are needed (p. 155). Therefore, if M kilograms are raised through H metres, the stored potential energy in joules is given by;

$$Potential\ Energy = MgH, \tag{1}$$

where g is represents the acceleration due to gravity, whose value is about $9.81\ ms^{-2}$. M represents the water mass and H represents the height of water storage tank as shown in Fig. 2.

The Law of Energy Conservation as the First Law of Thermodynamics stated that “In any change from one form of energy to other forms, the total quantity of

Fig. 2 Water with potential energy



energy remains constant”. Therefore, if energy is conserved, the potential energy loss by a freely falling object must appear as a gain in its kinetic energy, so an object that falls from rest (zero kinetic energy) through a height H will acquire kinetic energy [3].

6.3 *Effects of Water Flow and Head to the Power Output*

Micro-hydro turbines convert water falling into the distribution pipe (water pressure) into mechanical shaft power, which can be used to drive an electricity generator. The power available is proportional to the product of pressure head, volume water flow rate and must consider energy losses since in any real system frictional drag and turbulence will cause some energy loss to water [4]. The general formula for any hydro system’s power output is;

$$P = \rho \times g \times H \times Q \times \eta, \quad (2)$$

where P is the mechanical power produced at the turbine shaft (watts), η is the hydraulic efficiency of the turbine, ρ is the density of water volume (kg/m^3), g is the acceleration due to gravity (ms^{-2}), Q is the flow rate passing through the turbine (m^3/s) and H is the effective pressure head of water across the turbine (m).

6.4 *Turbine Runner*

These two types of turbines use different mechanics to rotate the runner.

- a. **Impulse Turbine Runner**—An impulse turbine operates into atmospheric pressure by using the kinetic energy of water jet to drive the runner and discharged to atmospheric pressure [5].
- b. **Reaction Turbine Runner**—The reaction turbine is fully immersed in water and specifically enclosed in a pressure casing. The runner blades are designed to rotate caused by the pressure difference across them which impose the lift force [6].

6.5 *Design Consideration*

These considerations are;

- i. **Flow rate measurement.** The volume flow rate Q of a fluid for this project taken from the water flow rate of a conventional water piping system.

- ii. **Head of measurement.** Head of measurement, H for this project taken from the different height of the water storage tank to the height of installation location of the micro-hydro turbine and this value will be constant.
- iii. **Diameter of inlet measurement.** Diameter of inlet measurement for this project taken from pipe diameter for distribution of conventional water piping system in the house. This value will be constant.
- iv. **Turbine power.** Power in watt generated in the turbine shaft calculated using Eq (2).
- v. **Turbine speed.** The turbine speed in RPM, to be determined using simulation test.
- vi. **Type of turbine runner selection**—should be based on the low head and low flow rate since for this project, the current design of micro-hydro turbine will be compressed to be a smaller design to be compatible with conventional water piping system in the house.
- vii. **Fabrication facilities.** The designed turbine runner should be able to be fabricated using common facilities in a current facilities in workshop.

7 Methodology

Figure 3 shows the steps of the project in brief which consist of the design stage, virtual simulation by virtual, fabrication of actual parts, assembly process and experimental comparison with actual design and simulation.

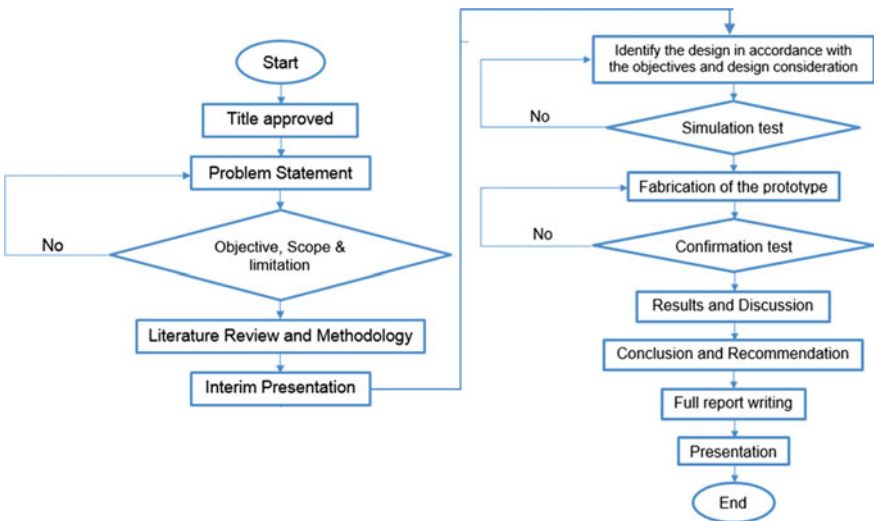


Fig. 3 Project flowchart

7.1 Designing Phase

In this process, the design of the micro-hydro turbine will be identified according to the objective and design consideration. It also includes information gathering and preparation for 3D modelling. After all data is collected, the 3D modelling process started according to the gathered information. Solidworks was used for the 3D modelling.

7.2 Simulation Test

After the 3D modelling process is done, a computational fluid dynamics (CFD) simulation test was run using ANSYS CFX. The output of this test was the required info to verify the confirmation test.

7.3 Fabrication of the Prototype

In this process, the G-code for generated tool path was generated to fabricate the prototype using a 3D printing machine. The process requires the use of a 3D model to tool path Slicer software which is the Cura and Stratasys Control Panel. Then the prototype was fabricated using two different models of 3D printers; the Odyssey X2 Series that uses Polylactic acid (PLA) as material for fabrication and the Stratasys FDM 200mc that uses Acrylonitrile butadiene styrene (ABS) as material for fabrication. Then, the finished parts were assembled.

7.4 Confirmation Test

Confirmation test is a process to verify the final output of prototype product with the theoretical data that was obtained from simulation test.

8 Results and Discussion

The design of the micro-hydro turbine also considered the characteristics from conventional pipelines as the boundary conditions. The limited space in house hold and low volume flow rate conventional water pipelines shows that the micro-hydro turbine requires a low head and low flow rate. The micro-hydro turbine was designed based on the standard design of the Francis turbine.

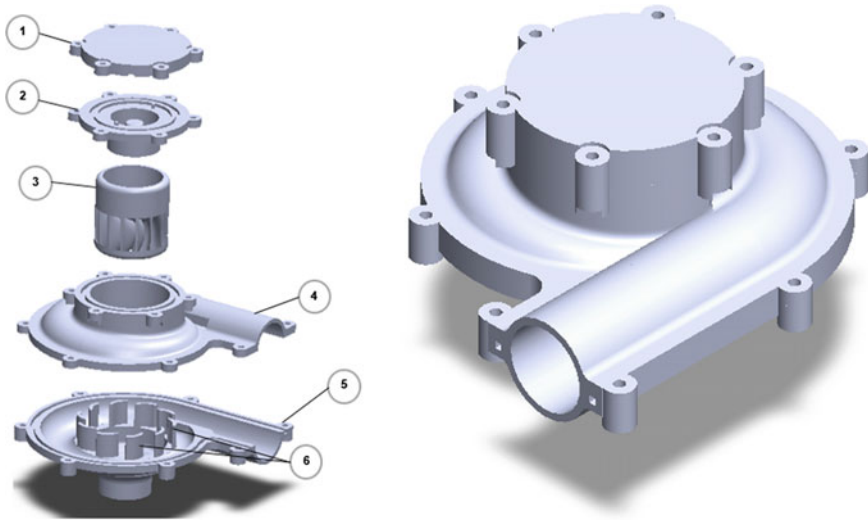


Fig. 4 Micro-hydro turbine assembly (on the right) and parts; (1) stator mount cover, (2) stator mount, (3) turbine rotor, (4) top spiral-casing, (5) bottom spiral-casing, (6) 'fixed' guide vanes

In standard design, the turbine runner is connected to the generator via a shaft. However, to reduce the space usage, the turbine runner and generator's rotor are combined. The inlet and outlet of the micro-hydro turbine are dimensioned according to a standard conventional pipeline. Figure 4 shows the exploded view and completed 3D model of the selected design.

8.1 Simulation Test

The relevant boundary conditions present during the measurements were reproduced in the simulations to ensure regularity of the comparison between computed and measured data. Computing hydraulic characteristics, CFD simulations give a detailed insight into the complex structure of the Francis turbine fluid flow, as shown in the following Figs. 5 and 6. The data computed from the CFD simulations were then sorted by percentage of valve opening as shown in Table 1.

8.2 Fabrication of the Prototype

The prototype was fabricated using two types of 3D printer machines with different types of materials. The reason for this were the time constraint, manufacturing feasibility and limited space of working area. The two types of material for

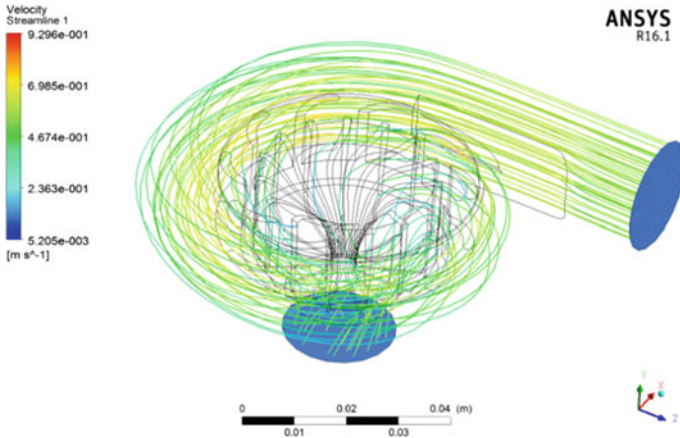


Fig. 5 Fluid flow streamlines

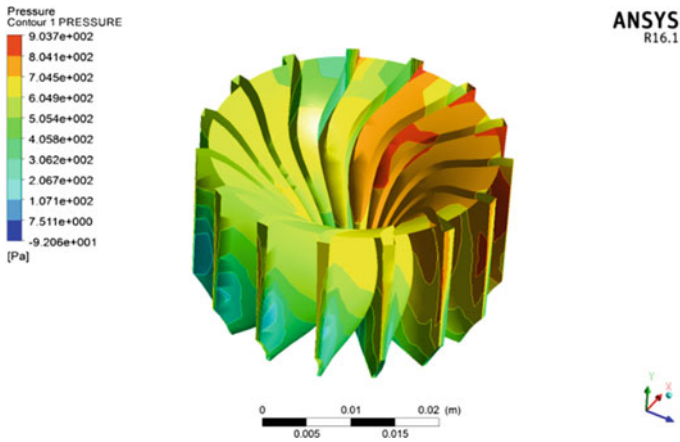


Fig. 6 Contours of static pressure on runner surfaces

Table 1 Analytical data from simulation test

Percentage of valve opening (%)	Velocity, v (m/s)	Angular speed, ω (rad/s)	Torque, τ (Nm)	Mechanical power, P (W)
25	9.296E-01	4.893E+01	1.870E-02	0.914946568
50	1.719E+00	9.047E+01	2.057E-02	1.860862737
75	2.310E+00	1.216E+02	2.185E-02	2.657037379
100	3.577E+00	1.883E+02	2.197E-02	4.135751874

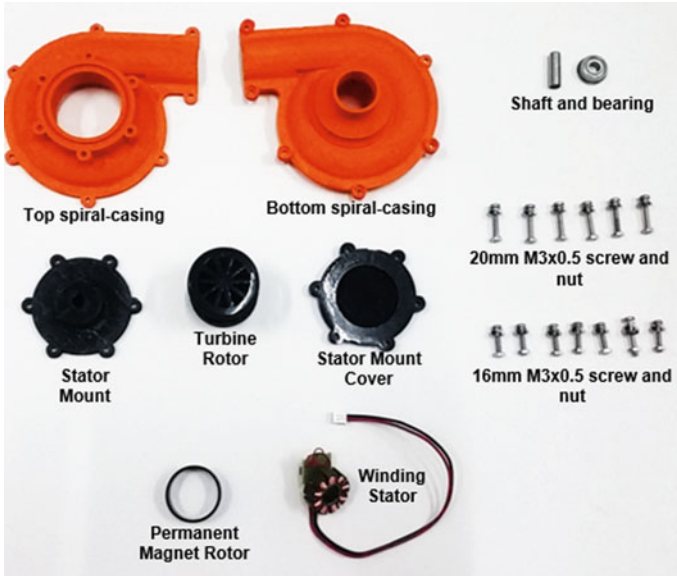


Fig. 7 Parts that required to assembly the micro-hydro turbine

fabrication are; Polylactic acid (PLA); in black and Acrylonitrile butadiene styrene (ABS), in orange. Despite the different types of the used materials, the quality of the fabricated parts was still the same in terms of tolerance and toughness.

Additional parts were required to complete the assembly of the micro-hydro turbine. Figure 7 shows all parts that were required to assemble the micro-hydro turbine including fabricated parts and commercial parts. The winding stator and permanent magnet were taken from the brushless motor in a commercial mini water pump.

Fig. 8 Final product of micro-hydro turbine

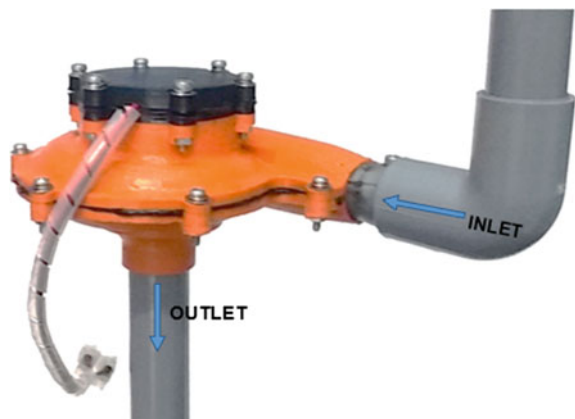


Figure 8 shows the final product of the micro-hydro turbine that was connected to UPVC PIPE 15 mm (SIRIM QAS CERT TO MS6828 PT-1:1999) and ready to be connected to the conventional water pipeline.

8.3 Confirmation Test

The micro-hydro turbine was tested with the same setup as boundary conditions present during the measurements and were reproduced in the simulations. The data obtained during the test and compiled is shown in Table 2. The value of the power, P (watts) from Tables 1 and 2 were combined and compared as shown in Fig. 9.

Table 2 Analytical data from confirmation test

Percentage of valve opening (%)	Avg. voltage, V (V)	Avg. currents, I (A)	Electrical power, P (W)
25	0.690	0.17	0.117
50	1.702	0.22	0.374
75	2.425	0.24	0.582
100	3.229	0.35	1.130

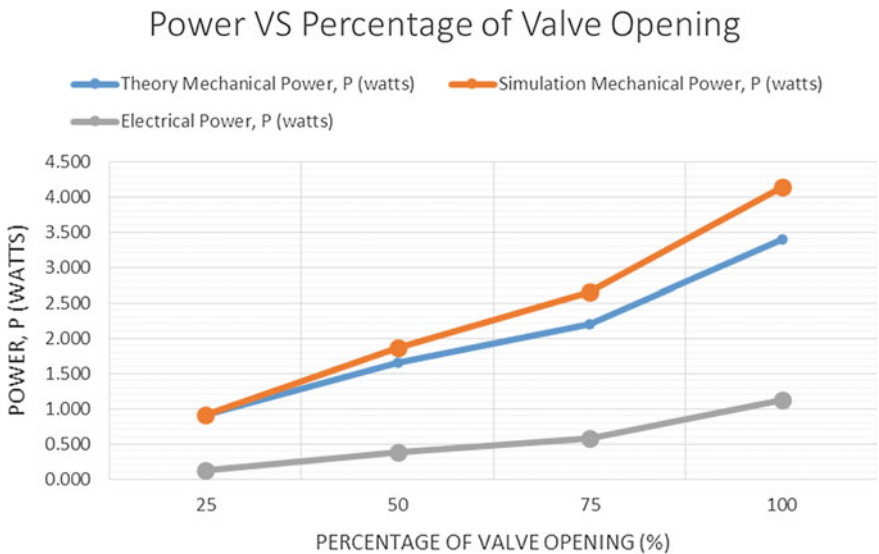


Fig. 9 Comparison of computed and measured turbine power output

9 Conclusion

The results from the confirmation test in Fig. 9 show that the flow rate of the water that enters through the turbine runner will affect the speed of the turbine runner. This will directly affect the power output from a micro-hydro turbine since the speed of the generator is proportional to the speed of the turbine. This is because the generator is connected directly to the turbine runner.

The confirmation test result also has a significant difference with the theoretical result. However, the same data trend shows that the correct turbines runner type has been used. The significant difference may be caused by;

- (1) fabrication defects,
- (2) high surface roughness,
- (3) Leaking that will reduce the flow rate, and
- (4) Inconsistency of flow rate caused by the turbulence flow.

The prototype of the micro-hydro turbine is able to supply additional electricity for household usage however it cannot achieve maximum output as required in the objective. In conclusion, some of the objectives for this project were successful achieved but some are partly achieved and required further improvement.

References

1. Boyle, G.: *Renewable Energy: Power for a Sustainable Future*, 4th edn. Oxford University Press, Oxford (2017)
2. Killingtveit, Å.: Hydroelectric power. In: Letcher, T.M. (ed.) *Future Energy*, 2nd ed., pp. 453–470. Elsevier, Boston
3. Everett, R., Boyle, G., Peake, S., Ramage, J.: *Specifications of Renewable Energy: Power for a Sustainable Future*, 3rd ed. Oxford University Press, Oxford (2015)
4. Everett, R., Boyle, G., Peake, S., Ramage, J.: *Energy systems and sustainability: Power for a sustainable future*, 2nd ed. Oxford University Press, Oxford (2012)
5. Okot, D.K.: Review of small hydropower technology. *Renew. Sustain. Energy Rev.* **26**, 515–520 (2013)
6. Barelli, L., Liucci, L., Ottaviano, A., Valigi, D.: Mini-hydro: a design approach in case of torrential rivers. *Energy* **58**, 695–706 (2013)

Design and Fabrication of a Magneto-rheological Fluid Based Torque Sensor for Automotive Application



Muhamad Husaini Abu Bakar and Amirul Qusyaini Alwi

Abstract A magneto-rheological (MR) based torque sensor is a device that transmits the torque by the cutting force of the MR fluid. The magneto-rheological fluids technology has been tested for many industrial applications, such as dampers, actuators, etc. A MR fluid is an intelligent material whose rheological characteristics change rapidly and can be easily controlled in the existence of an applied magnetic field. It presents a viscous coupling controllable by torque, the coupling consists of two types of discs, one is connected to a housing (fixed discs), and the other is connected to an axis (rotating discs). The drive discs and the follower discs are arranged in turn and are interleaved. The MR fluid is filled in the housing. The magnetic fields freeze the fluid so that the shearing torque is generated between the driving discs and the follower discs due to the shears between the slots in the discs below the magnetic fields. The torque is controlled by electromagnets. To have a large pair with small electrical power, the coil turns must be large, so that the response is delayed due to the inductance of the coil. A comparison between the magnetic flux and the intensity of the designs obtained from finite element analysis allow to derive the best design for the prototype in order to proof the concept. The turn of the winding coil and the current as a fixed value is 1500 turn and 1 A current.

Keywords Magneto-rheological (MR) fluid · MR fluid disc brake
Magnetic · Non-magnetic · Finite element

M. H. Abu Bakar (✉) · A. Q. Alwi
System Engineering and Energy Laboratory, Malaysian Spanish Institute,
Universiti Kuala Lumpur, Kulim Hi-Tech Park, 09000 Kulim, Kedah, Malaysia
e-mail: muhamadhusaini@unikl.edu.my

A. Q. Alwi
e-mail: amirul_0303@yahoo.com

© Springer Nature Switzerland AG 2020
A. Ismail et al. (eds.), *Advanced Engineering for Processes and Technologies*,
Advanced Structured Materials 102, https://doi.org/10.1007/978-3-030-05621-6_8

1 Introduction

Magneto-rheological (MR) fluids are smart and controllable materials, even though at first glance it does not look so impressive. They are a noncolloidal mixture of ferromagnetic particles randomly dispersed in oil or water, plus some surfactants useful to avoid the settling of the suspended particles. The overall aspect is like a greasy quite heavy mud, since the MR fluids density is more than three times the density of water.

The magneto-rheological fluid technology (MRF) is an old “newcomer” that reaches the market at high speed. Several industries, including the automotive industry, are full of possible MRF applications. Magneto-rheological fluid technology has been used successfully in several low and high volume applications. A structure based on MRF could be the next generation in design for products where power density, precision, and dynamic performance are the key features (Fig. 1).

Also, for products in which it is necessary to control the movement of the fluid by varying the viscosity, a structure based on MRF could be an improvement in functionality and costs. Two aspects of this technology, the direct cut mode (used in brakes and clutches) and the valve mode (used in dampers) have been thoroughly studied, and several applications are already present in the market. Excellent features such as fast response, a simple interface between the electrical power input and mechanical output power, and precise control capability make the MRF technology attractive for many applications. The thermal range of working of these materials without decay of their properties are 40–150 °C, depending mostly on carrier properties [1, 2]. The rheological properties of controllable fluids depend on the concentration and density of particles, particle size, shape distribution and properties of the carrier fluid, additional additives, applied field, temperature, and other factors. The interdependency of all these factors is very complicated [3].

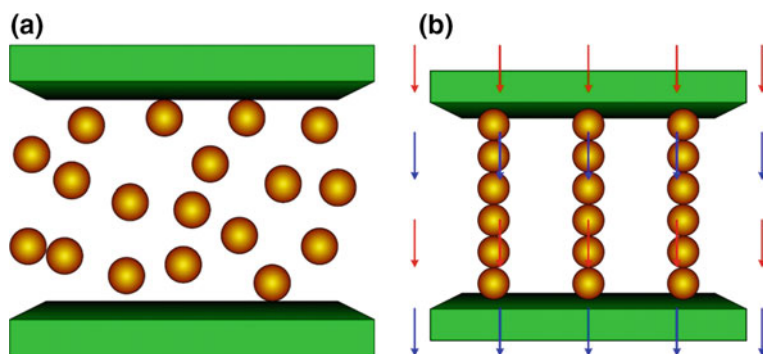


Fig. 1 Working principle of MR Fluid **a** MR fluid with no magnetic field, where particles are randomly dispersed; **b** MR fluid with an applied magnetic field with parallel chains

The magneto-rheological response of fluids is the result of polarization in the particles by applying an external magnetic field. At particle level, a dipole structure is assumed. Depending of an applied magnetic field, the particles are evenly distributed [4]. The fluid has a consistency similar to ordinary mineral oil. Its behavior is similar to a Newtonian fluid, with a linear dependency of the shear stress versus the tangential velocity gradient.

2 Methodology

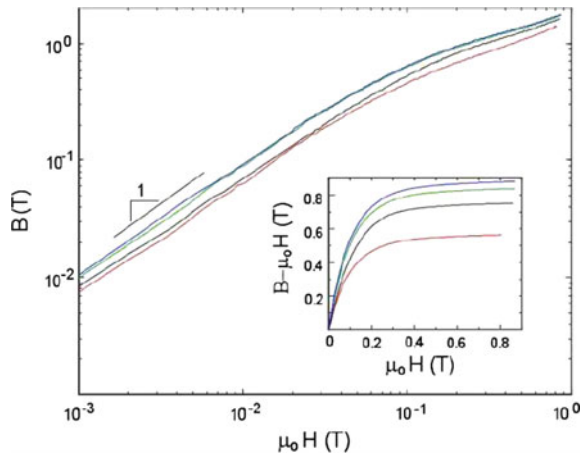
2.1 Magnetic Proprieties

The magnetic proprieties exhibit approximately linear behavior, as shown in Figs. 2 and 3, where there is a typical induction curve ($B-H$ curve) of commercial MR fluids. As can be seen, the MR fluids magnetic properties up to an applied field of about $0.02/\mu_o$ A/m, where μ_o is the permeability in a vacuum. In this region, the differential permeability of the magneto-rheological fluids, that is the slope of $B(H)$, is varying between 5 and 9 times that of a vacuum, can be considered relatively constant. Magnetic saturation can be observed out of the linear regime, which becomes complete for fields of more than 0.4/A/m [5].

2.2 MR Fluid Properties

The magnetic properties of magneto-rheological fluids vary significantly considering the properties of most ferromagnetic materials properties. Ferromagnetic induction can typically be linearized over a much broader range of the applied field,

Fig. 2 Magnetic properties of the magnetorheological fluid



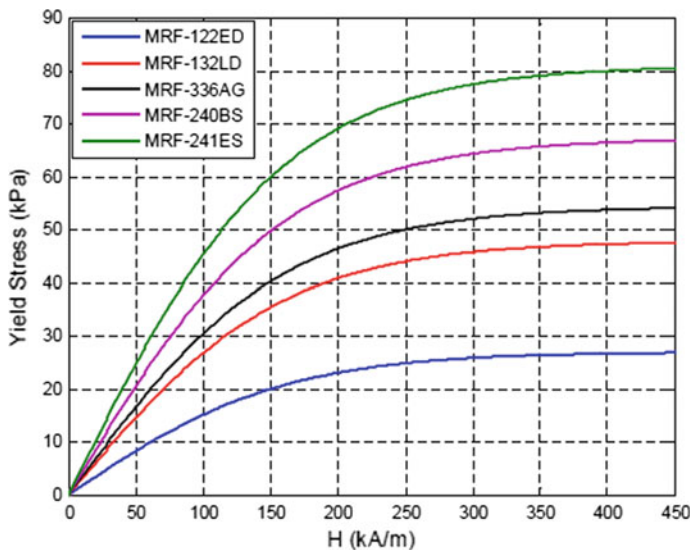


Fig. 3 Predicted yield stress as a function of applied field [6]

and the corresponding permeability is several orders of magnitude greater [7]. Little or no hysteresis can be observed in the induction curves. This super-paramagnetic behavior is a consequence of the magnetically soft properties of the iron used as particulate material in these fluids and the mobility of this particulate phase [8].

The mechanical energy required to yield the formation of MR fluid increases with the increase in magnetic field resulting in the yield shear stress to increase as well. Typical values of the maximum achievable yield strength are given in Table 1. It is observed that MR fluid behaves like Newtonian fluids when there is no magnetic field applied. The MR fluids performances are limited by the magnetic saturation of the particles. Iron particles have the highest magnetic saturation.

A conventional magneto-rheological fluid consists of 20–40 volume percent by volume of relatively pure iron particles, 3–10 μm in diameter, suspended in a carrier liquid such as mineral oil, synthetic oil, water or glycol. Varieties of patented additives, similar to those found in commercial lubricants to discourage gravitational adjustment and promote particle suspension, are commonly added to the magneto-rheological fluid to improve lubricity, modify viscosity and inhibit wear [10].

Table 1 Magnetorheological fluid properties [9]

Property	MR fluid
Yield stress τ	50–100 kPa
Maximum magnetic field	150–250 kA/m
Viscosity η (at 25 °C under no magnetic field)	0.2–0.3 Pa s
Density	3–4 g/cm ³

2.3 Experimental Setup

In order to achieve the aim from this study, there have several stages need to be consider. The stage starts with the analysis of MR fluid in the device. The analysis is conducted by using a commercial software. Several option are possible to select an appropriate software. In general, a magnetic finite element Method solution produce may be broken into the following stages.

2.3.1 MR Fluid Mixing Procedure

The ingredients of 100 ml of two types of magnetorheological fluid are shown in Table 2. Table 2 as weight measures of these ingredients. The table shows that the quantity of iron powder is the same for the two types of magnetorheological fluids, while the difference is only in the weight of the hydrocarbon oil. Thereby, the percentage of the volume is different. The added grease slows the settling and makes it easier to remix. This magneto-rheological fluid recipe results in a fluid having about 20–32% iron by volume. This fluid will have a maximum yield strength and magnetic properties that are somehow similar to the Rheonetic MRF 132-DL magneto-rheological fluid produced commercially by the LORD Corporation (2005). MR 132 was used in this study.

Initially, the appropriate amount of oil, grease and iron powder were measured. Next, the grease was added to the oil and was mixed thoroughly. Mixing is most effectively accomplished with a rotary mixer. The mixture was allowed to sit for a few hours (this allows the grease to dissolve in the oil) and then it was remixed for a few minutes. Finally, the iron powder was added to the oil and grease mixture. It started by adding about half of the iron powder. A stirring stick was used to get the dry iron powder to mix with the liquid. Once the mixture appears to be relatively uniform, and no dry iron powder is visible, the remainder of the iron powder was added and was continued to stir with the stick until the mixture appears without lumps. The final MR fluid was dark gray. The mixture was needed to be remixed or occasionally shaken as the iron particles slowly settle leaving a layer of clear oil on the top.

Table 2 Ingredient of 100 ml of 2 types of magnetorheological fluid [11]

Ingredients	MR 122	MR 132
Iron powder (g)	150	150
Hydrocarbon oil (g)	55	31
White lithium grease (g)	5	5
Percentage volume %	20–22	30–32

2.3.2 Modeling of Yield Shear Stress of MR Fluid

Another important relationship regarding the magneto-rheological fluid behavior is the yield stress as a function of the applied field strength. It is well recognized that the yield stress developed in the fluid increases monotonically with growing magnetic field strength. The yield stress remains to increase until the fluid reaches the magnetic saturation [7] has predicted yield stress as a function of the applied field strength should be predicted based on a theoretical model. The model is general and works for any magneto-rheological fluid. The model relates the yield stress to the magnetic field strength as:

$$\tau_0 = C \cdot 271,700 \cdot \Phi^{1.5239} \cdot \tanh(6.33 \cdot H), \quad (1)$$

where Φ is the particle loading and H is the field strength in MA/m. The constant C depends on the carrier fluid and is given in Table 3. Similarly, in this research, the same model has been adopted.

The expression in Eq. (1) accurately represents the yield stress for each of these fluids. The model proposed in this equation is a function of the magnetic field strength and certain fluid properties. However, the model does not account for the condition in which the fluid is being used. This model assumes that the yield stress is developed, regardless of the operating conditions of the fluid. Based on the above discussion the value of the C and Φ was set as 1 and 32% respectively.

2.3.3 The Finite Element Method (FEM) Software

Finite element magnetic method (FEMM) software is capable of reprocessing, post-processing, and monitoring the processing stage of the sewer; yet, the first phase can also be done by other companionable CAD software or even a text editor. The FEMM software package is suitable for the coil design, some turns of the coils wrapping around the core, the electric current values move during the coil, and materials type of each component involved in the device. These parameters were the keys to produce the best value for the magnetic field intensity H , which was associated with the magnetic flux density B the concept mode of squeeze mode, design parameters and conditions were envisaged by FEMM.

Table 3 The constant value for three types of fluid

Constant C	Carrier fluid
0.95	Silicone oil
1	Hydrocarbon oil
1.16	Water

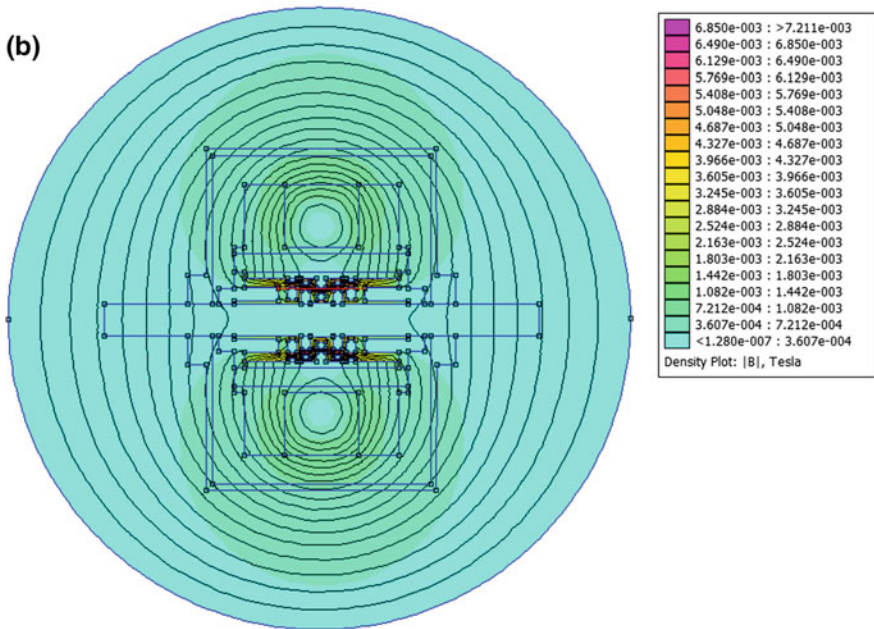
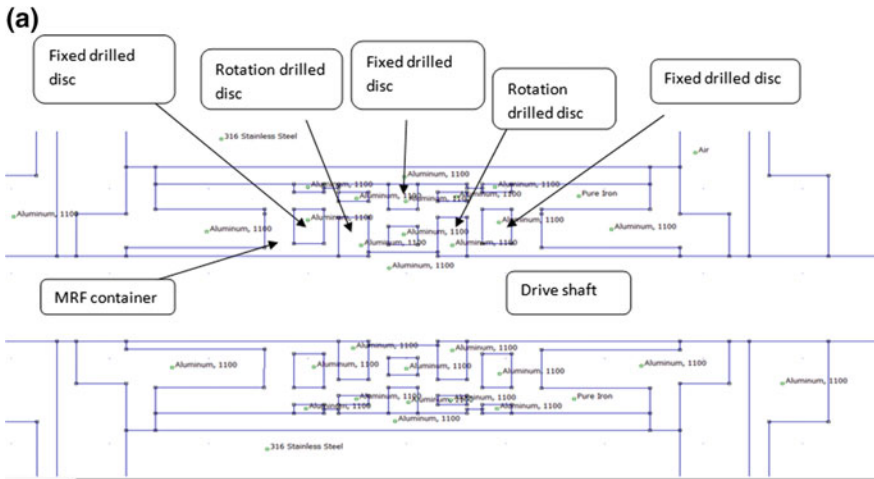


Fig. 4 a Finite element model of MRF based torque sensor; b magnetic flux density contour of MRF based torque sensor

3 Result and Discussion

In MRF torque sensor, the magnetic field is directly affected by the current. It is essential to study the outcome of current shapes on the magnetic field distribution in MRF based torque sensor to have a maximum magnetic field strength and the behavior of the MR fluid (Fig. 4).

In this research, five different designs have been tested, and five analyzes have been made. For the first analysis, we used a winding coil motor, 2pcs plain disc (1pcs rotation disc and 1pcs fixed disc arranged alternately) and all materials are non-magnetic materials. For the second analysis, we used a round winding coil, 2pcs plain disc (1pcs rotation disc and 1pcs fixed disc arranged alternately) and all materials are non-magnetic metals. For the third analysis, we used a round winding coil, 2pcs drilled disc (1pcs rotation disc and 1pcs fixed disc arranged alternately), and all materials are non-magnetic metals. On the fourth analysis, we used a round winding coil, 5pcs drilled disc (2pcs rotation disc and 3pcs fixed disc arranged alternately), and all materials are non-magnetic metals. Moreover, the last analysis is fifth analysis; we used round winding coil, 5pcs drilled disc (2pcs rotation disc and 3pcs fixed disc arranged alternately), and all materials are non-magnetic metals, except the drive shaft that only uses pure iron, i.e., magnetic metal (Table 4).

A FEMM software was used to analyze the behavior of the fluid and to characterize the fatigue behavior of the torque sensor structure with the presence of various load amplitudes. In this analysis using FEMM, some settings have been set between them, current is 1 A and turning coil (SWG 30) is 1500 turn.

Based on the magnitude of flux density graph, the maximum point is 7.73357 mT and the value obtained is from the fourth analysis. Moreover, the fourth analysis shows the best performance compared to other analyses (Fig. 5).

Based on the normal flux density graph, the maximum point is 4.17396 mT, and the maximum point for the tangential flux density graph is 7.52218 mT. The value obtained is from the fourth analysis. Moreover, the fourth analysis shows the best performance compared to other analyses (Fig. 6).

Based on the magnitude of field intensity graph, the maximum point is 0.51354 Amp/m, and the maximum point for the normal field intensity graph is

Table 4 Average result for fourth analysis

	Fourth analyze
Magnitude field energy (Joules)	1.3964×10^{-6}
Torque (Nm)	7.18467×10^{-2}
Average $B \cdot n^2$ (tesla ²)	2.97454×10^{-6}
Average $B \cdot n$ (tesla)	3.68429×10^{-6}
Normal flux density (webers)	6.6557×10^{-8}
Force in x-direction (N)	9.75373×10^{-9}
Force in y-direction (N)	-9.75957×10^{-6}
Average $H \cdot t$ (Amp/m)	0.306232

0.25441 Amp/m. The value obtained is from the fourth analysis. Moreover, the fourth analysis shows the best performance compared to other analyses (Fig. 7).

Based on the tangential field intensity graph, the maximum point is 0.55745 Amp/m and the value obtained is from the fourth analysis. Moreover, the fourth analysis shows the best performance compared to other analyses (Fig. 8).

Several factors affect the magnetic flux density and intensity. Among them is that the number of brake discs loaded into the system will directly affect the entire surface area of the brake disc in the system. Due to the increase in the number of disks, the overall surface area of the brake disc also increases exponentially. At the same time, due to the increase in the number of disks, the fluid will produce a vortex which will produce higher magnetic flux disruptions.

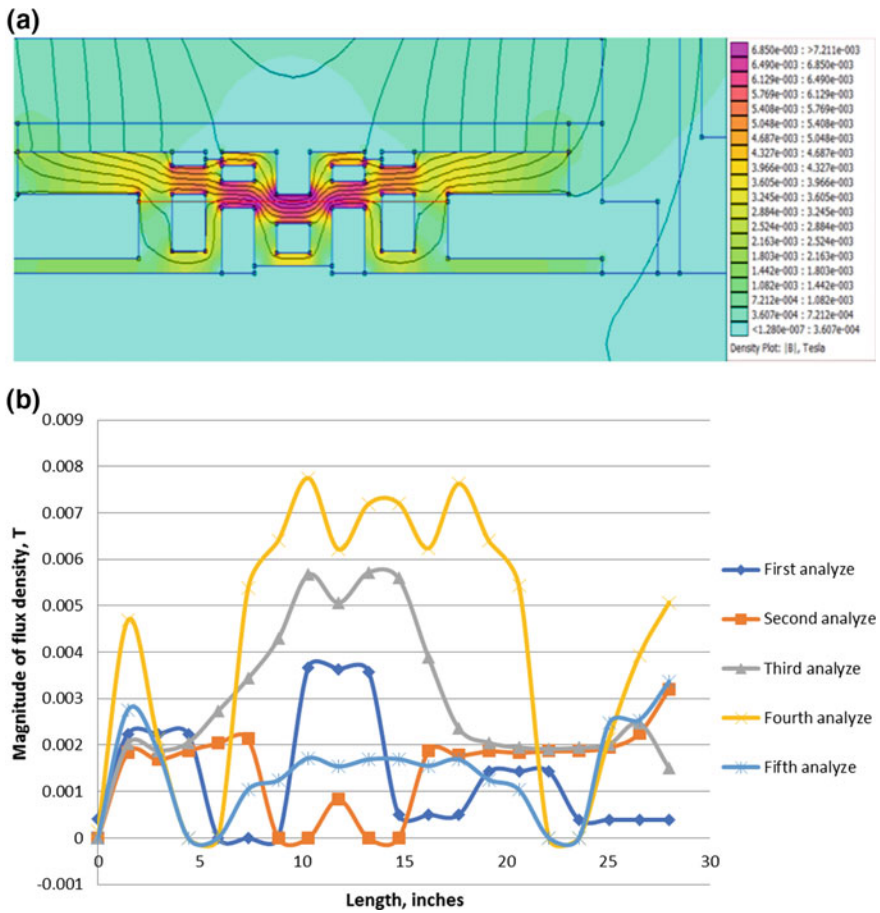


Fig. 5 a Magnetic flux density of MRF channel; b comparison of magnitude of flux density with various

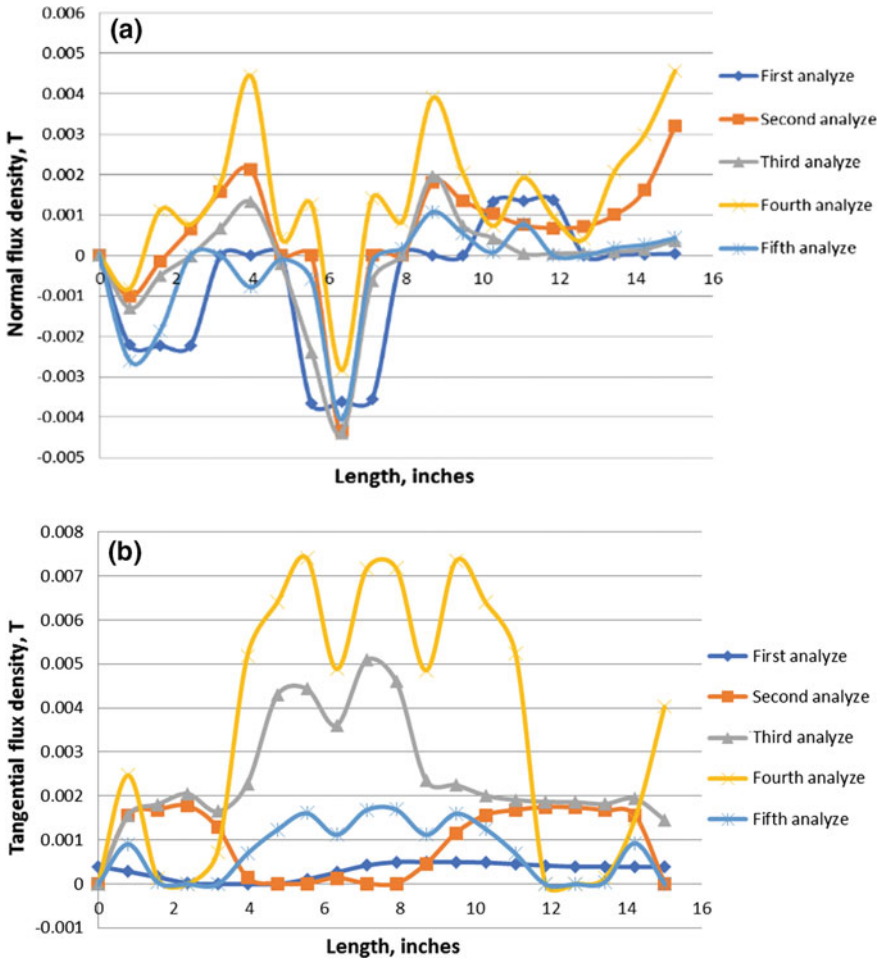


Fig. 6 **a** Analysis result comparison of normal flux density; **b** comparison of tangential flux density

The material selection for the various parts in the disc assembly is crucial, especially regarding the magnetism tendency in it. In the comparison between the usages of magnetic metal to nonmagnetic metal, it is found that the non-magnetic metal is capable of generating better stopping power compared to the magnetic metal. After having a look at the magnetic flux field, the magnetic metal is capable of influencing the magnetic field generated by the electro-magnetivity, resulting in the randomized distribution of magnetic flux and field, where a portion of the magnetivity is guided to the magnetic parts. In the case of non-magnetic metal, the electromagnetism is the focus in the shaft area, resulting in a highest possible density of magnetic flux and field, where the highest stopping power can be achieved when triggered.

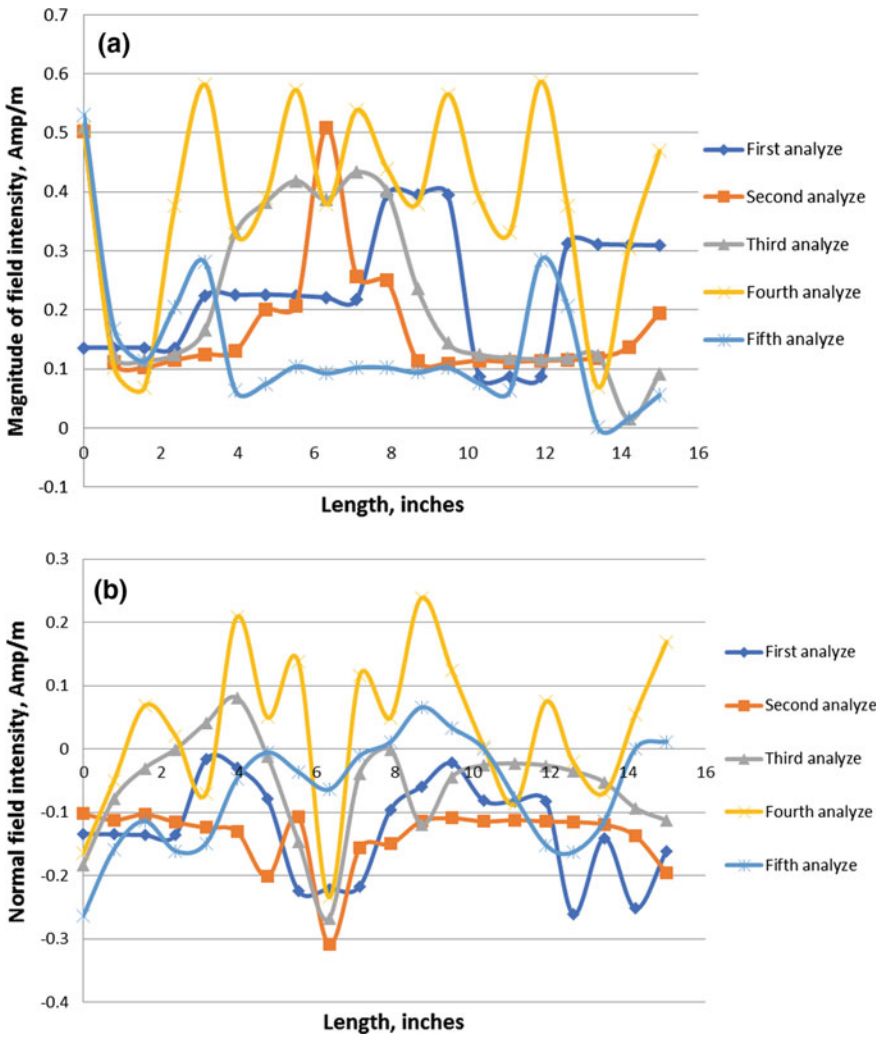


Fig. 7 **a** Analysis result comparison of magnitude of filed intensity; **b** analysis result comparison of normal field intensity

From the comparison of all results, the fourth analysis shows the best results compared to the other. This is evidenced by the value of the flux density and intensity generated from the simulation. The fourth analysis shows the highest value and a stable graph. From the simulation, the best choice of design is the fourth analysis to fabricate the prototype compared with other analyses.

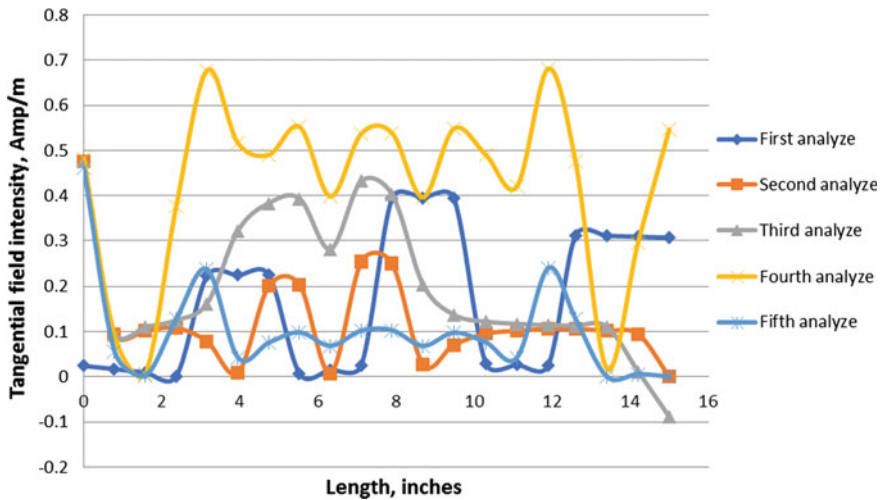


Fig. 8 Analysis result comparison of tangential field intensity

4 Conclusion

A new magneto-rheological fluid in MRF torque sensor simulation has been conducting. The software of magnetic FEMM (Finite Element Method Magnetics) was used to analyze the magnetic distribution in the torque sensor structure and to characterized the fatigue behavior in the torque sensor structure with the presence of various load amplitudes. The software is used because it contains the contour function. The steps of this project has been shown in the methodology. The result of the simulation shows the difference of behavior in the MRF.

From the result, several conclusions can be drawn. The magnetic flow rate increased in the MRF container where several factors influenced the amount of flux density and intensity of magnetic. The magnetic metal is capable of influencing the magnetic field generated by the electro-magnetivity, resulting in the randomized distribution of magnetic flux and field, where a portion of the magnetivity is guided to the magnetic parts.

Acknowledgements Alhamdulillah, with the will of Allah S.W.T, I had managed to complete this project in time. First of all, I would like to express my gratitude to my supervisor, Dr. Muhamad Husaini Bin Abu Bakar for accepting and giving me the opportunity to be my supervisor to finish this project. I am also grateful for his support and guidance that have helped me expand my horizons of thought and expression. He was accommodating in finding solutions to several problems that I had during to finish this project.

References

1. Ahmadkhanlou, F., Washington, G.N.: A magneto-rheological fluid-based torque sensor for smart torque wrench application, vol. 8688, p. 868819 (2013)
2. Jolly, M.R., Bender, J.W., Carlson, J.D.: Properties and applications of commercial magnetorheological fluids. *J. Intell. Mater. Syst. Struct.* **10**(1), 5–13 (1999)
3. Kumbhar, B.K., Patil, S.R., Sawant, S.M.: Synthesis and characterization of magneto-rheological (MR) fluids for MR brake application. *Eng. Sci. Technol. Int. J.* **18**(3), 432–438 (2015)
4. Olabi, G., Grunwald, A.: Design and application of magneto-rheological fluid. *Mater. Des.* **28**(10), 2658–2664 (2007)
5. Liu, J., Shirkoohi, G.H.: Anisotropic magnetic material modelling. **29**(6), 2458–2460 (1993)
6. Goncalves, F.D.: Characterizing the behavior of magnetorheological fluids at high velocities and high shear rates. Thesis (2005)
7. Dyke, S.J., Spencer Jr, B.F.: Characterizing the behavior of magnetorheological fluids at high velocities and high shear rates,. In: 2nd International Workshop on Structure Control, , pp. 163–173 (1996)
8. Li, J., Gong, X., Xu, Z.B., Jiang, W.: The effect of pre-structure process on magnetorheological elastomer performance. *Int. J. Mater. Res.* **99**(12), 1358–1364 (2008)
9. Kciuk, M., Turczyn, R.: Properties and application of Magnetorheological fluids. *JAMME* **18**(12), 127–130 (2006)
10. Xiu, S., Wang, R., Sun, B., Ma, L., Song, W.: Preparation and experiment of magnetorheological polishing fluid in reciprocating magnetorheological polishing process. *J. Intell. Mater. Syst. Struct.* **29**(1), 125–136 (2018)
11. Lord Corporation: Dr. Dave’s Do-It-Yourself MR Fluid, Designing with MR Fluid, Magnetic Circuit Design, FAQs, www.lord.com (2004)

Development of a 2-Dof Parallel Kinematics Machine for Macro Scale Products



Nor Liyana Maskuri, Muhamad Husaini Abu Bakar
and Ahmad Razlee Ab Kadir

Abstract This paper presents a new computer numerical control (CNC). The revolution of a parallel kinematics machine (PKM) is reducing many problems in the manufacturing process from a theoretical and practical point of view. The experimental setup was developed to optimize the kinematics design of a 2 Degree of Freedom (2 DoF) planar parallel manipulator. The excellent workspace design without link collision is presented in this paper. It was observed that increasing the precision in the PKM modeling, reduces the drawback of the existing product. The result is obtained from the various experiment which were plotted graphically and discussed in this paper.

Keywords Computer numerical control (CNC) · Parallel kinematics machine (PKM) · 2 degree of freedom (2 DoF)

1 Introduction

Nowadays, computer numerical control (CNC) machines are widely used in the manufacturing industry. Many industries use CNC machines for production, but they face difficulties in the machining process, i.e., complex shapes design, and various sizes in production [1]. Parallel kinematics machines offer various potential benefits for machine tools, but they also cause many disadvantages in the design process and radical efforts for precise control and calibration [2]. Parallel kinematics

N. L. Maskuri (✉) · M. H. Abu Bakar · A. R. Ab Kadir
System Engineering and Energy Laboratory, Malaysian Spanish
Institute - Universiti Kuala Lumpur, Kulim Hi-Tech Park,
09000 Kulim, Kedah, Malaysia
e-mail: nliyana.maskuri@s.unikl.edu.my

M. H. Abu Bakar
e-mail: muhamadhusaini@unikl.edu.my

A. R. Ab Kadir
e-mail: ahmadrazlee@unikl.edu.my

offer, for example, higher stiffness and at the same time higher acceleration performance than serial structures (serial manipulator) [3, 4]. Other features and concepts are based on the structure selected, the configuration selected for the central point of the device and the position with the interior of the workspace.

The problem arises when the limit workspace of the parallel kinematics machine is decreased because of the link collision problem. A huge machine requires a large space which is not suitable for the macro size fabrication and may cause some waste. In this paper, the focus has been chosen to take the links as the main purpose of the project to avoid the links collision with the wider reach in the workspace section.

2 Literature Review

2.1 Computer Numerical Control

Computer numerical control is the machine tools automation that is operated by precisely programmed commands encoded on a storage medium as a device to control manually, wheels, levers or mechanically automated by cams alone.

2.2 Parallel Kinematics Machine

The parallel kinematics machine is a revolution of a machine tool which was firstly shown at the 1994 in Chicago. There is a reliable and complex link among the type of parameters and its performance. It is difficult to choose the geometrical parameters in such a way as to optimize the performance. The configuration of parallel kinematics is more complicated due to the high sensitivity to variations of the design parameters [5]. This is the reason why the design process is an essential key to the overall performance of a parallel kinematics machines. Figures 1 and 2 show the concept of parallel kinematic machine.

2.3 Benefits of Parallel Kinematics Machines

High dynamical performance is achieved due to the low moving masses. Due to the closed kinematics, the movements of parallel kinematics machines are vibration free for which the accuracy is improved [6]. This can recover the drawback of the application of series manipulators. Furthermore, the modular concept allows the cost-effective production of the mechanical parts.

Fig. 1 Bipod parallel kinematics mechanism

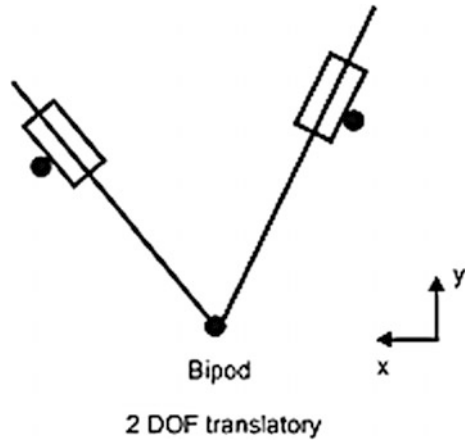
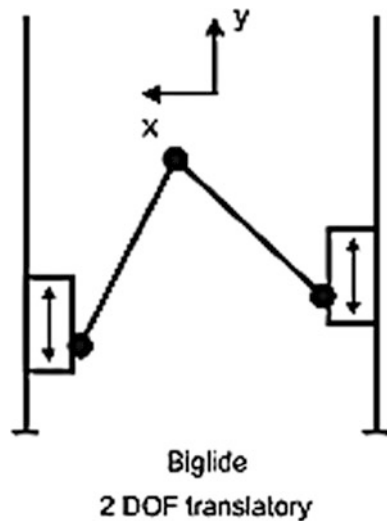


Fig. 2 Biglide parallel kinematics mechanism



2.4 Design and Simulation Analysis

SOLIDWORKS Simulation provides core simulation tools to test the designs and to make the decisions to improve quality. The full integration creates a short learning curve and eliminates the redundant tasks required with traditional analysis tools. Component materials, connections, and relationships defined during design development are fully understood for simulation.

2.4.1 Motion Analysis

This task includes to perform physics-based kinematic and dynamic analysis, using existing SOLIDWORKS software together with motion features to calculate the exact motion behavior. Furthermore, it allows to determine part and assembly displacements, velocities, and accelerations. Also, SOLIDWORKS Motion Study Analysis show the results as an animation or a graph. Selecting a point on the design allows the creation of a trace path that can be used in subsequent design processes.

3 Methodology

This part describes in detail the entire methodology on the two-degree-of-freedom parallel kinematics machine for macro scale product. The computer aided design (CAD) model of parallel kinematics machine is drawn in the SOLIDWORKS software and optimizes the workspace, kinematics chain (leg), prismatic (P) rotating (R), motion, and force transmission [7]. The model of parallel kinematics machine file was transferred to the simulation SOLIDWORKS software to synthesize the parallel kinematics machine model in detail by a simulation method. Then, based on the simulation method by the SOLIDWORKS software can be characterized the behavior of parallel kinematics machine. In this chapter describes the procedures to investigate the performance of parallel kinematics machine.

For the experimental setup, the analysis has been divided into three sections which are CAD model analysis, mathematical model analysis, and performance

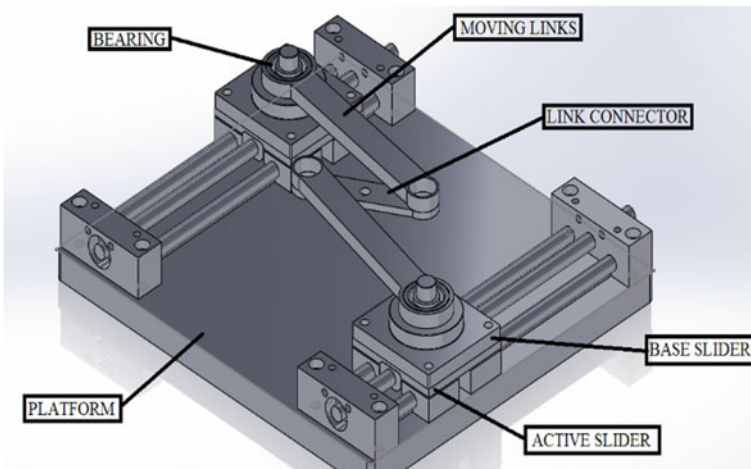
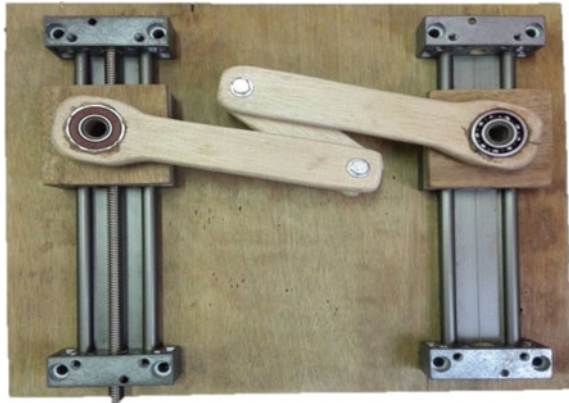


Fig. 3 Parallel kinematics machine in SOLIDWORKS

Fig. 4 Parallel kinematics machine prototype



analysis. The analysis has been done three times for every section. For the CAD model analysis and performance analysis, the point is gained from the SOLIDWORKS measurement in Fig. 3, and the actual size parallel kinematics prototype model in Fig. 4.

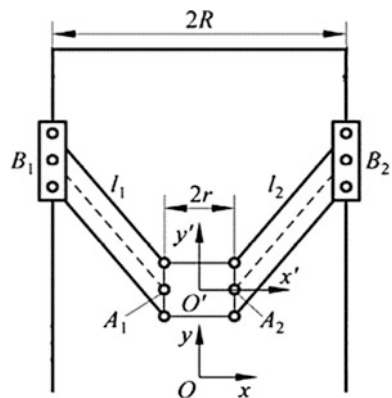
The mathematical model analysis has been done for the three types of the equations. The equation are the inverse solution of the kinematics, the direct kinematics of the manipulator and the singularity analysis. Figure 5 shows the assumed kinematics point for mathematical model.

Inverse Solution of Kinematics

$$y_1 = y + \sqrt{l_1^2 - (x - r + R)^2}$$

$$y_2 = y + \sqrt{l_1^2 - (x + r - R)^2}$$

Fig. 5 Parallel kinematics structural model



Direct Kinematics of the Manipulator

$$y = \frac{-(2af - 2y_1) \pm \sqrt{f^2 + 4(a^2 + 1)(l_1^2 - y_1^2 - f^2)}}{2a^2 + 1}$$

Singularity Analysis

$$\dot{y}_1 = \dot{y} - \frac{x - r + R}{\sqrt{l_1^2 - (x - r + R)^2}} \dot{x}$$

$$\dot{y}_2 = \dot{y} - \frac{x - r + R}{\sqrt{l_1^2 - (x + r - R)^2}} \dot{x}$$

4 Result and Discussion

The mechanism of the parallel kinematics machine is composed of a moving platform, effective slider, kinematics chain or links, and the center connector. Two parallelogram chains were used to make the structure symmetric and to increase the stiffness. The kinematics is analyzed to get an optimum kinematics design. The analysis has been divided into three sections which are the CAD model analysis, the mathematical model analysis, and the performance analysis. The analysis has been done three times for every section. For the CAD model analysis, the point is gained from the SOLIDWORKS measurement and the actual size parallel kinematics prototype model. The percentage error graph is presented in Figs. 6, 7, 8 and 9. The sliders motion is increased for every 15 mm for the single arm meanwhile another arm is fixed, and the data are collected, and the average of the percentage error is released. The experimental setup for this section to get data is fixing the left arm and let the right arm to move 15 mm above and so on. Then, the points are taken for three times and the percentage error is found. From the data of the percentage error, the average point is gained.

Fig. 6 Graph of the x-axis at right arm

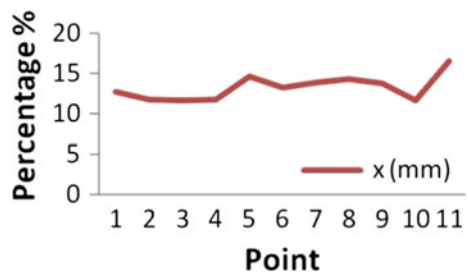


Fig. 7 Graph of the y-axis at right arm

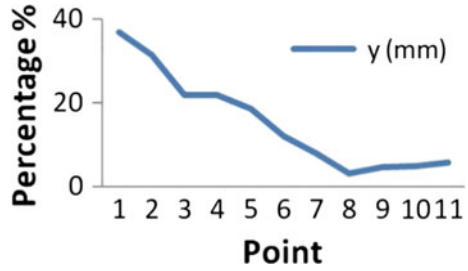


Fig. 8 Graph of the x-axis at left arm

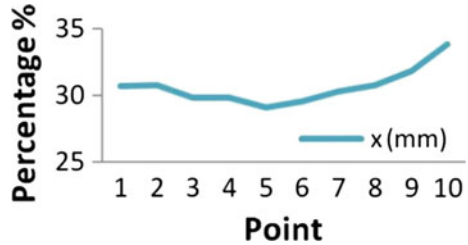
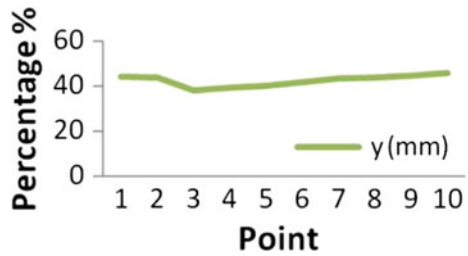


Fig. 9 Graph of the y-axis at left arm



$$x_t = \frac{x_{sw} - x_{ac}}{x_{ac}} \times 100$$

The graph in Fig. 6 shows that the result gained from the occurring percentage error occurs. For the x-axis at point 1 to point 4, the percentage is maintained but increases at point 5, the point is constant again and drops at point 10 but increases again at point 11. Meanwhile, for the y-axis in Fig. 7, the graph is a decreased from point 1 until point 3 but is constant in point 3 to point 4. Then, for the point 5 to point 8 the graph is decreasing but instantly increases at point 11. The error may cause the rotation by the bearing which is rough, and friction occurs.

The experimental setup for this section to get data is fixing the right arm and let the left arm to move 15 mm above and so on. Then, the points are taken for three times and the percentage error is found. From the data of the percentage error, the average point is gained. The graph in Figs. 9 and 10 show that the result gained from the percentage error occurs in point of the x-axis. For both of these graph, the point is in the average rate and stable. However, the error still occurs due to the

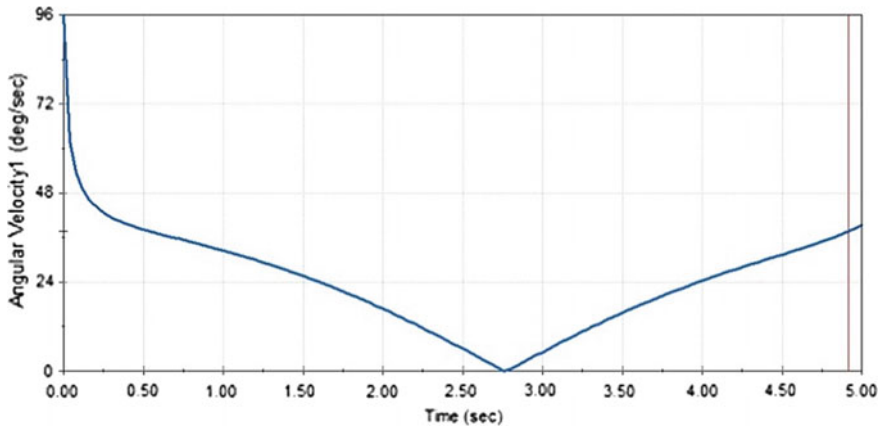


Fig. 10 Graph of the angular velocity

manufacturing error and enlargement of the actual size. The actual arm size is on the larger size because of the material is wood, and the drawback of wood is that may crack if the size is too thin.

The SOLIDWORKS motion analysis has been done, and these three graphs are released. The first one is the angular velocity graph. The angular velocity of a rotating body is defined as the rate of change of the angular displacement and is a vector quantity for more precisely specifies the angular speed or rotational speed of the links and the axis about which the object is rotating. In Fig. 10, the higher point is decreased due to the movement of both links downward and the point increased due to both links moving upwards.

The angular displacement of a body is the angle in radians is degrees and revolutions through which a point or line has been rotated in a specified sense about

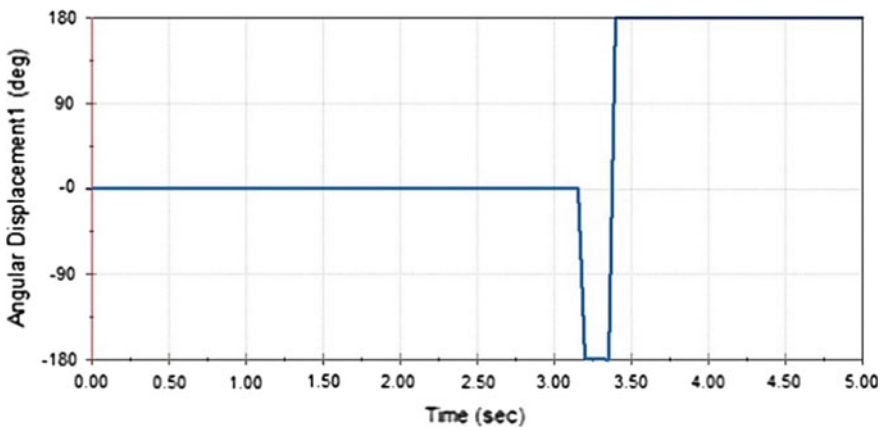


Fig. 11 Graph of angular displacement

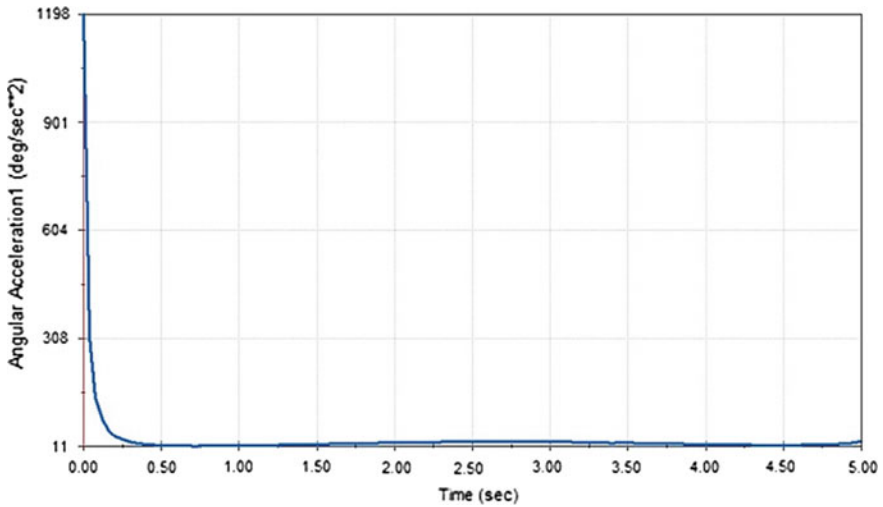


Fig. 12 Graph of angular acceleration

a specified axis. This situation can be described as an object rotates about its axis, the motion cannot merely be analyzed as a particle since in circular signal it undergoes a changing velocity and acceleration at any time (t). When dealing with the variation of an object, it becomes simpler to consider the body itself as rigid. In Fig. 11, the displacement motion is constantly stuck in the 0° position, and the line is decreased and increased back due to the movement of link, which change the motion position.

The angular acceleration is the amount of the conversion of angular velocity. In SI units, it is measured in radians per second squared (rad/s^2). The graph shown in Fig. 12 is about the point at the line graph which starts high and drops sharply and constant at the single point. This situation occurs due to the high acceleration when the motion starts, and the line graph was dropped and maintained caused by the angular acceleration is maintained to the single point. In the other hand, the third experiment is the mathematical model. In this section, the data collected from the actual fabrication size and the drawing size from the SOLIDWORKS to find the error. The result is valid, and the error percentage is small. For the mathematical model, the error between the actual size and the SOLIDWORKS size is only 2.364% for y_1 and 0.839% for y_2 .

5 Conclusion

The focus of this project was to develop the parallel kinematics machine with 2-DOF for macro scale products. About the research objectives, this project was successfully conducted where all objectives were achieved. The motivation is to

avoid the link collision, maximize the use of workspace in the compact size machine and performance evaluation of the parallel kinematic machine.

The analysis has been divided into three sections which are the mathematical model analysis, CAD model analysis, and performance analysis. The analysis has been done three times for every section. For the CAD model analysis, the point is gained from the SOLIDWORKS measurement and the actual size of the parallel kinematics prototype model.

The analysis done in SOLIDWORKS is to determine the maximum distance point with the new concept of parallel kinematics machine. These values are then used to calculate and differentiate with the prototype model data. With all of the data from the simulation and CAD model design, the parallel kinematics machine has been done as the most practical to use with the compact and simple device. The purpose of carrying out the design of the parallel kinematics machine prototype is to compare the data.

Moreover, the distance between two links is determined by optimum design, so the link collision problem has been avoided. Parallel kinematics machine performance has been evaluated by the comparison of CAD model and the actual fabrication. For the mathematical model, the error between actual size and SOLIDWORKS design size is only 2.364% for y_1 and 0.839% for y_2 .

Acknowledgements All the experiment and analysis conducted under System Engineering and Energy Laboratory, Universiti Kuala Lumpur, Malaysian Spanish Institute, Kulim Kedah, Malaysia.

References

1. Xie, F., Liu, X., Wang, L., Wang, J.: Optimum kinematic design of the 4R 2-DOF parallel mechanism. *Tsinghua Sci. Technol.* **14**(5), 663–668 (2009). [https://doi.org/10.1016/s1007-0214\(09\)70132-4](https://doi.org/10.1016/s1007-0214(09)70132-4)
2. Clark, L., Shirinzadeh, B., Bhagat, U., Smith, J., Zhong, Y.: Development and control of a two DOF linear–angular precision positioning stage. *Mechatronics* **32**, 34–43 (2015). <https://doi.org/10.1016/j.mechatronics.2015.10.001>
3. Balchanowski, J.: General Method of Structural Synthesis of Parallel Mechanism, pp. 256–268; 644–651 (2016)
4. Yang, Y., Yang, Y.: Optimal design of a 2-DOF planar parallel manipulator. In: 2010 International Conference on Mechanic Automation and Control Engineering (2010). <https://doi.org/10.1109/mace.2010.5535346c>
5. Wu, C., Liu, X., Wang, L., Wang, J.: Optimal design of spherical 5R parallel manipulators considering the motion/force transmissibility. *J. Mech. Des.* **132**(3), 031002 (2010). <https://doi.org/10.1115/1.4001129>
6. Qu, J., Chen, W., Zhang, J., Chen, W.: A piezo-driven 2-DOF compliant micropositioning stage with remote center of motion. *Sens. Actuators, A* **239**, 114–126 (2016). <https://doi.org/10.1016/j.sna.2016.01.025>
7. Lian, B., Sun, T., Song, Y., Wang, X.: Passive and active gravity compensation of horizontally-mounted 3-R P S parallel kinematic machine. *Mech. Mach. Theory* **104**, 190–201 (2016). <https://doi.org/10.1016/j.mechmachtheory.2016.05.021>

Development of a Capacitor Using a Rubber Based Magneto Rheological Elastomer



Muhamad Husaini Abu Bakar, Mohd Nor Hazwan Hadzir
and Muhamad Termizi Muhamad

Abstract A capacitor is a passive two-terminal electrical component that stores electrical energy in an electric field. The most famous capacitor current in use the market and industry is a ceramic capacitor. However, the dielectric material used in the industry nowadays involve high cost of material handling due to the fact that the dielectric material is hazardous. Thus, there is a need for exploring the potential of the new material to replace the current dielectric material used in the industry nowadays. In this study, a magnetorheological elastomer with different magnetic particle concentrations from 30 to 70% and different curing processes is proposed as a dielectric material. The MRE capacitor prototype was built by two non-magnetic layers, between there is a layer of the magnetorheological elastomer (MRE) as the dielectric. From the experimental result, the magnetic strength, magnetic particle concentration and curing process of the MRE influence the value of the capacitance. As a conclusion, the MRE material with high iron concentration and anisotropic type can be used as a dielectric to be applied in capacitor development.

Keywords Magnetorheological elastomer (MRE) · MRE capacitor
Dielectric

M. H. Abu Bakar (✉) · M. N. H. Hadzir · M. T. Muhamad
System Engineering and Energy Laboratory, Malaysian Spanish Institute,
Universiti Kuala Lumpur, Kulim Hi-Tech Park, 09000 Kulim, Kedah, Malaysia
e-mail: muhamadhusaini@unikl.edu.my

M. N. H. Hadzir
e-mail: mhazwan.hadzir@s.unikl.edu.my

M. T. Muhamad
e-mail: m.termizi.muhd@gmail.com

1 Introduction

A capacitor is a component which can store energy in the form of an electrical charge producing a potential difference across its plates, slightly like a small rechargeable battery [1]. A capacitor consists of two or more parallel conductive plates which are not connected or touching each other. However, they are electrically separated either by air or by some form of a suitable insulating material such as waxed paper, mica, ceramic, plastic or some form of a liquid gel as used in electrolytic capacitors [2]. The insulating layer between the plates of a capacitor is commonly called the dielectric. Perhaps, the most famous dielectric material used in capacitor development is ceramic. However, the limitation of ceramic dielectric is a high cost of material handling due to hazardous risk. Besides that, a material with naturally support the green environment and reduce any hazard to people, community, and the country is the need.

During the last few decades, magnetorheological elastomer (MRE) have attracted a significant quantity of attention for their massive potential in engineering application [3]. It is because they are a solid counterpart to MR fluids, i.e. a MRE shows a unique field-dependent material property when visible to a magnetic field, and they overcome significant problems played in magnetorheological fluids, such as the deposition of iron particles, sealing problems and environmental pollution [4]. MRE has an excessive potential for designing an intelligent device to be used in several engineering fields such as vibration absorbers, base isolators, and the capacitor dielectric [5]. There are two type of MRE, i.e. the isotropic and the anisotropic (Fig. 1). The differential MRE type depend on the curing process in the fabrication of MRE either as curing in the presence of a magnetic field or not [6]. The importance of understanding the properties of the MRE capacitor prototype is to explore the potential of the new material for neither future capacitor or supercapacitor.

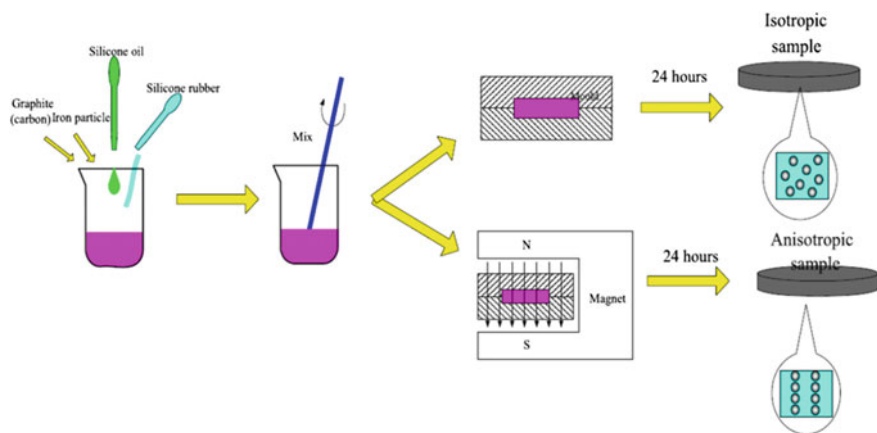


Fig. 1 Example of the fabrication of both isotropic and anisotropic MRE

Bica et al. [7], Balasoiu and Bica [8], Bica [9] and Bica et al. [10] used the MRE as the dielectric in developing a flat capacitor. The MRE proved to be one suitable part of the material used in the capacitor or supercapacitor. However, to make dielectric material available to industry application, the main characteristic of the material needs to be test and experiments needs to be performed to make sure the new dielectric material can be used in the industrial application.

In this study, to find the optimal magnetic particle concentration and the best type of MRE, a MRE layer with variable concentration from 30 to 70% and different MRE types were compared.

2 Methodology

2.1 Magnetorheological Elastomer (MRE) Portion Preparation

The material portion for the MRE fabrication needs to be calculated. The sample for 30% used as an example in conducting the portion calculation. To fabricate the MRE material, the volume percentage of the magnetic particles was calculated according to:

$$V\% = \frac{\rho_{tot} - \rho_{rubber}}{\rho_{iron} - \rho_{rubber}} \quad (1)$$

where ρ_{tot} is the density of the whole material, ρ_{rubber} is the density of the matrix = 1.1 gcm^{-3} , and ρ_{iron} is the density of iron particles = 7.9 gcm^{-3} .

$$\begin{aligned} 30\% &= \frac{\rho_{tot} - 1.1}{7.9 - 1.1} \\ (6.8)(0.3) &= \rho_{tot} - 1.1 \\ \rho_{tot} &= 3.14 \text{ gcm}^{-3} \end{aligned}$$

The value of the density of the whole material is used to find the mass of the whole material by using density formula.

$$\begin{aligned} \rho_{tot} &= \frac{m_{tot}}{V_{tot}} \\ 3.14 &= \frac{m_{tot}}{9.9} \\ m_{tot} &= 31.1 \text{ g} \end{aligned}$$

where m_{tot} is the mass of the whole material and V_{tot} is the volume of the whole material = 9.9 cm^3 . The value of the volume is obtained from the dimensions of the MRE sandwich plate that will be produced. Next, the mass of the iron particle, m_{iron} was calculated by using weight percentage formula.

Table 1 Composition of the MRE samples

Percentage of iron particles (%)	Iron particles (g)	Silicone rubber (g)	Silicone oil (g)
30	9.3	19.8	2.0
40	15.1	20.6	2.1
50	22.3	20.3	2.0
60	30.8	18.6	1.9
70	40.6	15.8	1.6

$$wt.\%_{iron} = \frac{m_{iron}}{m_{tot}} \times 100$$

$$30\% = \frac{m_{iron}}{31.086} \times 100$$

$$m_{iron} = 9.3 \text{ g}$$

The mass of the elastomer, $m_{elastomer}$ was determined according to:

$$m_{tot} = m_{iron} + m_{elastomer}$$

$$31.1 = 9.3 + m_{elastomer}$$

$$m_{elastomer} = 21.8 \text{ g}$$

Lastly, the ratio of matrix (elastomer) that contained silicone rubber and silicone oil was obtained.

$$m_{elastomer} = m_{matrix}$$

$$m_{matrix} = 21.8 \text{ g}$$

silicone rubber : silicone oil

$$10 : 1$$

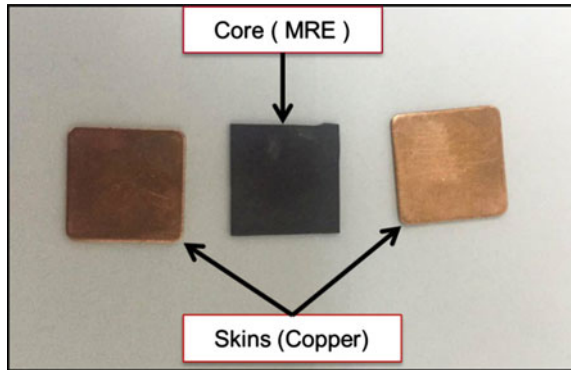
$$19.8 \text{ g} : 1.9 \text{ g}$$

The composition of magnetic particle, silicon iron, and silicon rubber for fabrication of the MRE layer prepared as given in Table 1. This portion was used for both type of MRE, because the difference in each type was only gained in the curing process.

2.2 MRE Specimens and MRE Capacitor Prototype Preparation

Materials used for preparing the MRE are silicone oil, silicone rubber, magnetic particle with a size of 10 μm , bowls, and a rectangular mould. The following steps were conducted to prepare the MRE: Firstly, mixing the silicone oil and the silicone

Fig. 2 MRE capacitor prototype



rubber in a bowl and proceed with a manual mixing during 10 min to obtain an elastomer gel with good homogenization. A second bowl containing a portion of the magnetic particles of a micrometric size to load the prepared elastomer. Then, a quantity of this gel obtained by silicone and silicone rubber is mixed during 30 min with the volume of magnetic particles until obtaining a homogeneous paw by this process, an elastomer loaded with 30% of magnetic particles is elaborated.

A rectangular mould made by Perspex was used as a mould. The mixture is loaded into the mould and stored for 24 h. Furthermore, for anisotropic behavior, the mould is placed under the magnetic field for 24 h. Next, for isotropic behavior, the mould is placed in the normal condition at room temperature. To have a healthy structure for the experimentation, the obtained elastomer is preserved at low temperature.

Figure 2 shows the prepared MRE specimens with a size of 20 mm × 20 mm × 0.5 mm as a core or dielectric, and two pieces of a copper plate with dimension 20 mm × 20 mm × 1 mm prepared as a conductive plate.

3 Experimental Setup

Figure 3 shows the experimental setup for MRE capacitor tester. The experiment was conducted by Digital multimeter (Keysight U1273A) to measure the value of the capacitor. Cylindrical permanent magnets of type Neodymium (N42 type, with dimension 30 mm × 5 mm) produce the magnetic field of 0.388T, which was used to identify the effect of the magnetic field when the external magnetic field was applied to the MRE capacitor. The housing to hold the MRE capacitor and permanent magnet was made of non-magnetic material (ABS) to avoid magnetic flow to the housing.

In the area of the MRE, the capacitor testing has two terminals, a negative and a positive to measure the value of capacitance. The testing started with compiling the copper plate with 30% magnetic particle concentration MRE specimens.

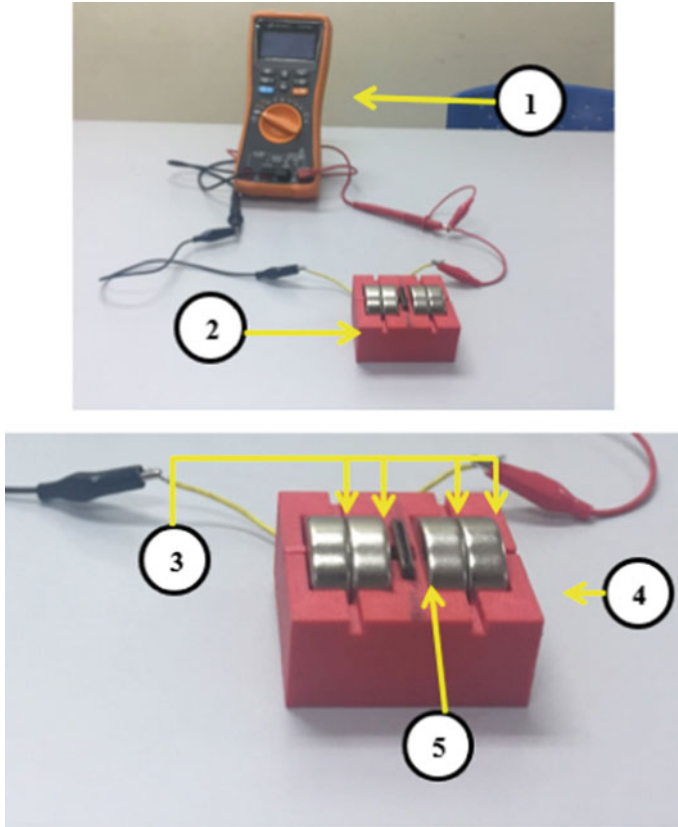


Fig. 3 Experimental setup, (1) Digital multimeter (Keysight U1273A), (2) area of MRE capacitor (3) permanent magnet (Neodymium, N42, cylindrical), (4) MRE holder, (5) MRE capacitor prototype

The prototype of the MRE capacitor was inserted into the MRE capacitor slot. The measurement started reading to identify the value of the MRE capacitor value without an external magnetic field. The experiment was continued by the presented external magnetic field to MRE capacitor. A permanent magnet was inserted into the slot of permanent magnet and the reading of the value of the capacitor was done at a digital multimeter.

4 Result and Discussion

The testing was conducted for different iron concentration of the MRE capacitor, range from 30 to 70%; the testing was continued by the presence of an external magnetic field at every percentage of iron concentration. The measurement was

done to collect and plot different graphs of the obtained data. Figure 4 shows the graph of the capacitance of the anisotropic MRE capacitor prototype with and without the absence of an external magnetic field for each iron particle concentration. From this graph, the 'x' axis represents the percentage volume of iron particle concentration in the MRE layer, the value in this axis is from 30 to 70%. The 'y' axis is presenting the value of the capacitor (in μF) when an external magnetic field was applied and without an external magnetic field. The data is recorded with and without the absence of the external magnetic field (0.388T) of 30, 40, 50, 60 and 70% iron particle concentration. From Fig. 4, it shows that each of the anisotropic MRE specimens with different iron particle concentration, the capacitance increases linearly with the absence of the magnetic field. This situation proves that each of this anisotropic MRE capacitor is charging when the magnetic field crosses the MRE dielectric layer. The maximum capacitance achieved is 6.139nF for the anisotropic MRE capacitor with 70% iron particle concentration in the presence of a magnetic field (0.388T) resulting in 1500.98% capacitance gain from 0.409nF without magnetic field.

Figure 6 shows the comparison of the capacitance between the anisotropic and isotropic MRE capacitor prototype with and without the absence of the magnetic field. The data from Figs. 4 and 5 are combined to visualise in a line graph the behaviour of the MRE capacitor prototype with and without magnetic field (0.388T) of 30, 40, 50, 60 and 70% iron particle concentration.

The MRE capacitor with an average capacitance gain above 700% in each of the iron particle concentration due to the alignment of the magnetic particles during the

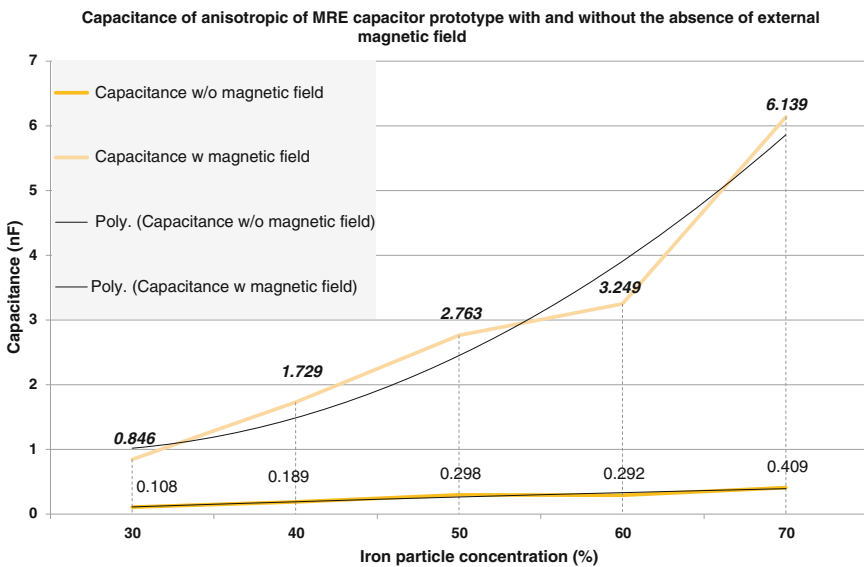


Fig. 4 Capacitance of anisotropic MRE capacitor prototype with and without the absence of external magnetic field

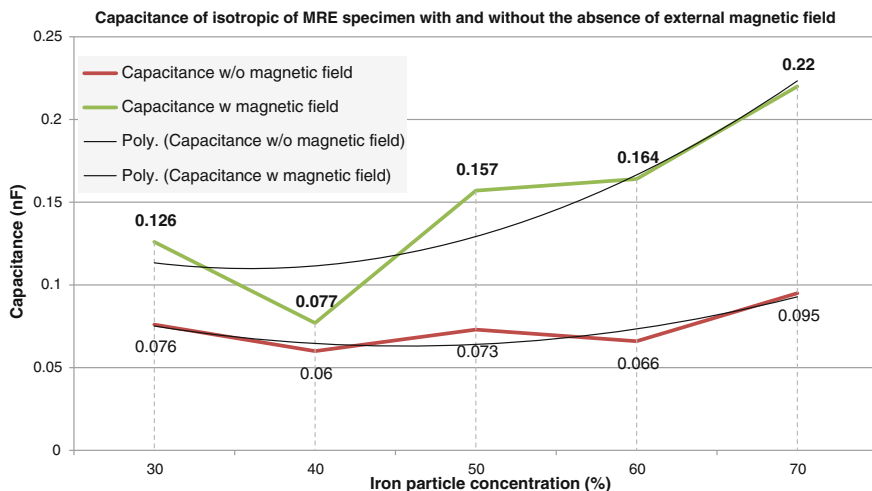


Fig. 5 Capacitance of isotropic MRE capacitor prototype with and without the absence of external magnetic field

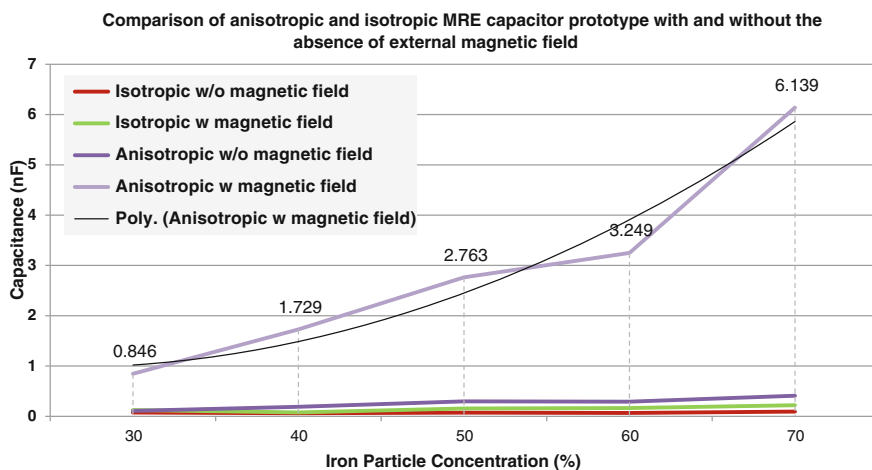


Fig. 6 Comparison of anisotropic and isotropic MRE capacitor prototype with and without the absence of external magnetic field

curing process under magnetic field absence and strengthens the magnetisation ability. Besides that, Fig. 6 concludes that 70% of magnetic particle concentration of anisotropic MRE capacitor prototype result in the optimal performance compared to the other specimens with 6.139nF with the absence of the magnetic field (0.388T) from no external magnetic field (0.409nF) and gain of 1500.98% in capacitance. The increase of the capacitance value in the MRE material is because

MRE can be considered as a magnetic material that has hysteresis behaviour. The magnetic material may have more than one possible magnetic moment in a given magnetic field, depending on how the field changed in the past.

5 Conclusion

This experiment has successfully achieved all the objectives by developing the capacitor using rubber-based magnetorheological elastomer as a new intelligent material. Based on the experimental results, the following conclusions can be done:

- A capacitor using rubber-based magnetorheological elastomer (MRE) as the dielectric was successfully developed.
- Anisotropic and isotropic MRE capacitor prototype were created with iron particle concentrations of 30, 40, 50, 60 and 70%. Both types of MRE capacitance increases with the absence of magnetic field.
- The maximum capacitance achieved in this case study is for the 70% iron particle concentration of anisotropic MRE capacitor prototype and results in 6.139nF with the absence of magnetic field (0.388T) from no external magnetic field (0.409nF) and a gain of 1500.98% in capacitance.
- A stronger magnetic field will increase the capacitance value of MRE capacitor prototype. However, the increases of iron particle concentration also affect the capacitance gain rely on the curing process.
- 70% iron particle concentration in the anisotropic type MRE capacitor prototype is proposed as the optimal iron particle percentage for different capacitance values.

Acknowledgements All the experiment and analysis conducted under System Engineering and Energy Laboratory, Universiti Kuala Lumpur, Malaysian Spanish Institute, Kulim Kedah, Malaysia.

References

1. Madsen, F.B., Daugaard, A.E., Hvilsted, S., Skov, A.L.: The current state of silicone-based dielectric elastomer transducers. *Macromol. Rapid Commun.* **37**, 378–413 (2016)
2. Ho, J., Jow, T.R., Boggs, S.: Historical introduction to capacitor technology. *IEEE Electr. Insul. Mag.* **26**(1), 20–25 (2010)
3. Li, Y., Li, J., Li, W., Du, H.: A state-of-the-art review on magnetorheological elastomer devices. *Smart Mater. Struct.* **23**(12), 123001 (2014)
4. Wang, X., Cai, J.Y.: Magnetorheological elastomer: state and application. *Adv. Mater. Res.* **393–395**, 161–165 (2011)
5. Kaluvan, S., Thirumavalavan, V., Kim, S., Choi, S.B.: A new magneto-rheological fluid actuator with application to active motion control. *Sens. Actuators, A Phys.* **239**, 166–173 (2016)

6. Biller, A.M., Stolbov, O.V., Raikher, Y.L.: Modeling of particle interactions in magnetorheological elastomers. *J. Appl. Phys.* **116**(11), pp (2014)
7. Bica, I., Anitas, E.M., Chirigiu, L.: Magnetic field intensity effect on plane capacitors based on hybrid magnetorheological elastomers with graphene nanoparticles. *J. Ind. Eng. Chem.* **56**, 407–412 (2017)
8. Balasoiu, M., Bica, I.: Composite magnetorheological elastomers as dielectrics for plane capacitors: effects of magnetic field intensity. *Results Phys.* **6**, 199–202 (2016)
9. Bica, I.: Influence of magnetic field upon the electric capacity of a flat capacitor having magnetorheological elastomer as a dielectric. *J. Ind. Eng. Chem.* **15**(4), 605–609 (2009)
10. Bica, I., Liu, Y.D., Choi, H.J.: Magnetic field intensity effect on plane electric capacitor characteristics and viscoelasticity of magnetorheological elastomer. *Colloid Polym. Sci.* **290**(12), 1115–1122 (2012)

Effect of the Magnetic Field on Magnetic Particles in Magnetorheological Elastomer Layers



Mohd Nor Hazwan Hadzir, Muhamad Husaini Abu Bakar
and Ishak Abdul Azid

Abstract A Magnetorheological Elastomer (MRE) can be categorized as a smart material as it can respond when it is subjected to a magnetic field against itself. Shrinking and changing shape in MRE is due to the displacement of magnetic particle in the MRE matrix. However, the lack of understanding of the magnetic flow through magnetic particle in the elastomer matrix causes difficulties to improve the best MRE matrix type and a magnetic circuit for use in MRE devices. In this paper, a finite element magnetic method (FEMM) software has been used to investigate and to study the effect of the magnetic flow when the angle of the magnetic particle in the MRE changed. The analysis was conducted in two-dimensional cross-section (axisymmetric type) with two magnetic particles in the elastomer matrix and the magnetic core. The result shows by changing the angle of the magnetic particle, the value of the magnetic flow and magnetic flux density also change. As a conclusion, the magnetic particle arrangement in the elastomer matrix plays a vital role in designing the MRE matrix layer and MRE device. By understanding the magnetic flow through the magnetic particle, one can improve the method in the preparation of MRE matrix and MRE magnetics circuit.

Keywords Magnetorheological elastomer · FEMM analysis · Magnetic particle

M. N. H. Hadzir (✉) · M. H. Abu Bakar · I. A. Azid
System Engineering and Energy Laboratory, Malaysian Spanish Institute,
Universiti Kuala Lumpur, Kulim Hi-Tech Park, 09000 Kulim, Kedah, Malaysia
e-mail: mhazwan.hadzir@s.unikl.edu.my

M. H. Abu Bakar
e-mail: muhamadhusaini@unikl.edu.my

I. A. Azid
e-mail: ishak.abdulazid@unikl.edu.my

1 Introduction

Any material that gives a response when an external energy is applied, is considered a smart material. The various smart materials exist nowadays, which is, piezoelectric material, that provides reactions when a voltage is applied, shape memory alloy (SMA) with magnetic and thermal sensitivity that responds during applied magnetism or heat and magnetorheological (MR) material that responds during applied magnetic field [1]. A Magnetorheological elastomer (MRE) is a viscoelastic material and considered as a smart material due to repeatability and fast response when a magnetic field is applied to it. There are various methods and types of elements in the preparation of MRE. Different magnetic particles are used in the development of MRE layers such as nickel, carbon, and carbonyl iron [2]. The most popular materials that is selected nowadays for MRE is carbonyl iron [3]. The size of the particles ranges from 5 to 100 μm . Furthermore, the matrix selection process also has variety and difference matrix, for example, natural rubber, silicon rubber and so on. In MRE, there are two different types of MRE, according to the used curing method. The first type is isotropic, which is the particle in the matrix are randomly arranged. The second type is anisotropic, which means that during the curing process a magnetic field was applied to it. As a result, the particles in the MRE will form a chain according to the applied magnetic field over it [4].

Due to its changing and controllable properties, it has high potential to be used in various applications in the industry such as a vibration isolator, base isolator, sensing device, and capacitor and so on. It was suggested in Ref. [5] to use MRE to develop a tunable vibration absorber (TVA). MRE and MRF were suggested in [6] for designing vibration insulators. MRE with multi-layer insulation was suggested in [7] for suppression of building vibration under seismic event. A tunable absorption system based on magnetorheological elastomer and Halbach array for energy absorption and mitigation of vibratory motions from an impact excitation was designed in [8]. Furthermore, MRE was used in [9] as a dielectric in an electric capacitor and a MRE capacitor was designed as a hybrid MRE with graphene Nano particles. However, to optimize the device performance, there is a need for understanding the behavior of MRE under the influence of an magnetic field, for preparing the MRE layer.

To understanding the behavior and magnetic distribution of the MRE layer, many researchers involved the computational investigation of the MRE behavior during the action of the magnetic field. A computer simulation and analysis of the shape effect in the experimental characteristic magnetorheological elastomer by using a multiscale simulation of typical experimental scenario in a two-dimensional setting was conducted in [10]. The magnetic flux distribution in the laminated MRE isolator with various iron particles filling by using a FEMM analysis software was investigated in [11]. From the literature, many researchers investigated the magnetic distribution in the system of the MRE device. However, understanding the effect of the magnetic field on the iron particle in the MRE layers is of great importance due to the main working in MRE layer is iron particle displacement. The effect of

magnetic field on the damping ratio was studied in [2] by investigating the amplification region of the transmissibility curve, viscoelastic dynamic damping natural by the force-displacement hysteresis graph and the effect of the magnetic field to the ion particle in the MRE layer at the various distances. The investigation shows that the distance and percentage of the magnetic particle influence of the performance of the MRE layer on the energy loss between the particles and also influence the stiffness when the iron particle filling is increased.

In this study, the geometry was prepared to investigate the effect of the magnetic field to a magnetic particle with various angles of the particle. The magnetic flux density and the rate of change of the magnetic density between two magnetic particles is also discussed. The geometry of the ion particle in the MRE layer with the magnetic core was prepared in a two-dimensional cross-section (axisymmetric type). The iron particle was made by various angles of the a particle with an increase of 15° from 0° to 90° with a constant current and distance of 0.5 A and 2 μm .

2 Methodology

2.1 Finite Element Method Magnetic Analysis

The effect of the magnetic flow to carbonyl iron particle is great importance in the magnetorheological elastomer layer design. Therefore, in this work, the finite element method magnetic (FEMM) software package was used to analyse the distribution of the magnetic flux in the MRE layer. FEMM is an open source software that validated to the simple and accurate result. In the FEMM, the Maxwell equation was used to solve the magnetic problem in the system. The equation for this problem solved by:

$$\nabla \times \left(\frac{1}{\mu_{eff}(\mathbf{B})} \nabla \times a \right)^n = -j\omega\sigma\alpha + \hat{J}_{src} - \sigma\nabla V \quad (1)$$

where \hat{J}_{src} is the phasor transform of the applied current sources, μ_{eff} is the effective magnetic permeability, V is the electric scalar potential, σ the medium of conductivity, ω the fixed frequency, ρ is the change in density and α is the complex amplitude of the phasor transformation. [12].

In this investigation, the model of the magnetic particle in MRE is divided into three sections, the magnetic core, the magnetic particles and the elastomer. The first section corresponds to the top and bottom of the magnetic core. The magnetic core section consists of wire copper AWG 12 with 100 turns. The second section referred to the magnetic particle and magnetic particle region, where magnetic particles with a diameter of 6 μm and the gap between the particle of 2 μm was set up. The third section referred to the elastomer matrix (natural silicon rubber).

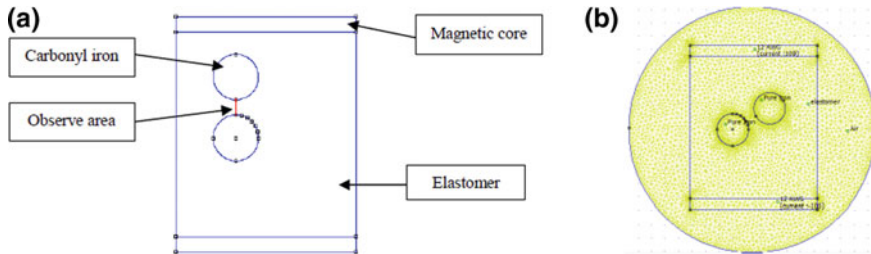


Fig. 1 Magnetorheological 2D Geometry (a) and meshing (b)

Details of each part are shown in Fig. 1a. In the FEMM software, the type of materials used for each part in this study can be found in the library of the software. In the first section, the type of copper coil (AWG 12), with 100 turns for magnetic core and the electric current supplied to the coils were then assigned. The second section, the magnetic particle was assumed as pure iron and the third section, an elastomer material is assigned to the non-magnetic material. After applying the boundary conditions and adding all material properties, the two-dimensional geometry of the magnetic particle in MRE layer is ultimately meshed with a fine triangular mesh at the critical region of the magnetic particle and the coarse triangular mesh at the outside region as shown in Fig. 1b. Various angles of the magnetic particle from 0° to 90° were decided to identify the effect of the magnetic flow in MRE layer.

3 Result and Discussion

The simulation of an iron particle in the MRE layer was finally archived. Figure 2 shows the observed area of the iron particle and the magnetic field distribution in the polymer matrix. Figure 2, show that the magnetic flux passes through the carbonyl iron and elastomer. Let's us look on region "A" in Fig. 2a referred; the magnetic flux flows smoothly to complete a circle of the magnetic flux region. These phenomena happen because in the elastomer matrix on that area there is no magnetic particle that deflects or attracts the magnetic flux flow. From the contour and magnetic flux on the whole of Fig. 2a, we can see that the magnetic flux densities on the magnetic particle area are higher because the magnetic flux was focusing to flow through both particles with the same magnetic flux and flow by their axis.

Region "A" and "B" in Fig. 2b show the magnetic flow in the elastomer matrix; magnetic flux density on the region "A" is higher than in region "B". The magnetic flux on region "A" shows a deflection of the magnetic flux by the presence of the magnetic particle; the magnetic particle was attracting the magnetic flux through it. Because of that, the contour of the magnetic density on that area is higher.

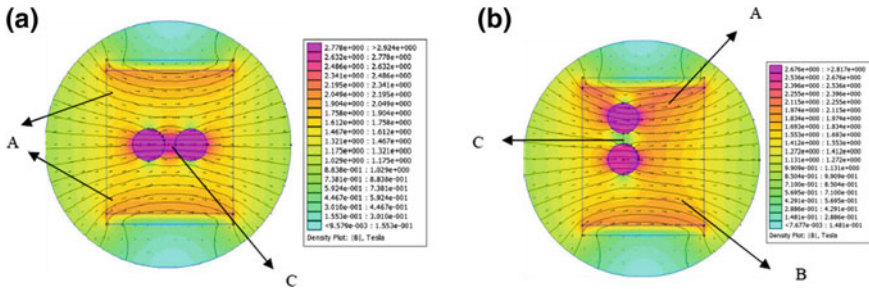


Fig. 2 Carbonyl iron particle in angle a 0° and b 90°

Furthermore, another reason is the iron particle neared with the magnetic core. The Magnetic flux on region “B” shows that the magnetic flux flow was smoothly to complete the circle of the magnetic field, because no magnetic particle crosses the magnetic flux.

By changing the angle of the magnetic particle, the magnetic flux density shows a different value. This statement can prove in Fig. 2a, b. The density of the magnetic flux changes because of the deflection of the magnetic flux in the magnetic field by the presence of a magnetic particle. Region “C” clearly shows the difference of the contour color at the area of observation. The Contour colour is presenting the density of the magnetic flux. Figure 2a shows that the magnetic density is higher with a value of 2.7 T for the magnetic flux density. This is because the magnetic flux was through the both of particle in the same magnetic field direction, deflection of magnetic field direction will lose the density of magnetic flux. Figure 2b shows that the magnetic density on observed area 90° is less than the angle of a particle in Fig. 2a with 0°. The magnetic flux shows that the magnetic flux flows through the particle with different magnetic flux, in the region C, no magnetic flux was through it. The figure also shows that the magnetic flux flows through each of the particle because the magnetic flux flows by their flux line.

Figure 3 shows the graph of a different angle of the magnetic particle and the difference of the magnetic flux density as observed in the area has shown in Fig. 1. The y-axis is the value of magnetic flux density in Tesla (T). The x-axis is representing the distance between two magnetic particles, legend show the color that represent the magntic flux density for every angle variable. The graph shows that, the angle on 0° are in concave shape and become convex when the angle of the particle changed until 90°. From the graph, one can observed that the magnetic flux density value between particle decreases when the angle of particle increases. The decrease in the magnetic flux density is because of the deflection of the magnetic flux, through the magnetic particle. From an angle of 0°, a high magnetic density was gained because the magnetic flux flowed through the both of magnetic particles, the magnetic flux flown without deflection, i.e. if there is no deflection of the magnetic flux, there is no loss.

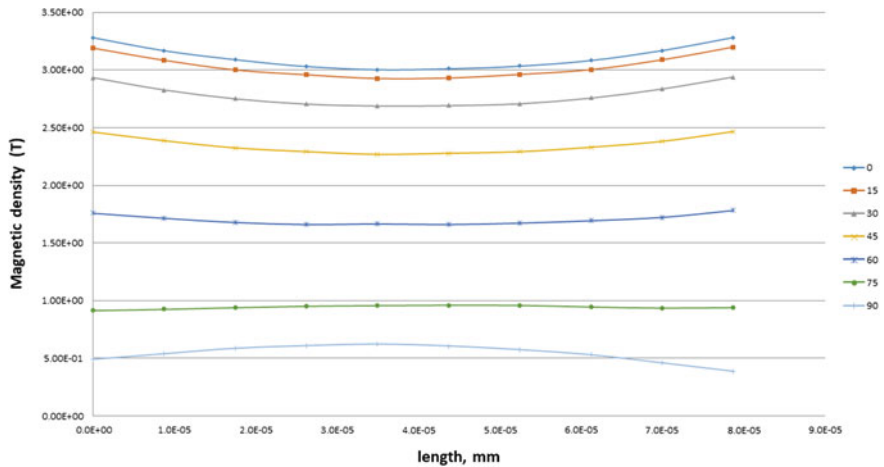


Fig. 3 Magnetic flux density

The magnetic flux density started to decrease when the magnetic particle was increased to 15° this is because the magnetic flux deflected from the existing flux. The angle of 60° and 90° show the difference of the curves, from concave change to a convex curve, the 60° and the 90° angle is the stage where the magnetic flux line breaks of still connected from the magnetic particle. The angle of 75° shows that the line of the graph is linear, the magnetic flux line in the stage is the end of broken linkage magnetic flux from particle a and b.

Figure 4 shows the rate of change of the magnetic flux density from 0° to 90°. The x-axis represents the magnetic particles angle, whereas the y-axis is the value of the magnetic flux density. This graph is relevant for the understanding of the rate of change in the magnetic flux density. This investigation is for identifying whether with every 15° angle, the magnetic flux density changes in a certain pattern or randomly. From the observations in Fig. 4, the rate of change of magnetic flux density in this study shown that, the paten of changing is not linear, the magnetic flux density was drop at angle 75° to 90°. The changing is because of the magnetic flux density slightly deflects from the origin. The largest is for transition from 60° to 75° with value 0.8 T.

Figure 5a, b show the contour and magnetic flux differences occurring for the angle of 60° and 75°. One can observe that the rate of change for 60 and 75 is experiencing a higher change than others. The region “A” in Fig. 4b is referred to; the contour indicates that the magnetic flow is passing through the area between the two particles and still produces a high magnetic flux density which produces a polar magnetic flux density in the concave state as shown in Fig. 3. This is the case because the magnetic flux distances through both particles have a close distance even though the magnetic flux between the two particles is not shared.

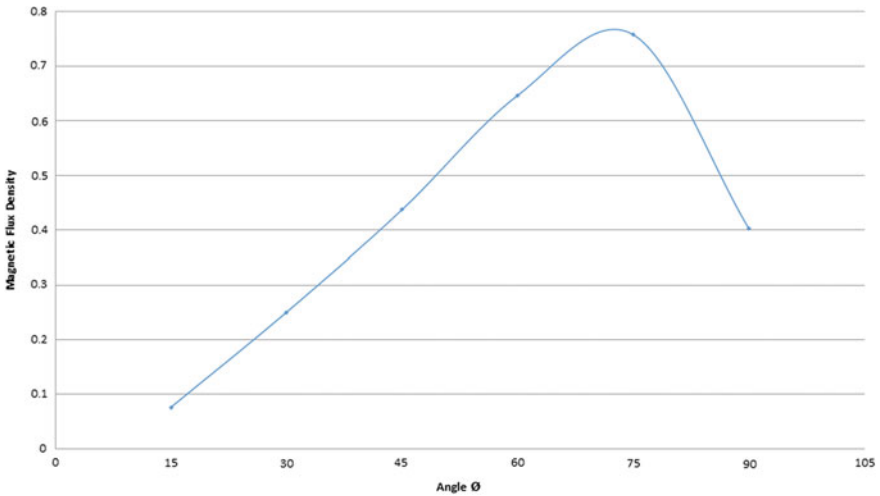


Fig. 4 Rate of change of magnetic flux density

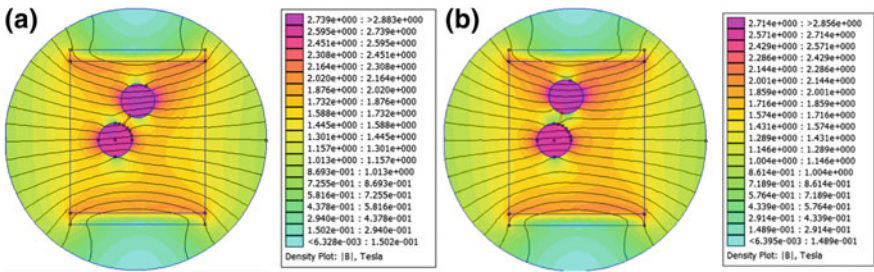


Fig. 5 Carbonyl iron angle 60° (a), 75° (b)

Figure 4c shows, the magnetic flux passing through magnetic particles to discuss the pattern at 70° in Fig. 3. The pattern produced at angle 70° is as if such as a straight line, and at this angle, we can see, it is the middle of the change of polar magnetic flux density of 60° and 90°. This situation occurs because at this angle began to break off the magnetic flux line on particles A and B. When there is no magnetic flux correlation between the particles as shown in Fig. 4b, c, the magnetic density prevailing at the observation area will decrease.

To answer the question of large rate of change at angle 60 and 70, we can compare region A to both Figs. 4b, c. A significant change occurred in the magnetic flux passing through particle “A”, an observation made, the magnetic flux through particle “A” 60° is more than through particle “A” at 75°. Furthermore, at the angle of 70°, no magnetic flux linkage connected between particles A and B. The strength of the magnetic flux density occurs when the magnetic flux flows straight to its axis without any magnetic field deflection and magnetic flux sharing between particle A and B becomes a critical factor increasing the magnetic flux density.

4 Conclusion

In this study, a two-dimensional geometry in a FEMM software was created to investigate the effect of the magnetic field flow in a Magnetorheological elastomer. The simulation consists of two particle magnetic particles that declare as pure iron and around of the magnetic particle is an elastomer polymer matrix. The objective of these studies is to study the effect of the magnetic flow in the MRE layer through the magnetic particle inside MRE layer. The result showed the different response if we change the angle of the magnetic particle. From these studies, we can conclude that the magnetic particles are a significant element in the working principle of the MRE. An elastomer matrix with no magnetic particles does not give any deflection of the magnetic flux, if there is no magnetic flux deflection, then the shrinkage of the matrix elastomer does not occur. With the presence of magnetic particles in the elastomer matrix, the magnetic flux generated from the magnetic core will decelerate and go towards the magnetic particles, by attracting magnetic flux to a magnetic particle which causes the elastomer matrix to shrink when the magnetic field is applied to it and is known as a magnetorheological elastomer. Angles for the arrangement of magnetic particles have been varied to study whether the change of angle on the magnetic particle arrangement affects the magnetic field changes in the MRE layer. From the observation and discussion, it was found that by the changing of magnetic particles angle also affects the magnetic flux density changes in the MRE Layer. With the changing of magnetic particle angle, we can see that the rate of change for each different angle. From the observation, the rate of the change of magnetic flux density changes in a random state because the magnetic flux affects the density of magnetic density. For the overall conclusion, we have understood that the arrangement of an iron particle in the MRE plays the vital issue to design the MRE matrix. Proper selection of the correct MRE type, either isotropic or anisotropic will increase the efficiency of the MRE layer in any application that uses MRE layer.

Acknowledgements All the experiment and analysis conducted under System Engineering and Energy Laboratory, Universiti Kuala Lumpur, Malaysian Spanish Institute, Kulim Kedah, Malaysia.

References

1. Rakotondrabe, M.: Smart Materials-Based Actuators at the Micro/Nano-Scale (2013)
2. Hegde, S., Kiran, K., Gangadharan, K.V.: A novel approach to investigate effect of magnetic field on dynamic properties of natural rubber based isotropic thick magnetorheological elastomers in shear mode. *J. Cent. South Univ.* **22**(7), 2612–2619 (2015)
3. Koo, J.H., Dawson, A., Jung, H.J.: Characterization of actuation properties of magnetorheological elastomers with embedded hard magnetic particles. *J. Intell. Mater. Syst. Struct.* **23**(9), 1049–1054 (2012)

4. Li, Y., Li, J., Li, W., Du, H.: A state-of-the-art review on magnetorheological elastomer devices. *Smart Mater. Struct.* **23**(12), 123001 (2014)
5. Ginder, J.M.: Magnetorheological elastomers in tunable vibration absorbers. *Proc. SPIE* **4331**, 103–110 (2001)
6. Sun, S.S., et al.: Development of an isolator working with magnetorheological elastomers and fluids. *Mech. Syst. Signal Process.* **83**, 371–384 (2017)
7. Yang, J., et al.: Development of a novel multi-layer MRE isolator for suppression of building vibrations under seismic events. *Mech. Syst. Signal Process.* **70–71**, 811–820 (2016)
8. Bocian, M., Kaleta, J., Lewandowski, D., Przybylski, M.: Tunable absorption system based on magnetorheological elastomers and Halbach array: design and testing. *J. Magn. Magn. Mater.* **435**, 46–57 (2017)
9. Bica, I., Anitas, E.M., Chirigiu, L.: Magnetic field intensity effect on plane capacitors based on hybrid magnetorheological elastomers with graphene nanoparticles. *J. Ind. Eng. Chem* **56**, 407–412 (2017)
10. Keip, M.A., Rambašek, M.: Computational and analytical investigations of shape effects in the experimental characterization of magnetorheological elastomers. *Int. J. Solids Struct.* **121**, 1–20 (2017)
11. Wahab, N.A.A., et al.: Fabrication and investigation on field-dependent properties of natural rubber based magneto-rheological elastomer isolator. *Smart Mater. Struct.* **25**(10), 107002 (2016)
12. Baltzis, K.B.: The finite element method magnetics (FEMM) freeware package: may it serve as an educational tool in teaching electromagnetics? *Educ. Inf. Technol.* **15**(1), 19–36 (2010)

Effects of the Coconut Pulp Fiber on the Mechanical Properties and Water Absorption of Reinforced Ethylene Propylene Diene Monomer



Mohamad Sabri Mohamad Sidik, Mohamad Taufiq and Nurulhuda Amri

Abstract This study investigated the effect of Coconut Pulp (CP) fiber on the mechanical properties of Ethylene Propylene Diene Monomer (EPDM). CP filled EPDM composites were prepared by using a mixer and hot press. There are four types of the composition of CP, 10, 20, 30 and 40%. In this study, the tensile strength, modulus of elasticity, elongation at break and water absorption of the composites were evaluated. The tensile strength and elastic modulus decreased while elongation at break increased with the increasing of CP fiber. A lab microscope used to study the morphology of CP in EPDM. Four different types of water used in the water absorption test: Sea, swamp, well and pipe water.

Keywords Coconut pulp fiber · EPDM · Mechanical properties
Water absorption

1 Introduction

Ethylene propylene diene monomer (EPDM) is one of the thermoplastics commonly used in the automotive industry. Several applications of EPDM in the automotive industry are known, such as dashboard wrap material; cushion wrap and some vehicles use it as roof cover [1]. EPDM properties such a resistance to stress, low density, high tensile strength, chemically inert, heat resistance and recyclable

M. S. Mohamad Sidik (✉) · M. Taufiq
Malaysian Spanish Institute, Universiti Kuala Lumpur, Kulim Hi-Tech Park,
09000 Kulim, Kedah, Malaysia
e-mail: msabri@unikl.edu.my

M. Taufiq
e-mail: mtaufiqs@unikl.edu.my

N. Amri
Faculty of Chemical Engineering, Universiti Teknologi Mara, Cawangan Pulau Pinang,
13500 Permatang Pauh, Pulau Pinang, Malaysia
e-mail: nurulhuda.amri@ppinang.uitm.edu.my

that make it an eco-friendly material [2]. However, the usage of degradable polymers is expensive. Thus, the usage of natural filler can reduce the cost of the entire composites. In addition, the natural filler can also act as a strengthening agent for polymer composites.

Many researchers have found that petrochemical-based fillers such as carbon black are suitable as filler material, utilizing the natural fiber as a substitute in composite materials. The coconut pulp (CP) fiber as shown in Fig. 1 is one of the highly potential substitute for synthetic filler and petrochemical filler. The low cost of coconut pulp is one of the major factors for this filler selection. The humidity on coconut pulp becomes the major problem for the natural fiber composites. It reduces the adhesion properties of the fiber. In order to counter this problem, surface treatment conducted to improve the surface roughness and it promotes the bonding between matrix and filler.

The natural fibers are environment-friendly as compared to the steel and synthetic fibers. Natural fibers are low cost, and the coconut fibers are abundantly available in tropical regions [1, 2]. In this study, the discrete (or chopped) fiber type is used for the composite. The disadvantage for this type of fiber is that the strength is lower than aligned fibers, however, the material used is isotropic and cheaper [3]. Figure 2 shows the illustration of a random fiber arrangement.

Thermoplastic elastomers (TPE) are elastomers as shown in Fig. 3 and can be processed like a thermoplastic. It does not require a complex system of chemicals for crosslinking as do normal rubbers and they can be recycled. The properties of TPE can be improved by the addition of different fibers. The composite mixed by using a hot mixing machine as shown in Fig. 4. High temperature and pressure ensured the CP mixed evenly in the elastomer [4]. A dumbbell-shaped specimen according to ASTM D638 has been molded using the hot press machine. Figure 5 shows the hot press machine and the mould.

Fig. 1 Coconut pulp



Fig. 2 Illustration of random fiber arrangement

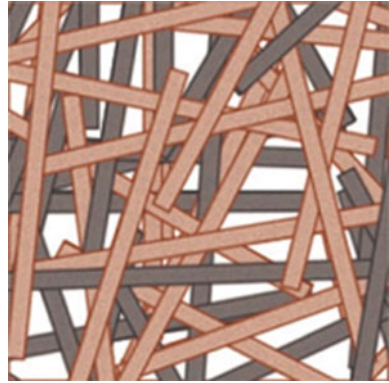
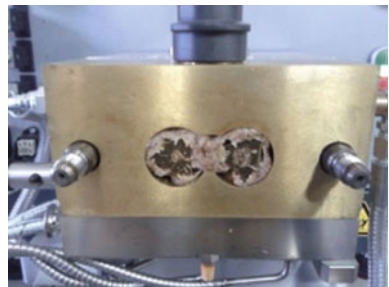


Fig. 3 Elastomer



Fig. 4 Hot mixing process



2 Methodology

Materials

The CP contains oil and humidity. The CP was washed and dried in an oven for about 12 h at 55 °C before being mixed. The loading ratio (wt%) for the filler is 10, 20, 30 and 40%. The elastomer or EPDM was pre-heated with 160 °C for 6 min. The CP fibers were added and heated for another 5 min. Dumbbell shape specimen was produced by using a mould and hot press machine. The temperature setup was 160 °C and pressed with 1000 N force.

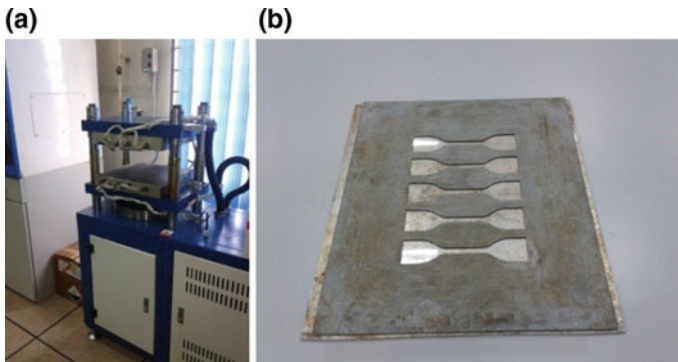


Fig. 5 a Hot press machine **b** Moulding

Tensile Test

The tensile test is conducted according to ASTM (D638) and dumbbell shape (Type IV) specimen is needed for the test. The test was conducted in a standard laboratory atmosphere of 23 ± 2 °C and $50 \pm 5\%$ relative humidity. The tensile testing machine cross-head speed is 10 mm/minute.

2.1 Water Absorption

In this experiment, the ability of composite to absorb the humidity was studied. The specimen was submerged in four types of water such as the sea, swamp, well and pipe water. The duration was one week. The change of the specimen at the surface was observed.

Morphology

The morphology was studied by using a laboratory microscope at the Universiti Kuala Lumpur Malaysian Spanish Institute.

3 Results and Discussion

Figure 6 shows the tensile strength results as a function of the filler content in different filler loading. From the results, it is obvious that the tensile strength (σ) and modulus elasticity (E) were decreased when the filler loading (wt%) increased. The elongation (%) increased when the filler loading (wt%) increased. The stress was distributed to the filler and as a result the tensile stress decreased when the filler content increased.

The modulus elasticity also decreased due to the changes in elastomer properties from elastic to plastic [5] as shown in Fig. 7. This is because the CP is harder than

Fig. 6 Tensile strength

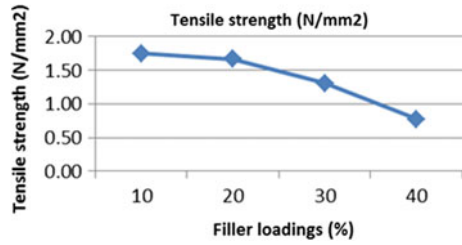


Fig. 7 Modulus of elasticity

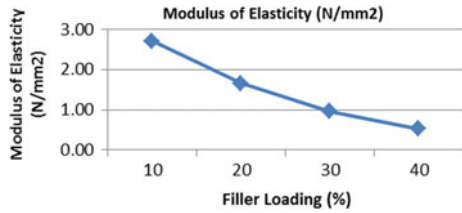
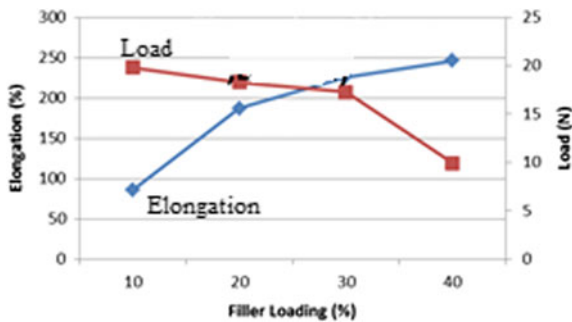


Fig. 8 Elongation and load



the EPDM. The elongation at break increased when the filler loading (wt%) increased as shown in Fig. 8. When subjected to a high load, the higher modulus of the composite will contribute to the higher stress value. When the stress on the composite logically high, it will cause the rate of elongation decreased [5, 6].

Water absorption results are shown in Figs. 9, 10 and 11. When the filler loading (wt%) increased, the water absorption (%) increased. It proved that the fiber absorbs

Fig. 9 Effect of Sulphur acid in swamp water changes colour from brown to white



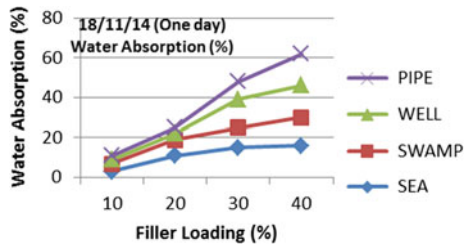


Fig. 10 Water absorption for a period of one day

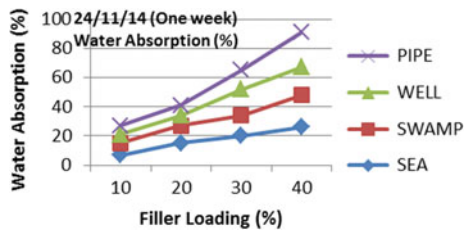


Fig. 11 Water absorption for a period of one week

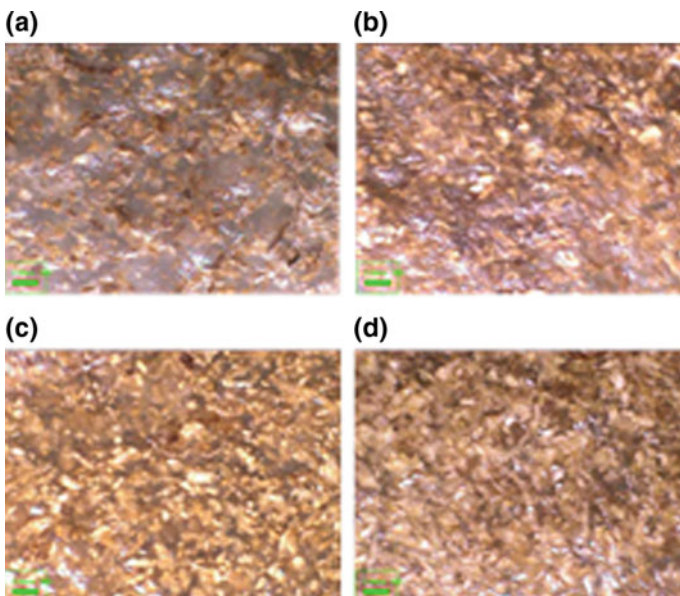


Fig. 12 Morphology results at different filler loading a 10 wt% b 20 wt% c 30 wt% d 40 wt%

the water or hydrophilic. The density of seawater is the lowest compared with another three types of water used in the water absorption testing. The sulfur acid that exists in swamp water has affected the surface of the composite. Morphology results in Fig. 12 show the distributions of fiber in every filler loading (wt%) were different. This is due to the amount of fiber or filler used in each mixture.

4 Conclusion

The study proved that with the addition of filler, the value of tensile strength, modulus of elasticity, elongation and water absorption of the composite have changed. As what has been discussed, with the addition of a filler, the tensile strength was decreased due to the stress which is distributed on the fiber weak point. Thus, a filler loading of 10 wt% has the highest strength to withstand induced stress. Moreover, the elasticity modulus decreases when filler loading increases. Apart from that, the elongation percentage of EPDM/ CP composite is increase when filler loading increased. This is due to the reduction of stress in the composite and it allows the composite to stretch longer.

Acknowledgements The authors would like to thank the Universiti Kuala Lumpur Malaysian Spanish Institute for the financial support for this research work via Final Year Project.

References

1. Akhtar, S., Bhowmick, A.K., De, P.P. et al.: Tensile rupture of short fibre thermoplastic elastomer. *J Mater Sci* **21**, 4179 (1986) <https://doi.org/10.1007/BF01106527>
2. Ismail, H., Pasbakhsh, P., Fauzi, M.A., Bakar, A.A.: Morphological, thermal and tensile properties of halloysite nanotubes filled ethylene propylene diene monomer (EPDM) nanocomposites. *Polym. Test.* **27**(7), 841–850 (2008). <https://doi.org/10.1016/j.polymertesting.2008.06.007>
3. Kalapakdee, A., Amornsakchai, T.: Mechanical properties of preferentially aligned short pineapple leaf fiber reinforced thermoplastic elastomer: effects of fiber content and matrix orientation. *Polym. Test.* **37**, 36–44 (2014). <https://doi.org/10.1016/j.polymertesting.2014.04.008>
4. Romanov, V., Lomov, S.V., Swolfs, Y., Orlova, S., Gorbatikh, L., Verpoest, I.: Statistical analysis of real and simulated fibre arrangements in unidirectional composites. *Compos. Sci. Technol.* **87**, 126–134 (2013). <https://doi.org/10.1016/j.compscitech.2013.07.030>
5. Würkner, M., Berger, H., Gabbert, U.: Numerical study of effective elastic properties of fiber reinforced composites with rhombic cell arrangements and imperfect interface. *Int. J. Eng. Sci.* **63**, 1–9 (2013). <https://doi.org/10.1016/j.ijengsci.2012.10.002>
6. El-Shekeil, Y., Sapuan, S., Haron, M.: Optimization of processing parameters and fiber content of cocoa pod husk fiber-reinforced thermoplastic polyurethane composites by Taguchi method. *Appl. Mech. Mater.* **564**, 394–399 (2014). <https://doi.org/10.4028/www.scientific.net/amm.564.394>

Flow Analysis Inside Coated Porous Media



**Ahmad Kamal Ismail, Mohd. Zulkify Abdullah,
Abdul Rashid Jamaludin, Mohammed Zubair
and Nor Haslina Ibrahim**

Abstract A numerical study has been done to investigate the flow inside porous media (PM). Foam type PM used in the study have been classified into different porosity. The different porosity was due to the fabrication technique which involved the dip coating process. Coating technique is known as a method to increase the performance of PM when used as a medium of combustion. In this study, CFD analysis had been performed with 2D models to observe the flow across the PM. The result shows that the CFD model has the ability to predict the pressure drop caused by different porosities on selected coating materials.

Keywords Porous media · Coating · Flow analysis · CFD

A. K. Ismail (✉) · N. H. Ibrahim
Universiti Kuala Lumpur, Malaysian Spanish Institute, Kulim Hi-Tech Park, 09000 Kulim,
Kedah, Malaysia
e-mail: ahmadkamal@unikl.edu.my

N. H. Ibrahim
e-mail: norhaslina@unikl.edu.my

Mohd.Z. Abdullah
School of Aerospace Engineering, Universiti Sains Malaysia, 14300 Nibong Tebal, Penang,
Malaysia
e-mail: mezul@usm.my

A. R. Jamaludin
Ceramic Research Company Sdn.Bhd. (180916-D), Lot 7110, 5½ Miles, Jalan Kapar, 42100
Klang, Selangor, Malaysia
e-mail: abdrashid@guoceratile.com.my

M. Zubair
Department of Aeronautical & Automobile Engineering, Manipal Institute of Technology,
Manipal, Karnataka, India
e-mail: mohammad.zuber@manipal.edu

1 Introduction

Porous media have been widely used in many applications. Among them, porous media are used as a medium of combustion to improve the combustion process which led to better emission and fuel efficiency [1, 2]. Many types of porous materials are available to be used as a medium for combustion. The materials can be generally classified into metallic and non-metallic types. Ceramic porous medium is among the non-metallic type of a porous material used in combustion. It has a very high thermal resistance with good thermal shock resistance. Porous alumina (Al_2O_3) is a type of porous ceramic being recently studied. Porous ceramics are made from materials such as kaolin [3], porcelain [4, 5], alumina [6], mullite [7], silicon carbide (SiC) [8], and zirconia-based ceramics [9]. Pickenacker [10] has identified alumina, silicon carbide (SiC), and zirconium dioxide (ZrO_2) to be used as media for combustion processes. The porous medium can be obtained in the form of pebbles or spheres with specific size or diameter arranged into a packed bed with relative porosities. It can be produced into a foam type by using the replication technique.

The effect of porosity to the flow inside porous media has been studied in some recent works [11–13]. It shows significant relation between the porosity and the pressure loss at different velocities. In this work, the relation between these parameter has been investigated by using different types of porous media with different coatings. A 2D model has been developed to visualize the flow inside the testing conduit.

2 Methodology

Alumina porous ceramics, Al_2O_3 has been prepared and tested in a previous work to investigate the pressure loss from the flow resistance created by different porosities. The study of pressure loss inside the alumina porous foam continued with the CFD analysis presented in this paper. The experimental setup used in the experiment consisted of PVC pipes with simple coupling at the middle of the pipe where the PM was located. The pipes with PM at the test section has been drawn in a 2D model for simple analysis. The flowchart in Fig. 1 below describes the step by step method to produce the Al_2O_3 porous foam followed by the dip coating process.

The flow through porous media can be calculated by using the equations given below. The PM porosity ε , can be defined as;

$$\varepsilon = \frac{V_v}{V_o} \quad (2.1)$$

$$1 - \varepsilon = \frac{V_s}{V_o} \quad (2.2)$$

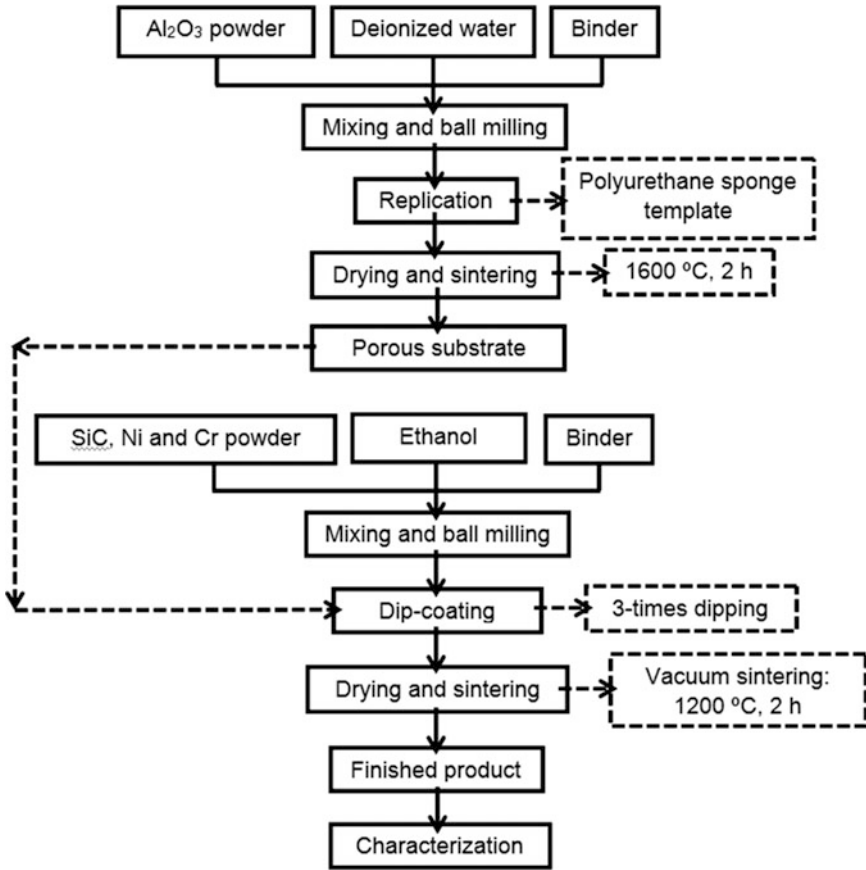


Fig. 1 The production of Al₂O₃ porous foam and coating methods

$$\rho_x \equiv \rho_o(1 - \varepsilon) \rightarrow \tag{2.3}$$

$$\varepsilon = 1 - \frac{\rho_x}{\rho_o} \tag{2.4}$$

$$d_c = 4 \cdot \frac{\text{volume available for flow}}{\text{total wetted surface}} = 4 \cdot \frac{(1 - \varepsilon)}{\varepsilon \cdot s_v} \tag{2.5}$$

$$d_p = \frac{6}{s_v} \tag{2.6}$$

$$d_p = 1.5 \cdot \frac{(1 - \varepsilon)}{\varepsilon} \cdot d_c \tag{2.7}$$

Darcy-and Forchheimer flow

The one dimensional empirical model for laminar flow through a porous media was introduced by Darcy [14]:

$$-\nabla p^* = \frac{\mu}{\alpha} u^* \quad (2.8)$$

The laminar flow through a porous media was then introduced in Forchheimer equation [15]:

$$-\nabla p^* = \frac{\mu}{\alpha} u^* + \beta \rho u^{*2} \quad (2.9)$$

$$\alpha = \frac{d_p^2}{150} \cdot \frac{\varepsilon^3}{(1-\varepsilon)^2} \quad (2.10)$$

$$\beta = \frac{1.75}{d_p} \cdot \frac{(1-\varepsilon)}{\varepsilon^3}. \quad (2.11)$$

The Eq. 2.10 and Eq. 2.11 are substituted in Eq. 2.9 to have Ergun equation [16, 17] as given below.

$$-\nabla p^* = \frac{150\mu(1-\varepsilon)^2 u^*}{d_p^2 \varepsilon^3} + 1.75 \frac{(1-\varepsilon)}{\varepsilon^3} \frac{\rho u^{*2}}{d_p} \quad (2.12)$$

The values of ε , d_c and d_p in Ergun equation are given in Eq. 2.4, Eq. 2.5 and Eq. 2.7 respectively.

3 2D Model Analysis

A two-dimensional steady state model was used using the viscous k- ε model with standard wall functions and no slip boundary conditions. The porosity of the PM and coating material properties for SiC, Nickel and Chromium have been set during the numerical analysis.

The standard k- ε model

For the standard k- ε model, the turbulent kinetic energy k and its dissipation rate are related by:

$$V_t = \frac{C_\mu k^2}{\varepsilon}. \quad (3.1)$$

The transport equations for k and ε are given by;

$$\frac{\partial}{\partial x_i}(\rho u_i k) = \frac{\partial}{\partial x_i} \left[\left(\mu + \frac{\mu_i}{\sigma_k} \right) \frac{\partial k}{\partial x_i} \right] + G_k - \rho \varepsilon + S_k \quad (3.2)$$

$$\frac{\partial}{\partial x_i}(\rho u_i \varepsilon) = \frac{\partial}{\partial x_i} \left[\left(\mu + \frac{\mu_i}{\sigma_\varepsilon} \right) \frac{\partial \varepsilon}{\partial x_i} \right] + C_1 \frac{\varepsilon}{k} G_k - C_2 \rho \frac{\varepsilon^2}{k} + S_\varepsilon \quad (3.3)$$

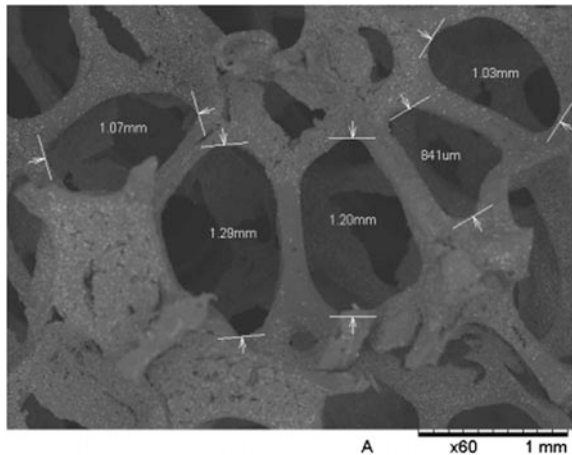
In these equations G_k is the generation of turbulence kinetic energy due to mean velocity gradients; C_1, C_2 and C_μ are constants; σ_k and σ_ε are the Prandtl numbers for k and ε , respectively; S_k and S_ε are source terms and can be used during combustion analysis.

4 Results and Discussion

In Fig. 2, the image of uncoated alumina template has been captured using SEM. This coated alumina was produced by using the method shown in Fig. 1. The pores and skeleton can be clearly observed with some of the pores has been blocked by the coating particles. This has decreased the porosity and provided higher resistance to the flow. The velocity contour inside the tube can be observed in Fig. 3. Obviously, the PM has created resistance to the flow at the middle of the pipe. It can be seen that the velocity has slowed down at the centre and started to propagated when passing the PM. A very high velocity can be found at the inlet while at the outlet, the velocity also increased as the result of constriction created by the pipe reducer.

Figure 4 explains in more details the velocity vectors inside the pipe. There was some backflow at the inlet due to the high speed of air pumped into the pipe and

Fig. 2 SEM micrographs of coated alumina



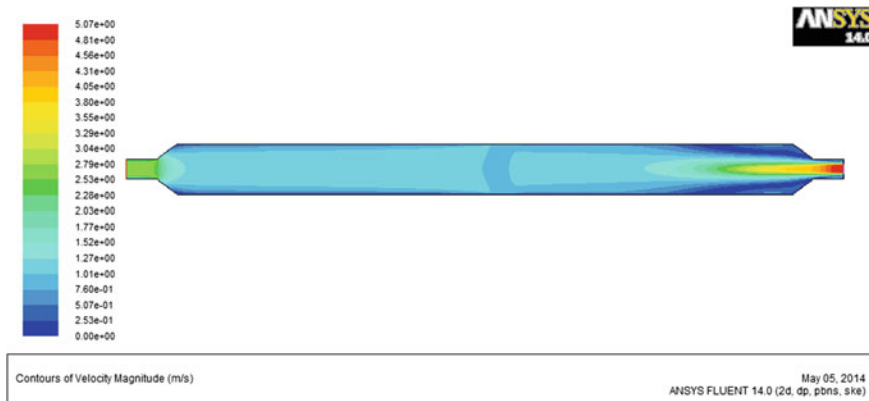


Fig. 3 Velocity profile in the pipe (m/s)

sudden enlargement in diameter. The flow of air at the wall was a bit lower than at the middle of the pipe. This can be related to the flow friction produced at the internal pipe wall.

The pressure losses were also measured by using the CFD model with the results shown in Fig. 5 below. Again it can be clearly observed that there was a pressure difference before and after the PM. The highest pressure was located almost at the centre of the pipe and slowly reduced after passing the PM. The values of pressure calculated by CFD at two different points both located before and after the PM being subtracted to get the pressure drop and compared for different types of coated PM as given in Table 1.

In Table 1, all the results produced by CFD analysis were compared with the experimental results obtained from the earlier work. The difference was only about 2% for SiC and Ni coated PM when compared with experimental data at low

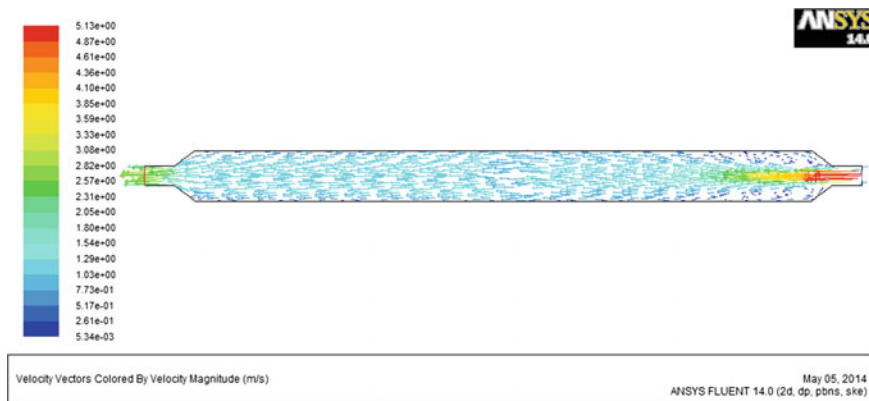


Fig. 4 Velocity vector in the pipe (m/s)

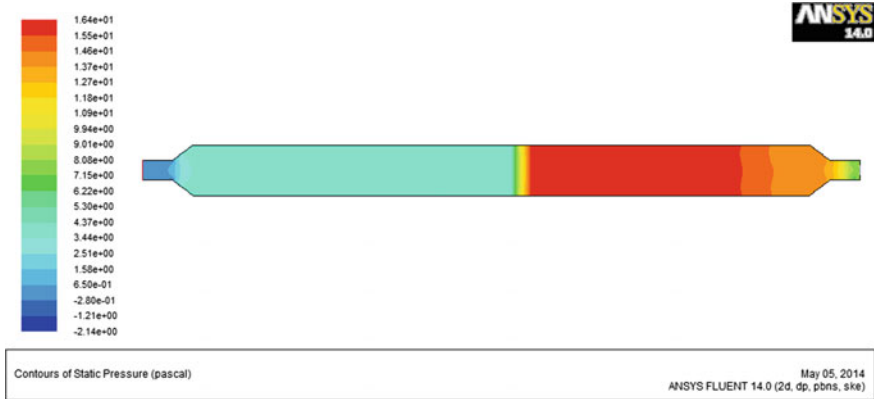


Fig. 5 Pressure losses inside the tube with PM in Pascal (Pa)

Table 1 Comparison between experimental results with CFD

m/s	Porosity							
	0.71		0.64		0.65		0.68	
	Pressure difference in Pascal (Pa)							
	Uncoated	CFD	SiC	CFD	Ni	CFD	CrO	CFD
5.26	8	12.4	13	13.22	14	13.22	11	13.21
9.21	21	41.2	35	41.15	36	41.2	30	41.2
13.16	41	84.5	71	84.31	71	84.30	60	84.31

velocity. While at the highest velocity, the different was about 16%. For CrO coated PM, the difference was 20% at low velocity and 40% at the highest velocity. The model was unable to predict the pressure drop for uncoated PM due to very high percentages of difference (>50%).

5 Conclusion

In this work the effect of coated ceramics to the flow inside porous media was carried out. It was found that coating PM has reduced the porosity as compared to uncoated PM. Therefore, the pressure drop increased by using coated PM. The pressure drop for SiC and Ni coated alumina were the highest followed by Ni coated alumina and the uncoated alumina. In general, porous ceramic is more suitable to be used with compressed air to reduce the effect of pressure drop on the self aspirated burner to avoid flashback when used as a medium of combustion. Further analysis must be carried out on the design of PM foam to reduce the pressure losses due to different coatings and porosities. From CFD analysis, the prediction on pressure drop suits on the results for SiC and Nickel coated but have a

large deviation with the results produced for Chromium coated and uncoated alumina. Therefore, extra work must be done in CFD in order to find the best prediction with very less differences.

Acknowledgements The authors would like to thank the Ministry of Higher Education, Malaysia and the Universiti Sains Malaysia (USM) for the financial support for this research work via PRGS Grant No. 6740002 and USM grant 1001/PMekanik/8044057.

References

1. Trimis, D.: Porous burner technology—an overview. *Porenbrennertechnologie - EinÜberblick* **147**(2), 92–99 (2006)
2. Wood, S., Harris, A.T.: Porous burners for lean-burn applications. *Prog. Energy Combust. Sci.* **34**(5), 667–684 (2008)
3. Nandi, B.K., Uppaluri, R., Purkait, M.K., et al.: Preparation and characterization of low cost ceramic membranes for micro-filtration applications. *Appl. Clay Sci.* **42**(1–2), 102–110 (2008)
4. Muhamad Nor, M.A.A., et al.: Preparation and characterization of ceramic foam produced via polymeric foam replication method. *J. Mater. Process. Technol.* **207**(1–3), 235–239 (2008)
5. García-Ten, J., et al.: Development of lightweight porcelain stoneware tiles using foaming agents. *J. Eur. Ceram. Soc.* **32**(4), 745–752 (2012)
6. Khattab, R.M., Wahsh, M.M.S., Khalil, N.M., et al.: Preparation and characterization of porous alumina ceramics through starch consolidation casting technique. *Ceram. Int.* **38**(6), 4723–4728 (2012)
7. Yang, F., et al.: Effects of sintering temperature on properties of porous mullite/corundum ceramics. *Mater. Lett.* **73**, 36–39 (2012)
8. Dey, A., Kayal, N., Chakrabarti, O., et al.: Preparation of porous SiCceramics by an infiltration technique. *Ceram. Int.* **37**(1), 223–230 (2011)
9. Garrido, L.B., et al.: Effect of starch filler content and sintering temperature on the processing of porous 3Y–ZrO₂ ceramics. *J. Mater. Process. Technol.* **209**(1), 590–598 (2009)
10. Pickenacker, O., et al.: Innovative ceramic materials for porous-medium burners. *Interceram.* **48**(5), 326–329 (1999)
11. Shakiba, S., Ebrahimi, R., Shams, M et al.: A new relation for pressure drop through ceramic foams based on dimensional analysis. In: Fourth International Conference On Experimental Mechanics. International Society for Optics and Photonics
12. Shakiba S, Ebrahimi R, Shams M et al (2009) A study on the effects of cold and hot fluids on pressure drop through ceramic foams. In: Fourth International Conference on Experimental Mechanics. International Society for Optics and Photonics
13. Shakiba, S., Ebrahimi, R., Shams, M., et al.: Experimental investigation of pressure drop through ceramic foams: an empirical model for hot and cold flow. *J. Fluids Eng.* **133**(11), 111105 (2011)
14. Liu, S., Afacan, A., Masliyah, J., et al.: Steady incompressible laminar flow in porous media. *Chem. Eng. Sci.* **49**(21), 3565–3586 (1994)
15. Macini, P., Mesini, E., Viola, R., et al.: Laboratory measurements of non-Darcy flow coefficients in natural and artificial unconsolidated porous media. *J. Petrol. Sci. Eng.* **77**(3–4), 365–374 (2011)
16. Innocentini, M.D., et al.: Permeability optimization and performance evaluation of hot aerosol filters made using foam incorporated alumina suspension. *J. Hazard. Mater.* **162**(1), 212–221 (2009)
17. Innocentini, M.D., et al.: Prediction of ceramic foams permeability using Ergun’s equation. *Mater. Res.* **2**(4), 283–289 (1999)

Francis Turbine Analysis Between Computational Fluid Dynamics (CFD) and Experimental Methods



Muhammad Naim bin Md. Kamal, Khairul Shahril bin Shaffee, Mohamad Sabri bin Mohamad Sidik, Ahmad Razlee Ab. Kadir and Johan Ihsan bin Mahmood

Abstract Hydroelectric power has become the most promising source in the power sector to sustain the growth of any nation. In any hydroelectric power plant, the hydraulic turbine plays a vital role which affects the overall performance of the plant and if utilized at suboptimal level, may lead to the loss of useful head. So, it becomes vital to predict the behavior of the hydro-turbine under actual working conditions. Francis turbines are the most well-known water turbines being used today. The Francis turbines works in water depths from 10 to 650 m (33–2133 ft) and are fundamentally utilized for electric power generation. This research consists of a simulation process and experimental research in order to compare both of the results. The geometry is modelled using the CATIA software and transferred into Ansys for the analysis. All the main parts that are included in the Francis turbine educational kit at the Universiti Kuala Lumpur Malaysian Spanish Institute such as the spiral casing, the runner blade, guide vane and the draft tube is constructed in the 3D model. The highest accuracy for the Francis turbine occurs at 1300 RPM and the highest inaccuracy percentage is within 30% and the lowest inaccuracy percentage is within 2%.

Keywords Francis turbine · CFD · CATIA · Ansys

M. N. bin Md. Kamal · K. S. bin Shaffee (✉) · M. S. bin Mohamad Sidik
A. R. Ab. Kadir · J. I. bin Mahmood
Malaysian Spanish Institute, Universiti Kuala Lumpur, Kulim Hi-Tech Park,
09000 Kulim, Kedah, Malaysia
e-mail: khairuls@unikl.edu.my

M. S. bin Mohamad Sidik
e-mail: msabri@unikl.edu.my

A. R. Ab. Kadir
e-mail: ahmadrazlee@unikl.edu.my

J. I. bin Mahmood
e-mail: johanihsan@unikl.edu.my

1 Introduction

Energy plays an important role in providing a steady growth of a country as well for the economy growth as the increase of citizen is also resulting in a higher power demand. As in Malaysia, the requirement of hydroelectric dam as power generators is increasing because of the suitable geographical terrain in Malaysia. The demand will continue to increase as the population of Malaysia continues to increase. The data of hydroelectric dam capacity in Malaysia from 2004 shows that hydro power generation consists 11.0% in the Peninsular Malaysia [1].

The Francis turbine educational kit simulates the condition of a real Francis turbine that is used in power generation in a real life condition. It is able to give almost the real experience in the understanding how the Francis turbine operates. By running the experiment, data from the Francis turbine educational kit and with some theoretical calculations from the data, the efficiency of the turbine can be obtained. The aim of this study is to compare efficiency data result from the conducted experiments using the Francis turbine educational kit and from running simulations using the Ansys computational fluid dynamics (CFD) code and to validate the data that were obtained in a real life condition and simulations condition.

Even though it is possible to predict turbine characteristics by model tests in the laboratory, time and budget limitations, prototype restrictions promoted the use of CFD tools for the turbine optimization. Developing technology enhanced the computational power and led to an improvement in the turbine design. An accurate prediction of the flow inside the hydraulic turbine is nowadays possible by the use of state-of-the-art CFD tools [2]. The latest CFD tools are the outcome of several researches handled during the last four decades. Validation of the lately developed tools proves that the accuracy of CFD tools are very high. This made the power of CFD tools undeniable in the design process [3].

One of the most desirable types of water turbine that is in use in power production is the Francis turbine. The Francis turbine is a type of water turbine that was developed by James B. Francis in Lowell, Massachusetts [4]. It is an inward-flow reaction turbine that combines the radial and axial flow concepts. Figure 1 shows the design of a Francis water turbine and the main components in the Francis turbine.

Francis turbines are the most well-known water turbines being used today. The Francis turbine works in water depths from 10 to 650 m (33 to 2133 ft) and is fundamentally utilized for electric power generation. The turbine controlled generator force yield large runs from 10 to 750 MW, however small hydro establishments may be lower. Penstock (input pipe) widths are between 1 and 10 m (3 and 33 ft). The speed rate of the turbine is from 83 to 1000 rpm [5]. The entryways around the outside of the turbine's pivoting runner conform the water stream rate through the turbine for diverse water stream rates and force generation rates. Francis turbines are just about constantly mounted with the pole vertical to keep water far

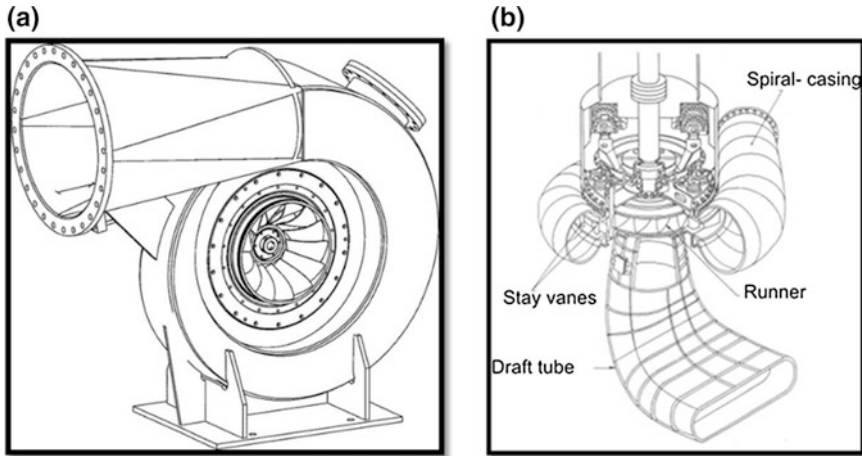


Fig. 1 a Francis turbine; b Francis turbine main component

from the connected generator and to allow installation and maintenance access to the turbine.

The Francis turbine is a kind of response turbine, a class of turbine in which the working liquid goes to the turbine under huge pressure and the energy is transferred to the turbine blade from the working liquid. A part of the energy is transferred from the fluid because of the pressure change in the blade of the turbine, quantified by the outflow of degree of reaction, while the remaining quantity of the energy is concentrated by the volute casing of the turbine. At the exit, the water follows up on spinning cup-shape runner features, leaving at low speed and low swirl with very little kinetic and potential energy left. The turbine's draft tube is molded to help decelerate the water stream and regain the pressure.

The centrifugal pump data were observed at a monitor that has been provided from the manufacturer of the Francis turbine educational kit. The following formula shows a theoretical calculation how the data is displayed on the monitor.

$$\text{Output Power (W)} = \rho g h Q = P Q \quad (1)$$

$$\text{Input Power (W)} = \text{Torque (Nm)} * \text{Average speed (rad/s)} \quad (2)$$

$$\text{Average speed (rad/s)} = \text{Average speed (rpm)} * 2\pi/60 \quad (3)$$

$$\text{Efficiency} = \text{Output Power} / \text{Input Power} \quad (4)$$

Turbine Equation

$$\text{Load (N)} = F1 - F2 \quad (5)$$

$$\text{Average speed (rad/s)} = \text{Average speed (rpm)} * 2\pi/60 \quad (6)$$

$$\text{Torque (Nm)} = \text{Load} * \text{radius of the wheel (0.026 m)} \quad (7)$$

$$\text{Input Power (W)} = \rho ghQ = PQ \quad (8)$$

$$\text{Output Power (W)} = \text{Torque (Nm)} * \text{Average speed (rad/s)} \quad (9)$$

$$\text{Efficiency} = \text{Output Power} / \text{Input Power} \quad (10)$$

Note:

Pressure, P = Reading from pressure gauge (must convert from bar to Pa)

Flow rate, Q = Must change from LPM to m³/s

CFD has emerged out as a powerful tool for predicting the performance of mechanical bodies subjected to dynamic flow conditions [6]. There are ample of evidences where analysts at various levels have taken the advantage of this tool to solve so many problems related to performance analysis. There is a lot of research that has been conducted in simulation analysis of the Francis Turbine using the CFD method such as the research done by ČARIJA where the research was conducted for a dam that is located near Rječina by constructing a 3D model for a simulation in Ansys CFD to find the efficiency data for optimization of the dam. The result that was obtain from the research is that the inaccuracy of computed results for all analyzed characteristic values was within $\pm 2\%$ over the whole analyzed operating range, increasing in accuracy towards the turbine optimal efficiency point to less than 0.5% inaccuracy [7]. As for a research that was conducted by Akin was to research a methodology for conducting an analysis using CFD for a

Table 1 Data of boundary condition for simulation

Boundary Condition	Value in experiment	Value in Ansys
Inlet	The inlet for Francis turbine	Define the inlet location in Ansys
outlet	The outlet for the Francis turbine	Define the outlet location in Ansys
wall	The runner blade of the Francis turbine	Define the runner location in Ansys
Flow rate	125.6 (Lpm)	5 (m/s)
Material	water	water
Guide vane opening	25% opening	25% opening
Average speed (rpm) of the runner blade	2300–700	Same with experiment data but unit is in rad/s

Francis turbine where the result for the developing design methodology was applied for the turbine design of an actual hydropower project. The overall results of each Francis-type turbine components designed with the help of CFD are presented in Table 1. According to the final CFD results, an overall turbine efficiency of 92.3% is reached. As the performance values of the design satisfy the requirements of the Yuvacik H.E.P.P project, the structural verification of the design is accomplished and the manufacturing process was started [5].

2 Methodology

This research consists of a simulation part and an experimental research in order to compare both of the result. Figure 2 shows the flowchart for planning the research from the start until the end of this research.

2.1 Geometry Modelling/Boundary Condition

2.1.1 Geometry Modelling

In order for the simulation to be successful, a geometry modelling is required with a scale that is the same as the Francis turbine educational kit. The geometry is modelled using the designing software CATIA before the model can be transferred into Ansys for further simulation. All the main parts that are included in the Francis turbine educational kit such as the spiral casing, the runner blade, guide vane and the draft tube is constructed in the 3D model so that the model can be transferred into Ansys software to perform the simulation. Figure 1 shows the 3D design, and then transferred model from CATIA into Abaqus designing software to do some

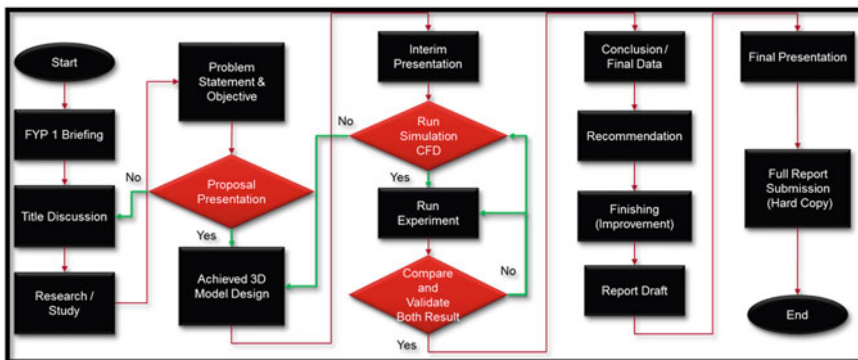
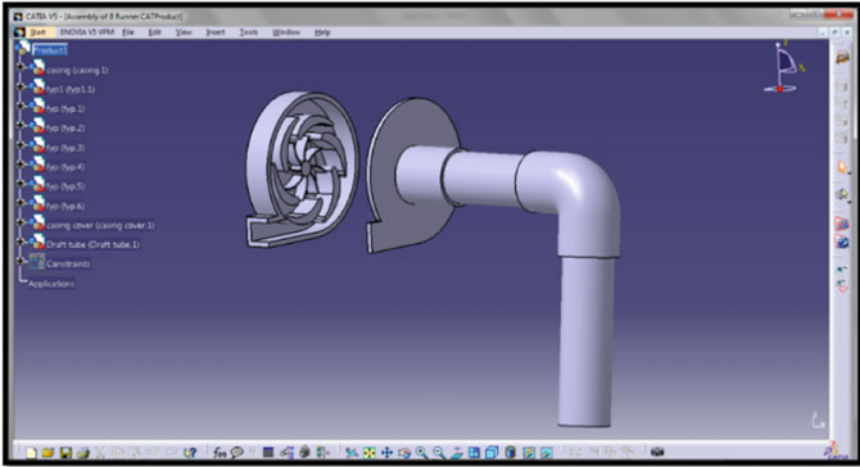


Fig. 2 Flowchart of research process

(a)



(b)

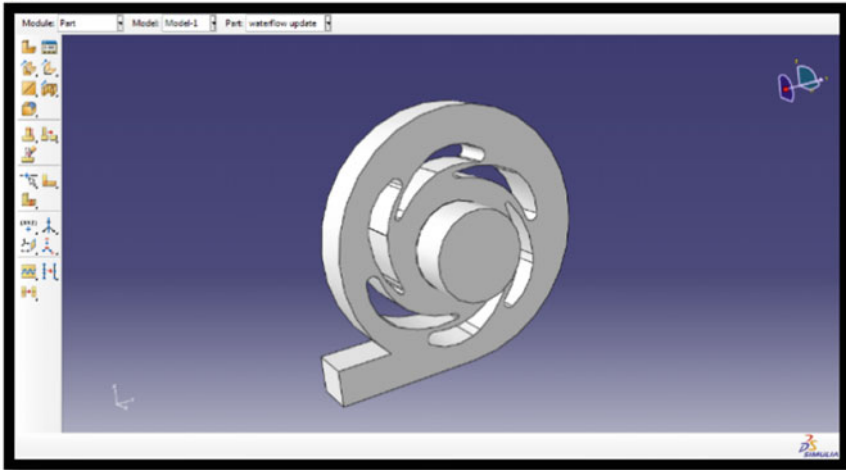


Fig. 3 a Complete assembly of Francis turbine in CATIA; b Final design of 3D model

Booleans operations to so that the final design can act as containment of the water for the simulations in Ansys to be successful. Ansys CFD can only read a fully closed system to be run. Figure 3 shows the final 3D design of the Francis turbine educational kit and the main parts that has been constructed into 3D model.

2.1.2 Boundary Condition

The final design is transferred into the Ansys software to run the simulation using Fluid Flow (Fluent). In Ansys the parametric data that need to be defined such as the inlet, outlet, and wall for the blade so that the data after the simulations can be interpreted. The boundary conditions for the simulation to be run will be set the same as the experimental setup of the Francis turbine educational kit, i.e. input values such as the flow rate, average speed (rotation per minute), guide vane opening, and material for the simulation to run which is water. Table 1 shows the parametric data and the boundary conditions that were used during the simulations in the Ansys CFD software.

2.2 Experimental Study

The experiments were executed based on the procedure that was stated in the lab manual of the Fluid lab. The procedure of this experiment and Fig. 4 of the Francis turbine educational kit is shown below.

2.2.1 Procedure

The apparatus was set up with the Francis turbine on the bench top and the computer as stated in the apparatus setup. The control valve opened and slowly closed the bypass valve. The adjustable handle guide vane was adjusted from the Francis



Fig. 4 Francis turbine educational kit

turbine to be half opened. The water was directed by the guide vane wall and caused the turbine to rotate. Then, the frequency was switched to 50 Hz by turning the turning knob of the frequency motor. The system was allowed to run for about 3 min to let the flow rate reading become stable. The last procedure was to repeat the same step but different types of guide vane opening in order to determine which type of opening will give the highest efficiency value. The data from the experiment was captured by the software in the computer. The procedure on how to use the software in the computer is shown below.

Turn on the computer for the first step and next is to start the program by double click the software icon. Next is to select the Francis turbine experiment icon. Click on the start button icon that is located at the bottom left of the program window. After finishing the experiment click on save file to save the file in the desired location. Lastly ensure that readings are available to run the experiment.

3 Results and Discussion

3.1 Simulations Result

There are several results that have been obtained during the simulations process which is depending on the guide vane opening. These results are selected based on which guide vane opening caused the highest efficiency in this case the guide vane opening is 25%. The results that obtain during the simulations process are shown in the Table 2.

Based on the result there are some consistencies from the data that has been obtained and the Fig. 5 shows the data of the average speed (rpm) versus the efficiency (%).

Table 2 Data of simulation

Average speed (rpm)	Average speed (rad/s)	Torque (Nm)	Output power (W)	Input power (W)	Efficiency (%)
1498	156.87	0.11617676	18.22467078	102.8389	0.17721573
1397	146.29	0.11702528	17.12003755	100.7401	0.16994263
1301	136.24	0.1172991	15.98087647	96.5426	0.16553186
1207	126.40	0.11834923	14.95895738	94.4439	0.15838987
1107	115.92	0.11864739	13.75417127	94.4439	0.14563324
1000	104.72	0.11882454	12.44327673	90.2464	0.13788114
901	94.35	0.1190762	11.23513708	88.1476	0.12745823
807	84.51	0.1194553	10.09502912	86.0489	0.11731735
706	73.93	0.11943101	8.829791001	81.8514	0.10787587

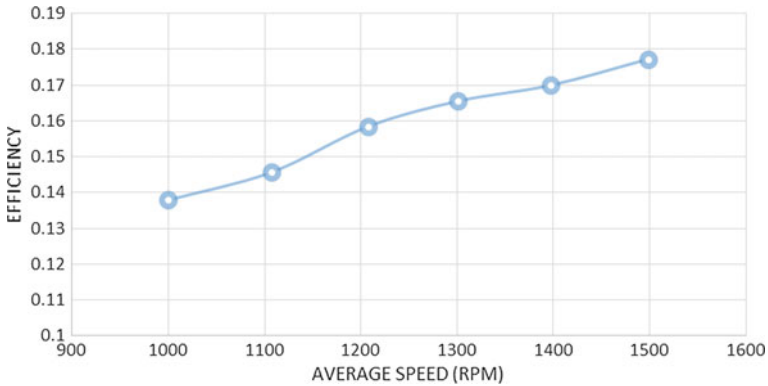


Fig. 5 Rpm versus efficiency (simulation)

From Fig. 5, the data of simulation is directly proportional between the efficiency and the average speed (rpm). As the average speed (rpm) was increasing so was the efficiency.

3.2 Experiment Results

There are several results that were been obtained during the experimental process which is depending on the guide vane opening. These results are selected based on which guide vane opening caused the highest efficiency in this case the guide vane opening is 25%. The result that obtained during the experimental process is shown in Table 3.

Table 3 Data of experiment

Average speed (rpm)	Average speed (rad/s)	Torque (Nm)	Output power (W)	Input power (W)	Efficiency
1498	156.8702	0.0936	14.6831	102.8389	0.1428
1397	146.2935	0.1061	15.5188	100.7401	0.154
1301	136.2404	0.1154	15.7276	96.5426	0.1629
1207	126.3967	0.1284	16.2344	94.4439	0.1719
1107	115.9248	0.136	15.7635	94.4439	0.1669
1000	104.7198	0.1526	15.9823	90.2464	0.1771
901	94.3525	0.1659	15.6512	88.1476	0.1776
807	84.5088	0.1755	14.8313	86.0489	0.1724
706	73.9321	0.1908	14.1092	81.8514	0.1724

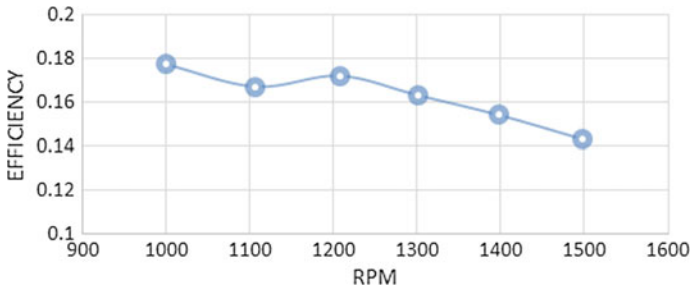


Fig. 6 Rpm versus efficiency (experiment)

Based on the results there are some consistencies from the data that has been obtained and Fig. 6 shows the data of the average speed (rpm) versus the efficiency (%).

The graph 2 shows a decrease in the result between the average speed (rpm) and efficiency. As the average speed (rpm) is increasing the efficiency will decrease.

3.3 Comparison Between Experiment and Simulation Data

The data that has been obtained from the simulation and experiment has been compared and analyzed to find the relationship between those two data. The graph below shows the combined data of experiment and simulation into one graph. Figure 7 shows the average speed (rpm) data versus the efficiency data.

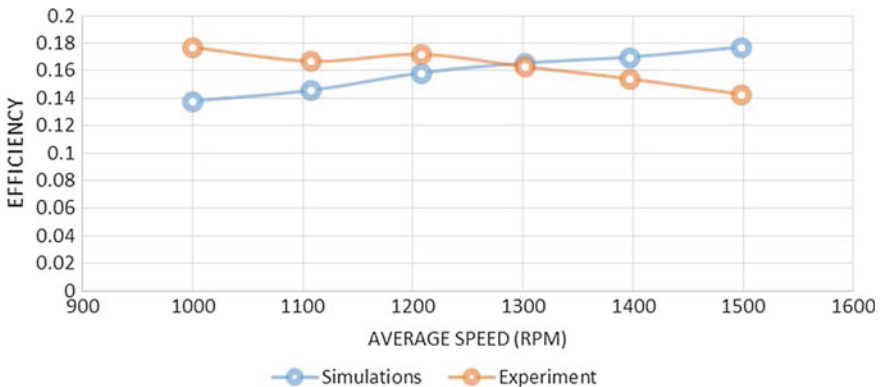


Fig. 7 Rpm versus efficiency for experiment and simulation

The compared data are supposedly to be similar or exactly with each other. Even both of data sets are not accurate, the data that was obtained from simulations and experiment are still in the accepted range. There are some errors that can be justified. One of the errors that can be justified during running the experiment is that the reading of the average speed (rpm) is not stable. This is because the reading needs some time to be stable due to the belting that is controlling the rotational speed did not have enough friction to slow down the rotating runner blade accurately that is causing the average speed (rpm) to increase back after it has been set. It required a lot of sensitive adjustment to tighten the pulley. Others errors that can be justified is the lack of computational power. Because of these factors the simulation cannot run at the most optimum meshing size as the refinement of the mashing increases the simulation time required to complete will also increase depending on the computational power.

From the references, errors that happen to other researcher are the reason for the slight difference of the computed data is due to the discretization of the domain and solution of the differential equation in the computational method and the rigidity of the computational numerical analysis than the theoretical hand calculation [8].

4 Conclusion

The experimental approach of evaluating the performance of the Francis turbine is costly as well as time consuming. Conversely, the CFD approach is faster and a large amount of results can be produced at virtually no added cost. The CFD approach for the prediction of the efficiency of Francis turbine was developed with accomplishment of analysis of the Francis turbine performance. CFD analysis shows the distribution of various parameters like the pressure, velocity at various points along the blade profile by using boundary conditions of pressure and mass flow rate at inlet and outlet. It can be concluded that the CFD approach assists in reduction in cost of model testing and saving in time which leads to cost-effective analysis and may enhance the viability of hydropower development.

Acknowledgements The authors would like to thank the Universiti Kuala Lumpur Malaysian Spanish Institute for the financial support for this research work via Final Year Project.

References

1. The Future of Hydropower in Malaysia, pp. 32–33 (May, 2005)
2. Drtina, P., Sallaberger, M.: Hydraulic turbines—basic principles and state-of-the-art computational fluid dynamics applications. **213**, 85–103 (1999)
3. Jain, S., Saini, R.P., Kumar, A.: CFD approach for prediction of efficiency of francis turbine, pp. 1–7 (2010)
4. Francis, J.B., Service, N.P.: Lowell Notes (1848)

5. Akin, H., Aytac, Z., Ayancik, F., Ozkaya, E., Arioiz, E., Celebioglu, K., Aradag, S.: A CFD aided hydraulic turbine design methodology applied to Francis turbines
6. Navthar, R.R., Tejas, J., Saurabh, D., Nitish, D., Anand, A.: CFD analysis of Francis turbine. **4** (07), 3194–3199
7. Čarija, Z., Mrša, Z.: Validation of Francis water turbine CFD simulations. **50**(1), 5–14 (2008)
8. Shukla, M.K.: CFD analysis of 3-D flow for Francis turbine. **1**(2), 93–100 (2011)

Refining 5S Awareness Through an Interactive Game Board



Jumázulhisham Abdul Shukor, Rahim Jamian
and Mohd Nizam Ab Rahman

Abstract The practice of 5S is a world-class business improvement approach. It is widely used to increase organization performance to achieve market competitiveness. However, successful implementation of 5S is heavily depending on 5S training programs as well as other several factors. In this context, teaching and learning or training process of 5S using conventional methods, either through seminars or lectures, may reduce the tendency of some individuals to think creatively and critically and subsequently affect the success of the 5S implementation. This study proposes an alternative novel method of 5S teaching and learning through an interactive game board (IGB). The use of IGB could encourage players to think creatively based on real experience of 5S implementations. The purpose of this study is to measure the effectiveness of the teaching and learning process. In this study, the construct of IGB which comprises of planning, implementation, auditing, and improvement activities has been built based on the concept of problem-based learning (PBL). A survey instrument is employed for quantitative data collection. Questionnaires are distributed to randomly selected university students and trainees as players or participants. The result shows that players who have undergone the teaching and learning process of 5S through IGB become more focused, creative, and reveal an improved understanding of the 5S practice.

Keywords 5S · Interactive game board · Problem-based learning
Teaching and learning

J. Abdul Shukor (✉) · R. Jamian
Malaysian Spanish Institute, Universiti Kuala Lumpur, Kulim Hi-Tech Park,
09000 Kulim, Kedah, Malaysia
e-mail: azulhisham@unikl.edu.my

R. Jamian
e-mail: rahimj@unikl.edu.my

M. N. Ab Rahman
Universiti Kebangsaan Malaysia, 43600 Bangi, Selangor, Malaysia
e-mail: mnizam@ukm.edu.my

1 Introduction

5S is a technique used to establish and maintain a quality environment in an organization effectively [1]. It was initially introduced by Takashi Osada in Japan in the 1990s [2]. This method was then being implemented as lean approach to minimize waste in manufacturing industry worldwide [3]. It is one of the best tools for enhancing implementation of a total quality management (TQM) [1]. The 5S practice could initiate an environment for work standardization and better working conditions by improving quality, focusing on waste elimination, providing safety for workers, keeping the workplace clean, maintaining the standards, ensuring that everyone follows them, and making it as a culture in an organization [2].

The philosophy of 5S is not just to be implemented in the industrial sectors, but it can also be practiced in any workplace environment including homes and schools. In this context, the implementation of 5S normally begins with teaching and learning processes [3]. Currently, most of teaching and learning processes of 5S are being carried out by using conventional methods, such as through several lectures, seminars and trainings. Empirical evidence shows that the use of the current methods may be difficult to push the limit of creative thinking and ideas of some training participants [4]. As a result, a full benefit of 5S could not be gained.

However, there are numerous ways to conduct the 5S training effectively. For examples, it can be successfully done by using information technology (IT) platform and software [4]. This study proposes an alternative way of 5S teaching and learning by using an interactive game board (IGB). The main objective is to boost up the effectiveness of 5S teaching and learning method. In this study, the concept of problem-based learning (PBL) has been adopted to create an active environment of teaching and learning process [5].

This paper outlines the proposed improvement method of 5S teaching and learning through IGB. An overview is also provided about the importance of 5S training and the use of IGB for the 5S teaching and learning method. Then, this paper presents the methodology of the study and highlights the results as well as conclusion of the study.

2 The Importance of 5S Training

Training is the key to success in 5S implementation [1]. The employees or students should receive adequate knowledge in the scope of their work to help the organization to achieve the objectives [6]. The emphasis on training that includes 5S philosophy and techniques to each employee is indispensable to obtain maximum benefits of 5S in an organization [7]. Without adequate knowledge, the effectiveness of 5S implementation is difficult to obtain [2]. Empirical evidence shows that there is a significant relationship between trained personnel in 5S implementation and organization performance in various sectors [8]. However, training courses and

programs are often conducted in a conventional way, such as through a one-way communication by means of seminars, lectures, and workshops [4]. Therefore, an IGB is proposed in this study as part of enhancement activities for an effective way of 5S training.

3 Use of IGB as Teaching and Learning Method of 5S

3.1 Development of IGB

The philosophy of 5S IGB is based on a real 5S implementation and could be embedded in a set of game board. In this study, the game board consists of nine main items or components as described in Table 1.

The IGB was designed and developed in a pentagon shape as shown in Fig. 1, which represents all of the five elements in 5S (sort, set-in-order, shine, standardize, sustain) and levels (initial stage of implementation, preparation and introduction, pre-audit, post-audit, improvement, self-sustain) of 5S. All items need to be distributed and spread out on the board to start the game. Then, the players are required to reorganize and rearrange each item. This activity emphasizes on sort, set-in-order, shine and standardization of items by referring to the status cards (question cards).

Meanwhile, there are three types of status cards (question) throughout all levels of IGB. Each level of the IGB has 24 cards (a total of 120 cards for all levels) as indicated in Table 2. The cards represent real 5S activities based on multiple choice questions, problem statement and open-ended questions. Thus, this helps the interaction among players, and subsequently promotes the concept of PBL. At this level, Collaborative Learning, Cooperative Learning and higher thinking skills were developed among players [9].

A closed-loop system has been used in this game where all players are given the opportunity to give their opinion, suggestion, arguments to obtain one decision. Meanwhile, an open-loop system is applied in the early stage including questions

Table 1 Main components of IGB

No	Item	Quantity
1.	Board base	1
2.	Phases triangle (large triangle)	5
3.	Starting triangle (small triangle)	5
4.	Rectangular shape tiles	40
5.	Status cards (question)	120
6.	Starting players (piece)	5
7.	Level piece	5
8.	Dice	1
9.	Status slots	5



Fig. 1 The 5S interactive game board (IGB) set

Table 2 Status cards (question) mapping

Type of question	Level				
	Inital	Pre	Post	Improve	Sustain
Multiple choice	1	1	1	2	1
Open ended	18	20	20	18	19
Problem statement	5	3	3	4	4
TOTAL	24	24	24	24	24

that are suitable for beginners or players who are in the early phase of gaining knowledge. Normally, a straight forward statement is considered an open-loop operation where players receive information, process understanding and then save it.

Through this activity, a player must answer the question taken from the status slot and the remaining players can argue or comment if the answer is incorrect. This creates interactive communication among players based on the problem given [10] and therefore a clear picture of 5S implementation could be seen. The game will be completed until all players have achieved the highest level or reached the final phase of sustain.

3.2 Concept of Learning for IGB

A series of questions for the IGB were formulated based on actual experience of 5S practice. The questions covered all components and levels of 5S implementation. Because of its ease of use, the authors believed that the game could suit with

various range of players, including from kindergarten, secondary and primary schools, college or universities, industries and firms.

Specifically, the difficulties level of the questions in the game were developed based on learning domains. The use of Bloom's Taxonomy in this game could significantly improve the understanding of the learning domain of the participants [3, 9]. In this study, three types of learning domains are stimulated towards the implementation of PBL, namely the cognitive, affective and psychomotor domain. It consists of low-order skills to higher-order skills [11, 12]. PBL is an educational strategy that helps one build the reasoning and communication skills necessary for success [4]. It educates players to actively contribute ideas and solutions to the problem. This could also transform the learning environment from passive to active [5].

3.3 *Playing the Game*

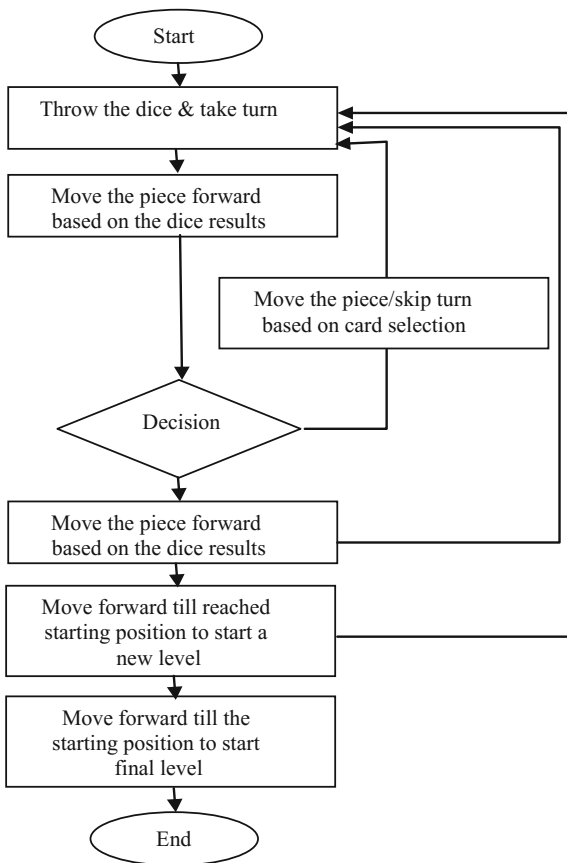
In one time, the game board could be played between two to five players in five different faces of pentagon shape. At the beginning, all players shall hold their own starting players (pieces) in different choices of color. Then, each piece must be placed on the phase triangle (large triangle) which is located at the center of the board. The piece is used to move to the next step or level in accordance to the results of the dice that was thrown earlier.

In this context, each player should place eight tiles on the board. However, only the red colored tile could be installed at any point of his/her place. The player needs to throw a dice and move his/her home according to the value of the dice. Once the home stays at the red colored slot, he/she must pick up a status card and answer the question. The game will keep on going until he/she decides the next step/movement, completes one cycle before shifting to the next level and finishes the game. The overall steps or sequences of playing the game are illustrated in Fig. 2.

4 Methodology

A set of questionnaires has been distributed to participants. The samples consist of trainees or students from local public and private universities. The survey questions were divided into five main parts, namely participants profile and background, general knowledge about 5S practice, previous understanding on 5S concept, experience in IGB and continuous improvement [13]. A four-point *Likert* scale (not good, moderate, good, outstanding) was used to rate the perspective of participants on the use of IGB. Meanwhile, descriptive analysis has been conducted to analyze and compare the data obtained from conventional and IGB methods.

Fig. 2 Flow of playing the 5S IGB



5 Results and Discussion

The feedbacks obtained from all respondents (n = 14) through questionnaire survey clearly demonstrate that IBG is an effective technique to improve understanding and enhance knowledge of the 5S practice among students in public and private universities. As depicted in Table 3, the background of respondents reveals that 50% of them have undergone 5S training and they have basic knowledge about the 5S practice. However, 71% of the trainees give responses that they were not fully satisfied with their level of 5S knowledge after attending 5S training through conventional methods including lectures, seminars and workshops.

Table 3 Background of respondents experiences in 5S (n = 14)

Item	Frequency	Percentage (%)
Basic knowledge of 5S practice	7	50
Unsatisfactory in conventional method	10	71

Meanwhile, Fig. 3 indicates the results of level of excitement between conventional method and IGB based on a three hours training period. Within the first hour of training, 79% of respondents stay focused on their 5S training by a conventional method, while 14% of them do enjoying themselves through IGB. However, the percentage of excitement reduced to 20% for a conventional method, whereas the level of excitement of participants using IGB increased to 50% for the next hour. The result apparently shows that the method of IGB for 5S training has potential influence in the evolution of teaching and learning concept.

Finally, the benefits of IGB as 5S training tools from the perspective of the payers based on survey questionnaires were presented. The overall result shows that 7% of the respondents perceived IGB as moderate, 86% as good and 7% of them described it as an outstanding method towards successful implementation of 5S practice as illustrated in Fig. 4. The benefits include increased motivation and curiosity of training, quick response for problem solving, improved knowledge of 5S implementation and increased interaction among players.

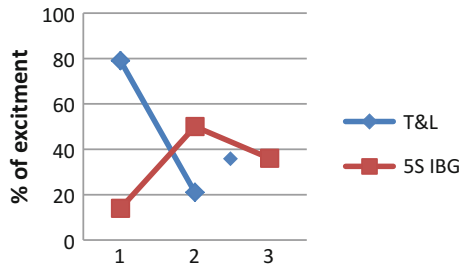


Fig. 3 Level of excitement by means of time between conventional method and IGB

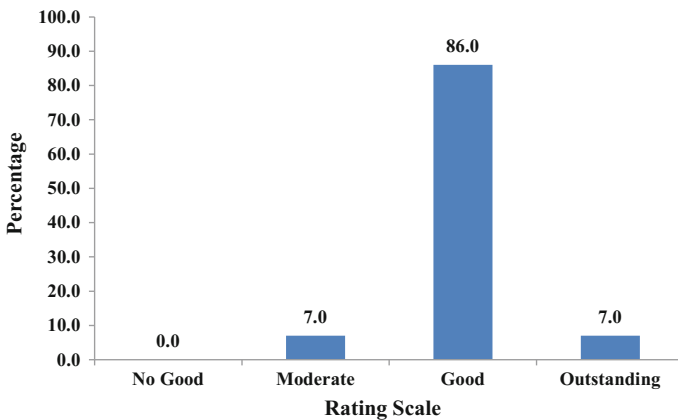


Fig. 4 Rating of 5S IGB given by participants

Specifically, they claimed that their knowledge is increased and able to teach others. They are also able to deliver good response in problem solving among players during the game. By playing the game, they have gained good and better knowledge of the 5S implementation because 5S management and audit criteria have been included in the game. In addition, the term “interactive” has been clearly defined during the game by means of interaction among players in contributing ideas, answers and explanation regarding the 5S implementation.

6 Conclusion

Systematic and effective training programs are crucial for the success of 5S implementation. This study introduces the IGB as an alternative for conventional methods to enhance the effectiveness of 5S training and learning. The proposed method comprises of preparation and planning, implementation, auditing and improvement activities based on the concept of PBL. In this context, a total of 14 students at local universities were randomly selected as sample for quantitative data collection through survey. The overall result reveals that the use of IGB could significantly improve student’s creativity, critical thinking and understanding of the 5S practice. Nevertheless, the sample size of the study should be increased in a future study to generalize the findings as well as to improve the physical construction of IGB for ease of use by different background of trainees.

Acknowledgements Special thanks to MPC Wilayah Utara auditor in providing comments and outstanding recommendations towards the creative method of enhancement of teaching and learning in 5S implementation.

References

1. Jiménez, M., Romero, L., Domínguez, M., del MarEspinosa, M.: 5S methodology implementation in the laboratories of an industrial engineering university school. *Saf. Sci.*, 163–172
2. Ab Rahman, M.N., Khamis, N.K., Zain, R.M., Deros, B.M., Mahmood, W.H.W.: Implementation of 5S practices in the manufacturing companies: a case study American. *J. Appl. Sci.* 7(8), 1182–1189 (2010)
3. Duch, B.J.: Why Problem Based Learning? A Case Study of Institutional Change in Undergraduate Education. Stylus Publishing, pp. 3–11 (2001)
4. Khamis, N., Ab Rahman, M.N., Jamaludin, K.R., Ismail, A.R., Ghani, J.A., Zulkiffi, R.: Development of 5S practice checklist for manufacturing industry. In: *World Congress on Engineering* (2009)
5. Lavin, A.M., Korte, L., Davies, T.L.: The impact of classroom technology on student behaviour. *J. Technol. Res.*, 1–13 (2010)
6. Aziz, W.A.W.A., Mat, A.C.: The effectiveness of implementation of 5S on employee motivation. *Bus. Soc. Sci. Rev.* 1(1), 41–52 (2011)

7. Liker, J.K., Hoseus, M.: *Toyota Culture: The Heart and Soul of The Toyota Way*. McGraw-Hill, New York (2008)
8. Ablanedo-Rosas, J.H., Alidaee, B., Moreno, J.C., Urbina, J.: Quality improvement supported by the 5S, an empirical case study of Mexican organisations. *Int. J. Prod. Res.* **48**(23), 7063–7087 (2010)
9. Sung, H.-Y., Hwang, G.-J.: A collaborative game-based learning approach to improving students' learning performance in science courses. *Comput. Educ.* **63**, 43–51 (2013)
10. Mina Tsay, M.B.: A case study of cooperative learning and communication pedagogy. *J. Sch. Teach. Learn.* 78–89 (2010)
11. Ghodrati, A., Zulkifli, N.: The impact of 5S implementation on industrial organizations. *Int. J. Bus. Manag. Invention.* 43–49 (2013)
12. Adams, N.E.: Bloom's taxonomy of cognitive learning objectives. *J Med Libr Assoc.* Jul **103** (3), 152–153 (2015)
13. Lingareddy, H., Reddy, G.S., Jagadeshwar, K.: 5S as a tool and strategy for improvising the work place. *Int. J. Adv. Eng. Technol.* **4**, 28–30 (2013)

Kinetic Modelling of a Particle Grinding Process in a Planetary Ball Mill Jar



Muhamad Husaini Abu Bakar, Ahmad-Fazireen Ahmad-Fauzi
and Nor Liyana Maskuri

Abstract This work is related to the kinetic modelling of mechanical milling. Many attempts have been made to simulate the kinetics of the milling process regarding ball velocity, friction force, and kinetic energy transferred during milling. The goal of this project is to fabricate a planetary ball mill jar and to defined the optimum parameter of planetary ball mill jar for milling processes by utilizing finite element analysis. By improving the design of the cylindrical jar with adding poles inside the jar, the graph shows that the kinetic energy becomes stable and is maintained. This happens because of the ball mill always bounces inside the jar reflection of the pole and the jar rotating on planetary gear while the jar design without pole only bounces because of jar rotation on the planetary gear. From the observation, the result, the cylindrical jar design without pole lost the kinetic energy because it only depends on the torque of the rotation jar on the planetary gear of the ball mill machine. The milling process takes 4 h, and the speed of the cylindrical ball mill jar with the pole is 250 rpm. The other parameter that have been utilized in this analysis is 100-g raw carbon, 4 pieces of steel balls with the diameter of 24 mm, and six-piece steel ball with the diameter of 19 mm. The particle has been measured by utilizing a telescopic microscope. The size reduction of the powder particles for a jar with pole and jar without pole is 69%.

Keywords Planetary ball mill · Kinetic modeling · Battery

M. H. Abu Bakar (✉) · A.-F. Ahmad-Fauzi · N. L. Maskuri
System Engineering and Energy Laboratory, Malaysian Spanish Institute—Universiti Kuala Lumpur, Kulim Hi-Tech Park, 09000 Kulim, Kedah, Malaysia
e-mail: muhamadhusaini@unikl.edu.my

A.-F. Ahmad-Fauzi
e-mail: ahmadfazireen@gmail.com

N. L. Maskuri
e-mail: nliyana.maskuri@s.unikl.edu.my

1 Introduction

Nano-powder materials have some possible way to engender weather by conventional or modern machines with incipient technology. Nowadays, the applications of nano-powder materials become more popular because of the current technology needs micro-sized components such as the application of nano-powder materials for lithium-ion batteries in the electric conveyance.

A planetary ball mill machine was developed to produce nano-powder material by utilizing the mechanical milling technique. A planetary ball mill machine consists of a planetary gear which is a sun gear, planet gear, and ring gear. The sun gear additionally kens as sun disc, and the jars rotate on the planet gear antithesis direction with the sun disc. However, the quality of the powder particle was the issue when the powder material becomes not uniform in size and the time for milling process was lengthy. By utilizing the kinetic modeling technique, the mentioned issues can be solved.

Ball milling is a mechanical process that enables the purposeful execution of physical and chemical transformations in powdered materials. The forces exerted on the ball in the jars, the friction resulting from the interactions between the ball and the jars, and the gravity drive the process. The ball inside the jars is considered as a point mass represented by the movement of its center of gravity. During the milling process carried out in the planetary mill, the impact velocity and the angle of impact has a significant effect on the energy transferred to the powder particle to be milled by the flying ball. Consequently, the movement and impact of the ball are important factors, on the inspection of which thorough mathematical studies have been carried out [1].

As an alternative to extensive experimental testing, deemed as expensive and time-consuming to the point of being most often unfeasible, a dynamic mechanical model of the planetary ball milling was adapted to fine tune milling parameters and to establish correlations with the end-product. This model, based on a simple contact scheme depending on a few easily assessable parameters, supplies quick and accurate predictions of the system efficiency under different operating conditions and is, in principle, valid for any material of interest.

The effect of jar and plate velocities was investigated, providing a detailed picture of the kinematics and dynamics of the milling bodies, together with a description of contact events, supporting an outright understanding of ball motion regimes. An assessment of the kinetic energy available, both along normal and tangential directions, was obtained and results were validated against experimental data [2].

2 Methodology

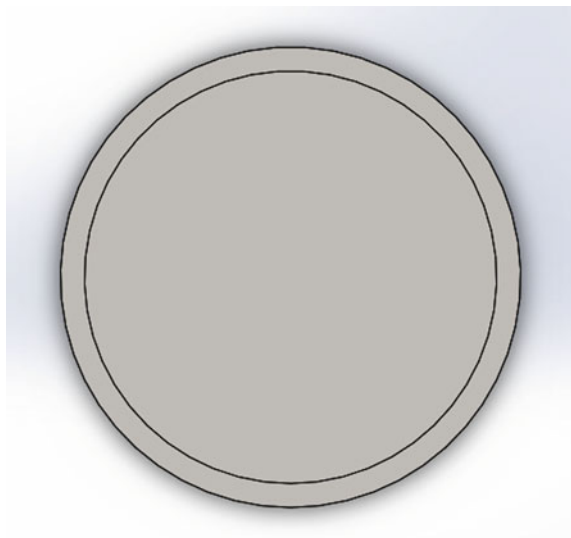
2.1 Jar Design

The cylindrical jar shape shown in Fig. 1 consists of a round shape of the jar. When the jar is rotated the ball inside the jar will rotate around the jar. However, the ball will change the direction when the balls meet the maximum angle of the inside of the jar because of jar rotation and the sun disc rotation. The balls change the direction to the opposite wall of the jar [1].

The cylindrical jar with pole shape shown in Fig. 2 consists round shape of the jar and three poles inside the jar. When the jar is rotated the ball inside the jar will rotate around the jar. Then, the steel ball additionally will hit the three poles inside the jar. The function of the three poles is to meet the maximum angle of the steel ball inside the jar and transmute the direction of the steel ball (Figs. 3, 4 and 5).

Motion studies are graphical simulations of the motion for assembly models. It can incorporate visual properties such as lighting and camera perspective into a motion study. Motion studies do not change an assembly model or its properties. They simulate and animate the motion prescribed for a model. By using this motion study, an analysis of energy and force can be completed. In this analysis, the kinetic energy of the ball mill will be measured by using this motion study. To analyze the kinetic energy, the selected CAD model need to be analyzed by the activated Solidworks Motion; the display was appearing similar to Fig. 6.

Fig. 1 Cylindrical jar without pole



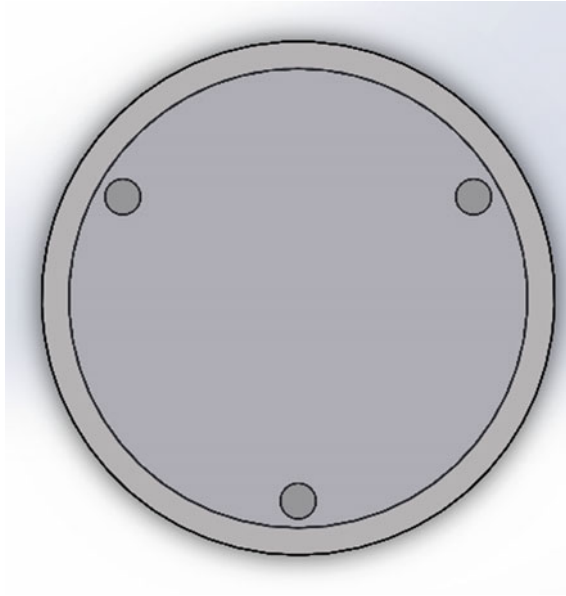


Fig. 2 Cylindrical jar with pole

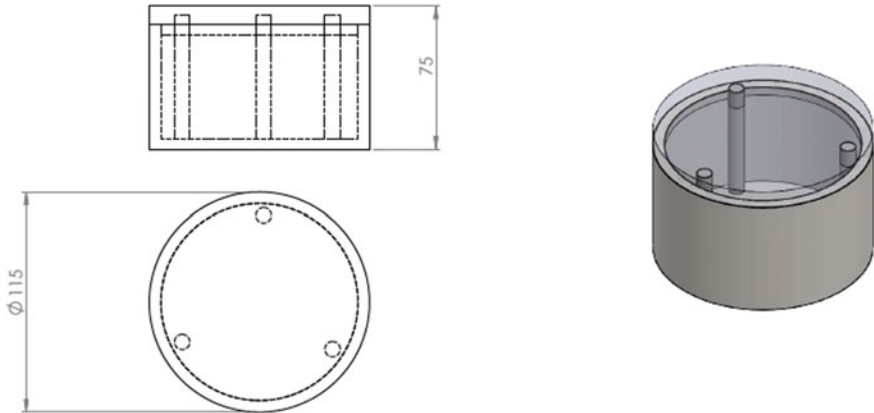


Fig. 3 Full assembly cylindrical jar with pole

To activate the motion, one needs to set up the direction of rotation of the motor and the speed of the motor as shown in Fig. 7.

Set the result to determine the kinetic energy, velocity, and another parameter as shown in Fig. 8. The parameter has been set as shown in Table 1.

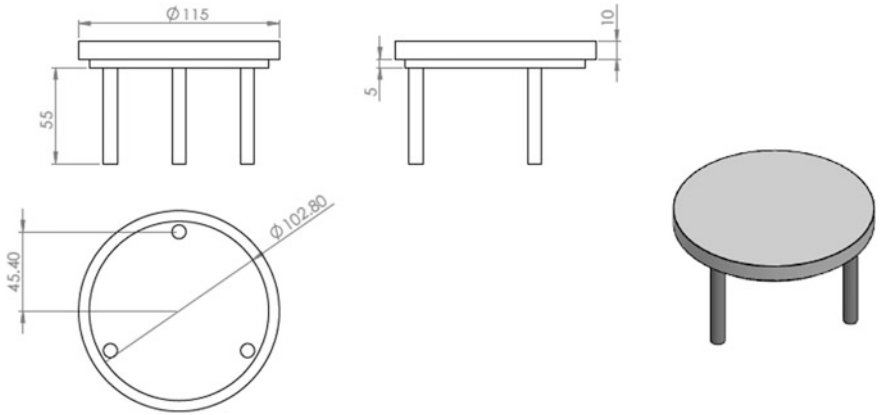


Fig. 4 Cylindrical jar cover with pole

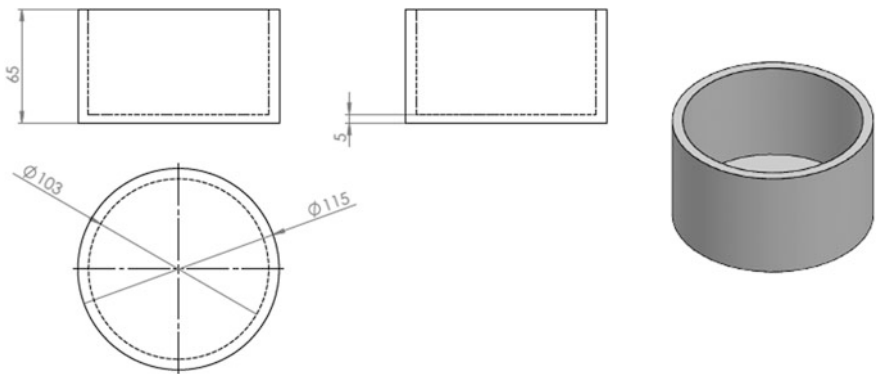


Fig. 5 Cylindrical jar

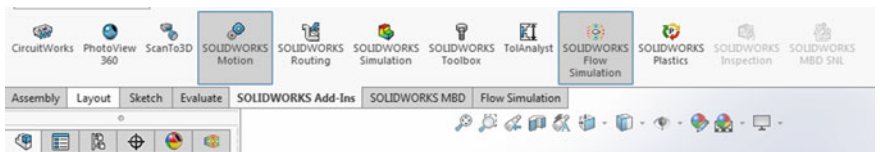
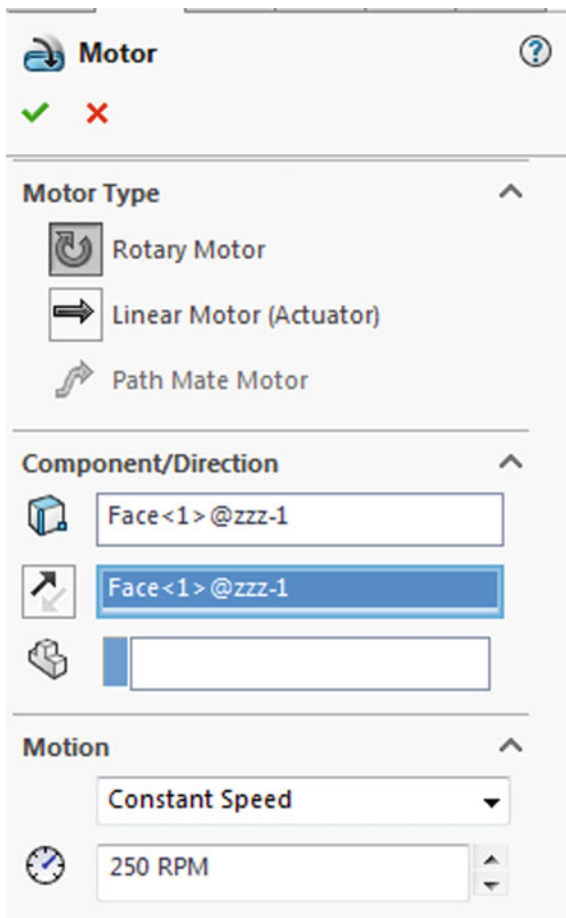


Fig. 6 Solidworks motion menu ribbon

3 Result and Discussion

The fabrication process needs to develop by a proper prototype model of the ball mill jar. Without the proper prototype model of the ball mill jar, the result of the powder particle cannot be defined. Besides, motion analysis also needs to develop

Fig. 7 Motor setup



to define the kinetic energy and another parameter of the cylindrical jar design. Also, an analysis of the powder particle size by using a microscope needs to be done because the size particle cannot measure with the naked eye.

3.1 Kinetic Energy

In this study, the revolution per minutes (rpm) of the jar which is 250 rpm for both jar designs and the jar size are same. All the data was interpreted utilizing Solidworks motion analysis. From the results shown in Fig. 9, the kinetic energies remain constant of both designs increases to 24 J at 14 s. After that, both kinetic energy constant until 22 s. Then the kinetic energy of the jar without pole drops rapidly until 0 J at 25 s while jar design with perpetual pole remains constant. Next, the kinetic energy of the jar without pole increases rapidly until 30 s at 24 J.

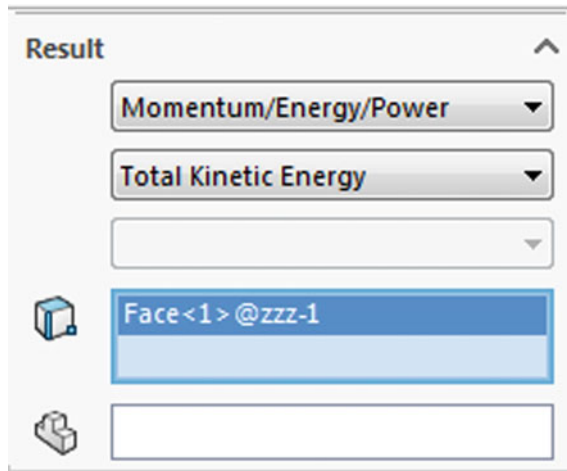


Fig. 8 Result of parameter

Table 1 Simulation parameter

Parameter	Cylindrical jar without a pole	Cylindrical jar with pole
Speed (rpm)	250	250
Time (sec)	30	30
Jar size (\emptyset)	103	103
Particle density (g)	100	100

From that, we can conclude that the kinetic energy was not stable and affected the result of the powder particle. The maximum kinetic energy from both designs is 24 J. The cylindrical jar without pole design has been re-designed by following the interior design. By improving the design of the cylindrical jar with integrating poles inside the jar, the graph shows that the kinetic energy becomes stable and is maintain. This transpires cause of the ball mill always bounce inside the jar reflection of the pole and the jar rotating on planetary gear while the jar design without pole only bounces because of the jar rotation on the planetary gear [3]. From the observation result, the cylindrical jar design without pole lost the kinetic energy because it only depends of the torque the rotation jar on the planetary gear of the ball mill machine.

3.2 *Ball Mill Velocity*

The ball mill inside the jar will smash the particle in the jar. When the balls smash the particle, the particle will break into a smaller particle. Figure 10 shows the

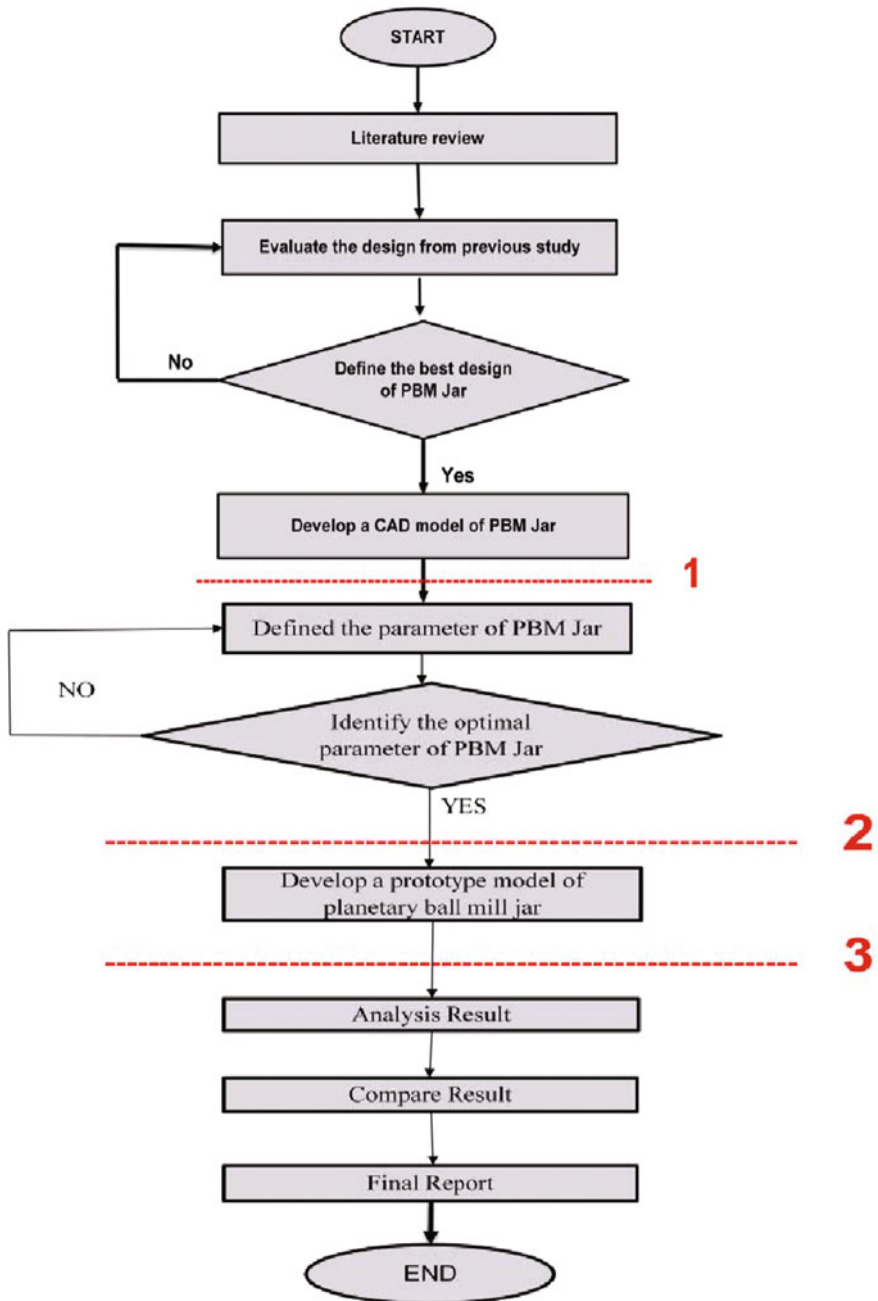


Fig. 9 Flow chart of the proposed methodology

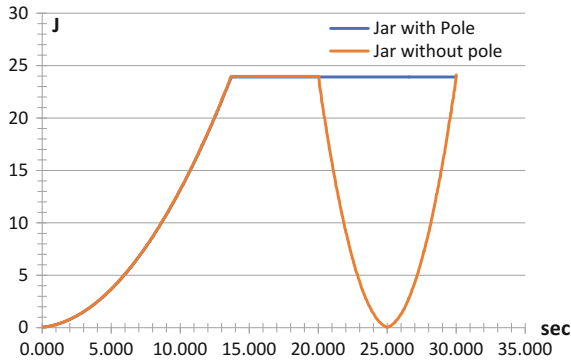


Fig. 10 Graph of kinetic energy

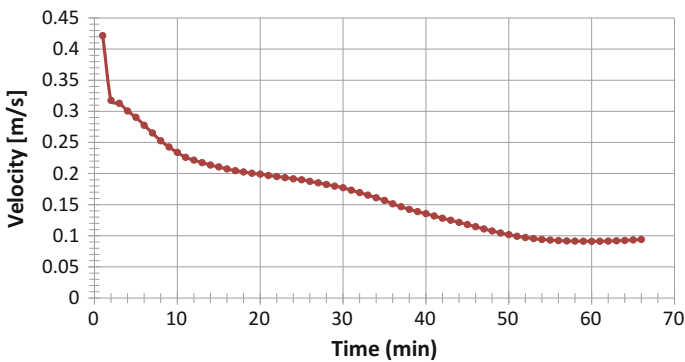


Fig. 11 Graph of velocity ball mill

velocity of the ball mill motion inside the cylindrical jar with poles. From this graph, the velocity of the ball mill decreases from time to time. This happens because particle inside the jar become a small particle. So that the speed of the ball and the velocity of the ball decrease. When the particle becomes smaller, the speed of the particle becomes slow because of the weight of a particle of light than the before the milling process. Also, the particle also will stick together and stick with the ball inside the jar.

3.3 Friction Force

When the particles become diminutive particles, the friction force between the ball mill and the jar surface will be affected. As shown in Fig. 11, the friction force becomes lower when the time of milling is increases. However, this graph shows

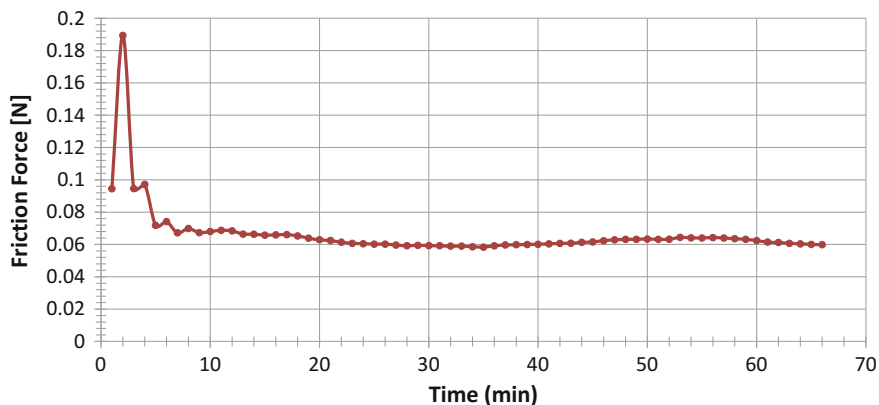


Fig. 12 Graph friction force between ball mill and jar

that the friction force is high at the early stages. What it causes of the particle size is astronomically immense, and the friction force between ball mill and jar surface is high. After a few minutes, the particle becomes smaller, and the friction force becomes lower because the particle will stick to the jar wall (Fig. 12).

3.4 Powder Particle Size

1. Carbon Before Milling Process

Carbon is taken from charcoal as shown in Fig. 13. The sized of carbon that was used before milling process by utilizing planetary the ball mill machine is around 10–15 mm. The carbon needs to be heated to ascertain the carbon is dry. If the



Fig. 13 Raw carbon before milling process

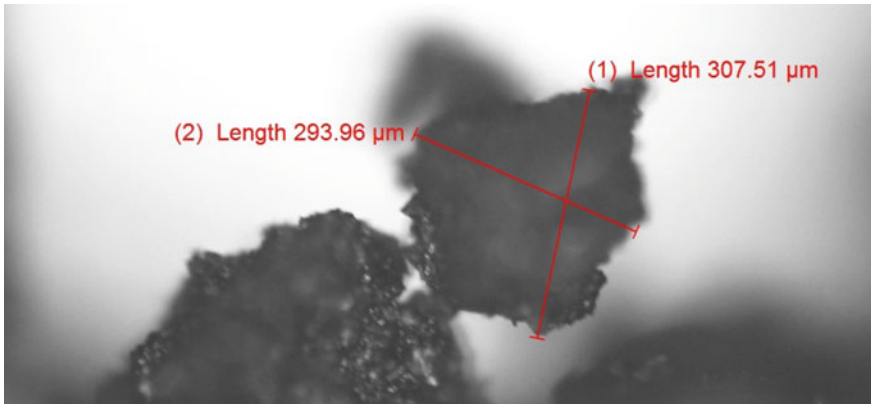


Fig. 14 Particle measure by telescopic microscope

carbon is wet, it will affect the quality and the size of the particle that has been milled. The way that has been used to dry the charcoal was filling into the chamber and put heat to the chamber.

2. 30 min Milling Process by Cylindrical Jar with Pole

From the result of the milling process that has been done by utilizing cylindrical ball mill jar with a pole, the result of powder particle has been defined. The milling process takes 30 min, and the speed of the cylindrical ball mill jar with the pole is 250 rpm. The particle has been quantified by utilizing a telescopic microscope as shown in Figs. 14, 15. The results that have been observed were around 175–433 μm . Next, when the milling process takes longer time the size of the particle becomes smaller and smoother.

3. 4 h Milling Process by Using Cylindrical Jar without Pole

From the result of milling process that has been done by the utilizing cylindrical ball mill jar without a pole, the result of powder particle has been defined. The milling process takes 4 h, and the celerity of cylindrical ball mill jar with the pole is 250 rpm. The particle has been quantified by utilizing telescopic microscope. The result that has been getting is around 108–206 μm in Figs. 16, 17.

4. 4 h Milling Process by Using Cylindrical Jar with Pole

From the result of the milling process that has been done by the utilizing the cylindrical ball mill jar with a pole, the result of powder particle has been defined. The milling process takes 4 h, and the speed of the cylindrical of the ball mill jar with the pole is 250 rpm. The results that have been observed are around 38–75 μm in Figs. 18, 19.

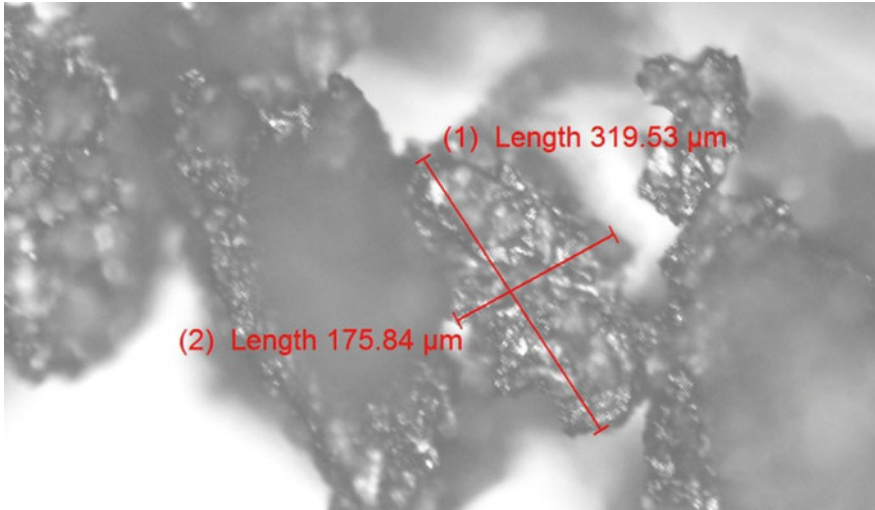


Fig. 15 Particle measure by telescopic microscope

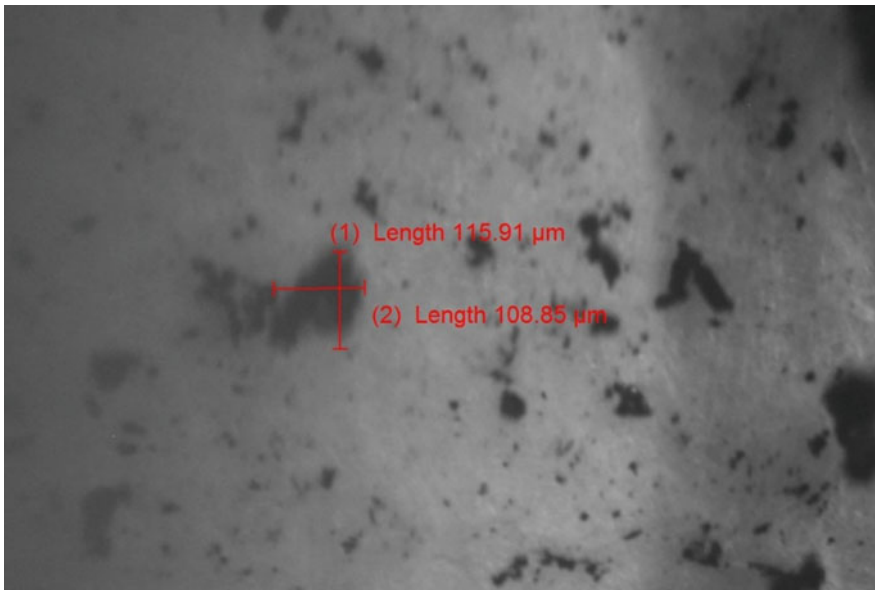


Fig. 16 Particle measure by telescopic microscope

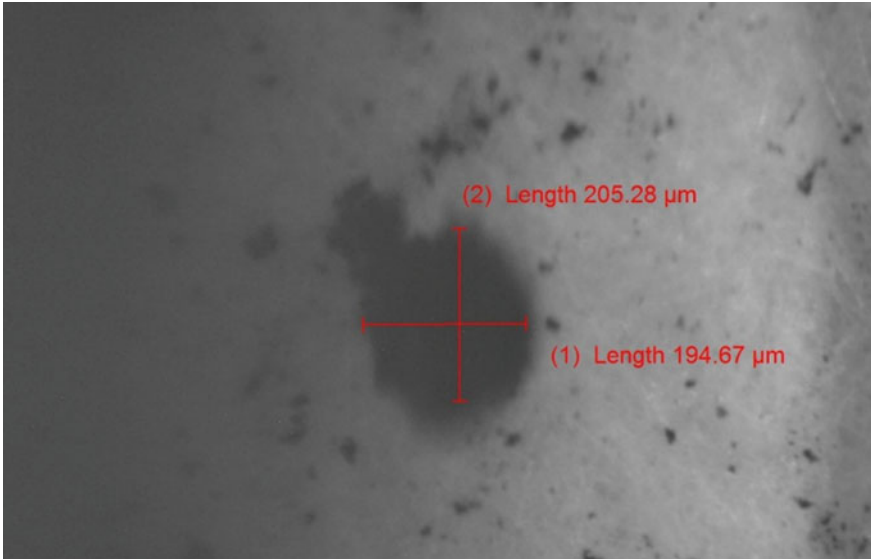


Fig. 17 Particle measure by telescopic microscope

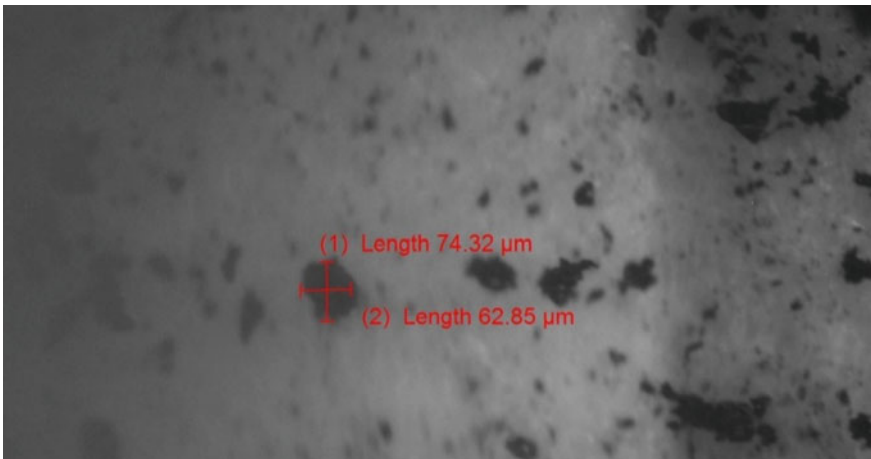


Fig. 18 Particle measure by telescopic microscope

5. Size Reduction Between Jar with Pole and Without Pole

From the graph shown in Fig. 20, the percentage of size reduction for a jar with pole and jar without pole is 69%. The cylindrical jar without pole shows that the size of particles is larger than a particle that was milled by utilizing cylindrical jar with a pole. This result from the fact that the ball inside the cylindrical jar with pole



Fig. 19 Particle measure by telescopic microscope

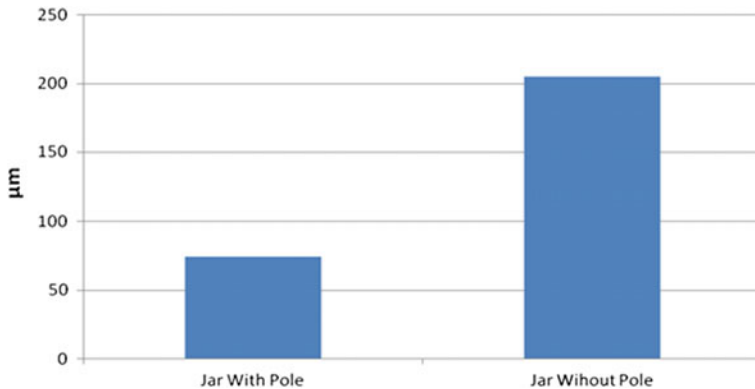


Fig. 20 Graph of powder particle

bounces more than the cylindrical jar without a pole. The ball inside the mill bounced more because of the pole inside the jar distracts the movement of the ball in the mill. The parameter of which is time, the weight of the material, number of steel ball and speed is constant. Time for milling process is 4 h, 100-g, four pieces steel ball in diameter of 24 mm, six pieces steel ball \varnothing 19 mm and speed is 250 rpm.

4 Conclusion

This analysis and research have successfully achieved the objectives by developing kinetic modeling for a ball mill jar. Regarding the analysis result, the following conclusion has been made that the cylindrical jar shape with pole gives more efficiency than the cylindrical jar shape without pole because the size reduction of the particle is 69% smaller. Also, the particle size will become smaller when the milling time is longer. Besides that, the shape of the jar affected the size and quality of the particle. The conclusion of this analysis, the cylindrical jar shape with pole gives more effect on the powder particle than the cylindrical jar shape without a pole. The kinetic energy of ball mill jar has been proposed and proven by the obtained result.

Acknowledgements All the experiment and analysis conducted by System Engineering and Energy Laboratory, Universiti Kuala Lumpur, Malaysian Spanish Institute, Kulim Kedah, Malaysia.

References

1. Kakuk, G., Zsoldos, I., Csanády, Á., Oldal, I.: Contributions to the modelling of the milling process in a planetary ball mill. *Rev. Adv. Mater. Sci.* **22**(1–2), 21–38 (2009)
2. Broseghini, M., D’Incau, M., Gelisio, L., Pugno, N.M., Scardi, P.: Effect of jar shape on high-energy planetary ball milling efficiency: simulations and experiments. *Mater. Des.* **110**, 365–374 (2016). <https://doi.org/10.1016/j.matdes.2016.06.118>
3. Broseghini, M., Gelisio, L., D’Incau, M., Azanza Ricardo, C.L., Pugno, N.M., Scardi, P.: Modeling of the planetary ball-milling process: The case study of ceramic powders. *J. Eur. Ceram. Soc.* **36**(9), 2205–2212 (2016). <https://doi.org/10.1016/j.jeurceramsoc.2015.09.032>

Large Eddy Simulation of Vehicle Aerodynamics Using Parallel Computational Fluids Dynamics



Abd-Munim Abd-Halim and Muhamad Husaini Abu Bakar

Abstract Large eddy simulation (LES) is used to study the flow around a simplified car model. The model consists of one bluff body slanted at the back-end. The LES was made at the Reynolds number of 0.51×10^6 based on the height of the rear model and the inlet air velocity. Four variants of the model were studied, one where the simulation was conducted with a single processor until combined all four processors to compute. The results of the LES simulations were used to analyze the flow field around the body and the back-end. Large vortical structures around the front box and in the gap were identified. The flow field analysis showed how these large vortical structures are responsible for the difference in the accuracy of drag force for the model that arises when the number of processors increase from one to eight processors along with different decomposing techniques.

Keywords Large eddy simulations · Parallel CFD · Aerodynamics

1 Introduction

The aerodynamic performance of road vehicles is an area in which improvements can be made even though there have been great achievements in the past half century. The aerodynamic forces that act on a vehicle during driving affect the operation of the vehicle in different ways. For commercial vehicles, overcoming the drag requires less fuel, that goes to overcome all the driving resistances (such as drag, rolling and climbing resistance) during cruising, when compared with a passenger car. The energy that can be saved for commercial vehicles by decreasing the aerodynamic drag is still apparent. Each simulation of a turbulent flow is

A.-M. Abd-Halim (✉) · M. H. Abu Bakar
System Engineering and Energy Laboratory, Malaysian Spanish Institute, Universiti Kuala Lumpur, Kulim Hi-Tech Park, 09000 Kulim, Kedah, Malaysia
e-mail: amunim.halim@s.unikl.edu.my

M. H. Abu Bakar
e-mail: muhamadhusaini@unikl.edu.my

performed for a particular purpose. The minimum goal is to determine the mean flow with acceptable precision. Further levels are the computation of higher moments or the determination of instantaneous unsteady features. Reynolds-Averaged Navier Stokes (RANS) models provide results for mean quantities with engineering accuracy at moderate cost for a wide range of flows [1]. An important feature of LES is the possibility of supporting LES models with mathematical analysis. A sound mathematical support is necessary for better understanding the advantages and drawbacks of turbulence models and it is also helpful for assessing the accuracy of computational results. Reducing the total time includes the time of developing the mesh from the computer-aided-design (CAD) model and simulation time is beneficial in order to perform large eddy simulation of complex geometries in an industrially relevant timeframe.

2 Methodology

2.1 Description of the Model

In the present work, LES simulations of the flow around the Ahmed-body are conducted. At a zero yaw angle, the flow physics will be explored around the model with square leading edges on the front body. The general dimensions of the model are shown in Fig. 1. In the round model, both the horizontal and vertical leading edges on the front box are rounded with the non-dimensional radius $0.08b$ which is the same as in the experiment. This necessarily extends the length of the front box for the round model by $0.08b$. The Reynolds number based on b and the free-stream velocity in the experiments was $Re = 0.51 \times 10^6$ and this is the same in the present simulations Figs. 2 and 3.

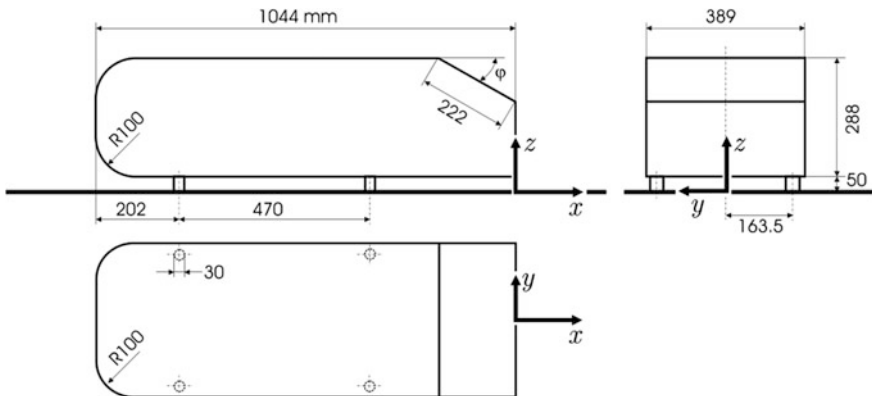


Fig. 1 Ahmed model dimensions are in mm

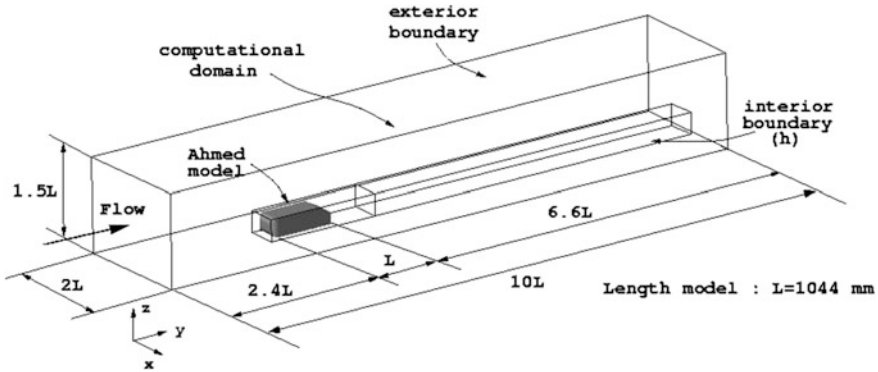


Fig. 2 Dimensions of the computational domain

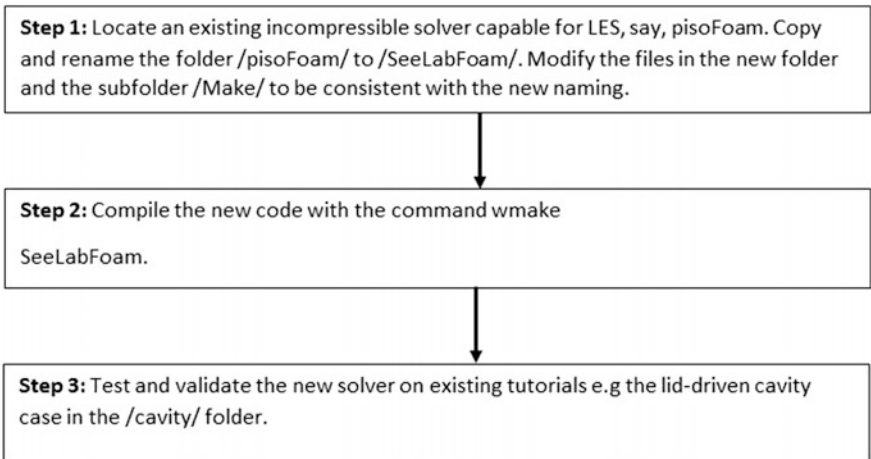


Fig. 3 Basic principle in steps 1–3 when implementing a new solver

3 Results and Discussion

From the simulations, one obtains the instantaneous and time-averaged flow fields around the body. According to the simulation, the flow field is affected by the model particularly at the edge of the body, which is noted to enhance the turbulence intensity locally. This is also seen from the instantaneous streamlines, where the flow can be seen to be separated at several positions after hitting model. The time-averaged streamlines reveal the forming of recirculation zones at the edge of the model. Similar patterns of reversed flow in the same region were observed also in the field experiment. Importantly, we note that the presence of the recirculation zone in the mean flow was not observed in the previous study Figs. 4 and 5.



Fig. 4 Slice at $z = 0$ for the mesh used on the Ahmed body. Three different zoom ratios

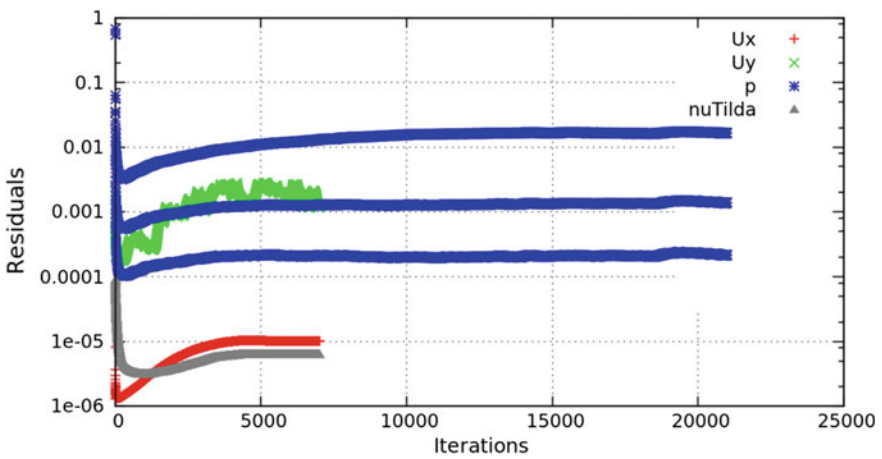


Fig. 5 LES approach converged to a suitable level of accuracy after just 5000 iterations

LES can more accurately model the turbulence that affects the value of the drag coefficient because of large eddy simulation is purposely developed to resolve larger scale turbulence.

For the front part, mean streamwise velocity profiles in the symmetry plane shows that the flow upstream of the body and in the freestream above is properly represented in the simulation. This is because in this region the level of turbulence is so low that the flow is nearly a potential flow Figs. 6 and 7.

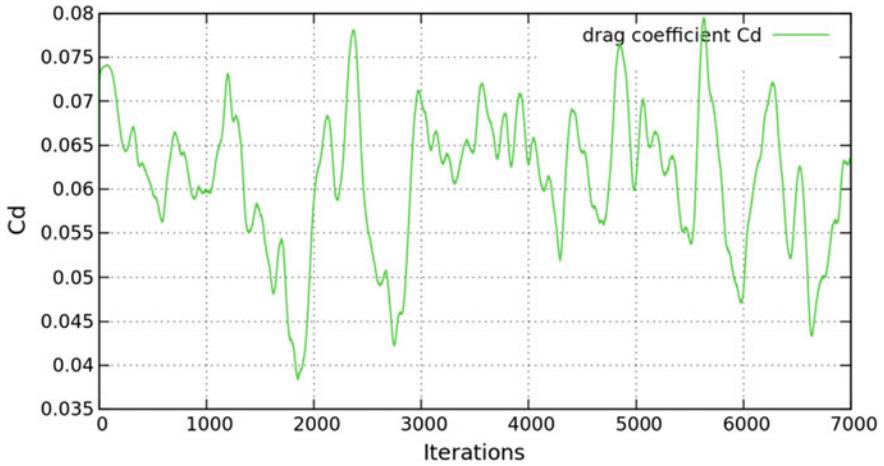


Fig. 6 Large eddy simulation drag coefficient

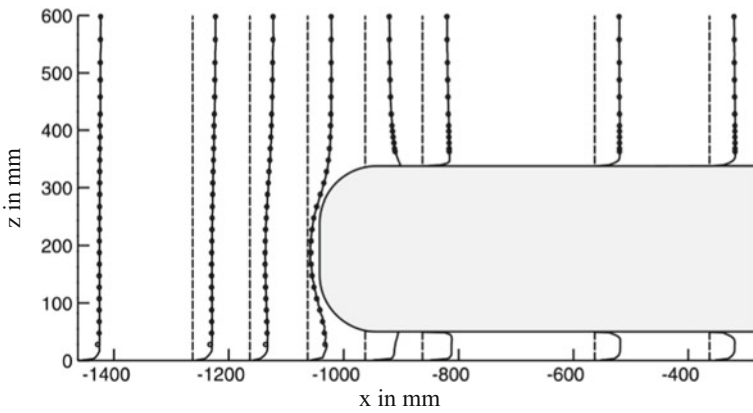


Fig. 7 Mean streamwise velocity profiles in the symmetry plane

Figure 8 shows the region of attachment/detachment and recirculation at the rear of the Ahmed model for the two slant angles of interest. The measurements were made along the plane of symmetry of the Ahmed model. The intention of this figure is to indicate the near wake flow fields.

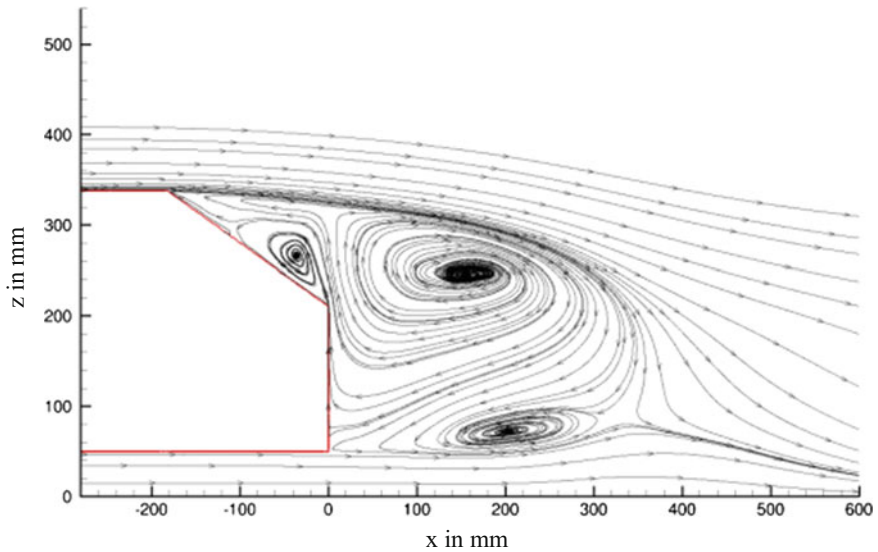


Fig. 8 The recirculating wake region and attached/detached flow

4 Conclusion

This paper presents the preliminary results of external flow on a simplified car body using the large eddy simulation approach, with validation from finite element analysis. The present work shows that LES can be used to gain knowledge about the flow structures around simplified models of cars which includes the variation of angle at the back-end of the body and shows how the flow structures affect the drag coefficient of the model. As conclusion it can be said that the computational cost depends on the number of processors used. Techniques, methods and algorithms for efficient implementations on parallel machines are largely developed. A strategic decomposition can provide more convenient results by developing algorithm in different size of blocks. The different computational work in some points essentially during the simulation process and the computational workload needs to be rearranged among processors more times during the evolution of the run to make the flow solver to operate. The relationship between the multiprocessors and the time elapsed to complete the simulation can clearly be seen as shown in the experimental results. The accuracy of the method could be further improved with a GPU (graphics processing unit) and more numbers of processors.

Acknowledgements Firstly, I am grateful to the Almighty God for the good health that is important in keeping me completing this technical paper. Next I would like to thank my supervisor, Dr. Muhamad Husaini for being a great mentor in giving guidance throughout the project duration. I take this opportunity to thank all the department faculty members for their help and

support in any way. Thanks to my parents and family as well for their never ending encouragement and support. I also place on record, my sense of gratitude to one and all, which directly or indirectly, have lend their hand in this venture.

Reference

1. Casey, M., Wintergerste, T.: European research community on flow, turbulence and combustion. In: ERCOFTAC Best Practice Guidelines: ERCOFTAC Special Interest Group on "Quality and Trust in Industrial CFD" (Version 1). London, England (2000)

Performance Characteristics of a Small Engine Fueled by Liquefied Petroleum Gas



Mohamad Shukri bin Mohd Zain, Shahril Nizam bin Mohamed Soid, Mior Firdaus bin Mior Abd Majid and Mohd Nurhidayat bin Zaelem

Abstract This paper presents the results of an investigation on the performance characteristics of a small spark ignition (SI) engine fueled by liquefied petroleum gas (LPG) to be compared with gasoline fueled. The LPG delivery systems used was fuel injection while carburetor was used for gasoline. In the experiment, wide open throttle (WOT) was run on a four stroke single cylinder engine that was coupled to a 20 kW generator dynamometer to measure the engine performance such as engine torque, and fuel consumption. Others parameters included are brake power (BP), brake specific fuel consumption (BSFC) and brake thermal efficiencies (BTH). The results were compared, analyzed and suggestions were made for modification for further improvement of using LPG in a small SI engine. It was found that the engine fueled by LPG had a lower performance compared to the gasoline fueled engine.

Keywords Engine · Internal combustion · Liquefied petroleum gas (LPG) Spark ignition (SI)

M. S. bin Mohd Zain (✉) · S. N. bin Mohamed Soid · M. F. bin Mior Abd Majid
M. N. bin Zaelem
Malaysian Spanish Institute, Universiti Kuala Lumpur, Kulim Hi-Tech Park,
09000 Kulim, Kedah, Malaysia
e-mail: mshukrimz@unikl.edu.my

S. N. bin Mohamed Soid
e-mail: shahrilnizam@unikl.edu.my

M. F. bin Mior Abd Majid
e-mail: miorfirdaus@unikl.edu.my

M. N. bin Zaelem
e-mail: mnurhidayat@unikl.edu.my

1 Introduction

Liquefied Petroleum Gas is obtained from the refining of petroleum, is quite flammable, and is normally used as fuel for cooking appliances. The use of LPG as fuel for vehicles started as early as 1912. A lot of cars and heavy duty vehicles have been using LPG either as propane, mixtures of propane and butane, or pure butane are going well. The engine lifespan is also longer when using LPG due to the lower quantity of sulfide that reduces the wear and tear of the engine [1]. Engine oil maintenance was also decreased due to longer changing periods [1]. During the last decade, LPG has been widely used on compression ignition (CI) engines due to its high octane number where it will produce less smoke and no smell or odor from its exhaust gas. LPG has a low carbon and high octane number, which produces lower carbon dioxide (CO₂) index emission as compared to gasoline and is better in terms of fuel economy [2]. The LPG composition will depend on its usage and will be different between parts of the world according to seasons, country, supply and so on. In automotive industries applications, LPG would have to comply with certain commercial standards.

LPG which mostly contains propane (C₃H₈) and butane (C₄H₁₀) is a mixture of hydrocarbons with various percentage from a mixture of both to pure propane and butane in the same container with specific ratio. LPG can be used in internal combustion engine (ICE) as its octane number is between 92 and 110 where our currently used gasoline is between 90 and 100 octane number [2]. It has a higher octane number (105) than gasoline (91–97), and therefore can be operated at higher compression ratio with increased efficiency [3]. It can be used as an alternative fuel for gasoline in internal combustion engines with minimum modification. LPG has a slightly lower performance due to its lower density and stoichiometric fuel-air ratio than gasoline at the same time reducing the specific fuel consumption and exhaust emission [3].

In a study conducted by Yoong and Watkins, simulation results confirmed that the use of LPG in internal combustion engines yielded a higher thermal efficiency and better fuel economy compared to unleaded gasoline. This is due mainly due to the higher octane rating which permits greater engine compression ratio without the occurrence of knocking [4]. Furthermore, LPG also has a higher heating value compared to other fuels and can be liquefied in a low pressure range of 0.7–0.8 MPa at atmospheric pressure [5].

Ceviz and Yuksel in their study on cyclic variation on LPG and gasoline fueled lean burn spark ignition (SI) engine have stated that LPG is a more suitable fuel for lean combustion engines compared with unleaded gasoline [6]. The fuel consumption is reduced compared to unleaded gasoline and this is due to the high energy content in the LPG fuel. The power output is slightly reduced in LPG operation as compared to unleaded gasoline due to the poor volumetric efficiencies effect [3]. There are several alternative methods to improve the performance for the engine fueled by LPG due to the losses of volumetric efficiencies. The present work is therefore carried out with the particular attention of comparing the performance

characteristics of a single cylinder four-stroke SI engine running on both gasoline and LPG. The experimental data obtained in this study are useful to establish and compare the performance of LPG and gasoline fueled engine.

2 Methodology

The experiments were conducted using an engine test bed. The engine used in the study is a Modenas 120cc, four-stroke spark ignition naturally aspirated. The engine specifications are listed in Table 1. Figure 1 shows the schematic of the engine test bed. The performance of the engine was measured for both gasoline and LPG. The data was obtained from the dynamometer under stabilized operating conditions with adequate fresh air supply to the engine. The test engine was analyzed for wide-open throttle (WOT) at a wide range of loads from 0 to 100%. This experiment was registered into two modes.

The first mode was registered for the engine with the gasoline fuel system, Fig. 1a, the second mode was registered for the engine with the LPG vaporizer, Fig. 1b. Engine load variation was realized with the help of the engine dynamometer load unit to measure the torque output and the engine power was calculated from the torque and engine speed data. Engine fuel consumption was measured using a weight scale.

Since the spark ignition engine is equipped with a carburetor, it has to be added with LPG conversion kits when running with gaseous fuel of LPG. The gaseous fuel injector was placed upstream of the carburetor inside the intake manifold of the engine and throughout the experiments the air control valve was fully opened. The position of the gaseous fuel injector caused minimal flow losses since the LPG was injected directly into the intake manifold during the entire experiments. The experimental set-up for both fuels is shown in Fig. 2. The engine was mounted to a test stand and the sprocket coupling was used to deliver power output from the engine to the Focus Applied Technology dynamometer model G7.5LC. The engine is started and warmed up at idling condition for ten minutes. A huge fan was

Table 1 Engine specifications

Description	Specifications
Engine type	4-stroke, singled cylinder, SOHC
Cooling system	Air cooled
Fuel system	Carburettor
Bore	55.0 mm
Stroke	50.6 mm
Cubic capacity	120cc
Compression ratio	9.8:1
Max. torque	9.1 Nm at 4500 rpm
Max. power	7.3 kW at 8500 rpm

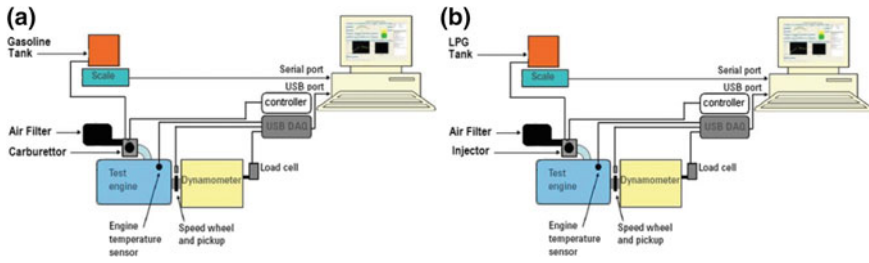


Fig. 1 a Schematic diagram of experimental set-up with gasoline fuel, b schematic diagram of experimental set-up with LPG fuel

arranged in the test room which supplied forced air on the engine for cooling purpose. Different parameters like torque, speed, and fuel consumption were recorded after the engines speed were maintained constant for two minutes. All measurements were made for all two modes for the engine speed range from 2000 to 6000 rpm.

3 Results and Discussion

All experiments were conducted at all above mentioned engine operating speeds to investigate the influence of LPG on the engine performance output variable compared to gasoline. The effect of LPG and gasoline on the engine performance is presented as brake power (kW) against engine speed (rpm) curve, and is shown in Fig. 3. The power obtained from LPG is less than for gasoline by 14.11% at 6000 rpm. It is clearly plotted in Fig. 3 that the engine fueled by LPG suffered on power produced compared to the engine fueled by gasoline. This is because the engine designed to operate on gasoline, obtains more power when gasoline is

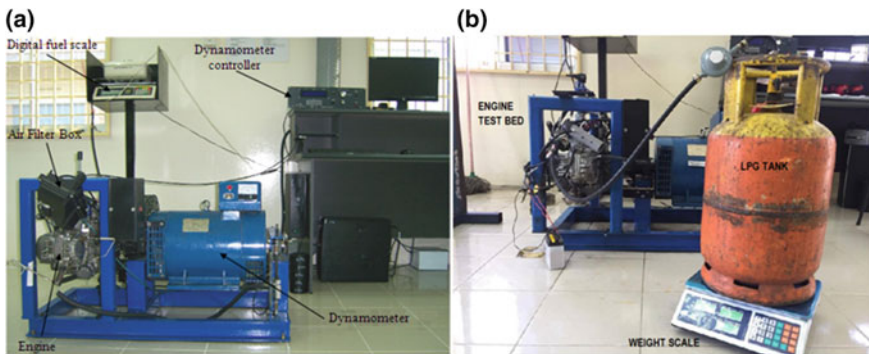


Fig. 2 a Engine test bed with gasoline fuel system, b engine test bed with LPG fuel system

applied. The power and torque produced from internal combustion engines mainly depend on the engine's cylinder mixture mass and type of fuel used. Therefore, the volumetric efficiency plays one of the most important roles when dealing with different properties of fuel with the same engine compared to the other engine parameters.

As the gasoline is the liquid fuel, therefore it enters to the combustion chamber as vapor, there will be an increase in intake mixture density and consequently in volumetric efficiency and it act as the cooling agent to the engine. Unlike the gaseous fuels like LPG, which are vapor at ambient temperature, not only have no cooling effect, but also are factor in decreasing the volumetric efficiency, due to larger volume of fuel in the inlet mixture [7]. In addition, ignition timing was not altered and remained constant throughout the study. Since LPG has a slower burning velocity than gasoline, an increase in the LPG fraction in gasoline would have resulted in a slower overall burning velocity. This needs the advancement of the ignition timing to avoid power loss due to the extended combustion duration.

Since the brake power is the function of torque and speed, it was expected that the maximum value of brake power peaks at higher speed than the maximum torque published by the manufacturer as provided in Table 1. The results show that as the engine speed was gradually increased, the torque contrarily decreased and it is clearly indicated that the engine fueled by LPG has less torque compared to gasoline. The engine torque (Nm) against engine speed (rpm) is shown on Fig. 4. Engine output torque peaks obtained from LPG is less than for gasoline by 8.34% at 4000 rpm.

Figure 5 illustrates the brake specific fuel consumption (BSFC) against the engine speed (rpm). The results show that as the engine speed was gradually increased, the BSFC decreased to a minimum value at an engine speed of 4000 rpm and then increased as the speed was increased to 6000 rpm. Since the BSFC is the

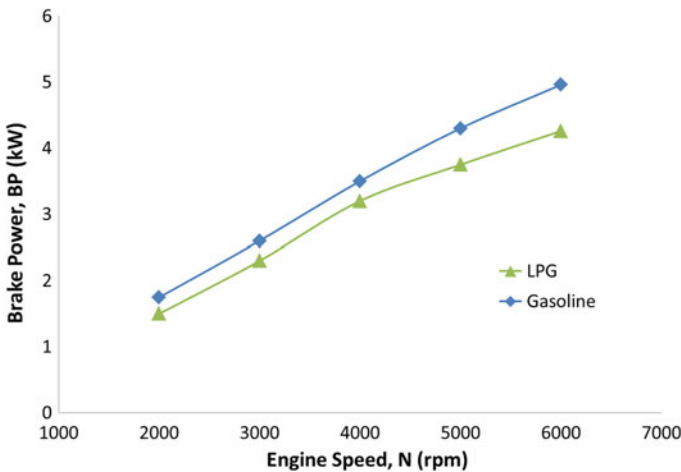


Fig. 3 Brake power (kW) versus engine speed (rpm)

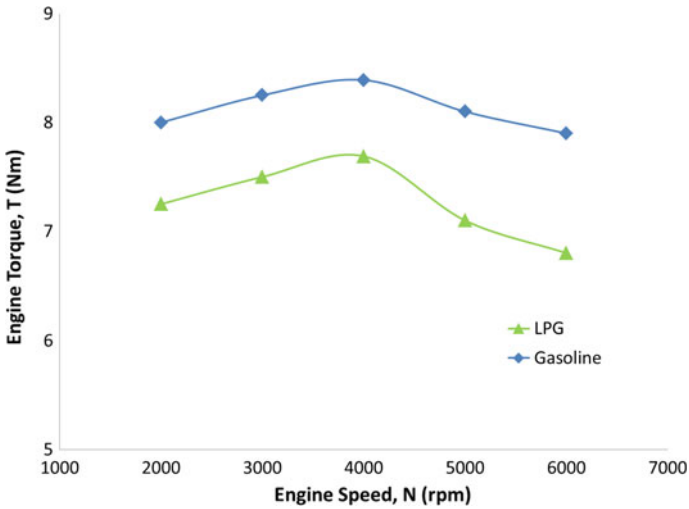


Fig. 4 Engine torque (Nm) versus engine speed (rpm)

measure of the “fuel economy”, lower BSFC should be the ultimate target in all engine designs, but the results of LPG obtained from this experiment is slightly higher and contrary with previous studies by other researcher. The difference of the minimum value of BSFC is 4.81% at 4000 rpm, and the BSFC of gasoline is lower than the BSFC of LPG. This phenomenon may be due to excessed LPG, which is injected to the intake manifold. It is a factor in decreasing the volumetric efficiency, due to larger volume of fuel in the inlet mixture.

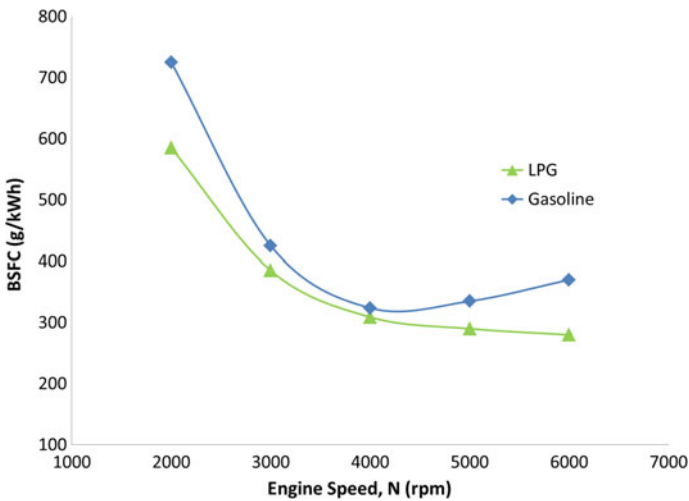


Fig. 5 Brake specific fuel consumption (BSFC) versus engine speed (rpm)

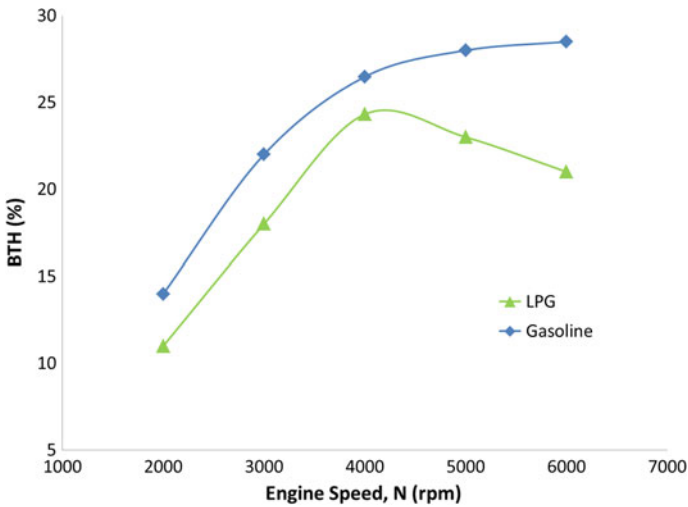


Fig. 6 Brake thermal efficiency (BTH) versus engine speed (rpm)

Figure 6 shows the efficiency map (brake thermal efficiency) for five values of the engine operating speed from 2000 to 6000 rpm. The peak brake thermal efficiency, BTH in LPG was reached at 4000 rpm and for gasoline at 6000 rpm. The difference of peak BTH at 4000 rpm is 8.16% and it shows that the BTH of gasoline is higher compared to LPG. This result is also contrary with previous studies. The higher heating value of LPG (46.4 MJ/kg) compared to gasoline (44 MJ/kg) should lead to a better BTH in engines fueled by LPG. Thus, at a given engine operational speed, the amount of heat released will be greater with the increase of LPG volumetric. This will subsequently lead to a higher engine brake thermal efficiency. Once again, this contrary result may be due to the excess amount of LPG, which was injected into the intake manifold during the experiments.

4 Conclusion

The performance of Modenas 120cc, single cylinder four-stroke engine fueled by LPG and gasoline have been experimentally evaluated. From the analysis of experimental results, it was found that the engine fueled by LPG experiences some degradation in performance when compared to the gasoline engine. As a conclusion, LPG produced lower engine performance compared to gasoline and it is suggested to perform the best setting for injector fuel mapping for LPG fueled engine to improve fuel consumption.

Acknowledgements I would like to give my highest praise to my entire colleague and who has directly or indirectly involved in this project. Also special acknowledge to Professor Dr. Horizon Walker Gitano Briggs for their lending of LPG conversion kits to Engine Performance Laboratory, Universiti Kuala Lumpur Malaysian Spanish Institute.

References

1. Bayraktar, H., Durgun, O.: Investigating the effects of LPG on spark ignition engine combustion and performance. *Energy Convers. Manag.* **46**, 2317–2333 (2005)
2. Yeom, K., Jang, J., Bae, C.: Homogeneous charge compression ignition of LPG and gasoline using variable valve timing in an engine. *Fuel* **86**, 494–503 (2007)
3. Erkuş, B., Sürmen, A., Karamangil, M.I.: A comparative study of carburation and injection fuel supply methods in an LPG-fuelled SI engine. *Fuel* **107**, 511–517 (2013)
4. Yoong, A.P.F., Watkins, A.P.: Study of Liquefied Petroleum Gas (LPG) Spray Modelling, ILASS-Europe 2001, Zurich (2001)
5. Lee, K., Ryu, J.: An experimental study of the flame propagation and combustion characteristics of LPG fuel. *Fuel* **84**, 1116–1127 (2005)
6. Ceviz, M.A., Yuksel, F.: Cyclic variation on LPG and gasoline-fuelled lean burn SI engine. *Renew Energy* **31**, 1950–1960 (2005)
7. Mustafa, K.F., Gitano-Briggs, H.W.: Liquid petroleum gas (LPG) as an alternative fuel in spark ignition engine: Performance and emission characteristics. In: 3rd International Conference on Energy and Environment (ICEE) 2009, Malacca (2009)

Machining Performance of AlSi/10% AlN Metal Matrix Composite Material in Milling Process Using Uncoated Insert



Nurul Na'imy Wan, Mohamad Sazali Said, Norzalina Othman, Ahmad Razlee Ab Kadir and Baizura Zubir

Abstract This paper presents the machining performance of aluminum silicon alloy (AlSi) metal matrix composite which has been reinforced with aluminum nitride (AlN) using the uncoated tool of inserts. Experiments were conducted at various cutting speeds, feed rates, and depths of cut, according to a fractional factorial array L_9 of Taguchi method for both cutting tools. Statistical analysis including the signal-to-noise (S/N) ratio and analysis of variance is applied to study the characteristic performance of cutting speeds, feed rates and depths of cut during the milling operation. The machining performances are observed through surface roughness, and tool wear and these measurements are analyzed using the Taguchi method. From the Taguchi analysis, it was found that cutting speed of 230 m/min, feed rate of 0.4 mm/tooth, a depth of cut of 0.3 mm were the optimum machining parameters for surface roughness and tool wear, indicated that lower level for all machining parameters gave the best result in machining of AlSi/10%AlN metal matrix composite.

Keywords Metal matrix composite · Milling process · Surface roughness Taguchi method

N. N. Wan (✉) · M. S. Said · N. Othman · A. R. Ab Kadir · B. Zubir
Malaysian Spanish Institute, Universiti Kuala Lumpur,
Kulim Hi-Tech Park, 09000 Kulim, Kedah, Malaysia
e-mail: nurulnaimy@unikl.edu.my

M. S. Said
e-mail: msazali@unikl.edu.my

N. Othman
e-mail: norzalina@unikl.edu.my

A. R. Ab Kadir
e-mail: ahmadrazlee@unikl.edu.my

B. Zubir
e-mail: baizura@unikl.edu.my

1 Introduction

Metal matrix composites (MMCs) are composite materials widely used in aerospace, automotive, electronics, and medical industries. These materials possess outstanding properties such as high strength, low weight, high modulus, low ductility, high wear resistance, high thermal conductivity, and low thermal expansion. These desirable properties are mainly manipulated by the matrix, the reinforcement element, and interface [1]. MMCs exhibit poor machinability because of the hard and abrasive reinforcement used [2]. These materials are usually applied in bearings, automobile pistons, cylinder liners, and piston rings, connecting rods, sliding electrical contacts, turbocharger impellers, and space structures. The most popular reinforcements are silicon carbide (SiC) and alumina (Al_2O_3). Aluminum, titanium, and magnesium alloys are commonly used as the matrix phase [1].

MMCs possess the combined properties of metals and ceramics [3, 4]. The structure and properties of MMCs are affected by the type and properties of the matrix, reinforcement, and interface [5]. Thus, these materials have been increasingly used to replace conventional materials in numerous applications [4]. Surface roughness has been given significant attention for many years [6] and has been considered in fatigue load, precision fits, fasteners hole, and aesthetic requirements. In addition to tolerance, surface roughness imposes one of the most critical aspects in the selection of machine and cutting parameter in the planning process [6, 7].

In general, optimization of the cutting parameters is determined by the researcher's experience and knowledge or by the Design of the Experiment (DOE) [8]. DOE is a powerful statistical tool used to study the effect of multiple variables simultaneously, and the technique provides an approach to efficiency design real-time experiments which will improve the understanding of the relationship between product and process parameters with the desired performance characteristic [9]. Also, a statistical analysis of variance (ANOVA) was performed to see which parameters were significant. The optimal cutting parameters were then predicted. Meanwhile, Taguchi's parameter design is an important tool for a robust design. It offers a simple and systematic approach to optimize designs for performance, quality, and cost.

Taguchi's approach is wholly based on the statistical design of experiments [10]. This can economically satisfy the needs of problem solving and product or process design optimization. Several previous works have used the Taguchi method as a design tool for experiments in various areas, including metal cutting, are listed in the references section [11, 12]. Factors should be included as many as possible; the method also can identify non-significant variables at the earliest possible opportunity. Taguchi creates a standard orthogonal array to accommodate this requirement. Depending on the number of factors, interactions, and levels needed, the choice is left to the user to select the standard, column-merging, or idle-column method, etc. Two of the applications, within which the concept of S/N ratio is useful, are the improvement of quality through variability reduction and the

improvement of measurement. S/N ratio characteristics can be divided into three categories; when the characteristic is continuous [10]:

$$\text{Nominal is the best characteristic; } S/N = 10 \log \frac{\bar{y}}{s_y^2} \tag{1}$$

$$\text{Smaller is better characteristics; } S/N = -10 \log \frac{1}{n} \left(\sum y^2 \right) \tag{2}$$

$$\text{Larger is better characteristics; } S/N = -10 \log \frac{1}{n} \left(\sum \frac{1}{y^2} \right) \tag{3}$$

2 Methodology

2.1 Surface Roughness and Tool Wear Measurement

In machining process, it is necessary to obtain a good surface finish on the surface of the material, whereby for tool wear can be measured through machining time for a tool of an insert used to wear at the certain height. These surface roughness and tool wear values are measured through various cutting speeds, feed rate and depth of cut are shown in Table 1.

2.2 Materials and the Milling Process

AlN reinforced Al–Si alloy matrix composite was fabricated using the stir casting method, where Al–Si alloy ingot, called the matrix material, was reinforced with AlN particles of 10wt% reinforcement. The experimental study was carried out in a CNC Vertical Milling Center Lagun-GVC1000 milling machine. Cutting inserts were attached to the tool with a body diameter of Ø20 mm. The tool holder used was CoroMill R390-020C4-11L and the tool inserts was uncoated cemented carbide ISO catalog no: R390-11T08E-NL. The experiment has three different cutting speeds (230, 300 and 370 m/min) with constant feed rate (0.4, 0.6, 0.8 mm/rev) and depth of cut (0.3, 0.4 and 0.5 mm) under dry cutting condition. The worked material was fabricated in the form of block 120 mm length × 50 mm width × 50 mm thickness.

Table 1 Factors and levels used in the experiment

Factor/level	Low	Medium	High
A—cutting speed (m/min)	230	300	370
B—feed rate (mm/tooth)	0.4	0.6	0.8
C—depth of cut (mm)	0.3	0.4	0.5

2.3 Taguchi Method

In this experiment, with three factors (each with three levels), the fractional factorial design used was a standard L_9 (3^3) orthogonal array. The orthogonal array was chosen because of its minimum number of required experimental trials. Each row of the matrix represented one trial [13]. The smaller, the better characteristic is used to optimize the surface roughness and for the tool wear measurement is analyzed using the larger, the better characteristic in the milling process of aluminum silicon metal matrix composite.

3 Results and Discussion

3.1 Machining Performance and S/N Ratio

Machining performance of AlSi/10%AlN was analyzed based on the Taguchi method and S/N ratio as in Table 2. The surface roughness was analyzed according to Taguchi's smaller-is-better characteristic while the analysis for tool wear was conducted using the larger-is-better characteristic.

3.2 Optimization of Machining Conditions Using the Taguchi Method

This study was conducted to determine the optimum condition for surface roughness and tool wear when AlSi/10%AlN metal matrix composite is cut using uncoated. In Taguchi method, the analysis focuses on process optimization through

Table 2 Experimental design with the L_9 orthogonal array and the S/N ratios for Uncoated cutting tools

Test no.	Cutting speed	Feed rate	Depth of cut	SR (μm)	S/N ratio	Tool wear (min)	S/N ratio
1	230	0.4	0.3	0.430	7.33063	75.33	37.5394
2	230	0.6	0.4	0.528	5.54732	82.43	38.3217
3	230	0.8	0.5	0.702	3.07326	94.59	39.5169
4	300	0.4	0.4	0.648	3.76850	67.86	36.6323
5	300	0.6	0.5	0.785	2.10261	66.31	36.4316
6	300	0.8	0.3	0.842	1.49376	82.02	38.2784
7	370	0.4	0.5	0.791	2.03647	50.79	34.1156
8	370	0.6	0.3	0.848	1.45259	47.95	33.6158
9	370	0.8	0.4	0.907	0.84785	75.61	37.5716

S/N ratio, and the result will be supported by the analysis of variance. Both analyses for surface roughness and tool wear using the uncoated tool obtained using Minitab 17.

3.3 Surface Roughness

Figures 1 and 2 show the mean S/N ratio and means of surface roughness using uncoated tool obtained. The slope of the graphs clearly shows that the cutting speed is the most significant factor, followed by the feed rate, and depth of cut. Based on Fig. 1, the optimum parameters for surface roughness is cutting speed of 230 m/min; feed rate of 0.4 mm/tooth and depth of cut of 0.3 mm. It indicated that the best surface finish in the milling process of AlSi/10%AlN was at the lower level of the machining parameters.

3.4 Tool Wear

Figures 3 and 4 show the mean S/N ratio and means of tool wear using the uncoated cutting tool in the milling process. The slopes of the graphs also clearly show that the cutting speed is the most significant factor, followed by the feed rate and depth of cut. Based on Fig. 3, the optimum parameters for surface roughness is disclosed at cutting speed of 230 m/min; feed rate of 0.8 mm/tooth and depth of cut of 0.4 mm.

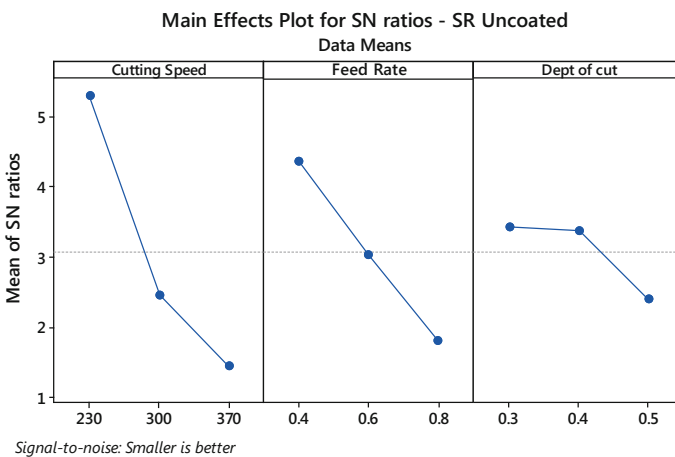


Fig. 1 Main effect plot for S/N ratios of surface roughness

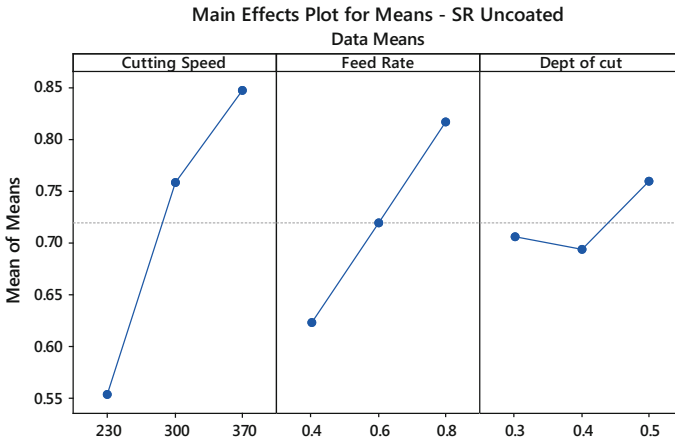


Fig. 2 Main effect plot for means of surface roughness

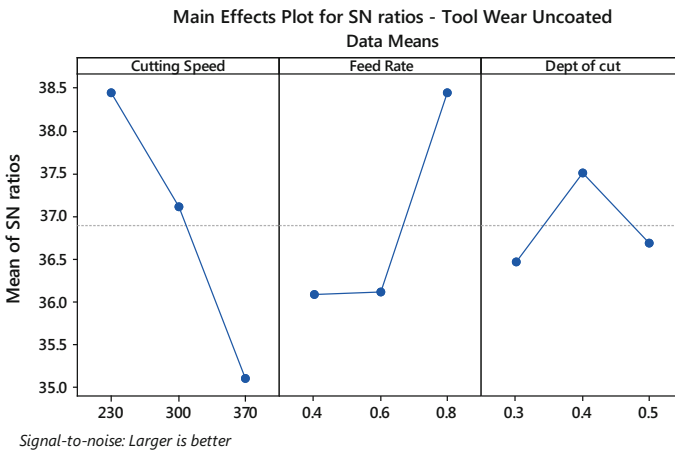


Fig. 3 Main effect plot for S/N ratios of tool wear

3.5 Analysis of Variance (ANOVA)

The analysis of variance was conducted to determine which machining parameters significantly affect the tool life. ANOVA was performed to find whether individual factors that affect the material removal rate and cutting force were meaningful. From the ANOVA results of S/N ratio presented in Table 3, the factor of feed rate and depth of cut significantly affected the surface roughness of AlSi/10%AlN composite which its P-value were less than 0.05. From Table 3, the most influential factor was found to be the depth of cut with 65.72%, followed by feed rate with

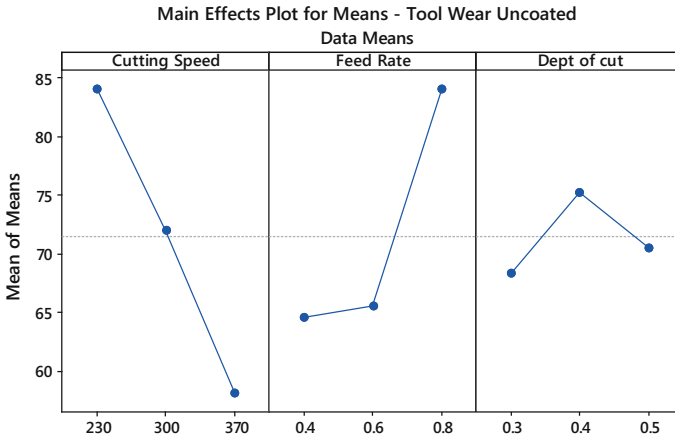


Fig. 4 Main effect plot for means of tool wear

Table 3 ANOVA of S/N ratio for surface roughness

Factors	DF	SS	MS	F	P*	PD
Cutting speed	2	24.1984	12.0992	36.34	0.027	65.72
Feed rate	2	9.9416	4.9708	14.89	0.063	27.00
Depth of cut	2	2.0128	1.0064	3.01	0.249	5.67
Residual error	2	0.6677	0.3338			1.81
Total	8	36.8205				100

DF Degree of freedom, SS sum of square, MS mean of square, PD percentage distribution

*Significance level = 0.05

27.00% and the remaining percentage were explained by cutting speed and residual error. This contribution has been supported by the value of S/N ratios in Table 4.

Tables 5 and 6 represented the ANOVA results and response values of S/N ratio for tool wear. Based on Table 5, the factor of cutting speed and feed rate significantly affected the tool wear in the machining process of the composite as its P-value was less than 0.05. Based on the percentage contribution from Table 4, the most influential factor was found to be the cutting speed with 56.27%, followed by feed rate and depth of cut with 36.15 and 5.85% respectively.

Table 4 Response table for S/N ratios (smaller is better) of surface roughness

Level	Cutting speed V (m/min)	Feed rate f (mm/tooth)	Depth of cut d (mm)
1	5.317	4.379	3.426
2	2.455	3.034	3.388
3	1.446	1.805	2.404
Rank	1	2	3

Table 5 ANOVA of S/N ratio for tool wear

Factors	DF	SS	MS	F	P*	PD
Cutting speed	2	17.1408	8.5704	32.50	0.030	56.27
Feed rate	2	11.0109	5.5055	20.87	0.046	36.15
Depth of cut	2	1.7797	0.8899	3.37	0.229	5.85
Residual error	2	0.5275	0.2637			1.73
Total	8	30.4589				100

DF Degree of freedom, SS Sum of square, MS Mean of square, PD percentage distribution

*Significance level = 0.05

Table 6 Response table for S/N ratios (larger is better) of tool wear

Level	Cutting speed V (m/min)	Feed rate f (mm/tooth)	Depth of cut d (mm)
1	38.46	36.10	36.48
2	37.11	36.12	37.51
3	35.10	38.46	36.69
Rank	1	2	3

4 Conclusion

The Taguchi method was applied in experimental design to optimize multi-response process parameters of end milling, while the machining of AlSi/AlN MMC was optimized using an L_9 orthogonal array. The results of this study were drawn based on the experiments. The optimum machining parameters found for surface roughness were: cutting speed, 230 m/min; feed rate 0.4 mm/tooth; and depth of cut, 0.3 mm; and the optimum parameters for tool wear were: cutting speed, 230 m/min; feed rate 0.8 mm/tooth; and depth of cut, 0.4 mm. These optimum parameters obtained will help the automotive industry to have a competitive machining operation from economic and manufacturing perspective.

References

1. Srinivasan, A., Arunachalam, R.M., Ramesh, S., Senthilkumaar, J.S.: Machining performance study on metal matrix composites—a response surface methodology approach. *Am. J. Appl. Sci.* **9**(4), 478–483 (2012)
2. Chandrasekaran, M., Devarasiddappa, D.: Development of predictive model for surface roughness in end milling of Al-SiCp metal matrix composites using fuzzy logic. *World Acad. Sci. Eng. Technol.* **68** (2012)
3. Tomadi, S.H., Ghani, J.A., Haron, C.H., Daud, A.R.: Optimization of cutting parameter on tool life and surface roughness in end milling of AlSi/AlN MMC. In: *Taguchi Method and Grey Relational Analysis ICRQE 13, Proceeding* (2013)

4. Abdullah, Y.: Fabrikasi dan pencirian komposit Al-Si diperkuat zarah halus SiC dengan menggunakan tuangan anduk. Universiti Kebangsaan Malaysia, Bangi, Selangor (2009)
5. Hari Babu, N., Fan, Z., Eskin, D.G.: Application of external fields to technology composite materials. In: TMS2013 Annual Meeting Supplemental Proceedings TMS
6. Tomadi, S.H., Ghani, J.A., Che Hassan, C.H., Daud, A.R.: Effect of machining parameter on tool wear and surface roughness of Al-AlN reinforce MMC in end milling machining. *J. Eng. E-trans. (ISSN 1823-6379) Electron. J. Univ. Malaya (EJUM)* (2011)
7. Wang, X., Feng, C.X.: Development of empirical model for surface roughness prediction in finish turning. *Int. J. Adv. Manuf. Technol.* **20**(5), 348–356 (2002)
8. Tomadi, S.H., Ghani, J.A., Che Hassan, C.H., Daud, A.R.: Optimisation of cutting parameters for End Milling AlSi/AlN metal matrix composite using the Taguchi method. *Mater. Sci. For.* **773–774**, 437–444 (2014)
9. Radika, N., Subramaniam, R., Babudeva Senapathi, S.: Machining parameter optimization of an aluminium hybrid metal matrix composite by statistical modelling. *Ind. Lubr. Technol.* **65**(6), 425–435 (2013)
10. Park, S.H.: *Robust Design and Analysis for Quality Engineering*. Chapman and Hall, London (1996)
11. Yang, W.H., Tarng, Y.S.: Design optimisation of cutting parameters for turning operations based on the Taguchi method. *J. Mater. Process. Technol.* **84**, 122–129 (1998)
12. Lin, T.R.: Experimental design and performance analysis of TiN-coated carbide tool in face milling stainless steel. *J. Mater. Process. Technol.* 1–7 (2002)
13. Jaharah, A.G., Choudhury, I.A., dan Hassan, H.H.: Application of Taguchi method on the optimization of end milling parameters. *J. Mater. Process. Technol.* **154**, 84–92 (2004)

Numerical Investigation of Magneto-hydrodynamics in a Magnetic Peristaltic Pump



Faizah Osman and Muhamad Husaini Abu Bakar

Abstract This paper presents a finite element analysis and a two-dimensional computational fluid dynamics (CFD) simulation for a magnetic peristaltic pump. In this paper, we attempted to summarise the most important results, and the purpose of this study is to establish ideas on magneto-hydrodynamic (MHD) turbulence in flows of a magnetorheological (MR) fluid containing inside the tube of a magnetic peristaltic pump. A finite element method magnetics (FEMM) analysis was used as a tool to design the geometry in order to determine the magnetic fields occurred due to the different currents applied to the magnetic peristaltic pump. Moreover, the purpose of this study is to develop a numerical tool that is able to simulate MR fluid flow and determine the effect of the applied magnetic field effect on the flow velocities by using the Open Source Field Operation and Manipulation (OpenFOAM) software. The uniform transverse external magnetic fields are applied perpendicular to the flow direction. It was observed that an increase in the magnetic field leads to a decreased flow velocity. Results are obtained from the numerical study and are plotted graphically and discussed in the present paper.

Keywords Magneto-hydrodynamics (MHD) · Magnetic peristaltic pump
Magnetorheological (MR) fluid · Magnetic fields effect · Velocities

1 Introduction

Magneto-hydrodynamics (MHD) is the flow of a fluid which is conducting an electric flow in the presence of an electromagnetic field. The word *magneto-hydrodynamics* is composed of the words *magneto* meaning magnetic, *hydro* meaning

F. Osman (✉) · M. H. Abu Bakar
System Engineering and Energy Laboratory, Malaysian Spanish Institute,
Universiti Kuala Lumpur, Kulim Hi-Tech Park, 09000 Kulim, Kedah, Malaysia
e-mail: faizah.osman23@s.unikl.edu.my

M. H. Abu Bakar
e-mail: muhamadhusaini@unikl.edu.my

water (or liquid) and *dynamics* referring to the movement of an object by forces. The main point of the MHD theory is that conductive fluids that can support magnetic fields with the presence of magnetic fields lead to forces that in turn act on the fluid (typically a plasma), thereby potentially altering the geometry and strength of the magnetic fields themselves [1].

There are a lot of smart fluids that are used in the study of liquid metal fluid flow. One of it is the magnetorheological (MR) fluid. MR fluids are smart and controllable materials. They are a mixture of micro-sized magnetic particles randomly dispersed in the liquid such as hydrocarbon and silicon oil [2]. The micro-sized magnetic particles become magnetised when an external magnetic field is applied to them. They can move and align themselves like chain with the direction of the magnetic field [3]. MR fluid are categorized in groups depending on the controlled liquid. The fluid usually increases its apparent viscosity, to becoming a viscoelastic solid. When the fluid is in the active state, i.e. the magnetic force is used, the yield stress of the fluid can be controlled by converting the magnetic field strength. There are three different modes of MRF operation: the valve mode, the direct shear mode and the squeeze mode [4].

The study of a conducting liquid metal fluid flow under a transversely applied magnetic field has become the basis of many scientific and engineering applications and in many devices such as MHD pumps, MHD power generation and others else [5]. The project's idea is to use a MR fluid in a magnetic peristaltic pump and to observe the behavior of the fluid when it is opposed to the magnetic field. Peristaltic pumps are mechanical displacement pumps. They induce flow within a fluid-filled flexible tube through forwarding travelling wall contraction. Peristaltic pumps are available in a variety of configurations, usually comprising rotating tube displacement/contraction, driven by a step motor that moves several circularly arranged rollers [6]. The peristaltic effect can be maintained by adding different values of magnetic field tested on the fluid to determine their electrical conductivity and their orientation.

Nowadays the fluid flow inside a pump is was modelled using analytical approaches in order to explain the behavior of the fluid. Understanding of MR fluid flow inside the channel is significantly improving the design process of the peristaltic pump. Since the use of this smart material is growing, it is essential to study its behavior. However, the modelling is complicated due to the fact that the behavior is considered as magneto-hydrodynamic where the conducting fluid is moving across the magnetic field. The geometry of the pump is also complex and makes the analytical solution almost impossible. The combination of channel geometry, fluid flow rates, diffusion coefficients and possible chemical interaction are extremely complex. Thus, the behavior of this particular system and the visualisation of complex phenomena are quite complicated to predict through numerical modelling.

Besides, it is challenging to study the variation of the magnetic field intensity and the magnetic flux density with respect to the current supplied. The different value of the provided magnetic will change the different configurations of the MR fluid. In the absence of a magnetic field, the fluid may freely flow through the gap

since the polarizable particles are randomly distributed in the fluid. An external magnetic field application produces controllable shear stress in the fluid that is nearly proportional to the magnetic field's magnitude itself.

In this paper, we have investigated the flow of an incompressible MR fluid in the magnetic peristaltic pump in the presence of a uniform magnetic field applied perpendicularly to the flow direction. The MR fluid is based on iron micro-particles in a carrier liquid and was investigated numerically by using the OpenFoam module, an open source software for computational fluid dynamics analysis based on the magnetic induction equation solver method [7]. The magnetic field induction, B , takes values between 0 and 1.5 T with 0.5 T step size, and was applied externally to determine magnetic field effects on the fluid flow. Steady, laminar, incompressible MR fluid flow was investigated by using the valve mode which is described in details in the results and discussion section. By using this mode, the problem geometry was designed and created in the FEMM software, and then it was imported into OpenFoam software for two-dimensional numerical computations. The numerical solution for the velocity was obtained for different magnetic field values. It was observed that an increase in B leads to an increase in the yield stress and consequently a decrease of the flow velocity.

2 Methodology

2.1 *Magnetic Field Function Development via Finite Element Method*

The magnetic field generated by the current induced to the coil in the magnetic peristaltic pump's channel was simulated using the finite element method. In this study, a FEMM software was used as a tool to analyze the magnetic field response with current variation. The development of the magnetic field function consists of 5 main steps:

Step 1: Draw the channel in the magnetic peristaltic pump

The regions of space that contain the object need to be determined for the finite element solver. The channel is drawn by placing nodes at all points and connecting lines as the geometry for the magnetic peristaltic pump.

Step 2: The boundary condition

The boundary condition was made so that the magnetic field produced by the coil is in the bound space. In this study, the boundary is at the outermost line of the geometry.

Step 3: The material selection

To identify the material and other properties, the program uses block diagrams to differentiate the regions in the geometry. All parts of the channel were labelled. All materials can be selected from the material library. In this case, the selected material is 1060 steel, pure iron as MR fluid, 36 AWG (0.124 diameters) copper wire, and air. The FEMM analysis was running five times. The difference between these analyses is about the current selection. The current applied takes a value between 0.5 and 2.5 A with 0.5 A step size. The number of turn of coils for each analysis is 50 turns times four, and it is equal to 200 turns.

Step 4: Generating mesh and running FEMM

For the finite element method, small triangular shaped elements were used. The size of the triangle is called mesh size. The larger the mesh size, it will take a shorter time to calculate, while a small mesh will take a long time to calculate. The smaller mesh will produce much more accurate results compared to the larger mesh. However, the calculation time has a lot of changes. In this paper, the triangular mesh was created for the model as shown in Fig. 1.

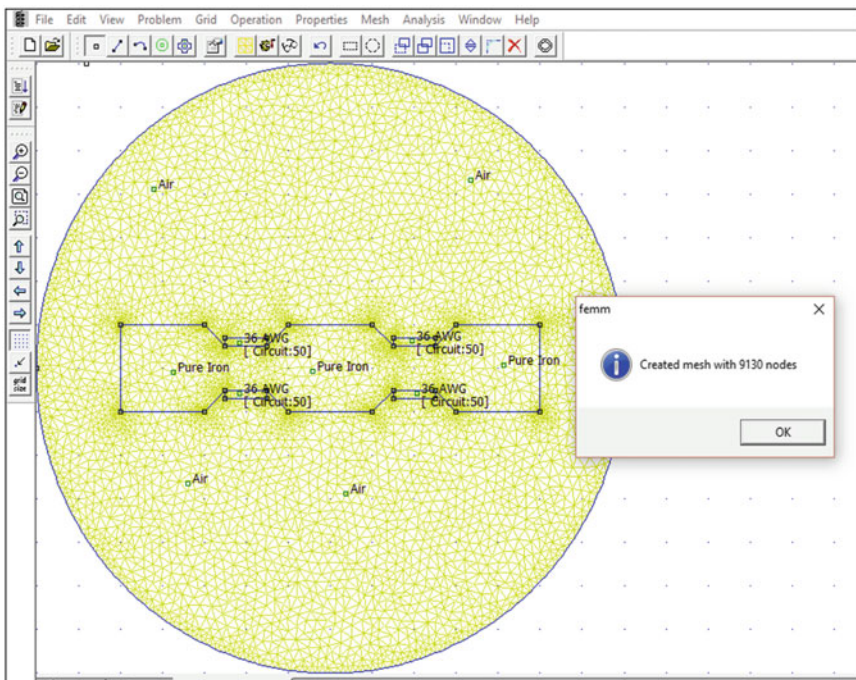


Fig. 1 Magnetic flux meshing

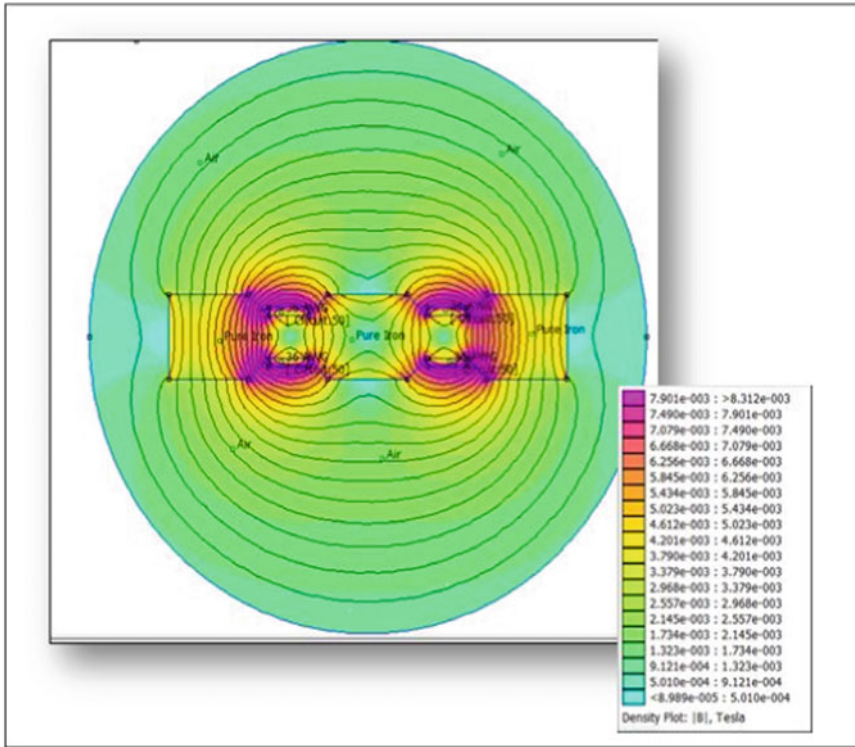


Fig. 2 Magnetic flux density

Step 5: Method to analysis the result

The result from the FEMM can be shown in colour contour for the magnetic flux in Fig. 2. The colour presents the magnetic flux density and the magnetic field strength. The plotted value was defined as a defined contour. From the result, we can determine that the ‘B’ is the magnitude of the flux density.

2.2 CFD Analysis of Magnetic Peristaltic Pump’s Channel

The fluid behavior in a channel gives a significant indication of the final performance of the system. This section investigates the fluid flow behavior of the MR fluid inside the magnetic peristaltic pump channel by using the OpenFOAM software. The characteristic of the fluid in the presence of a magnetic field is explored to provide knowledge of the volume flow rate during operation. The analysis started with the validation of the CFD codes as shown in Fig. 3. The code’s development is

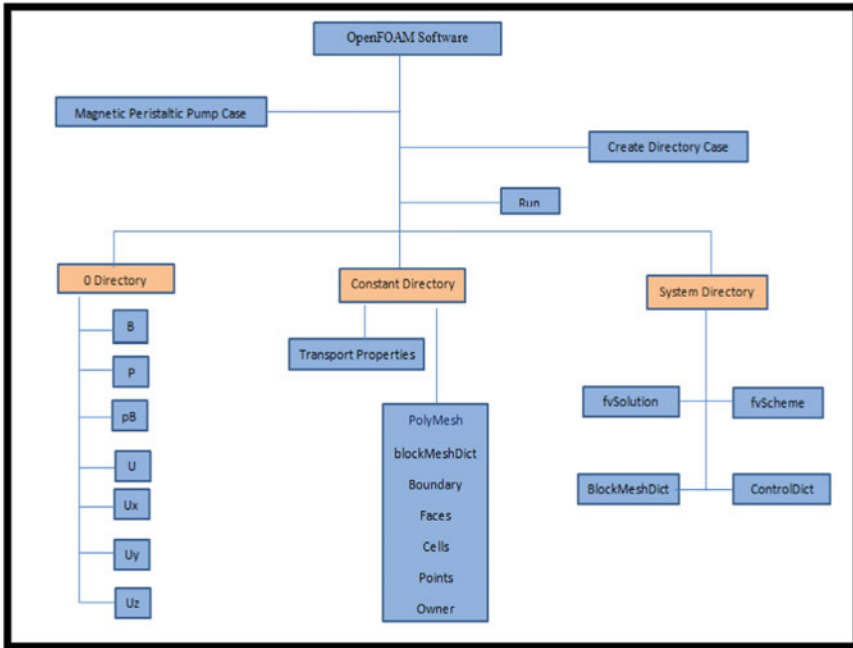


Fig. 3 Modelling and simulation procedure

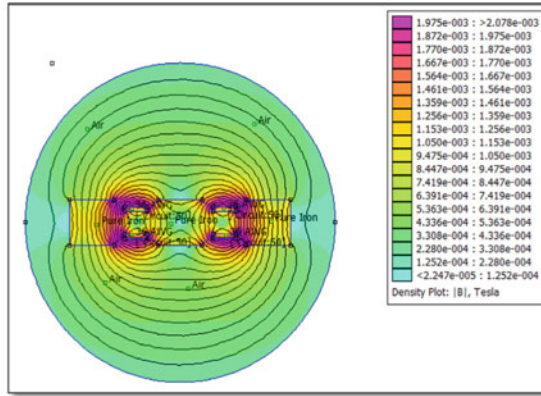
depending on the MHD case. The study then developed a correlation between the parameters such as velocity profile and volume flow rate in the channel.

3 Result and Discussion

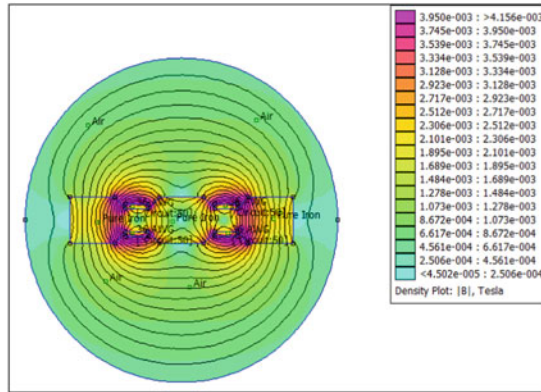
3.1 Finite Element Method Magnetics Analysis

In the magnetic peristaltic pump, the coils affected the MR fluid. It is important to develop the effect of the current applied on the coils to the magnetic field distribution in the fluid in the magnetic peristaltic pump. In this research, five different currents have been tested, 0.5–2.5 A with a step size of 0.5 A. A FEMM software was used to analyze the magnetic field produced by an electromagnet.

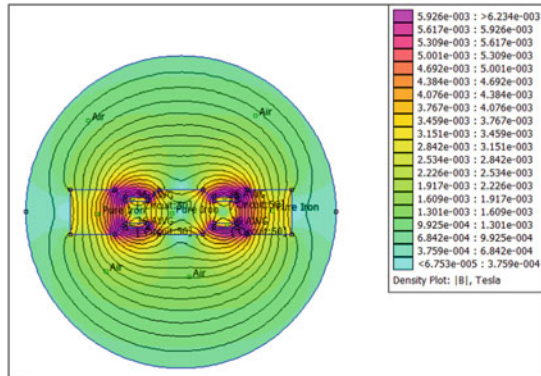
The result from the FEMM analysis can be shown in colour contour for the magnetic flux as shown in Fig. 4. The colour represents the magnetic flux density and the magnetic field strength. The plotted value is defined along a defined contour. From the result, we can identify the maximum magnetic flux density, B through the graph in Fig. 4. As we can see, the purple region shows the highest Tesla value. The design with 2.5 A current applied in Fig. 4e has the highest Tesla



(a) 0.5 Ampere

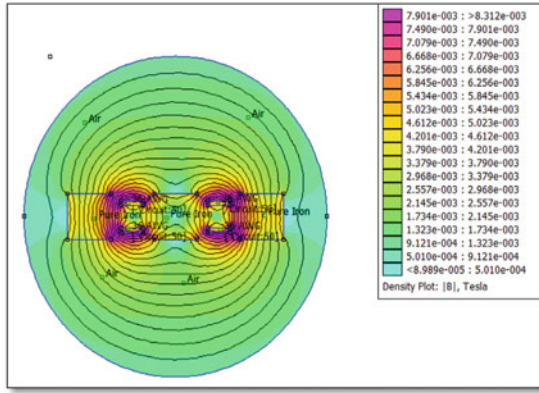


(b) 1.0 Ampere

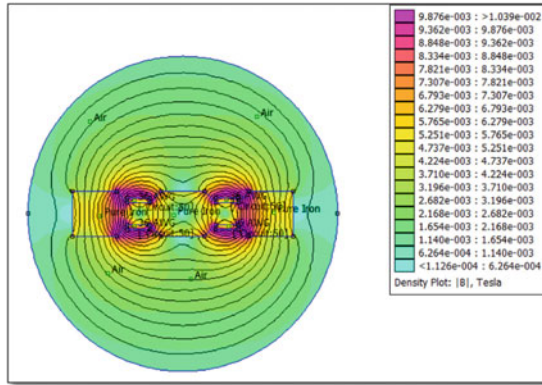


(c) 1.5 Ampere

Fig. 4 Contour of magnetic field densit



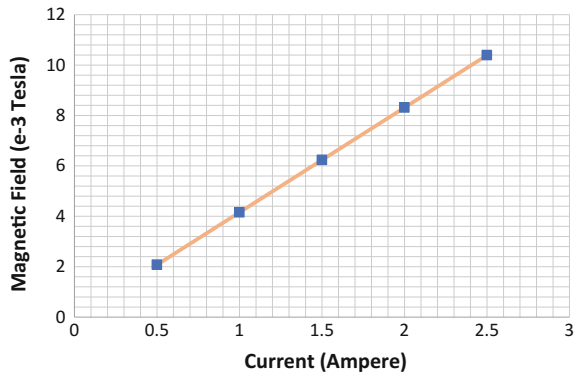
(d) 2.0 Ampere

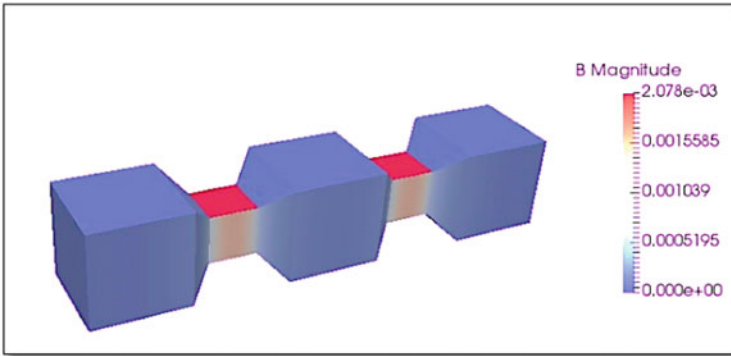


(e) 2.5 Ampere

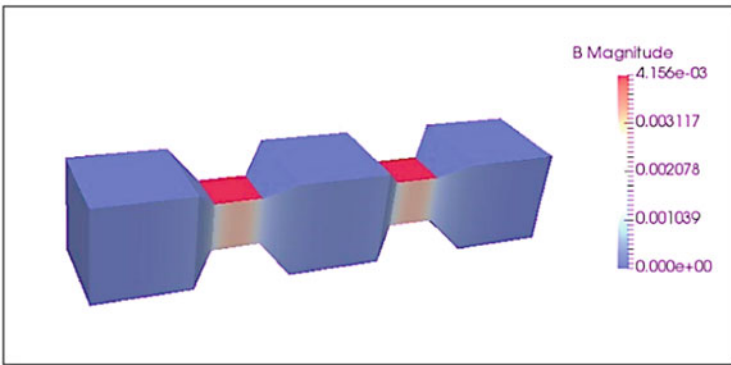
Fig. 4 (continued)

Fig. 5 Graph of magnetic field against current applied

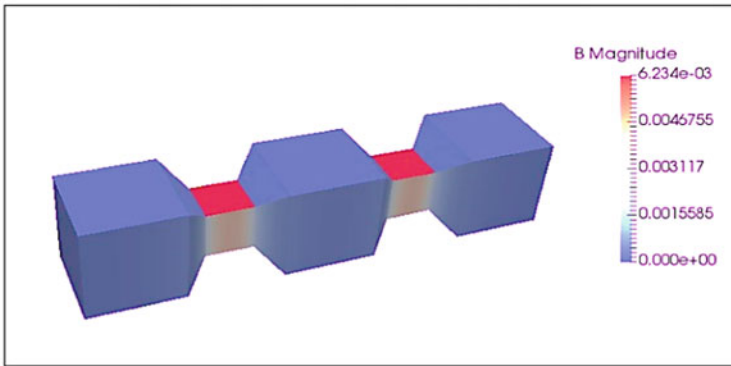




(a) $B = 2.078 \times 10^{-3}$ Tesla, 0.5 Ampere

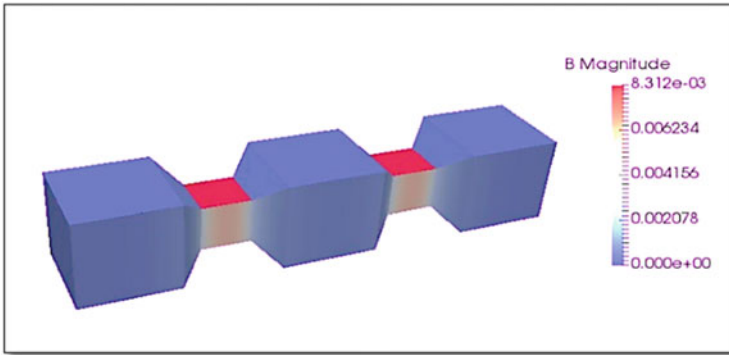
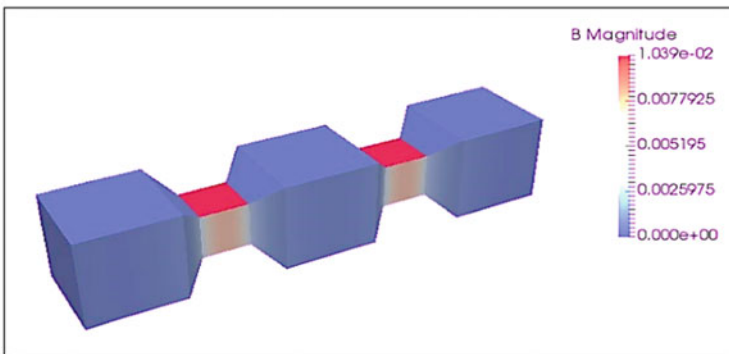


(b) $B = 4.156 \times 10^{-3}$ Tesla, 1.0 Ampere



(c) $B = 6.234 \times 10^{-3}$ Tesla, 1.5 Ampere

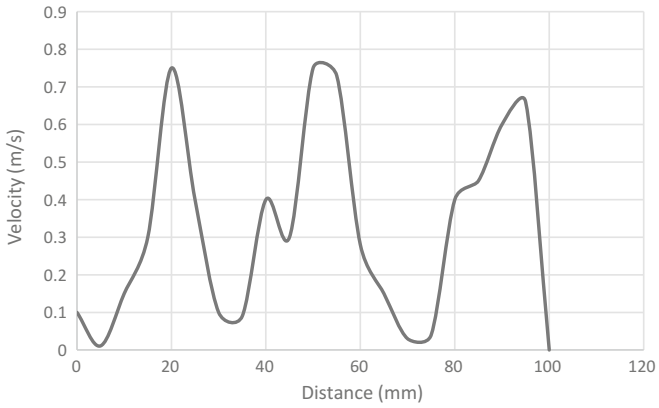
Fig. 6 Magnetic field contour in magnetic peristaltic pump's channel

(d) $B = 8.312 \times 10^{-3}$ Tesla, 2.0 Ampere(e) $B = 1.039 \times 10^{-2}$ Tesla, 2.5 Ampere**Fig. 6** (continued)

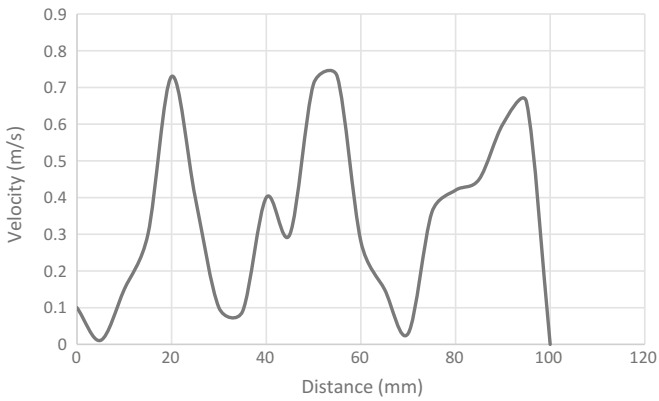
value compared to the other configurations. The highest Tesla value is needed in order to have a high magnetic field.

Magnetic flux density is the amount of magnetic flux per unit area of a section, perpendicular to the direction of flux. From the graph in Fig. 5, we can see that there is a slightly increasing value of the normal flux density (B) from 2.078×10^{-3} T to 1.039×10^{-2} T when the current is increased from 0.5 to 2.5 A. It shows that the value of Tesla is increased due to the increasing current value.

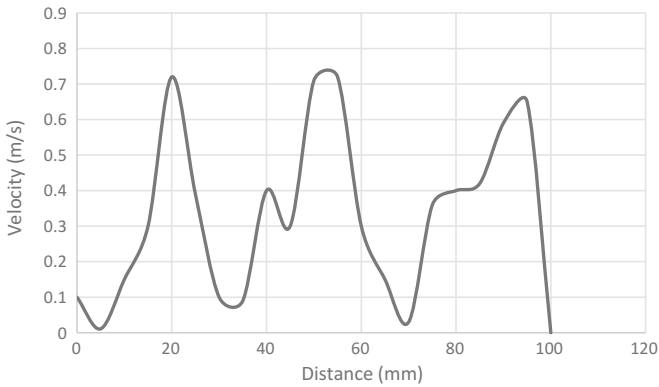
The main difficulty in the modelling of MR fluid was due to its viscosity change dependent on the magnetic field. The viscosity of the fluid in the magnetic channel varied with changes in the magnetic field. The viscosity behavior needed to be modelled correctly in order to reduce the error in the simulation. In this research, the viscosity was related to the current induced by the coil. From the reference current, the magnetic field was calculated using the correlations that were developed using the finite element method.



(a) $B= 2.078e-3$ Tesla, 0.5 Ampere



(b) $B=4.156e-3$ Tesla, 1.0 Ampere



(c) $B= 6.234e-3$ Tesla, 1.5 Ampere

Fig. 7 Graph of velocity across the magnetic field

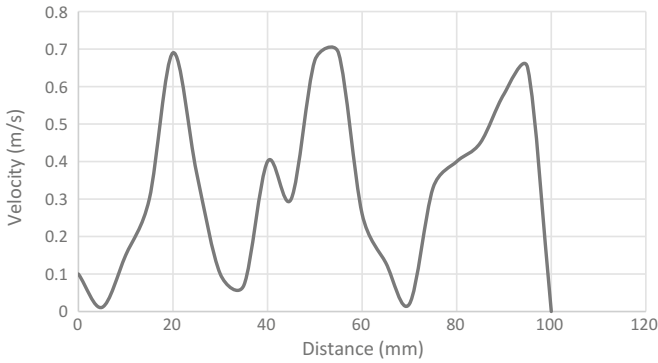
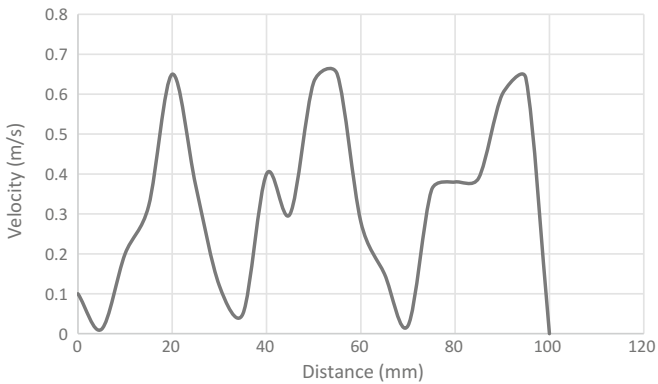
(d) $B = 8.312 \times 10^{-3}$ Tesla, 2.0 Ampere(e) $B = 1.039 \times 10^{-2}$ Tesla, 2.5 Ampere

Fig. 7 (continued)

3.2 CFD Analysis Using Open Source Field Operation and Manipulation (OpenFOAM)

By using the same parameters for all geometries in Fig. 6, and set $B = 2.078 \times 10^{-3}$, $B = 4.156 \times 10^{-3}$, $B = 6.234 \times 10^{-3}$, $B = 8.312 \times 10^{-3}$ and $B = 1.039 \times 10^{-2}$ respectively, these contours of the magnetic field can be obtained when the magnetic field is placed perpendicular to the flow of the MR fluid in a certain area which is between 2.5 to 3.5 cm and 6.5 to 7.5 cm. The dark blue colour of the contour indicates that there is no magnetic field applied on it. Thus, the magnetorheological fluid acts as a Newtonian fluid. Meanwhile, the dark red colour indicates the maximum magnetic field on the geometry, and at this moment the fluid became a non-Newtonian fluid.

From the obtained results from the numerical solution, the local velocity profiles have been plotted depending on the magnetic field, coordinates and the physical parameters of the fluid. It provides the velocity distributions that occurred

Fig. 8 Velocities distribution along the flow

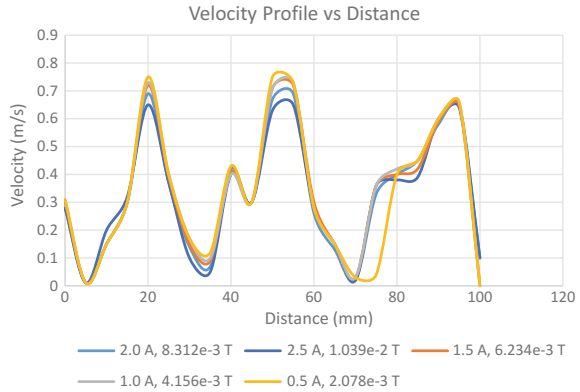


Table 1 Magnetic field density and the maximum velocity profile across the channel

Magnetic field density (T)	Maximum velocity profile across the channel (m/s)
2.078e-3	0.752
4.156e-3	0.733
6.234e-3	0.721
8.312e-3	0.694
1.039e-2	0.652

throughout the flow at the channel of the magnetic peristaltic pump. The initial value of the inlet velocity is 0.5 m/s. Figure 7 shows, at point 20 mm, the fluid achieved high velocities due to the 0 magnetic field and at 30 mm started slowly to change into a non-Newtonian fluid due to the impact of the magnetic field strength on 35 mm area. Meanwhile, at 50 mm, the fluid achieved the maximum velocities of 0.752, 0.733, 0.721, 0.694 and 0.652 m/s and at 70 mm, the velocity values were decreasing depending on the applied magnetic field. These decreases were larger in the area where the magnetic field was applied, whereas they were smaller in areas where the magnetic field was not applied.

The comparison of each graph has been plotted in Fig. 8. As we can see, the pink line represents the lowest magnetic field strength and is below of the other lines which means it has the highest velocity compared to other lines. Other than that, the red line represents the highest magnetic field strength is on the below of other lines which mean it has the lowest velocity. The maximum velocity profiles across the channel of the magnetic peristaltic pump are shown in Table 1. It is shown that the higher the magnetic field density, the lower the maximum velocity profile across the channel.

4 Conclusions

The main objective of this research was to investigate the numerical analysis of magneto-hydrodynamics in a magnetic peristaltic pump. As research methodology and from the results gathered, the following conclusions can be made.

In a magnetic peristaltic pump, the magnetic field is the primary parameter, which needs to be considered in order to see the characteristics of the MRF. The magnetic field is affected by coils with the current. Finite element method magnetic was used to analyze the magnetic field distribution produced by the coil. The same number of turns of the coil but different current applied to magnetic peristaltic pump's channel filled by MR fluid was used in this study. As a result, magnetic fields increase with the increase of current to the coils.

Other than that, a numerical model of the magnetic peristaltic pump has been made by using codes in the OpenFOAM software. In order to run the analysis, mesh generation, boundary condition, fluid properties, MHD solver have been selected. As a result, the geometry of the magnetic peristaltic pump can be viewed, and the simulation can be proceeded. MHD flow by using MR fluid can be evaluated as the result of the fluid flow in the magnetic peristaltic pump. It was observed that the magnetic field applied to the MR fluid decreased its flow velocity depending on the increase of the magnetic field. It is found that the electromagnetic force is affecting the MR fluid flow and the magnetic field can give us the ability to control the MR fluid which needs to operate the process in the magnetic peristaltic pump.

Acknowledgements All the experiment and analysis conducted under System Engineering and Energy Laboratory, Universiti Kuala Lumpur, Malaysian Spanish Institute, Kulim Kedah, Malaysia.

References

1. Zakaria, K.A., Amin, N.S.: peristaltic flow of magnetohydrodynamics Oldroyd-B fluid in an asymmetric channel. *Int. J. Appl. Math. Mech.* **8**(18), 18–37 (2012)
2. Olabi, G., Grunwald, A.: Design and application of magneto-rheological fluid. *Mater. Des.* (2006). <https://doi.org/10.1016/j.matdes.2006.10.009>
3. Wang, J., Meng, G.: Magnetorheological fluid devices: principles, characteristics and applications in mechanical engineering. *Proc. Inst. Mech. Eng. Part L J. Mater. Des. Appl.* (2001). <https://doi.org/10.1243/1464420011545012>
4. Salloom, M.Y., Samad, Z.: Magneto-rheological directional control valve. *Int. J. Adv. Manuf. Technol.* (2011). <https://doi.org/10.1007/s00170-011-3377-4>
5. Aitavade, E.N., Patil, S.D., Kadam, A.N., Mulla, T.S.: An overview of peristaltic pump suitable for handling of various slurries and liquids. *J. Mech. Civil Eng.* **2278-1684**, 19–24 (2011). [http://www.iosrjournals.org/iosr-jmce/papers/sicete\(mech\)-volume1/4.pdf](http://www.iosrjournals.org/iosr-jmce/papers/sicete(mech)-volume1/4.pdf). Accessed 24 Aug 2018
6. Neto, A.G., Lima, A.M., Neff, H., Gomes, C.L., Moreira, C.: Linear peristaltic pump driven by three magnetic actuators: Simulation and experimental results. In: 2011 IEEE International

- Instrumentation and Measurement Technology Conference (2011). <https://doi.org/10.1109/imtc.2011.5944300>
7. Armour, N., Dost, S.: The effect of a static magnetic field on buoyancy-aided silicon dissolution into germanium melt. *J. Cryst. Growth.* (2007). <https://doi.org/10.1016/j.jcrysgro.2007.04.033>

Parametric Study of the Two-Stage Pyrolysis Process for Activated Carbon Preparation from *Pithecellobium Jiringa*



Muhamad Husaini Abu Bakar, Mohamad-Syafiq Mohd-Kamal and Mohd-Nazri Che-Adnan

Abstract Activated carbon is a type of carbon processed to have small and low volume pores that improve the surface area available for chemical reactions. Currently, the cost of activated carbon is inefficient and it is difficult to obtain activated carbon. *Pithecellobium jiringa* (Jering) is an organic material that is potentially used as raw material for activated carbon. However, the use of Jering waste as activated carbon is new; the previous researchers never obtained data on the correlation between the parameters. The objective of the project is to design a two-stage pyrolysis process to evaluate the effect of hydroxide (KOH) on the conductivity of activated carbon and to evaluate the effect of ambient temperature on activated carbon. There are two stages in the pyrolysis process; to remove moisture and activate the carbon with KOH. The performance of the heating rate for this space is 5 °C per minute at 30 °C per minute. The highest temperature for this heating coil is 235 °C. The amounts, and molar volumes of KOH can affect the performance of the voltage.

Keywords Activated carbon · Pyrolysis process · *Pithecellobium jiringa*

1 Introduction

Activated carbon has attracted many researchers due to its excellent properties such as thermal stability, high yield, high adsorbent effect, large surface area and advanced structure [1–3]. The commercially activated carbon is provided from

M. H. Abu Bakar (✉) · M.-S. Mohd-Kamal · M.-N. Che-Adnan
System Engineering and Energy Laboratory, Malaysian Spanish Institute,
Universiti Kuala Lumpur, Kulim Hi-Tech Park, 09000 Kulim, Kedah, Malaysia
e-mail: muhamadhusaini@unikl.edu.my

M.-S. Mohd-Kamal
e-mail: msyafiq.kamal@s.unikl.edu.my

M.-N. Che-Adnan
e-mail: nazrienazz93@gmail.com

compact solid carbonates, such as concise, wood and grape seed [4–6]. However, the production margin for activated carbon is a significant challenge facing the industry [7]. Therefore, many studies have been carried out to discover new, cheap and renewable raw materials. It includes the use of agricultural waste with high carbon content and low ash content. According to recent studies, raw materials containing lignin, cellulose, and lignocellulose can be used to produce active carbon grades to return carbon to the market. The properties of activated carbon depend to a large extent on the activation method used, that is, the physical and chemical methods. The activation of physical activity involves the carbonization of raw materials in an inactive atmosphere and the activation of carbon in the presence of carbon dioxide or vapor [2, 8, 9]. Chemical activation consists in the destruction of chemical products in raw materials followed by pyrolysis.

Pyrolysis is the thermochemical decomposition of organic matter at high temperatures when there is no oxygen [10–12]. It involves simultaneous changes in chemical composition and physical phases and cannot be recovered. Pyrolysis is a type of thermolysis and is most commonly observed in organic materials exposed to high temperatures [13]. In general, pyrolysis of organic substances produces gas and liquid products and leaves a solid residue richer in carbon content, char [6]. Extreme pyrolysis, which leaves mostly carbon as the residue, is called carbonization. Therefore, this paper aims to design a two-stage pyrolysis chamber and analyze the production of activated carbon mixed with Potassium hydroxide (KOH) solution preparation from *Pithecellobium jiringa* (Jering).

2 Methodology

2.1 Two-Stage Pyrolysis Process

The synthesis of carbon activated by chemical activation can be done in two ways. The first method is the single-pyrolysis which is the direct activation of natural biomass with subsequent pyrolysis levels [14]. The second approach consists of two-stages of pyrolysis processes where the biomass dissolves for the first time at a specific temperature. In this stage, the elimination of non-volatile substances and extractable organic compounds (which are not covalently bound to a matrix) is carried out. As a result, the high temperatures during the biochar synthesis increase the carbon and aromatic condensate. Subsequently, the chemically generated carbon is activated, and the sample is pyrolysis for the second time [16, 17]. After chemical activation, either through a one- or two-stage process, the samples should be washed with water or weak acid at a neutral pH. In general, from energy, the one-step process is better [6, 15, 16].

2.2 Application of Activated Carbon

Active carbon with the highly developed surface area is widely used in many fields, such as water treatment processes, environmental protection, catalyst support, toxic protection, solvent recovery, discoloration, biomedical engineering and metal recovery [9, 17]. The development of technologies develops active applications of carbon, such as supercapacitors, electrodes, and gas storage [18]. Activated carbon is essential for the performance of the air-metal battery, such as aluminum-air batteries and zinc-air batteries. Activated carbon is used as an air cathode for the current collector in the aluminum and air battery [19, 20].

2.3 *Pithecellobium Jiringa* (Jering)

Pithecellobium jiringa (Jering) is an abundant organic material that is potentially used as a raw material for activated charcoal [21]. It comes from Southeast Asia only. Figure 1 shows the image of *Pithecellobium jiringa* (Jering). The previous researcher studied the use of Jering as the functional properties of seeds as a function of concentration, pH and ionic strength, which can be adjusted accordingly for the development of new food products [21, 22]. However, the use of Jering waste as activated carbon is unique. The previous researchers did not examine any data on the correlation between the parameters.

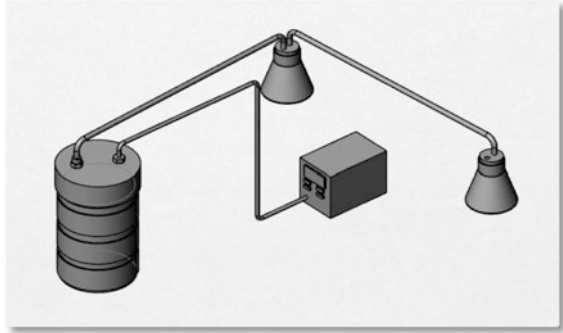
2.4 Geometry Design of Pyrolysis Chamber

The manufacturing process starts with the 3D design model using the SolidWorks software [23–25]. This configuration is done by installing all the sections to run experiments. There are some essential parts of this structure; the chamber, the heating coils, screw valve to combine the transfer of the pipes, thermostat to control the temperature of the air, the pickups to collect bio-oil, transistor and temperature controllers. Figure 2 shows the isometric design for the pyrolysis space using the SolidWorks software.

Fig. 1 *Pithecellobium jiringa* (Jering)



Fig. 2 Isometrics design for pyrolysis chamber using solid work software



2.5 Experimental Setup

The *Pithecellobium jiringa* (Jering) was dried in the oven for 48 h at the temperature of 120 °C. The drying procedure is presented in Fig. 3. The dried *Pithecellobium jiringa* (Jering) was then placed in a vacuum combustion chamber and first stage pyrolysis with a temperature of 235 °C for 2 h to produce biochar. Figure 4 shows the experimental setup of pyrolysis used to combust a dried Jering.

3 Result and Discussion

3.1 The Temperature Change

In Fig. 5, the data collected from the combustion chamber of the pyrolysis process is shown. In this experiment, three heating coils are provided to obtain a constant temperature in the bottom, middle and upper of the chamber. The performance of heating rate for this chamber is in the range from 5 °C per minute to 30 °C per minute. The highest temperature for this heating coil is 235 °C.

Fig. 3 Drying oven process for *Pithecellobium jiringa* (Jering)





Fig. 4 Experimental setup of the pyrolysis process

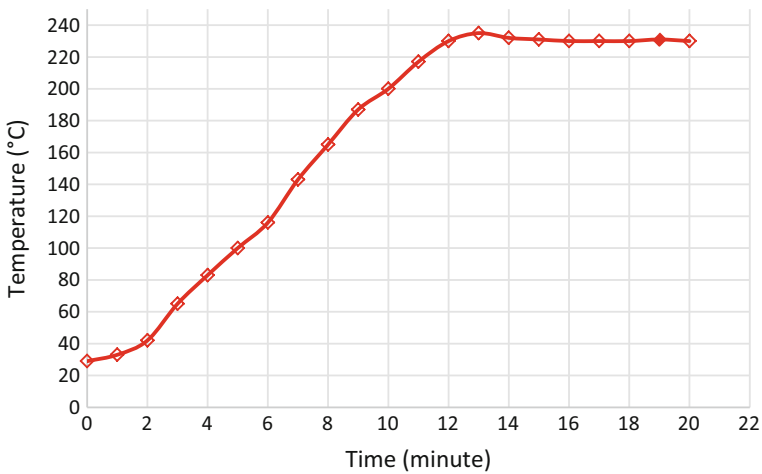


Fig. 5 Temperature change versus time

3.2 Volume of Bio-oil Yield for the Pyrolysis Process

The next observation is to discover the effect of different temperatures to collect the bio-oil products as seen in Fig. 6. This figure shows the data for first and second stage experiments. For this experiment, three samples were made at different temperatures, that is, sample A, B, and C. The combustion process time for the entire sample was 120 min. The original weight for each sample is 64 g. The temperatures for all the samples are small but still get different results.

For the first stage of combustion, at a sample temperature A of 230 °C, it can produce 31.75 ml of bio-oil. This sample has the highest number compared to sample B and C because the temperature is higher than the other. The temperature

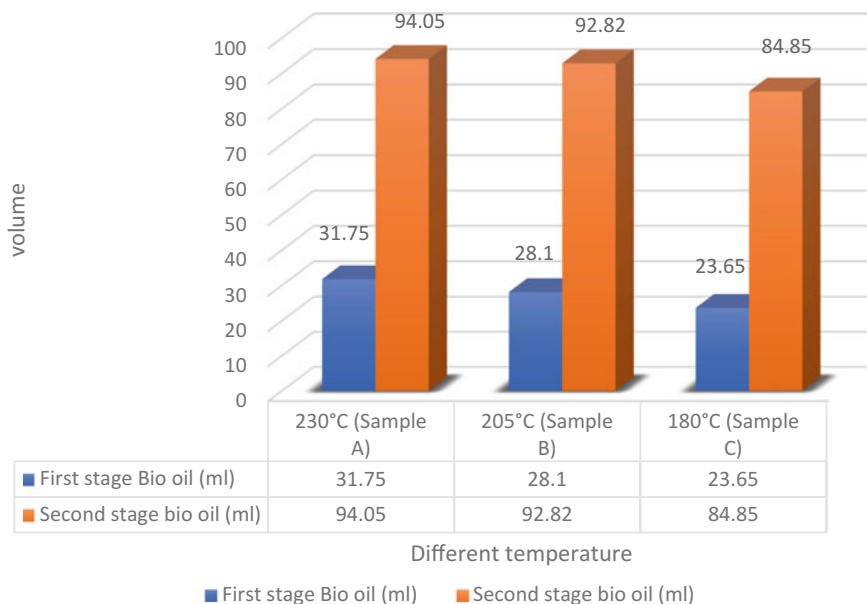


Fig. 6 Data collection for bio-oil yield with different temperature

for sample B is 205 °C, and the bio-oil production is 28.1 ml. This sample is the average compared to other samples, and the temperature of sample C is 180 °C, the total amount of bio-oil yield is 23.65 ml. High temperatures can achieve a high amount of bio-oil; Low temperatures can produce a low amount of bio-oil. It can be observed that with the increase in temperature, bio-oil yields production tend to be lower. Due to the increase in temperature, more energy will be given, and more carbon atoms will be used to reactivate the reaction. Before the second stage of combustion, all samples must be soaked or mixed with KOH for 24 h. The temperature for the whole sample is constant at 120 °C and the constant time is 120 min.

3.3 Percentages of the Carbon Yield

In Fig. 7, sample A shows the low percentage of carbon yield produce compared with other samples due to the difference in temperature at the first stage. Sample B is the average percentage, and sample C is the high percentage because the temperature is low compare to with sample A and sample B. This result shows that the quantity of bio-oil is still high for sample C compare to sample A is a low quantity of bio-oil because of a different temperature is applied.

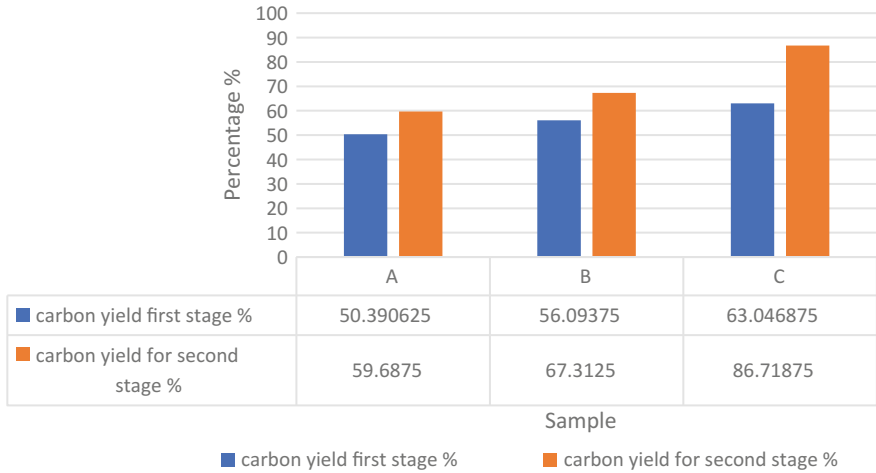


Fig. 7 Percentage of carbon yield with different sample

The carbon yield was calculated based on the weight of Jering on a dry basis from the following equation:

$$\begin{aligned} \text{The weight of jering} &= 64 \text{ g} \\ \text{Carbon Yield (wt\%)} &= \frac{\text{weight of carbon}}{\text{weight of Jering}} \times 100\% \end{aligned} \tag{1}$$

It can be seen that activated carbon yields tend to be lower when temperatures increase. This is because with the increase in temperature, more energy will be given and more carbon atoms will be used to activate the reaction.

In Fig. 8 shows the weight of the activated carbon for the first and second level. The results show that the ambient temperature is essential to obtain higher carbon emissions. Example A shows the highest temperature, that is, 230 °C, but the carbon production is lower than for the other samples. Example C shows that the ambient temperature is 180 °C. Example C shows the mass with the highest carbon value.

3.4 Application Carbon for Aluminium Air Battery

Each sample of carbon was soaked by KOH for 24 h and the second stage burning process temperature is 120 °C and 120 min. In Fig. 9, the voltage data was measured by a voltmeter. The result shows the voltage for three samples for one molar KOH and two molar KOH. In order to test this carbon performance, the air cathode for aluminum batteries in the air is generated using carbon. From there, the value of voltage for the aluminum-air battery is collect. The air cathode was produced by 3 samples of carbon from pyrolysis process.

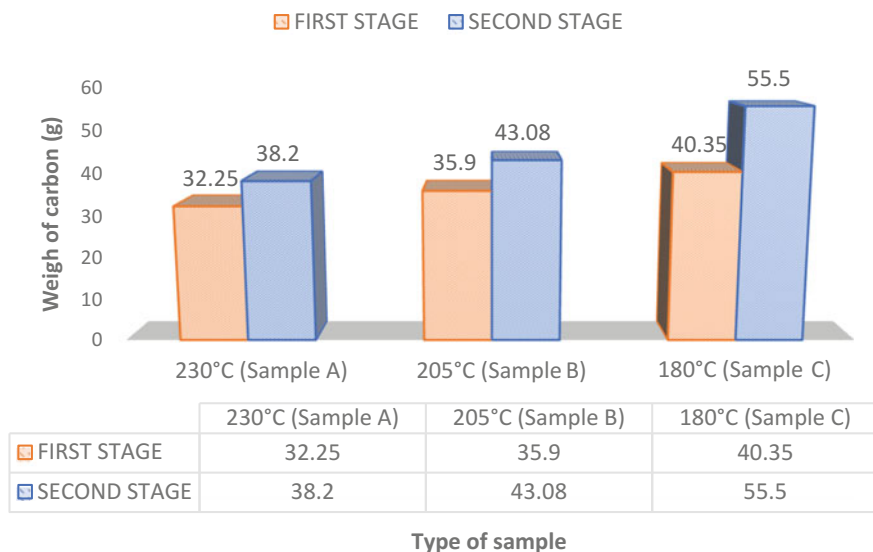


Fig. 8 The weight of carbon in gram unit versus different temperature

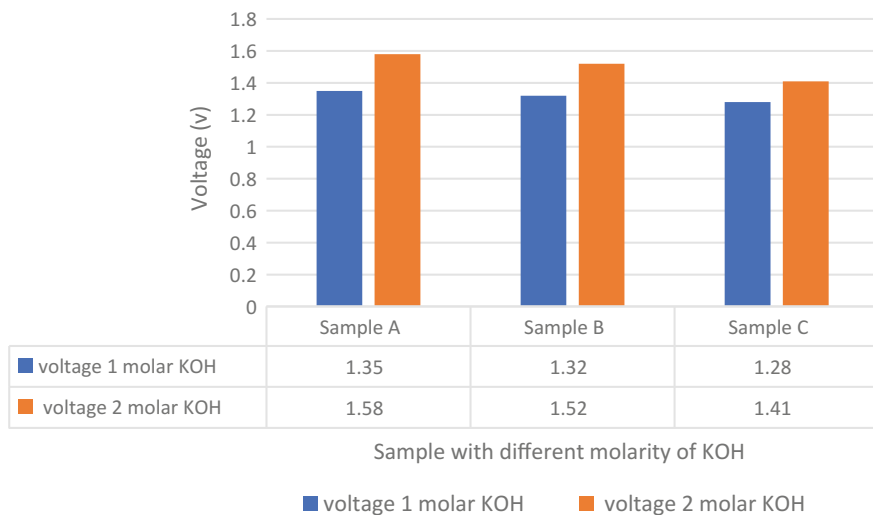


Fig. 9 Voltage collector with different molar of KOH

Sample A, B, and C is a different temperature with one molar of KOH; it shows the small different voltage data because the reaction of KOH is low. Secondly, sample A, B and C at different temperature with 2 M of KOH, it shows the high

voltage. Its mean the quantity of molarity KOH can affect the voltage performance. A higher quantity of molarity KOH can get the better or best-activated carbon. Low quantity of molarity KOH can get the low voltage performance.

4 Conclusion

The activated carbon can be generated from various sources. In this research, the *Pithecellobium jiringa* (Jering) was used to produce activated carbon. The performance or quality of activated carbon depends on the methods that have been used. The mixed and correct way can produce the best-activated carbon. In this study of design, a pyrolysis chamber has been done developed by a simple design and pure raw materials. Each part of the developed pyrolysis chamber can be designed entirely according to the actual concept.

The finding of this study shows that different temperature and volume of KOH can get a different value of voltage and current. The effect of Potassium hydroxide (KOH) can be seen from the performance of activated carbon and temperature effect can be seen. The best of temperature in this experiment is 235 °C, and the volume of KOH molarity is 2 M to generate the high performance of battery voltage and current. Therefore, it can be concluded that this 2 stage pyrolysis process is an excellent improvement in the producing the activated carbon as an air cathode for aluminum-air batteries.

Acknowledgements All the experiment and analysis conducted by System Engineering and Energy Laboratory, Universiti Kuala Lumpur, Malaysian Spanish Institute, Kulim Kedah, Malaysia.

References

1. Farzana, R., Rajarao, R., Bhat, B.R., Sahajwalla, V., et al.: Performance of an activated carbon supercapacitor electrode synthesised from waste compact discs (CDs). *J. Ind. Eng. Chem.* (2018)
2. Zhang, E., Wang, F., Yu, Q., Scott, K., Wang, X., Diao, G., et al.: Durability and regeneration of activated carbon air-cathodes in long-term operated microbial fuel cells. *J. Power Sources* **360**, 21–27 (2017)
3. Plaza-Recobert, M., Trautwein, G., Pérez-Cadenas, M., Alcañiz-Monge, J., et al.: Preparation of binderless activated carbon monoliths from cocoa bean husk. *Microporous Mesoporous Mater.* **243**, 28–38 (2017)
4. Purnomo, C., Castello, D., Fiori, L., et al.: Granular activated carbon from grape seeds hydrothermal char. *Appl. Sci.* **8**(3), 331 (2018)
5. Rashidi, N.A., Yusup, S., et al.: Potential of palm kernel shell as activated carbon precursors through single stage activation technique for carbon dioxide adsorption. *J. Clean. Prod.* **168**, 474–486 (2017)

6. Zubrik, A., Matik, M., Hredzák, S., Lovás, M., Danková, Z., Kováčová, M., Briančin, J., et al.: Preparation of chemically activated carbon from waste biomass by single-stage and two-stage pyrolysis. *J. Clean. Prod.* **143**, 643–653 (2017)
7. Vilella, P.C., Lira, J.A., Azevedo, D.C.S., Bastos-Neto, M., Stefanutti, R., et al.: Preparation of biomass-based activated carbons and their evaluation for biogas upgrading purposes. *Ind. Crops Prod.* **109**, 134–140 (2017)
8. Li, S., Han, K., Li, J., Li, M., Lu, C., et al.: Preparation and characterization of super activated carbon produced from gulfweed by KOH activation. *Microporous Mesoporous Mater.* **243**, 291–300 (2017)
9. Yang, I., Kwon, D., Kim, M.S., Jung, J.C., et al.: A comparative study of activated carbon aerogel and commercial activated carbons as electrode materials for organic electric double-layer capacitors. *Carbon N Y* **132**, 503–511 (2018)
10. Choi, M., Park, H.C., Choi, H.S., et al.: Comprehensive evaluation of various pyrolysis reaction mechanisms for pyrolysis process simulation. *Chem. Eng. Process. Process Intensif.* **130**, 19–35 (2018)
11. Kabir, G., Mohd Din, A.T., Hameed, B.H., et al.: Pyrolysis of oil palm mesocarp fiber and palm frond in a slow-heating fixed-bed reactor: a comparative study. *Bioresour. Technol.* **241**, 563–572 (2017)
12. Czajczyńska, D., Nannou, T., Anguilano, L., Krzyżyńska, R., Ghazal, H., Spencer, N., Jouhara, H., et al.: Potentials of pyrolysis processes in the waste management sector. *Energy Procedia* **123**, 387–394 (2017)
13. Gagliano, A., Nocera, F., Bruno, M., Blanco, I., et al.: Effectiveness of thermodynamic adaptative equilibrium models for modeling the pyrolysis process. *Sustain Energy Technol Assess.* **27**, 74–82 (2018)
14. Kumar, A., Jena, H.M., et al.: Removal of methylene blue and phenol onto prepared activated carbon from Fox nutshell by chemical activation in batch and fixed-bed column. *J. Clean. Prod.* **137**, 1246–1259 (2016)
15. Idrees, M., Rangari, V., Jeelani, S., et al.: Sustainable packaging waste-derived activated carbon for carbon dioxide capture. *J. CO2 Util.* **26**, 380–387 (2018)
16. Li, S., Han, K., Si, P., Li, J., Lu, C., et al.: High-performance activated carbons prepared by KOH activation of gulfweed for supercapacitors. *Int. J. Electrochem. Sci.* **13**, 1728–1743 (2018)
17. Horax, K.M., Bao, S., Wang, M., Li, Y., et al.: Analysis of graphene-like activated carbon derived from rice straw for application in supercapacitor. *Chinese Chem Lett* **28**, 2290–2294 (2017)
18. Li, S., Han, K., Li, J., Li, M., Lu, C., et al.: Preparation and characterization of super activated carbon produced from gulfweed by KOH activation. *Microporous Mesoporous Mater.* **243**, 291–300 (2017)
19. Volperts, A., Dobelev, G., Zhurinsk, A., Vervikishko, D., Shkolnikov, E., Ozolinsh, J.: Wood-based activated carbons for supercapacitor electrodes with a sulfuric acid electrolyte. *Xinxing Tan Cailiao/New Carbon Mater.* **32**(4), 319–326 (2017)
20. Zhang, G., Chen, Y., Chen, Y., Guo, H., et al.: Activated biomass carbon made from bamboo as electrode material for supercapacitors. *Mater. Res. Bull.* **102**, 391–398 (2018)
21. Sridaran, A., Karim, A.A., Bhat, R., et al.: *Pithecellobium jiringa* legume flour for potential food applications: studies on their physico-chemical and functional properties. *Food Chem.* **130**, 528–535 (2012)
22. Cheng, Y.F., Bhat, R., et al.: Functional, Physicochemical and Sensory Properties of Novel Cookies Produced by Utilizing Underutilized Jering (*Pithecellobium Jiringa* Jack). *Legume Flour*. Elsevier (2016)
23. Bock, S.: New open-source ANSYS-SolidWorks-FLAC3D geometry conversion programs. *J Sustain Min* **14**, 124–132 (2015)

24. Zhang, J., Zhang, R., Ren, G., Zhang, X., et al.: A method for using solid modeling CAD software to create an implant library for the fabrication of a custom abutment. *J. Prosthet. Dent.* **117**, 209–213 (2017)
25. Zhang, H., Li, T., Li, Z., et al.: Modeling in SolidWorks and analysis of temperature and thermal stress during construction of intake tower. *Water Sci. Eng.* **2**, 95–102 (2019)

Performance of a Small Engine Fueled by Methane Using a Simulation Tool



Shahril Nizam Mohamed Soid, Muhammad Najib Abdul Hamid,
Mohd Suyerdi Omar and Muhammad Iqbal Ahmad

Abstract Climate change and increased demands for energy, tends the researchers to search for environmental friendly resources of alternative fuels that can be used in internal combustion engines. There are many types of existing alternative fuels that can be used in internal combustion engines, but the fundamental information about their combustion process is still limited. This study focus on the performance of methane fueled engines in a small spark ignition gasoline engine. The engine performance was measured on the brake torque, brake power, brake mean effective pressure (Bmep) and in-cylinder peak pressure. A Modenas Kriss 110cc gasoline engine was selected for experimentation and engine modelling. The 3D engine model was created using CATIA and the engine performance simulation was performed using GT-Suite v7.4.3. The engine performance results for the methane fueled engine were found to be lower at about 20.1% for engine torque, brake power and bmep and 12.0% for in-cylinder peak pressure when compared to the gasoline engine. From these results it can be concluded that the methane fuel can be used as an alternative fuel but it produces lower engine performance compared to a gasoline engine.

Keywords Methane · GT-Suite · Engine

S. N. M. Soid (✉) · M. N. A. Hamid · M. S. Omar
Malaysian Spanish Institute, Universiti Kuala Lumpur, Kulim Hi-Tech Park,
09000 Kedah, Malaysia
e-mail: shahrilnizam@unikl.edu.my

M. N. A. Hamid
e-mail: mnajib@unikl.edu.my

M. S. Omar
e-mail: msuyerdi@unikl.edu.my

M. I. Ahmad
Faculty of Bioengineering and Technology, Universiti Malaysia Kelantan,
17600 Jeli, Kelantan, Malaysia
e-mail: iqbal.a@umk.edu.my

1 Introduction

The unstable market price for crude oil encourages the researchers to find alternative or renewable green energies to fulfill the users need. There are few options of renewable and alternative energies in the current markets, but they do not help much in preserving the quality of environment and even do more polluting it. There are many previous researches that have studied the performance of alternative fuels [1–3]. This study focused on the potential of methane fuel usage in a small spark ignition engine. Methane is one of the largest components in natural gas. Additionally, compressed natural gas (CNG) that is available in the market contains of about 75–98% methane with small percentages of ethane, propane, butane [4]. Still, the detailed information and findings about pure methane fueled engines is still limited.

The usage of CNG as alternative fuel will degrade the power, torque and Bmep compared to gasoline engines [5]. However, the brake specific fuel consumption of natural gas is lower compared to gasoline [6]. The carbon monoxide (CO) and carbon dioxide (CO₂) emission is also lower than for a gasoline engine [7]. Other research work also found that the natural gas lacks in terms of power and torque compared to gasoline engines [8].

This study is conducted with the purpose to investigate the performance of a methane fueled engine in terms of brake torque, brake power, BMEP and in-cylinder peak pressure and compared its performance to a gasoline engine.

2 Methodology

The objectives of this study are to evaluate the performance of a methane fuel engine. The engine performance was tested using a dynamometer along with a gas analyzer attached to the Modenas Kriss 110cc engine, in the internal combustion engine lab located at UniKL MSI. The wide open throttle (WOT) method was used during running the gasoline engine performance tests. Furthermore, different engine speeds were tested with different configurations of air-fuel ratio from 2000 to 8000 rpm and the results obtained from it were used for the purpose of validation and comparisons of the graphically developed engine model. Figure 1 show the experimental setup used in this work and Table 1 indicates the technical specifications of the engine.

A single cylinder engine model is built using the commercial software called GT-Suite. The technique in modelling the engine can be referred in the GT-Suite manual [9]. GT-Power, which is one of the modules under the GT-Suite, is a powerful tool that has been used by many researchers in internal combustion engine modeling [10, 11]. Some of the inputs in 1D engine modeling require a detailed the geometry of engine components. Components like airbox, intake runner and exhaust system have been developed in 3D CAD model. The 3D model



Fig. 1 Experimental setup for gasoline engine performance measurement

Table 1 Engine technical specifications

Type	4-stroke SOHC, single cylinder
Bore × Stroke	53 × 50.6 mm
Displacement	110cc
Maximum torque	9.3 Nm at 4000 rpm
Intake Valve Open (IVO)	20°BTDC
Exhaust Valve Open (EVO)	55°BBDC
Duration time intake/exhaust	260°

development process involves in taking the dimensions of the engine such as runner length, diameter of pipe throat and radius of pipe bends. Here, the 3D model is performed using the CATIA software. The 3D CAD model is then imported into one of the GT-Suite modules called GEM-3D in order to convert it into an one-dimensional engine diagram. Then, GT-Power is used to run the simulation and to obtain the performance of the engine. The validation of the engine model is performed by comparing the engine performance results between simulations of the gasoline engine with the experimental results [10]. After the engine model fueled with gasoline has been validated, then the gasoline fuel is changed to methane fuel. The stoichiometry of the air-fuel ratio between gasoline and methane is different. Therefore, the usage of an equivalence ratio is applied to find the new air-fuel ratio for methane fuel. In achieving the optimum methane fuel engine performance, it is very much dependent on the configuration of the engine.

3 Results and Discussion

3.1 Model Verification

For validation process, both engine performance results were compared and the difference between them was set to be in the range of 5%. At the initial stage, the result from the model shows quite a significant amount of differences between the experimental results. It shows that the model needs to be calibrated so that the results will be close to the experimental results. In order to calibrate the model, the lift angle multiplier was set to 0.83 thus the duration of the IVO and EVO is the same as in the engine specifications. The forward coefficient was set to 0.95 and the maximum lift was changed to 5 mm height which changes the flow array. A new setting of flow array was redefined at 5 mm lift to generate the new flow array and was used in the model valves flow array. The validation of the model to the experimental data is shown in Fig. 2.

After the validation process, the simulation was run with the aim to obtain less than 10% differences which makes the model reliable and ready to be used for the next simulation. From the analysis, it was found that the average percentage of difference between the model and experiment is at about 4.1% for engine torque,

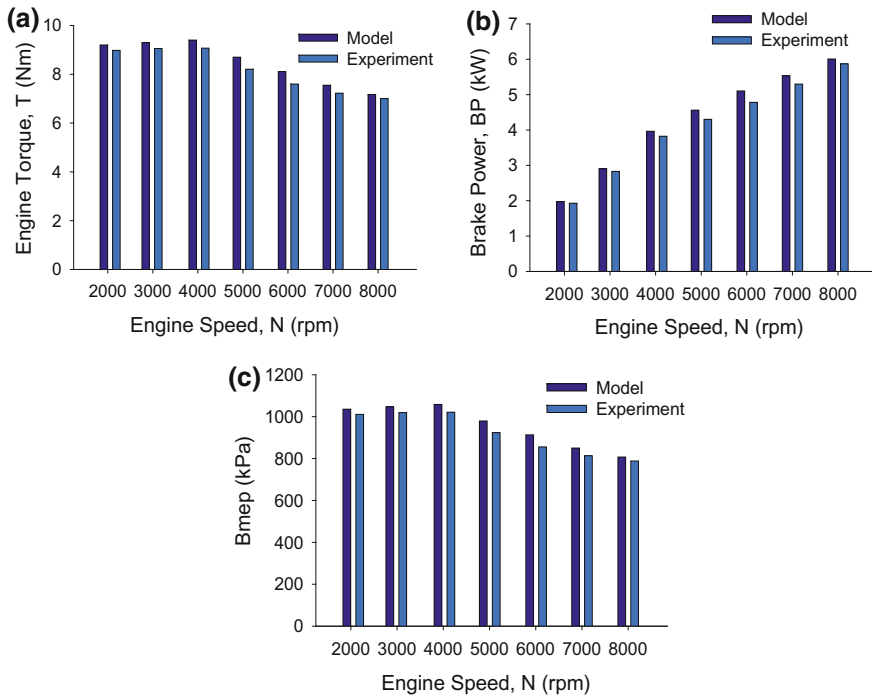


Fig. 2 Validation of gasoline model according to **a** engine torque **b** brake power and **c** bmep

brake power and bmep. The trends also have shown similarities for both model and experimental data. Therefore, the Modenas Kriss 110cc engine model was successfully developed into an one-dimensional model using the GT-Suite software. It represents the real engine at which the output of the model gives nearly the same results as the experimental results.

3.2 Methane Fuel Engine Performance

For methane fuel, the *methane_vap* type of fuel was selected from the GT-Suite library. In order to provide the comparison to gasoline, the air-fuel ratio was set based on the same equivalence ratio as for the gasoline engine. The details of the modelling condition are shown in Table 2. The stoichiometric air-fuel ratio for gasoline was referred as 14.7:1. The equivalence ratio was found by dividing the stoichiometric air-fuel ratio to the air-fuel ratio obtained from the experiment. Hence, the obtained equivalence ratio was used to find the actual ratio of methane by dividing the stoichiometric ratio of methane which is 17.2 to the equivalence ratio. This method was used for all rpm as well.

Figure 3 shows the performance of methane compared to gasoline. From the figures, it was found that the methane fueled engine experienced a power degradation at about 20.1% for the engine torque, brake power and bmep and 12.0% for the in-cylinder peak pressure when compared to gasoline. At lower speed it can be observed that the methane engine performance is close to gasoline for brake power. However, when the speed increases to at about 3500 rpm the difference in engine performance increases mostly due to lower energy density for methane. Although there is a large difference in engine performance, but when it comes to emission and brake specific fuel consumption (BSFC) methane produced better results compared to gasoline [12]. Moreover, in-cylinder peak pressure trace had exposed that the gasoline engine produced higher peak pressure than methane. With the high in-cylinder pressure, the gasoline engine will produce a higher torque, power and bmep compared to methane.

Table 2 Modeling AFR for gasoline and methane

Engine speed (rpm)	Equivalence ratio	AFR (gasoline)	AFR (methane)
2000	1.1	13.41	15.64
3000	1.13	13.05	15.22
4000	1.32	11.16	13.03
5000	1.38	10.66	12.46
6000	1.39	10.54	12.37
7000	1.3	11.74	13.23
8000	1.38	10.68	12.46

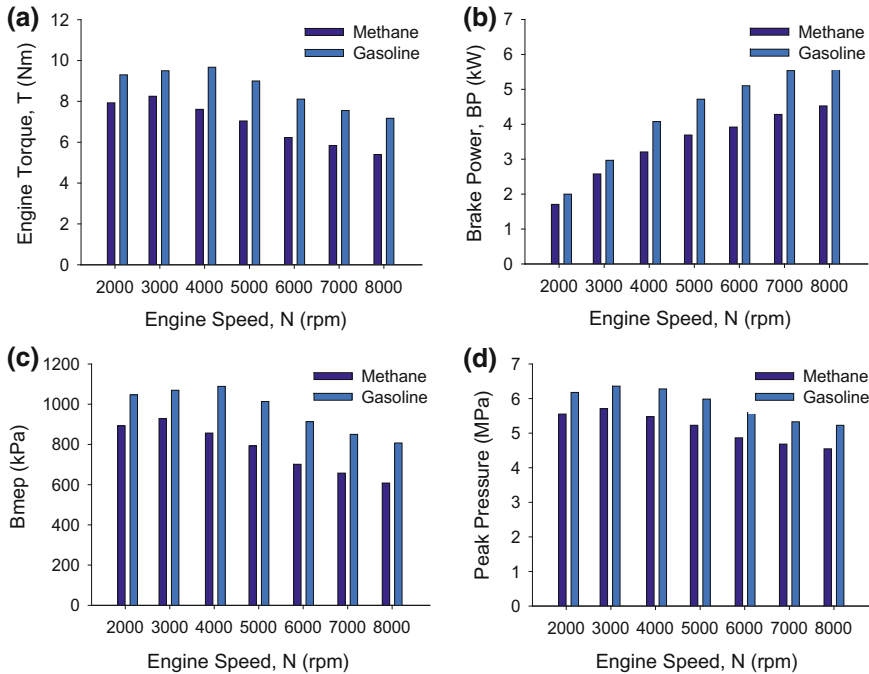


Fig. 3 Comparison of **a** engine torque **b** brake power **c** bmep and **d** in-cylinder peak pressure between methane and gasoline

4 Conclusion

The Modenas 110cc engine model was successfully developed into an one-dimensional model using the GT-Suite software. It represents the real engine at which the output of the model gives nearly the same results as the experimental results. The major findings from this study are as follows:

- i. The behavior of the gasoline engine and methane fueled engine were found to be the same. However, the methane fueled engine experiences some degradation in performance when compared to the gasoline engine.
- ii. Due to lower engine performance compared to gasoline, it is suggested to implement different cam timing angles for methane fueled engine.

Acknowledgements The authors would like to thank Universiti Kuala Lumpur Malaysian Spanish Institute for the financial support for this research work via UniKL STRG grant UniKL/CoRI/str15028.

References

1. Malenshek, M., Olsen, D.: Methane number testing of alternative gaseous fuels. *Fuel* **88**, 650–656 (2009)
2. Ibrahim, A., Bari, S.: A comparison between EGR and lean-burn strategies employed in a natural gas SI engine using a two-zone combustion model. *Energ. Convers. Manage.* **50**, 3129–3139 (2009)
3. Rahman, M., Mohammed, K.M., Bakar, R.A.: Effects of air-fuel ratio and engine speed on performance of hydrogen fueled port injection engine. *J. Appl. Sci.* **9**, 1128–1134 (2009)
4. Chandra, R., Vijay, V.K.: Performance evaluation of a constant speed IC engine on CNG, methane enriched biogas and biogas. *Appl. Energ.* **88**, 3969–3977 (2011)
5. Ajmali, S., Mahmood, W.W., Abdullah, S., et al.: Comparison of performance and emission of a gasoline engine fueled by gasoline and CNG under various throttle positions. *J. Appl. Sci.* **14**, 386–390 (2014)
6. Ameri, M., Kiaahmadi, F., Khanaki, M.: Comparative analysis of the performance of a dual-fuel internal combustion engine for CNG and gasoline fuels. *J. Power Technol.* **92**, 214–226 (2012)
7. Bordelanne, O., Montero, M., Bravin, F., et al.: Biomethane CNG hybrid: A reduction by more than 80% of the greenhouse gases emissions compared to gasoline. *J. Nat. Gas Sci. Eng.* **3**, 617–624 (2011)
8. Semin, Bakar R.A.: A technical review of compressed natural gas as an alternative fuel for internal combustion engines. *Am. J. Eng. Appl. Sci.* **1**, 302–311 (2008)
9. Gamma Technologies.: GT-SUITE-Flow Theory Manual, in Gamma Technologies Inc. (2012)
10. Bos, M.: Validation GT-power model cyclops heavy duty diesel engine. M.Sc, Eindhoven University of Technology (2007)
11. Said, M.F.M., Aziz, A.B.A., Latiff, Z.A., et al.: Investigation of Cylinder Deactivation (CDA) Strategies on Part Load Conditions. SAE Technical Paper 2014-01-2549 (2014)
12. Kaleemuddin, S., Amba Prasad Rao, G.: Development of dual fuel single cylinder natural gas engine an analysis and experimental investigation for performance and emission. *Am. J. Appl. Sci.* **6**, 929–936 (2009)

Simulation Analysis on the Performance of a Hydrogen Port Fuel Injection Engine



Shahril Nizam Mohamed Soid, Surenthar Magalinggam
and Muhammad Iqbal Ahmad

Abstract Over the past few years, many researchers have conducted experimental and simulation studies using alternative fuels for internal combustion engines. Selected fuels should contain less or no carbon products from combustion process and eventually decrease the primary energy usage. Hydrogen has been taken into consideration. Previous researchers found that hydrogen can be used in spark ignition internal combustion engines. However, the optimum performance of an engine could not be achieved due to some limitations in regards the configurations of the air fuel ratio and compression ratio. In this work hydrogen fuel was tested in a single cylinder port fuel injection engine as the preliminary study in optimizing the engine performance. The engine performance study was based on the brake torque, brake power, brake mean effective pressure (Bmep) and peak pressure. The engine model was developed based on the Modenas Kriss 110 cc 4-stroke single cylinder gasoline engine. The CATIA software was used in developing the 3D engine model and followed by utilization of GT-Suite software in analyzing the engine performance. From the analysis, it was found that the performance of the hydrogen fueled engine is lower compared to the gasoline engine.

Keywords Engine · GT-Suite · Hydrogen · Air-fuel ratio · Compression ratio

S. N. M. Soid (✉) · S. Magalinggam
Malaysian Spanish Institute, Universiti Kuala Lumpur, Kulim Hi-Tech Park,
09000 Kedah, Malaysia
e-mail: shahrilnizam@unikl.edu.my

S. Magalinggam
e-mail: surenthar1437@gmail.com

M. I. Ahmad
Faculty of Bioengineering and Technology, Universiti Malaysia Kelantan,
17600 Jeli, Kelantan, Malaysia
e-mail: iqbal.a@umk.edu.my

1 Introduction

The needs in finding renewable energy resources are keep growing to fulfill the energy demand that keeps increasing years after years. Fluctuating of oil price and environmental issues have increased the activities in finding alternatives fuel resources that will provide a sustainable energy and achieve greener environment. There are many researches were done by various researchers using various types of fuel and hydrogen is one of non-carbonaceous fuels that exists on the earth [1]. It can be used in internal combustion engines. Experimentation and studies were performed by previous researchers using hydrogen as a fuel in internal combustion engines [2, 3], ended up with the results showing there are some limitations in configuring the air-fuel ratio and compression ratio. Changing both parameters will give optimum performance of the hydrogen engine.

The studies of hydrogen addition in internal combustion engines have found that hydrogen fueled engines suffer from output power reductions due to the very low heating value on volume basis which results in lean mixture operation [4]. High stoichiometry of hydrogen to air ratio also causes the mass of the intake air being reduced for any engine sizes. Increasing the compression ratio increases the maximum cylinder gas pressure and the maximum gas mean temperature [5]. A desirable Bmep can be achieved at lean mixture at low engine speed but is unacceptable for higher engine speed [1].

Performance improvements can be achieved by retarding the spark timing and together with a change in compression ratio [6, 7]. This project attempts to analyze the engine performance characteristics of a hydrogen port fuel injection engine and its potential as an alternative fuel for internal combustion engines.

2 Methodology

The model development starts with collecting the overall engine performance results from the experimental setup. The first step taken is determining the performance of a gasoline engine by using an experimental setup. An engine dynamometer was used simultaneously with a gas analyzer to determine the gasoline engine performance and air-fuel ratio. The engine performance test is performed at wide open throttle (WOT) condition. The experimental results are used for validation of the developed engine model.

The engine modelling starts by creating a 3D model of engine parts by referring to the actual geometry from the Modenas Kriss 110 cc engine. The CATIA V5R21 CAD software was used to model the air box, intake runner 1 and 2, intake port, exhaust port and exhaust runner. The precise dimensions of parts in terms of their volume, diameters of runner's throat, radius of bending on intake and exhaust port and also the length of parts were taken into consideration during modeling. Every part was created separately in order to be exported in GEM-3D which is a module

in the GT-Suite v7.4.3 software. Once the parts were successfully modelled in a 3D version, they were imported in GEM-3D to be discretized which transforms every part to 1D diagrams. During the discretization of every part in GEM-3D, the diameter of every pipe section and the wall temperature were set according to the factory settings of the engine.

After the discretization process completed, every part was dragged to the GT-Power module in the GT-Suite v7.4.3 software. Here the 1D converted part diagrams were arranged according to the original arrangements from the actual engine starting from the air box until the tail pipe and connected with a string called junction [8]. Then, using the engine technical specifications as shown in Table 1 and temperature for engine parts in GT-Suite v7.4.3 software as shown in Table 2, the detailed configurations were set for every parameters and engine components involved. Manuals and tutorials from the GT-Suite software were used during the modeling process. Valves diameters, wall temperatures, flow arrays, valves opening and closing durations were taken into serious priority to achieve the same output performance as the actual engine. The next step was the setting of different air fuel ratios for different engine speeds and separated to several cases. Based on the simulation runs of the different sets, the output performance can be compared to the actual experimentation results which run with different configurations of air fuel ratios for each different engine speed. The output from the successfully performed simulations was shown in GT-Post. The results were collected and tabulated to be used for the validation [8] and comparison.

Table 1 Engine technical specifications

Engine parameter	Value
Bore × Stroke	53 mm × 50.6 mm
Total displacement	111 mL
Maximum torque	9.3 N.m at 4000 rpm
Maximum horsepower	6.6 kW at 8500 rpm
Compression ratio	9:3:1
Intake valve open (IVO)	20° BTDC
Intake valve close (IVC)	60° ABDC
Exhaust valve open (EVO)	55° BBDC
Exhaust valve close (EVC)	25° ATDC
Total duration intake/exhaust	260°

Table 2 Parts temperature in GT-Suite software

Engine parts	Temperature (K)
Cylinder head	550
Piston	590
Cylinder block wall	450

3 Results and Discussion

3.1 Model Validation

To validate the constructed model, verification to the experimental data is needed. The accuracy of the constructed model was verified by comparing the engine performance between model and experiment. Both of the results were correlated based on their trends and values. At the early stages of the verification, the simulation results show a quite significant difference when compared to experimental results. Thus, the parameter set in the simulation model was rechecked and some minor alterations were performed. There are some increments shown from the alteration of cam timing angle, angle multiplier, lift multiplier and flow array. The cam timing angle for the intake valve was set to 231° and for the exhaust to 123.9° . The angle multiplier was 0.83 and the lift array was 0.5 for both intake and exhaust valve. The flow array was configured using an excel self-calculating file in GT-Suite. The forward coefficient was adjusted to 0.95 to obtain the flow array values.

Engine performance results were plotted in GT-Post after the 10 cycle runs of the simulation. Differences between the average value of experiment and model are in the range of 0.6–3% for brake torque, brake power and Bmep. Thus, the accuracy and precision of the developed model was validated with the output results achieving no more than 5% difference compared to the experimentation engine. The outcome from engine performance results are plotted in graphs as shown in Fig. 1.

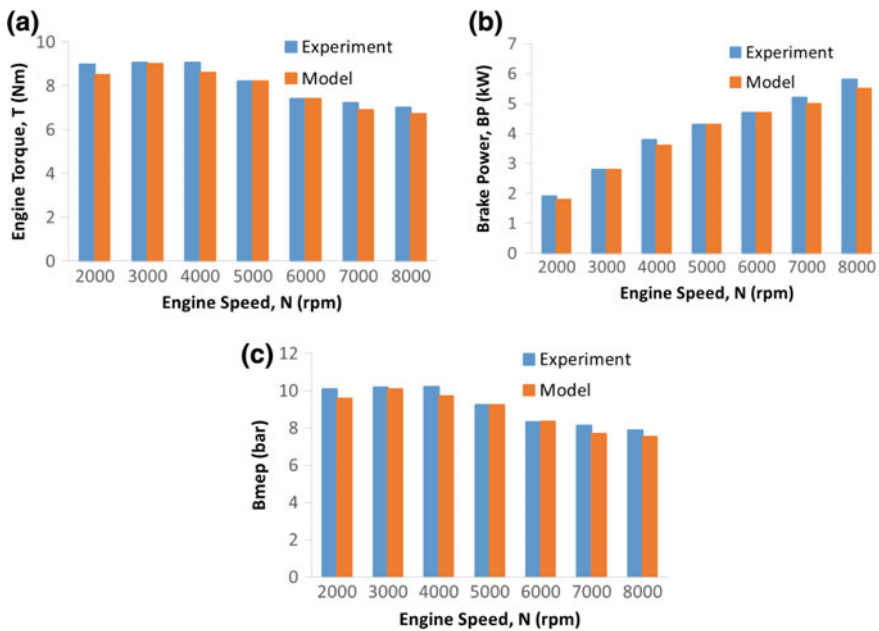


Fig. 1 Validation of gasoline model according to a engine torque, b brake power and c Bmep

3.2 Hydrogen Fueled Model

For hydrogen fueled engine, the air-fuel ratios from the gasoline experimentation and modeling is calculated to suit hydrogen model. The stoichiometric air-fuel ratio for hydrogen is 34.3:1 meanwhile for gasoline it is 14.7:1. If the same settings of the air-fuel ratios from gasoline were used for hydrogen, the simulation was not completed and ended with errors. To eliminate this problem, an equivalence ratio from gasoline fuel was obtained by dividing the stoichiometric of gasoline with air-fuel ratio set during the experiment [9]. Then, the stoichiometric of hydrogen was divided by the equivalence ratio to have the output value of air-fuel ratios needed for the hydrogen model as shown in Table 3.

The same procedure was followed as in the case of gasoline model, and the results from GT-Post were collected and plotted as shown in Fig. 2. A comparison between the gasoline and hydrogen graphs shows some significant differences for the overall engine performance. An increase in the equivalent ratio of hydrogen fuel lead to higher value of air-fuel ratio and this created non-consistent differences between the gasoline and hydrogen model. An average value of 30% performance difference was observed from the gasoline to hydrogen comparisons results for brake torque, brake power and also Bmep, that can be considered as performance degradation. The loss in brake torque and brake power is due to the knock and backfiring. Buildup of a small amount of hydrogen in the intake manifold when the injection duration is longer than the intake valve opening duration creates backfire by ignition of the hydrogen leftover in it with hot exhaust gases released at the exhaust stroke [7, 10]. Meanwhile, drops in Bmep are due to improper combustion as increasing of the hydrogen fraction in the overall fuel intake which reduces the air intake [5].

For the peak pressure, an average value of 15% difference was observed from the comparisons. A lower peak pressure was achieved due to the low compression ratio. Finally, the Bsfc for hydrogen gives a two times better value than the gasoline because of the rich mixture of the air-fuel ratio. The fuel consumption of the hydrogen fueled model achieved improvements at an average value of 60% difference compared to the gasoline fueled engine. Although the overall engine performance of hydrogen is low compared to gasoline except for Bsfc, an optimization could lead to increments in outputs.

Table 3 AFR configurations of gasoline and hydrogen using the same equivalence ratio

Engine speed (rpm)	AFR (Gasoline)	Equivalence ratio	AFR (Hydrogen)
2000	13.41	1.09	31.46
3000	13.05	1.12	30.62
4000	11.16	1.32	25.9
5000	10.66	1.38	24.8
6000	10.54	1.39	24.6
7000	11.34	1.29	26.5
8000	10.68	1.37	25.0

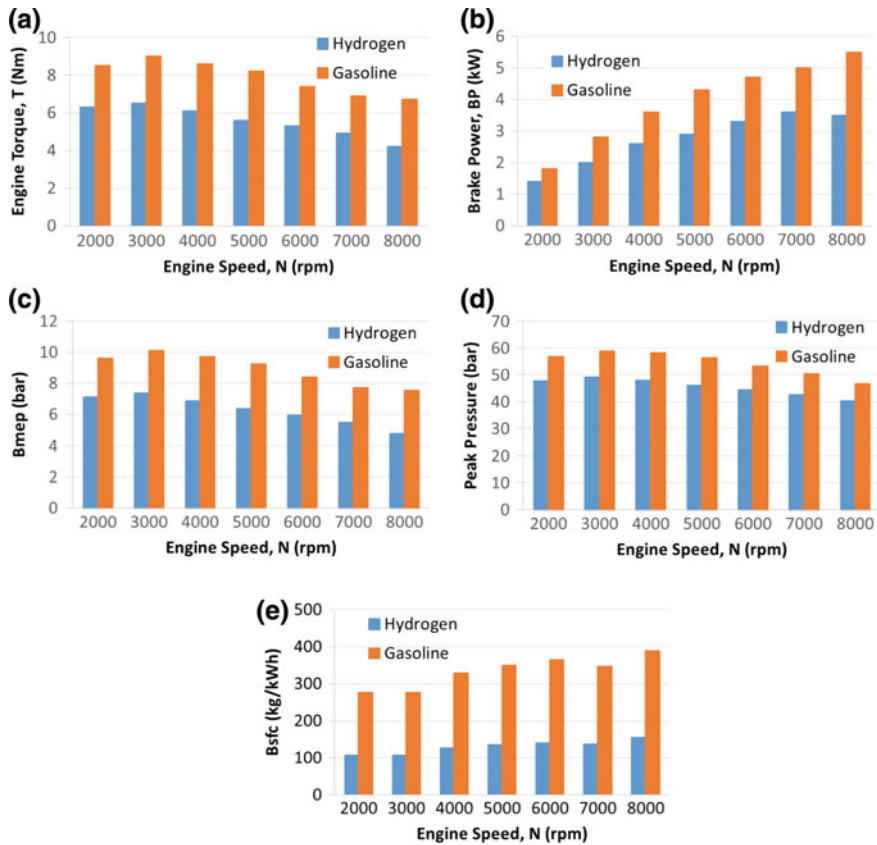


Fig. 2 Comparison of **a** brake torque, **b** brake power, **c** Bmep, **d** peak pressure and **e** Bsfc at various engine speeds

4 Conclusion

As a conclusion it was found that hydrogen fuel produced a lower engine performance with an average value of 29% performance difference compared to hydrogen comparisons results for brake torque, brake power and also Bmep. Other findings are as follows:

- i. A loss in brake torque and brake power is due to the knock and backfiring. The buildup of a small amount of hydrogen in the intake manifold when the injection duration is longer than the intake valve opening duration creates backfire by ignition of the hydrogen leftover in it with hot exhaust gases released at the exhaust stroke.
- ii. Drops in Bmep are also due to improper combustion as increasing of hydrogen fraction in the overall fuel intake which reduces the air intake.

- iii. For the peak pressure, an average value of 15% difference was observed from the comparisons due to low energy density of hydrogen.
- iv. Bsfcr for hydrogen gives a two times better value than the gasoline due to its gaseous fuel form.

Acknowledgements The authors would like to thank Universiti Kuala Lumpur Malaysian Spanish Institute for the financial support for this research work via UniKL FRGS grant UniKL/CoRI/str15028.

References

1. Rahman, M.M., Mohammed, M.K., Bakar, R.A.: Effects of air fuel ratio and engine speed on performance of hydrogen fueled port injection engine. *J. Appl. Sci.* **9**, 1128–1134 (2009)
2. Xu, J., Zhang, X., Liu, J., et al.: Experimental study of a single-cylinder engine fueled with natural gas-hydrogen mixtures. *Int. J. Hydrogen Energ.* **35**, 2909–2914 (2010)
3. Verhelst, S., Wallner, T.: Hydrogen-fueled internal combustion engines. *Prog. Energ. Combust.* **35**, 490–527 (2009)
4. Karim, G.A.: Hydrogen as a spark ignition engine fuel. *Int. J. Hydrogen Energ.* **28**, 569–577 (2003)
5. Zheng, J.J., Wang, J.H., Wang, B et al.: Effect of the compression ratio on the performance and combustion of a natural-gas direct-injection engine. *Proc. Inst. Mech. Eng. Part D J. Automobile Eng.* (2009) <https://doi.org/10.1243/09544070jauto976>
6. Park, C., Lim, G., Lee, S et al.: Effects of the ignition timing retard and the compression ratio on the full-load performance and the emissions characteristics of a heavy-duty engine fuelled by hydrogen-natural-gas blends. *Proc. Inst. Mech. Eng. Part D J Automobile Eng.* (2013) <https://doi.org/10.1177/0954407013495528>
7. Hari Ganesh, R., Subramanian, V., Balasubramanian, V., et al.: Hydrogen fueled spark ignition engine with electronically controlled manifold injection: an experimental study. *Renew. Energ.* **33**, 1324–1333 (2008)
8. Bos, M.: Validation GT-Power model cyclops heavy duty diesel engine. Eindhoven University of Technology, MSc (2007)
9. Sonthalia, A., Rameshkumar, C., Sharma, U., et al.: Combustion and performance characteristics of a small spark ignition engine fuelled with HCNG. *J. Eng. Sci. Tech.* **10**, 404–419 (2015)
10. Verhelst, S., Maesschalck, P., Rombaut, N., et al.: Efficiency comparison between hydrogen and gasoline on a bi-fuel hydrogen/gasoline engine. *Int. J. Hydrogen Energ.* **34**, 2504–2510 (2009)

Simulation of Flange Modeling by Using the Finite Element Method



**Khairul Shahril Shaffee, Khairulanwar Haris,
Khairul Akmal Shamsuddin, Mohamad Sabri Mohamad Sidik
and Megat Mohd Amzari Megat Mohd Aris**

Abstract This project focuses on studying an existing off-road buggy component which is a flange. The study includes modeling the flange using a solid model as references to an existing part used for an off-road buggy using the CATIA software. Stress analysis was conducted using the finite element method in the ABAQUS software. The performance of proposed design was compared to the existing part of the flange. A buggy is an automobile with wheels that project beyond the vehicle body. In European countries, a dune buggy is a recreational vehicle with large wheels and wide tires, designed for use on sand dunes or beaches. From the result in running the first analysis of the design datum analysis, it was found that the von Misses stress had maximum values compared with new design of the flange.

Keywords Buggy · Stress · Flange · Coordinate measurement machine

1 Introduction

This project focuses on studying an existing off-road buggy component which is a flange. Flanged or also known as Spacer Flanged is a major component for connection between hubs and wheels. The study includes modeling the flange using a solid model as reference to an existing part used for an off-road buggy using the

K. S. Shaffee (✉) · K. Haris · K. A. Shamsuddin · M. S. M. Sidik
M. M. A. M. Mohd Aris
Malaysian Spanish Institute, Universiti Kuala Lumpur, Kulim Hi-Tech Park,
09000 Kulim, Kedah, Malaysia
e-mail: khairuls@unikl.edu.my

K. A. Shamsuddin
e-mail: khairulakmal@unikl.edu.my

M. S. M. Sidik
e-mail: msabri@unikl.edu.my

M. M. A. M. Mohd Aris
e-mail: megatamzari@unikl.edu.my

CATIA software. Stress analysis was conducted using the finite element solver in ABAQUS. This analysis is used to determine the critical area of stress distribution on the flange. The new model design should have an improvement in terms of stress distribution. The existing flange that is installed to the buggy car is a solid surface type. The material of this solid surface type is carbon steel. For the beginning, the analysis was done on the existing component. This determined the critical area of stress distribution area that is needed to be improved.

Load distribution occurs when a load is applied to a structure and will influence the dynamic balance of the vehicle. A good design will increase the toughness of the flange. The maximum stress occurs at the flange during the movement of the vehicle and load application.

The purpose of this analysis is as follows:

1. To develop the existing model of the flange using CATIA
2. To conduct a stress analysis of the flange using the ABAQUS solver package.

To achieve these objectives various parameters were observed by using computer simulation. The performance of the proposed design was compared to the existing part of the flange. Theoretical aspects of the proposed design on its load can be supported by the spacer and will be accomplished by using theoretical aspects of the finite element analysis. The performance of the load that can be carried by the flange were observed by using extensive computer simulation that were performed using ABAQUS and CATIA solver package subjected to various types of parameters.

a. Buggy

In European countries, a dune buggy is a recreational vehicle with large wheels and wide tires, designed for use on sand dunes or beaches. This vehicle can move on any kinds of surface ground with smooth movements. The design is usually a modified vehicle with a modified engine mounted on an open chassis. The modifications usually attempt to increase the power to weight ratio by either lightening the vehicle or increasing the engine power or both. Those with an open frame chassis are called sand rails. Sand rails are close to dune buggies [1].

A more recent generation of off-road vehicles, often similar in appearance to a sand rail buggy but designed for different use, is the off-road go kart. The difference between a dune buggy or go kart and an off-road buggy or kart is sometimes nothing more than the type of tires fitted such as sand tires or all terrain tires.

Initially dune buggies were designed for navigating through deserts or beaches (hence the word "dune"). However, dune buggies have become more diversified in terms of the terrain they can handle and are being built for more generic off-road tasks, indoor track racing. Some are even built for and used as on-road vehicles.

Typically the function is determined before the buggy is created in order to maximize the comfort or abilities of the vehicle. Although dune buggies can be bought (as a kit), many drivers make their own. This is done by separately buying

the chassis, engine, tires, steering wheel, and axles. Some builders make their own chassis, which creates a special, customized vehicle.

A 1961 or later Volkswagen sedan is the preferred donor to create a dune buggy. The engine, transaxle, wheels, and instruments can be used from these models. Other parts that can be salvaged from a donor Volkswagen for use in a dune buggy include the front axle and suspension, frame, pedal assembly, shock absorbers, seats, battery, fuel tank (1961 or later), steering column, brakes, instruments and switches, windshield wiper, horn and emergency flasher unit.

b. Structure of the Buggy

For the structure of the buggy, tube framed and fibreglass buggies are commonly used. Tube frame buggies have been altered to allow maximum recreational use. They are now available in varying sizes. The most common form of non-racing buggy consists of the tube frame which is simple to construct and sturdy. If the frame bends or breaks, it is simple to fix. Steel tubing is preferred to “pipe” as a pipe is rolled and welded, tubing is mandrel drawn, making it stronger and with consistent wall thickness. The engine size varies depending on the suspension, frame strength and performance needs. The engine size has varied from 50 cc for small light buggies to 7+ litre engines designed for professional racing. Dune buggies use either automatic or manual transmissions, sometimes based on application and engine power, but often based simply on personal choice and fibreglass buggies bodies come in many shapes and sizes. Many companies worldwide have attempted to copy the original fibreglass dune buggy. These types of buggies are known as clones.

c. Buggy Design

Before determining the appropriate design for the space flange there are several studies that have been done to obtain a suitable design of the space flange. From the previous study, a diploma student at Universiti Kuala Lumpur, Malaysian Spanish Institute (2009) has developed a vehicle called the military buggy military (Fig. 1). The model was built with a good design and followed the required specification. But it still has some weaknesses at certain parts such as the size of the spacer flange is not the same. Besides, the design did not undergo any analysis test for the load of the buggy.

d. Design of the flange (Datum)

In regards to the size of the spacer flange, the problem is that they have different sizes between the hub and rim (Fig. 2). From that it will effect the dynamic balance for this vehicle and also the size of the rib and the hollow tube of the part.

As seen in Fig. 3, the part was developed by using CATIA, the small diameter connects to the hub and the larger diameter connects to the wheel.

Ribs are the parts to support the other part and reduce the stress. As shown in Fig. 4 the size of the rib is very thin around 2 mm and the angle of the rib not suitable.

Fig. 1 Design model at UNIKL MSI



Fig. 2 The existing part (Datum) of flange



e. New Design of the flange

After the observations from the existing part, the design optimization for the flange resulted in a configuration as shown in Fig. 5. The rib size has been increased from 5 mm to 10 mm and at a certain angle a fillet was placed because the stress concentration will reduce if we put the fillet at the angle, as shown in Fig. 6.

Fig. 3 CAD model of existing flange

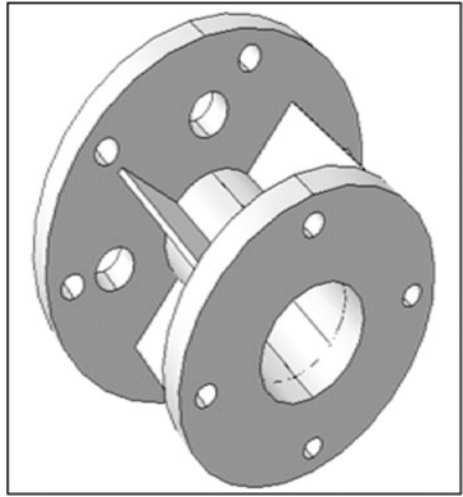


Fig. 4 The rib of the existing flange

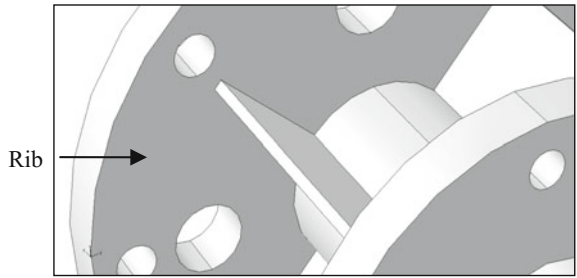


Fig. 5 New flange design

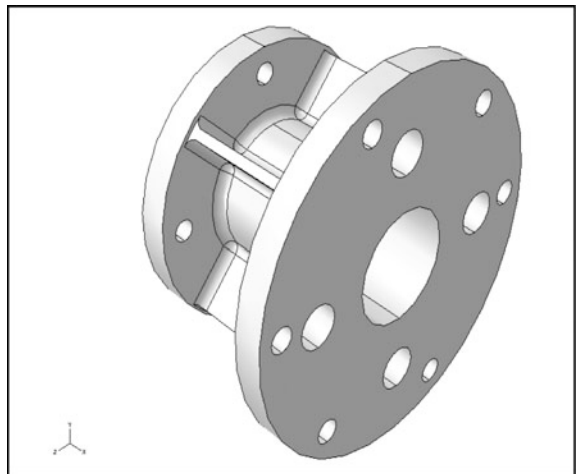
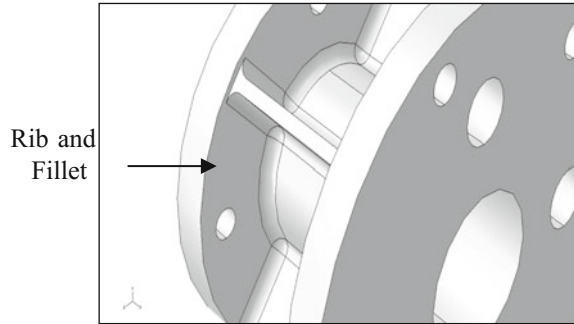


Fig. 6 Rib and fillet of new flange design



2 Methodology

In the beginning, there were two tasks that needed to be done simultaneously. Besides doing a literature review, exercise and tutorial needed to be done for mastering the simulations tools and some preliminary simulation needed to be carried out to be as well. Then, the problem of this research was stressed on the buggy and the main task was to find the type of flange that is suitable for this vehicle. It is very important because this may affect the dynamic balance of the buggy and the motion may make the vehicle unstable. Various parameters were observed such as the relationship between load of the buggy and load that can be supported by spacer flange.

After preliminary research, the existing part was sketched and calibrated by using a coordinate measuring machine (CMM). After that the datum was developed by using CATIA and was imported to ABAQUS to be analyzed. After the analysis was done, the existing part was optimized into the new design and analyzed by using ABAQUS [2].

From the result analysis the comparison between the existing and the optimized part then the two parts was done and evaluated. Depending on the outcome, it was preceded to the next step or returned to the design and analysis.

3 Results and Discussion

The first analysis that was carried out was the datum design and analysis. This analysis was conducted to compare between the datum design and the new design. The new design that was developed also underwent some analysis. The analysis that was conducted for this part was a stress analysis, for the space flange. The purpose of carrying out the analysis for this component is to identify the maximum stress for both designs [3].

Table 1 Material properties of the flange [4]

Material properties	Carbon steel
Density	7850 kg/m ³
Young’s modulus	207 GPa
Poisson’s ratio	0.3
Yield stress	220–250 MPa

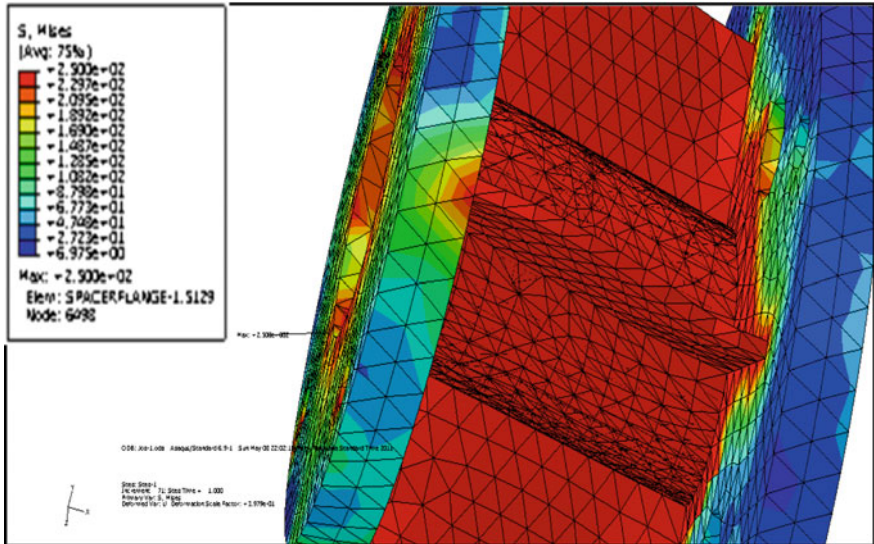


Fig. 7 Maximum stress of datum design

a. Datum Analysis

The datum space flange for off-road buggy was selected and studied at Universiti Kuala Lumpur Malaysian Spanish Institute. The material for this datum component is carbon steel as shown in Table 1, and the force exerted at this part was referred to the component that was available at the buggy. Refer to the Fig. 7 and Table 2, the maximum stress obtained from datum design was 250 MPa.

Table 2 Von Mises stress of datum design

Node label	Von Mises stress
Minimum	6.97504
At node	540
Maximum	250
At node	6724
Total	1.04457E + 06

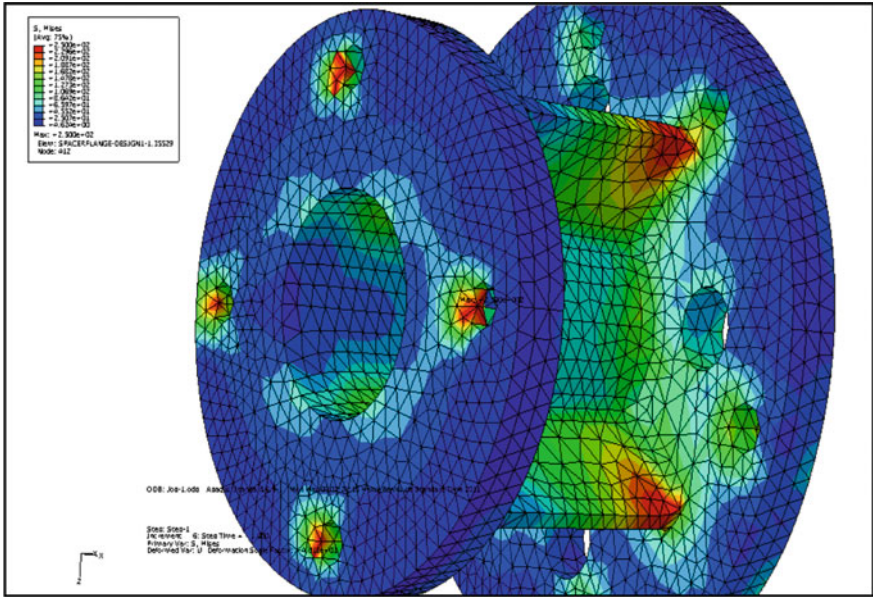


Fig. 8 Maximum stress of new design

Table 3 Von Misses stress of new design

Node label	Von Misses stress
Minimum	4.62
At node	1934
Maximum	200
At node	9225
Total	576.524E + 03

b. New Design Analysis

The maximum stress in Fig. 8 and Table 2, for the new design was reduced to 200 MPa. It was reduced due to the effect of dimensions changed for this new design.

From Table 3, it was found that the stress at the minimum for the optimization part is 4.62 MPa and the maximum stress has reduced from 250 to 200 MPa or 20% reduction.

4 Conclusions

The analysis was made to compare an existing and an optimized design. From the result in the first analysis of the datum design, it was found that the von Misses stress and displacement was very high. While the von misses stress and displacement for the new design was decreased. These results were influenced by the parameters diameter tube hollow and thickness for both designs which is datum and the new design. The objective of the project was achieved and the new flange design outperforms the datum.

References

1. Saeed Information. [http://en.wikipedia.org/wiki/Buggy_\(automobile\)](http://en.wikipedia.org/wiki/Buggy_(automobile)) (2012). Accessed 8 March 2012
2. Mohd, A.S., Shahril, K.: Fundamental analysis of bracket modeling for proton wira bumper. In: Proceedings for 3rd International Conference on Engineering Technology (ICET) at Renaissance Hotel, Kuala Lumpur (2011)
3. bin Shafee, K.S.: Design and Analysis of Neuroendoscopic Scissors. Universiti Sains Malaysia (2005)
4. General Properties of Steels. http://www.efunda.com/materials/alloys/alloy_home/steels_properties.cfm (2012). Accessed 9 March 2012

Material Removal Rate and Cutting Force of AISi/10% AlN Metal Matrix Composite Material in Milling Process Using Uncoated Inserts



Mohamad Sazali Said, Nurul Na'imy Wan, Norzalina Othman,
Ahmad Razlee Ab Kadir and Baizura Zubir

Abstract A machining process has been conducted to study the machining performance of aluminum silicon alloy (AlSi) metal matrix composite which has been reinforced with aluminum nitride (AlN) using the uncoated tool of inserts. Experiments were conducted at various cutting speeds, feed rates, and depths of cut, according to a fractional factorial array L9 of the Taguchi method. Statistical analysis including the signal-to-noise (S/N) ratio and analysis of variance was applied to study the characteristic performance of cutting speeds, feed rates and depths of cut during the milling operation. The machining performances were observed through material removal rate and cutting force, and these measurements were analyzed using the Taguchi method. From the Taguchi analysis, it was found that a cutting speed of 300 m/min; feed rate of 0.8 mm/tooth and depth of cut of 0.4 mm were the optimum machining parameters for the material removal rate, while the cutting speed of 370 m/min; feed rate of 0.4 mm/tooth and depth of cut of 0.3 mm were the optimum machining parameters for the cutting force.

Keywords Metal matrix composite · Milling process · Surface roughness
Taguchi method

M. S. Said (✉) · N. N. Wan · N. Othman · A. R. Ab Kadir · B. Zubir
Malaysian Spanish Institute, Universiti Kuala Lumpur, Kulim Hi-Tech Park,
09000 Kulim, Kedah, Malaysia
e-mail: msazali@unikl.edu.my

N. N. Wan
e-mail: nurulnaimy@unikl.edu.my

N. Othman
e-mail: norzalina@unikl.edu.my

A. R. Ab Kadir
e-mail: ahmadrazlee@unikl.edu.my

B. Zubir
e-mail: baizura@unikl.edu.my

1 Introduction

Porous media have been widely used in many applications. Among them, porous media are used as a medium of combustion to improve the combustion process which led to better emission and fuel efficiency [1, 2]. Many types of porous materials are available to be used as a medium of combustion. The materials can generally be classified into metallic and nonmetallic types. Ceramic porous media are among the nonmetallic type of porous materials used in combustion. They have a very high thermal resistance with excellent thermal shock resistance. Porous alumina (Al_2O_3) is a type of porous ceramic being recently studied. Porous ceramics are made from materials such as kaolin [3], porcelain [4, 5], alumina [6], mullite [7], silicon carbide (SiC) [8], and zirconia-based ceramics [9]. Pickenacker [10] has identified alumina, silicon carbide (SiC), and zirconium dioxide (ZrO_2) to be used as a medium of combustion. The porous medium can be in the form of pebbles or spheres with specific size or diameter arranged into a packed bed with relative porosities. It can be produced into a foam type by using the replication technique.

The effect of the porosity on the flow inside porous media has been studied in some recent works [11–13]. It shows a significant relationship between the porosity and the pressure loss at different velocities. In this work, the relation between these parameter has been investigated by using different types of porous media with different coatings. A 2D model has been developed to visualize the flow inside the testing conduit.

Metal matrix composites (MMCs) are composite materials widely used in aerospace, automotive, electronics, and medical industries. These materials possess outstanding properties such as high strength, low weight, high modulus, low ductility, high wear resistance, high thermal conductivity, and low thermal expansion. These desirable properties are mainly manipulated by the matrix, the reinforcement element, an interface [1]. MMCs exhibit poor machinability because of the hard and abrasive reinforcement used [2]. These materials are usually applied in bearings, automobile pistons, cylinder liners, and piston rings, connecting rods, sliding electrical contacts, turbo charger impellers, and space structures. The most popular reinforcements are silicon carbide (SiC) and alumina (Al_2O_3). Aluminum, titanium, and magnesium alloys are commonly used as the matrix phase [1].

MMCs possess the combined properties of metals and ceramics [3, 4]. The structure and properties of MMCs are affected by the type and properties of the matrix, reinforcement, and interface [5]. Thus, these materials have been increasingly used to replace conventional materials in numerous applications [4]. Surface roughness has been given significant attention for many years [6] and has been considered in fatigue load, precision fits, fasteners hole, and aesthetic requirements. In addition to tolerance, surface roughness imposes one of the most critical aspects in the selection of machine and cutting parameters in the planning process [6, 7].

In general, optimization of the cutting parameters is determined by the researcher's experience and knowledge or by the design of the experiment

(DOE) approach [8]. DOE is a powerful statistical tool used to study the effect of multiple variables simultaneously, and the technique provides an approach to efficiency design real-time experiments which will improve the understanding of the relationship between product and process parameters with the desired performance characteristic [9]. Also, a statistical analysis of variance (ANOVA) was performed to see which parameters were significant. The optimal cutting parameters were then predicted. Meanwhile, Taguchi's parameter design is an important tool for a robust design. It offers a simple and systematic approach to optimize designs for performance, quality, and cost.

The Taguchi's approach is based on the statistical design of experiments [10]. This can economically satisfy the needs of problem-solving and product or process design optimization. Several previous works have used the Taguchi method as a design tool for experiments in various areas, including metal cutting, and are listed in the references section [11, 12]. Factors should be included as many as possible; the method also can identify non-significant variables at the earliest possible opportunity. Taguchi creates a standard orthogonal array to accommodate this requirement. Depending on the number of factors, interactions, and levels needed, the choice is left to the user to select the standard, column-merging, or idle-column method, etc. Two of the applications, within which the concept of S/N ratio is useful, are the improvement of quality through variability reduction and the improvement of measurement. The S/N ratio characteristics can be divided into three categories; when the characteristic is continuous [10]:

$$\text{Nominal is the best characteristic; } S/N = 10 \log \frac{\bar{y}}{s_y^2} \quad (1)$$

$$\text{Smaller is better characteristics; } S/N = -10 \log \frac{1}{n} \left(\sum y^2 \right) \quad (2)$$

$$\text{Larger is better characteristics; } S/N = -10 \log \frac{1}{n} \left(\sum \frac{1}{y^2} \right) \quad (3)$$

2 Methodology

2.1 Surface Roughness Measurement

Coated carbide cutting tools are usually better performing than uncoated cutting tools in terms of surface finish. The surface roughness values using various cutting speeds, feed rate, depth of cut, and type of insert are shown in Table 1.

Table 1 Factors and levels used in the experiment

Factor/Level	0	1	2
A—cutting speed (m/min)	230	300	370
B—feed rate (mm/tooth)	0.4	0.6	0.8
C—depth of cut (mm)	0.3	0.4	0.5

2.2 Materials and the Milling Process

AlN reinforced Al–Si alloy matrix composite was fabricated using the stir casting method, where Al–Si alloy ingot, called the matrix material, was reinforced with AlN particles of 10 wt% reinforcement. The experimental study was carried out in a CNC Vertical Milling Center Lagun-GVC 1000 milling machine. Cutting inserts were attached to the tool with a body diameter of $\varnothing 20$ mm. The tool holder used was CoroMill R390-020C4-11L and the tool inserts was uncoated cemented carbide ISO catalog no: R390-11T08E-NL. The experiment has three different cutting speeds (230,300 and 370 m/min) with constant feed rate (0.4, 0.6, 0.8 mm/rev) and depth of cut (0.3, 0.4 and 0.5 mm) under dry cutting condition. The worked material was fabricated in the form blocks of 120 mm length \times 50 mm width 50 mm thickness.

2.3 Taguchi Method

In this experiment, with three factors (each with three levels), the fractional factorial design used was a standard L_9 (3^3) orthogonal array. The orthogonal array was chosen because of its minimum number of required experimental trials. Each row of the matrix represented one trial [13]. The smaller, the better characteristic is used to optimize the surface roughness and for the tool wear measurement is analyzed using the larger, the better characteristic in the milling process of aluminum silicon metal matrix composite.

3 Results and Discussion

3.1 Machining Performance and S/N Ratio

The machining performance of AlSi/10%AlN was analyzed based on the Taguchi method and S/N ratio as shown in Table 2. The cutting force was analyzed according to Taguchi's smaller-is-better characteristic while the analysis for material removal rate was conducted using the larger-is-better characteristic.

Table 2 Experimental design with the L_9 orthogonal array and the S/N ratios for uncoated cutting tools

Test no	A	B	C	Material removal rate	S/N ratio	Cutting force	S/N ratio
1	0	0	0	25.030	27.9692	83.717	-38.4563
2	0	1	1	39.680	31.9714	262.102	-48.3694
3	0	2	2	48.550	33.7238	403.179	-52.1100
4	1	0	1	44.166	32.9018	200.578	-46.0457
5	1	1	2	43.042	32.6778	293.202	-49.3433
6	1	2	0	36.592	31.2677	152.064	-43.6405
7	2	0	2	44.458	32.9590	173.153	-44.7686
8	2	1	0	25.604	28.1662	43.133	-32.6962
9	2	2	1	57.287	35.1611	225.831	-47.0757

3.2 Optimization of Machining Conditions Using the Taguchi Method

This study was conducted to determine the optimum condition for the material removal rate and cutting force when AISi/AlN is cut using uncoated inserts. In the Taguchi method, the analysis focuses on process optimization through the S/N ratio, and the result will be supported by the analysis of variance. Both analyses for the material removal rate and cutting force using the uncoated tool are obtained using Minitab 17.

3.3 Material Removal Rate

Figures 1 and 2 show the mean S/N ratio and means of material removal rate using the uncoated tool obtained. The slopes of the graphs clearly show that the depth of cut is the most significant factor, followed by the feed rate, and cutting speed. Based on Fig. 1, the optimum parameters for the material removal rate is cutting speed of 300 m/min; feed rate of 0.8 mm/tooth and depth of cut of 0.4 mm.

3.4 Cutting Force

Figures 3 and 4 show the mean S/N ratio and means of cutting force using the uncoated cutting tool in the milling process. The slope of the graphs also clearly show that the depth of cut is the most significant factor, followed by the cutting speed, and feed rate. Based on Fig. 3, the optimum parameters for surface

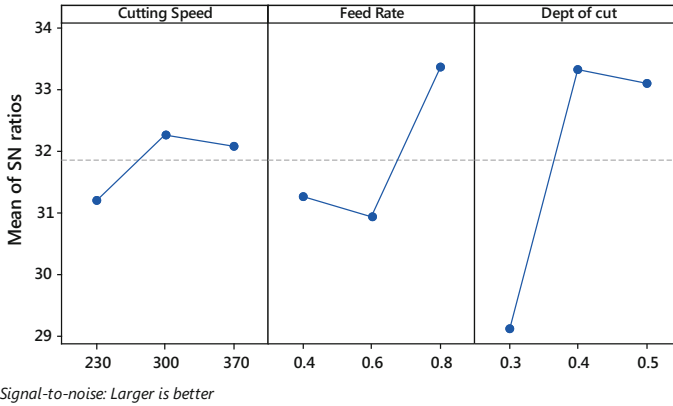


Fig. 1 Main effect plot for S/N ratios of the material removal rate

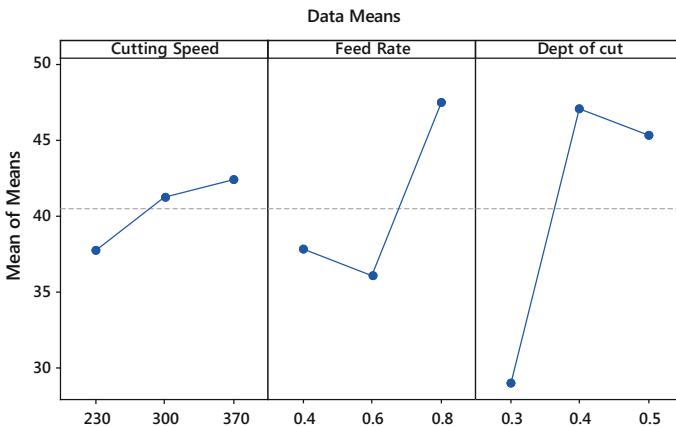


Fig. 2 Main effect plot for means of material removal rate

roughness is disclosed at cutting speed of 370 m/min; feed rate of 0.4 mm/tooth and depth of cut of 0.3 mm.

3.5 Analysis of Variance (ANOVA)

The analysis of variance was conducted to determine which machining parameters significantly affect the tool life. ANOVA was performed to find whether individual factors that affect the material removal rate and cutting force were meaningful. From the ANOVA results of S/N ratio presented in Table 3, the factor of feed rate and depth of cut significantly affected the material removal rate at which its P-value

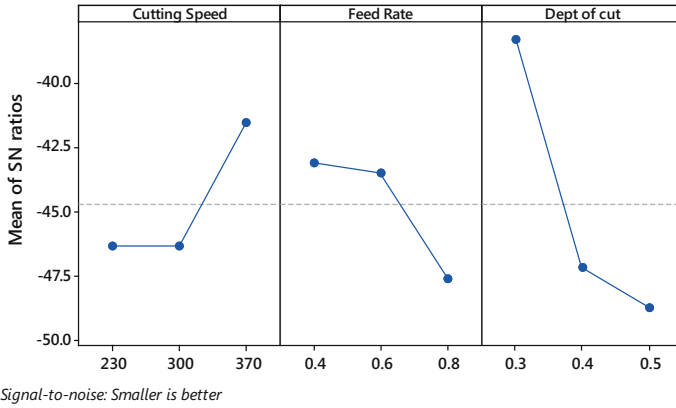


Fig. 3 Main effect plot for S/N ratios of cutting force

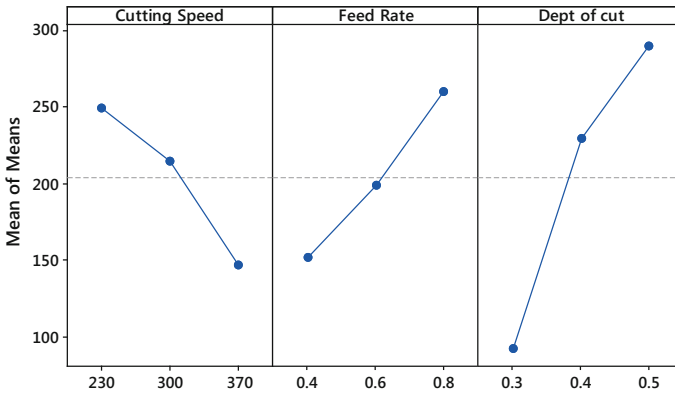


Fig. 4 Main effect plot for means of cutting force

was less than 0.05. From Table 3, the most influential factor was found to be the depth of cut with 72.43%, followed by feed rate with 22.67% and the remaining percentage were explained by cutting speed and residual error.

In Table 4 which represented the ANOVA results of S/N ratio, the only factor of the depth of cut was significantly affect the cutting force as its P-value was less than 0.05. Based on the percentage contribution from Table 4, the most influential factor was found to be the depth of cut with 67.99%, followed by cutting speed and feed rate with 16.46% and 13.39% respectively.

Table 3 ANOVA of S/N ratio for the material removal rate

Factors	DF	SS	MS	F	P*	PD
Cutting speed	2	1.9244	0.9622	5.47	0.154	4.14
Feed rate	2	10.5377	5.2689	29.98	0.032	22.67
Depth of cut	2	33.6649	16.8325	95.78	0.010	72.43
Residual error	2	0.3515	0.1757			0.76
Total	8	46.4785				100

DF Degree of freedom, *SS* Sum of square, *MS* Mean of square, *PD* Percentage distribution

*Significance level = 0.05

Table 4 ANOVA of S/N ratio for cutting force

Factors	DF	SS	MS	F	P*	PD
Cutting speed	2	46.351	23.176	7.59	0.116	16.46
Feed rate	2	37.693	18.847	6.18	0.139	13.39
Depth of cut	2	191.437	95.718	31.36	0.031	67.99
Residual error	2	6.104	3.052			2.16
Total	8	281.585				100

DF Degree of freedom, *SS* Sum of square, *MS* Mean of square, *PD* Percentage distribution

*Significance level = 0.05

4 Conclusion

In comparing the machining performance between uncoated and TiN cutting tools for milling process of AlSi/10%AlN MMCs, it was found that the uncoated cutting tools gave a better surface finish which is smoother. Through the Taguchi method, the optimum parameters for the milling process using uncoated cutting tools were set at 230 cutting speed, 0.4 feed rate and 0.3 depth of cut. These optimum parameters will progress the competitive machining operation from the economical and manufacturing perspective in the automotive industry.

References

1. Srinivasan, A., Arunachalam, R., Ramesh, S., Senthilkumaar, J.S.: Machining performance study on metal matrix composites-a response surface methodology approach. *Am. J. Appl. Sci.* **9**(4), 478–483 (2012)
2. Chandrasekaran, M., Devarasiddappa, D.: Development of Predictive Model for Surface Roughness in end Milling of Al-SiCp Metal Matrix Composites using Fuzzy Logic, vol. 68, World Academy of Science, Engineering and Technology (2012)
3. Tomadi, S.H., Ghani, J.A., Haron, C.H., Daud, A.R.: Optimization of cutting parameter on tool life and surface roughness in end milling of AlSi/AlN MMC. In: Taguchi Method and Grey Relational Analysis. ICRQE 13, Proceeding (2013)

4. Abdullah, Y.: *Fabrikasi Dan Pencirian Komposit Al-Si Diperkuat Zarah Halus SiC Dengan Menggunakan Tuangan Anduk*. Universiti Kebangsaan Malaysia, Bangi, Selangor (2009)
5. Babu, N.H., Fan, Z., Eskin, D.G.: Application of external fields to technology composite materials. In: TMS2013 Annual Meeting Supplemental Proceedings TMS (2013)
6. Tomadi, S.H., Ghani, J.A., Che Hassan, C.H., Daud, A.R.: Effect of machining parameter on tool wear and surface roughness of Al-AlN reinforce MMC in end milling machining. *J. Eng. E-trans. Electron. J. Univ. Malaya (EJUM)* (ISSN 1823-6379) (2011)
7. Wang, X., Feng, C.X.: Development of empirical model for surface roughness prediction in finish turning. *Int. J. Adv. Manuf. Technol.* **20**(5), 348–356 (2002)
8. Tomadi, S.H., Ghani, J.A., Che Haron, C.H., Daud, A.R.: Optimisation of cutting parameters for end milling AlSi/AlN metal matrix composite using the taguchi method. *Mater. Sci. Forum* **773–774**, 437–444 (2014)
9. Radika, N., Subramaniam, R., Babudeva Senapathi, S.: Machining parameter optimization of an aluminium hybrid metal matrix composite by statistical modelling. *Ind. Lubr. Technol.* **65** (6), 425–435 (2013)
10. Park, S.H.: *Robust Design and Analysis for Quality Engineering*. Chapman and Hall (1996)
11. Yang, W.H., Tarng, Y.S.: Design optimisation of cutting parameters for turning operations based on the taguchi method. *J. Mater. Process. Technol.* **84**, 122–129 (1998)
12. Lin, T.R.: Experimental design and performance analysis of TiN-coated carbide tool in face milling stainless steel. *J. Mater. Process. Technol.* 1–7 (2002) (in Press)
13. Jaharah, A.G., Choudhury, I.A., Hassan, H.H.: Application of taguchi method on the optimization of end milling parameters. *J. Mater. Process. Technol.* **154**, 84–92 (2004)

Synthesis of Polypropylene Solid State Electrolytes for Batteries Using a Polymerization Heat Chamber



Muhamad Husaini Abu Bakar and Kartina Farah Hana

Abstract Polypropylene solid-state electrolytes are a material of solid electrolytes. The solid electrolytes were prepared by mixing a hydroxide solution and polypropylene. However, the electrolyte is very sensitive to the temperature change. Temperature is an essential factor in producing an optimal cheap solid-state electrolyte. This study aimed at determining the temperature effect on the solid state electrolyte polymerization. The different solid-state electrolyte were synthesized by varying the number of molarity of the potassium hydroxide, the weight of the polypropylene and the temperature that was used to heat the polypropylene. The solution molarities that were used are 1, 2, and 3 M and the propylene weight was 5, 10 and 15 g and the six temperature levels were used, i.e. 160, 170, 180, 190, 200, and 210 °C. As a result, the voltage is 1.1 V for 2 M of KOH, and the temperature is 180 for the highest voltage production. As a conclusion, with the increase of the molarity of KOH the voltage also increases. A specific temperature needs to be determined to ensure that the maximum voltage is produced by the battery with the solid-state electrolyte. This temperature and molar configuration is important to search a better solid state electrolyte for the battery.

Keywords Polypropylene (PP) • Solid-state electrolyte • Potassium hydroxide solution (KOH) • Battery

M. H. Abu Bakar (✉) • K. F. Hana
System Engineering and Energy Laboratory, Malaysian Spanish Institute,
Universiti Kuala Lumpur, Kulim Hi-Tech Park, 09000 Kulim, Kedah, Malaysia
e-mail: muhamadhusaini@unikl.edu.my

K. F. Hana
e-mail: kartinafarah@gmail.com

1 Introduction

Solid state electrolyte a very active field of science. A solid electrolyte was first discovered in 1970. Solid electrolytes are made from polymer and are also known as polymer electrolytes. The polymer electrolyte is from a new research area in inorganic material. The new application for the solid electrolyte is the lithium battery, the dye-sensitized solar cell, and the fuel cell. Among all the applications, the lithium battery plays a significant role in daily life not only because of its widely use in portable devices but also its application can be used in electric vehicles.

Lithium-ion batteries are mainly composed of cathodes, anodes, separators, and liquid electrolytes. Furthermore, batteries composed of solid polymer electrolyte materials are also lighter and more flexible. However, the ionic conductivities of current solid polymer electrolytes are too low for commercialization. Traditional lithium-ion batteries have critical safety issues because of using highly flammable organic liquid electrolytes or polymer electrolytes which have a low thermal stability and a low flame point that can cause fire accidents and explosions if they are in improper used.

Due to these safety issues, the use of highly flammable organic liquid electrolytes was avoided so that the solid-state electrolytes become a good choice. This is because the organic liquid electrolytes have been replacing the organic solid state that has high thermal stability.

Besides that, the solid-state electrolyte have many other advantages, e.g. there which are there are no liquids used so that it also can reduce weight in the battery. Secondly, solid state electrolytes have much better electrochemical stability and compatible with higher potential cathode materials to increase the energy density compared to the organic liquid electrolytes. Solid state electrolytes also have excellent mechanical properties.

Solid state electrolytes in solid batteries are capable of high voltage, long life cycle and are safer due to their compact size compared to liquid batteries that are considered to be flammable and dangerous [1]. This solid-state electrolyte has more advantages than the liquid electrolytes. A solid state battery is traditionally expensive to make so that this experimental work aims at using a material that can be easily found and that is cheaper. Because of that, there is a need to explore the new material of solid-state electrolytes.

The objective of this project is to develop an experimental setup for polypropylene solid-state electrolytes. Then, based on the experimental setup, the aim is to continue to study the effect of the potassium hydroxide concentration on the nominal voltage in the battery and the effect of temperature of the polymerization rate. The main objective of this project is to find the voltage of the polypropylene solid-state electrolyte.

2 Methodology

2.1 The Potassium Hydroxide Solution

The solution for the solid state electrolytes was prepared first. The molar weight of the concentration needs to be calculated to get the exact weight before to dilute it in distilled water. The weight of potassium hydroxide (KOH) needs to be measured. The solution was prepared by mixing the potassium hydroxide was mixed with the distilled water and put aside for 30 min before the solution was mixed with the polypropylene (PP).

The molar concentration can be calculated according to the following relation:

$$\text{Molar concentration} = \frac{\text{mol solute}}{L \text{ solution}} \quad (1)$$

This equation can be solved for the moles of the solution. Inserting the molar concentration and volume gives the moles of potassium hydroxide solution.

$$\begin{aligned} \text{mol solute} &= \text{molar concentration} \times L \text{ solution} \\ &= 1\text{M} \times 0.05\text{L} = 0.05 \text{ mol} \end{aligned} \quad (2)$$

The moles of potassium hydroxide solution can be converted to grams using the molecular weight.

$$\text{g KOH} = 0.05 \text{ mol} \times \frac{56.1\text{g}}{1 \text{ mol}} = 2.81 \quad (3)$$

2.2 The Weight of the Polypropylene

First, the polypropylene was divided into three types of weight which are 5, 10, and 15 g. The 5 g polypropylene was heated at 170 °C in the polymerization heat chamber for 6 min. After 6 min, the polypropylene (PP) was mixed with 20 ml the solution of 1 M and heated at the same temperature for 11 min. The electrolyte will be formed after 11 min of the heating. After that, when the mixture was already dissolved by each other, and it became like a plastic plate with a certain thickness. Then the electrolyte was taken out to rest at room temperature for 1 h before the first reading of the voltage was taken.

This step was repeated for the 2 and 3 M of the concentration, but the difference is the time taken for the first heat of the polypropylene which are 10 min for the 10 g of the polypropylene and 15 min for the 15 g of the polypropylene. However, for the second heating of the solution is the same time which is 11 min.

This is because 10 and 15 g of the polypropylene are slowly melting due to its different weight and resizing quantities of the resins.

3 Result and Discussion

3.1 *The Different of Potassium Hydroxide Concentration and Voltage*

For the potassium hydroxide concentration, the voltage will increase depending on the number of moles that have been used in the solution. The higher the molar weight of the concentration that has been used, the higher the voltage. This is because the number of moles also affected the voltage of the solid polypropylene state.

In Fig. 1 below, the graph shows the different potassium hydroxide concentration and the voltage. The result has been recorded from day one until day seven to see the difference between the voltage and the number of the concentration.

To get this result, there are using constant temperature which is 170 °C; the time is taken for the second heat which is 11 min and the same size of the beaker. The first voltage is taken after the solid electrolytes are has been rested for 1 h. For the next reading has been taken at the same time every night.

The graph shows the difference of the voltage reading for the different numbers of concentration for 5 g of the polypropylene. The voltage reading for the 1 M of the potassium hydroxide concentration is increasing for the three days, constant for two days and decreasing at the seventh day. This shows that the electrolyte can be

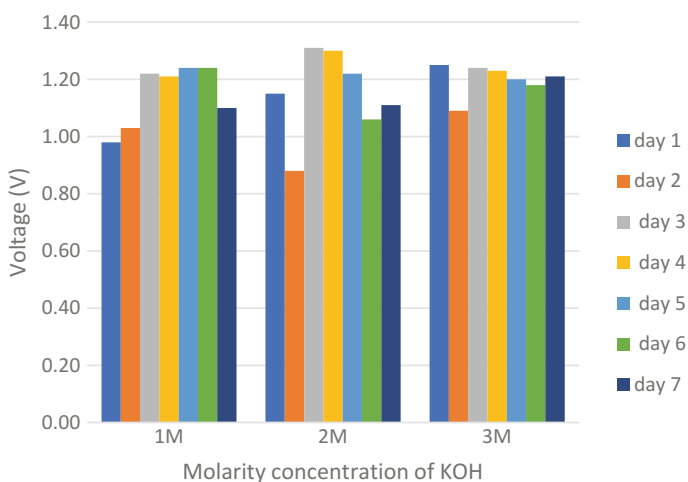


Fig. 1 Different between potassium hydroxide concentration and the voltage (5 g pp)

used for a long time and at a specific time it is still increasing the voltage. For 2 M of the potassium hydroxide concentration also similar to the 1 M of the concentration because it also has increased and decreased the voltage at the specific time. For 3 M of the concentration, it is more stable than that 1 and 2 M of the concentration because the chart shows that the voltage is very high and the voltage that is decreasing is smaller compared to the 1 and 2 M of the concentration. The average voltage for 1 M of the concentration is between 0.9 until 1.24 V, for 2 M of the concentration between 0.8 until 1.3 V and for 3 M of the concentration between 1.1 until 1.3 V.

Figure 2 shows the difference between the concentrations of the potassium hydroxide and the voltage for 10 g of polypropylene. The result shows that the chart is increasing from the 1 M until the 3 M of the concentration. For the 1 and 2 M of the concentration, the difference between the voltages is not so much but for different but for 3 M of the concentration, there is a significant difference compared to 1 and 2 M of the concentration. The average voltage for 1 M of the concentration is between 0.64 until 0.9 V, for 2 M of the concentration between 0.8 until 1.0 V and for 3 M of the concentration between 1.2 until 1.3 V.

Figure 3 shows the difference between the concentrations of the potassium hydroxide and the voltage for 15 g of polypropylene. The result shows that the chart is decreasing for the 1 M of the concentration. For the 2 M of the concentration, the result shows that the voltage is more stable than for 1 M of the concentration. The difference between the voltages is not much different but for 3 M of the concentration, there is a significant difference compared to 1 and 2 M of the concentration. The average voltage for 1 M of the concentration is between 0.6 until 0.85 V, for 2 M of the concentration between 0.6 until 0.7 V and for 3 M of the concentration between 1.0 until 1.15 V.

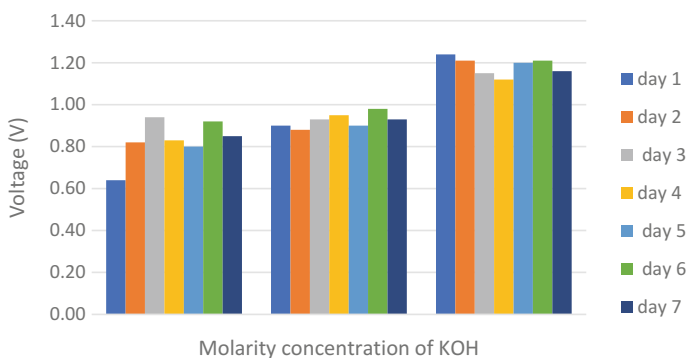


Fig. 2 Different between potassium hydroxide concentration and the voltage (10 g pp)

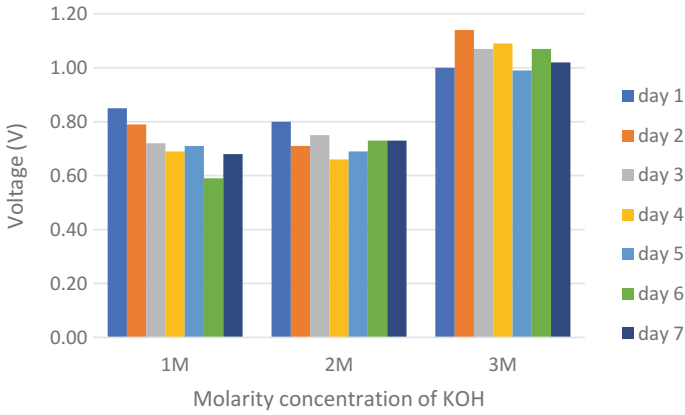


Fig. 3 Different between potassium hydroxide concentration and the voltage (15 g pp)

3.2 The Different Between Weight of Polypropylene and Voltage

Figure 4 shows that the difference between weight that has been used for the polypropylene and the voltage reading for the solid state. The graph shows the voltage decrease when more polypropylene is used. This is because the polypropylene takes time to melt and dilute with the potassium hydroxide solution. For 1 M of the concentration, the voltage is very high, and the lowest voltage is for 3 M of the concentration.

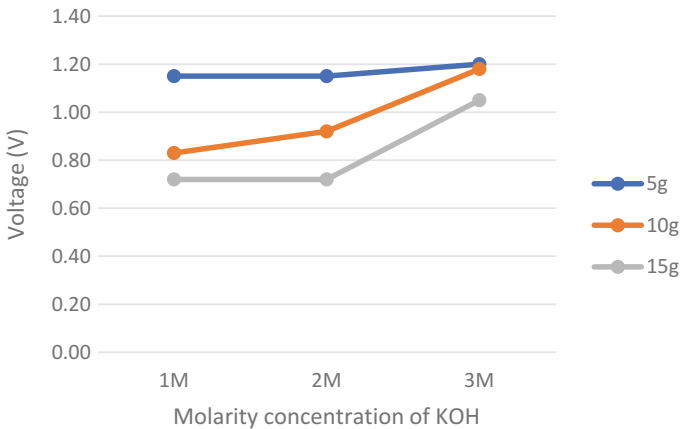


Fig. 4 The different between weight of polypropylene and voltage

The polypropylene will take time to dilute with the solution because the resin took much time to melt undoubtedly and to achieve the desired temperature to dilute with the solution. If the polypropylene is not properly melted, it is hard to dilute, and this will affect the voltage of the solid-state electrolyte, and it also will not become the exact solid-state electrolyte.

3.3 *The Different Between Temperature and Voltage*

Figure 5 shows the difference between the temperature and the voltage. This graph shows that when the temperature is 190 °C, the voltage reading of the polypropylene solid-state electrolyte is decreasing until 0.2 V. This is because when the temperature is higher than 180 °C, the polypropylene becomes vaporized. This happens when the melting point of the polypropylene exceeds the desired temperature. So that, the voltage is decreasing. It also happens because of the polypropylene cannot dilute with the solution to become the solid-state electrolyte.

To get this result, a constant weight of 5 g of the polypropylene is used; time taken for the second heating is 11 min and the same size of the beaker. The first voltage was taken after the solid electrolytes rested for 1 h.

3.4 *Solid State Electrolyte*

The solid state electrolyte was measured by putting the electrolyte between the metal. The voltage is taken for several times to make sure that the voltage is correct. Figure 5 shows how the solid-state electrolyte has been measured. This show that the solid-state electrolytes are easy to use, lightweight and the size is compact.

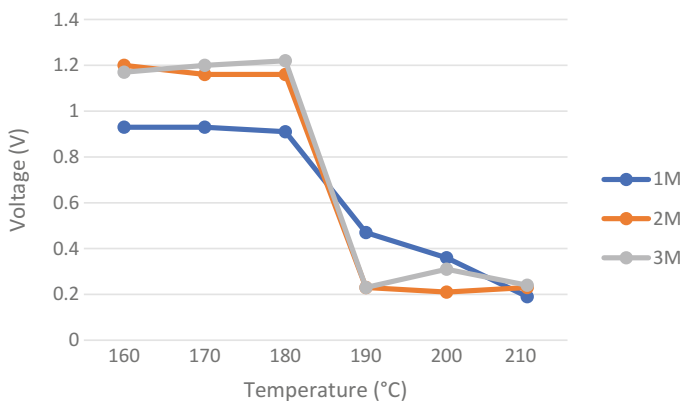


Fig. 5 The different between the temperature and the voltage

So that it helps to reduce space when used and it is easy to carry. It is also safer than a liquid battery due to its compact size.

This solid state also has a stable structure because it has been made from a polymer and it is also easy to reshape the structure. The structure can be reshaped by heating the polymer at a specified temperature and time. This solid-state electrolyte has more advantages compared to the liquid electrolytes.

4 Conclusion

In this study, the potassium hydroxide concentration that has been used can affect the voltage of the polypropylene solid-state electrolyte. The higher the molar weight of the concentration, the higher the voltage. However, there are several problems to get the current which is the resistance of the polypropylene solid-state electrolytes are very high so that it cannot conduct the electricity [2]. Besides that, the surface of the polypropylene solid-state electrolyte also needs to touch the metal surface to get the exact reading entirely.

The voltage will decrease if weight of polypropylene is used because the polypropylene takes time to absorb the solution. The solution and the polypropylene should be absorbed so that the potassium hydroxide is affected by the whole polypropylene.

Lastly, the polypropylene will be vaporized at 190 °C and above. The solid-state electrolyte cannot be formed because of the vaporization. The best temperature for the polymer is 160, 170, and 180 °C this is because of the melting point of the polypropylene.

For the future recommendation, these solid-state electrolytes need to focus on reducing the resistance since the resistance is so high so that the current ampere is low. Because of the resistance is so high it cannot generate the current. Besides that, there are still needs to measure the conductivity of this solid-state electrolyte based on the resistance and the voltage of the solid-state electrolytes.

Acknowledgements All the experiment and analysis conducted by System Engineering and Energy Laboratory, Universiti Kuala Lumpur, Malaysian Spanish Institute, Kulim Kedah, Malaysia.

References

1. Takada, K.: Progress in solid electrolytes toward realizing solid-state lithium batteries. *J. Power Sources* **394**, 74–85 (2018). <https://doi.org/10.1016/j.jpowsour.2018.05.003>
2. Liu, Q., Geng, Z., Han, C., Fu, Y., Li, S., He, Y., Li, B.: Challenges and perspectives of garnet solid electrolytes for all solid-state lithium batteries. *J. Power Sources* **389**, 120–134 (2018). <https://doi.org/10.1016/j.jpowsour.2018.04.019>

The Effect of Cutting Fluid Condition on Surface Roughness in Turning of Alloy Steel



Baizura Zubir, Mohd Zaki Abdul Razak,
Ahmad Fauzie Abd Rahman and Mohamad Sazali Said

Abstract During machining processes heat is generated. The use of a cutting fluid provides lubrication and cooling effects which improve the final quality of the workpiece. Nevertheless, cutting fluid application provides some problems involving costs, environmental and health issues. In this paper, the relationship between the cutting lubricant and the surface roughness of 4340 alloy steel using three different lubricant conditions; i.e. dry machining, minimum quantity lubrication (MQL) and wet machining, is investigated. The turning parameters include the cutting speed, feed rate, cutting depth and time were considered using a carbide insert (CNMG 12 04 08-QM) H13A for light and medium turning. Then, the effects of these parameters on the surface roughness were studied. The results shows that the surface roughness is the best when using MQL on the light turning followed by wet and dry machining. Meanwhile for medium turning, the preferred condition is wet machining compared to MQL and dry machining.

Keywords Turning · Cutting fluid · Surface roughness · Alloy steel

B. Zubir (✉) · M. Z. Abdul Razak · M. S. Said
Malaysian Spanish Institute, Universiti Kuala Lumpur,
Kulim Hi-Tech Park, 09000 Kulim, Kedah, Malaysia
e-mail: baizura@unikl.edu.my

M. Z. Abdul Razak
e-mail: mzaki@unikl.edu.my

M. S. Said
e-mail: msazali@unikl.edu.my

A. F. Abd Rahman
Politeknik Tuanku Sultanah Bahiyah, Kulim Hi-Tech Park,
09000 Kulim, Kedah, Malaysia
e-mail: fauzie@ptsb.edu.my

1 Introduction

The use of cutting fluid now very common in the manufacturing industry. It will determine the quality of the surface finish produce after machining process. In order to achieve a good surface finish, specified coolants or lubricants are utilized to reduce the friction coefficient between the grain and the workpiece by way of cooling and lubricating the cutting site of the machine tools. The main purpose of using a cutting fluid in machining processes is to reduce the cutting temperature and it helps to remove the heat and chips produced during machining. It also can improve the tool life and surface conditions.

The advantages of using a cutting fluid have been questioned lately, due to several negative effects. The cutting fluid can cause skin and lung diseases to the operator and air pollution to the nature. For companies, the costs of the cutting fluid influence the amount of total machining costs. This means that these companies are forced to spend a lot of money for cutting fluids. Elimination of using cutting fluids or dry machining can be a significant economic incentive but can cause tool wear problems and low surface finish.

Some of the alternatives that have been sought to minimize the use of the cutting fluid without decrease in surface quality. For these situations, semi dry or a minimum quantity of lubricant is the best way because this will produce a better surface finish, and it also will bring down manufacturing cost and relieve pollution and risk of lung disease.

During performing the machining processes, such as turning, a cutting fluid can be applied due to various reasons. First, it will cause the chip to evacuate. Second, its coolant capacity plays an important role in the removal of heat from the contacts. Third, it will improve the tribological behavior of the different interactions (tool rake face/chip and tool flank face/workpiece). Lastly, the additives in the fluid will affect the lubrication capability.

The surface roughness usually effects the machined surfaces. It is defined as the finer irregularities of the surface texture, which result due to the action of the production process in a great impact on the product quality. Furthermore a good-quality machined surface significantly improves fatigue strength, corrosion resistance, and creep life [1].

1.1 Propose of the Study

The purpose of this study is to investigate the effect of the cutting fluid condition on the cutting performance of turned parts. The cutting fluid quantities are; dry machining, minimum quantity lubrication (MQL) and wet machining. An approach based on the tool work combination method has been performed to identify the ideal testing parameters range. The study helps to give better understanding of the behavior of the tool and the surface roughness under medium and light cutting

conditions, excluding high thermal and mechanical loads. During each test, the surface roughness and chip formation are measured and compared.

1.2 Objectives of the Study

The objectives of the study are to identify the comparison between minimum quantity lubricant with dry and wet machining process and how this effects the surface roughness and to identify the effectiveness of a minimum quantity lubricant proportional to the cutting parameter.

1.3 Cutting Fluids

Typically, cutting fluids are essential in metal cutting operations in order to maintain and improve the cutting conditions [2, 3]. A cutting fluid practically can act as a coolant and as a lubricant which are the two most important ways in machining [3]. These two kinds of cutting fluids carry out the different actions which is at low cutting speeds, the lubricating action is more important, whereas at the higher cutting speeds, the cooling effect is more important due to the heat generated [3]. The main purpose of using a cutting fluid in machining operations is to reduce friction, heat and wear generated during the cutting process [1, 2, 4]. It is necessary to improve the tool life and surface finish condition of the workpiece beside in carrying away the heat and chips produced during machining from the cutting zone [1, 3, 4].

Even though the cutting fluid provides positive effects on the machining process, there are some considerations that need to be mentioned such as the environmental effect and cutting fluid maintenance. There are a number of potential environmental concerns with cutting fluids which is that the bacterial growth can lead to skin reactions and the release of small fluid droplets into the atmosphere [3]. Because the machine tool operator is usually in direct contact with the working environment, the health effects resulting from the operator's contact with fluids is the primary concern. Mist, fumes, smoke and odors from cutting fluids also can cause severe skin reaction and respiratory problems [1].

The significant costs associated with the cutting fluid application places particular importance on good maintenance of these fluids to extend the life span. However, these fluids are difficult to dispose and expensive to recycle. In industrial companies, the costs of the cutting fluid will be influenced by the amount of total machining. Furthermore, it has been estimated that metal working fluids constitute about 7–17% of the total machining costs in each year [1].

Generally, there are four basic categories of cutting fluids which is straight or neat oils, soluble oils, synthetic fluids and semi synthetic fluids. Many practical cutting fluids have a mineral or vegetable oil base, mineral oil being the more

widely used [3]. The cutting fluid contains coolant, lubricant and additives such as surfactant, evaporator, stabilizer, emulsifier, biocide and deodorizing agent.

2 Methodology

The experiments were conducted on the conventional lathe machine and have been carried out by turning rods of 50 mm diameter and 150 mm length. Alloy steel was selected as work material to be machined as shown in Table 1. From the experiment, the cutting speed, feed rate and depth of cut were fixed as specific parameters both during light and heavy operations. Cemented carbide was selected as cutting tools. The experiments were performed under three different coolant environments of dry cutting, minimum quantity lubricant and wet machining conditions as shown in Table 2. The surface roughness for these specimens was evaluated using a profilometer known as SURFPAK.

Table 1 Experimental conditions

No.	Item	Description
1	Machine used	CNC lathe Lathe machine Universal precision lathe
2	Machining lubricant condition	<ul style="list-style-type: none"> • Dry machining • Minimum quantity lubricant • Wet machining
3	Type of turning operation	Turning operation <ul style="list-style-type: none"> • Medium machining • Light machining
4	Machining parameters	<ul style="list-style-type: none"> • Cutting speed: specific • Depth of cut: specific • Feed rate: specific
5	Cutting tools	Insert carbide (CNMG 12 04 08-QM)H13A
6	Material of workpiece	Alloy steel/round bar (sae 4340/40CrNiMo)
7	Measurement device	Surface roughness tester (SURFPAK)

Table 2 The specific parameter according to the 2 types of condition

No	Item	Light condition	Medium condition
1	Cutting depth (mm)	0.96	2
2	Feed rate (mm/r)	0.18	0.3
3	Cutting speed (rpm)	140	255
4	Time	40–45 min	50–60 min

3 Results and Discussion

After all experiments had been conducted, the surface roughness for AISI 4340 (Alloy Steel) of each condition were measured using the surface roughness tester (Surfpak). All the data is collected in Tables 3 and 4 based on their cutting conditions which are light cutting for turning and facing operation and medium cutting for turning and facing operation with different machining conditions. Each condition takes the average of three readings to improve the accuracy.

Table 3 Surface roughness based on turning operation

Surface roughness (Ra)		Type of operation: turning			
No of test	Operation parameter	Dry machining			
		Reading 1 (µm)	Reading 2 (µm)	Reading 3 (µm)	Average (µm)
1	Medium cutting	9.210	10.00	9.849	9.686
2	Light Cutting	4.281	4.471	4.450	4.400
No of test	Operation parameter	Wet machining			
		Reading 1 (µm)	Reading 2 (µm)	Reading 3 (µm)	Average (µm)
3	Medium cutting	4.964	4.801	4.228	4.664
4	Light cutting	4.625	4.620	4.353	4.533
No of test	Operation parameter	MQL machining			
		Reading 1 (µm)	Reading 2 (µm)	Reading 3 (µm)	Average (µm)
5	Medium cutting	10.408	10.030	6.835	9.091
6	Light cutting	3.358	3.296	3.340	3.331

Table 4 The value of surface roughness for turning operation

Surface roughness (Ra)	Machining condition		
Cutting parameter	Dry machining (µm)	Wet machining (µm)	MQL machining (µm)
Light cutting	4.400	4.533	3.331
Medium cutting	9.686	4.664	9.091

Note The smooth surface roughness for light cutting was during MQL machining where it shows the lowest value of 3.331 µm. Meanwhile for medium cutting, the smooth surface finish was 4.664 µm when using wet machining

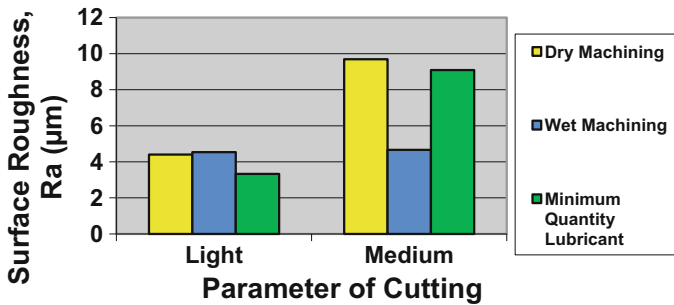


Fig. 1 Graph cutting parameter versus surface roughness for turning operation

Figure 1 shows the cutting parameter versus surface roughness for the turning operation. The reading was taken for different parameter conditions which are light condition and medium condition. There are 3 different color columns which are yellow, blue and green and they represent the different conditions. Yellow column represent for dry machining, blue the wet machining and green the minimum quantity lubricant.

Figure 1 also shows the lowest and highest value of surface roughness according to the light cutting on minimum quantity lubricant and wet machining. Meanwhile, for the medium cutting, the lowest and highest value of surface roughness is obtained respectively to the wet and dry machining.

The minimum quantity lubricant machining condition is only appropriate and effective when applied on light cutting parameter on turning operation. By looking at the circumstances of these operations, the reaction of the minimum quantity lubricant will provide a better surface than the others machining conditions. The capability of the coolant at minimum quantity lubricant is completely enough to reduce the temperature which is commonly elevating if the lubrications are not applied. The function of the coolant on minimum quantity lubricant will prevent the probability of tool wear that occurred on carbide cutting tool.

According to the function and usage of coolant, generally it is essential for each machining process to produce a good surface quality. Even the requirements of machining are barely, the condition of wet machining also influences the irregularity of the surface when the amount of lubrication is flooding the workpiece during operation.

When the cutting parameters are changed to the medium cutting, the effectiveness of the coolant usage is proven by wet machining operation. The lowest value of surface roughness was obtained on wet machining. The coolant properties are crucial to decrease tool wear and to extend the tool life. During wet machining applied on medium cutting, the functions of the coolant are important in achieving the desired size, finish and shape of the workpiece. The condition of the wet machining will remove away chips and metal fines from the tool and workpiece interface to prevent a finished surface from becoming marred and also to reduce the

occurrence of built-up edge (BUE). The surface of the workpiece will become better when the coolant plays a major role in maintaining the machined material at ambient temperature.

Meanwhile, the highest value of surface roughness was obtained on dry machining. The contact between the chip and tool will gain the chip temperature and thus affect directly to the cutting tool that will causes tool wear. The defect of the cutting tool will affect the surface quality of the workpiece. The condition of minimum quantity lubricant is not sufficient when applied on medium cutting. The weaknesses of minimum quantity lubricant and dry machining are the same when the cutting speed is in low running thus the chips will be trapped at the cutting area. When the chips stuck at the cutting tool, more or less it will be influencing the surface of the workpiece because it has the potential to scratch it.

Images of chip formation were taken for each cutting parameter and condition for both machining operations that consists of the turning and facing operation. There are 3 types of chips produced which are the continuous chip, continuous chip with BUE and discontinues chip. The continuous chip which is like a ribbon flows along the rake face. Thus, on a continuous chip one does not see any notches. It can be assumed that each layer of metal flows along the slip plane till it is stopped by working hardening. The condition which favors continuous types of chip is high temperature, sharp cutting tool, larger rake angles, low cutting speed and ductile work material. Discontinuous chips are always produced when machining in very low or high cutting speeds. It may also be produced when machining in large cutting depth.

There are many factors that influence the type of chip produced such as cutting speed, depth of cut, type of coolant, rake angle and lubrication condition. In these experiments, all the factors are varied except the type of coolant used and rake angle.

From Fig. 2, it can be seen that wet machining produces a continuous chip which provides a better surface finish when applied low speed on hardness material. Compared to the dry machining and minimum quantity lubricant, their chips formed are the same which is resulting to the non-continuous chip. This is proven when machining at medium cutting operation, the function of cutting in wet plays the important role to give the better surface finish compared to the other machining conditions.

For light turning operation as shown in Fig. 3, the chip produced at all machining conditions is still continuous chip and it is different on the rake angle. For minimum quantity lubricant, it is only produced a small chip curl diameter of continuous chip compared to the others conditions. As a result, the minimum quantity lubricant will produce a good surface finish.

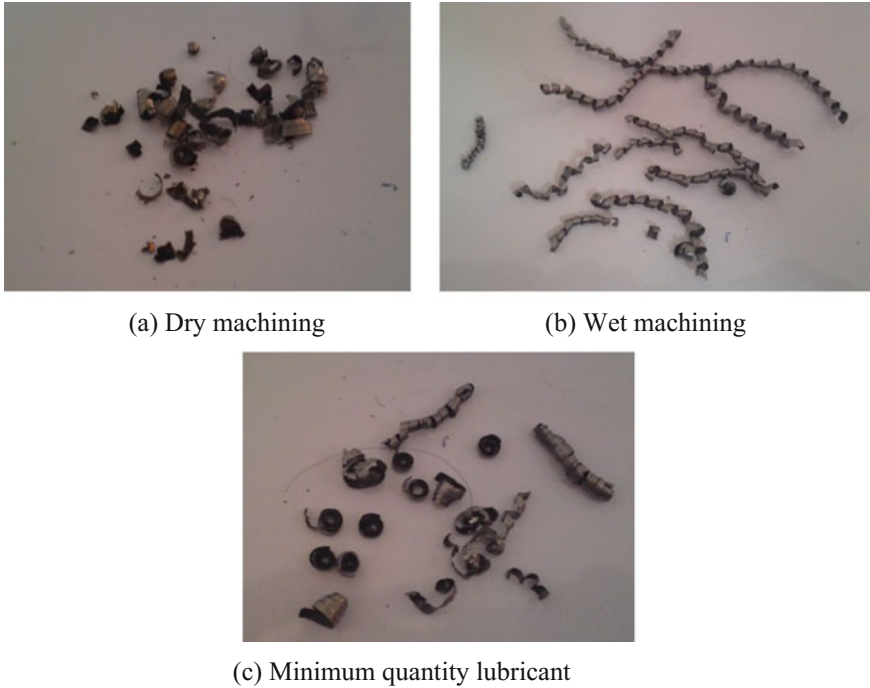


Fig. 2 Chip formations for medium turning operation

4 Conclusion

As a conclusion, this experimental work investigated the effect of the lubrication condition to surface roughness by using a CNC Lathe machine. Based on the result of the present experimental investigation, we know that the lubrication condition is one of the factors that affect the surface roughness. The important conclusion drawn from this research can be summarized as follows:

- A minimum quantity lubricant produced a better surface finish continued by wet machining and dry machining on the light cutting parameters only.
- The cutting performance of minimum quantity lubricant machining and dry machining is poorer than wet machining when medium cutting is applied because minimum quantity lubricant and dry machining cannot provide the benefit mainly by reducing the cutting temperature, which cannot improve the chip—tool interaction and maintains the sharpness of the cutting edges.
- Minimum of lubricant is not necessarily being regarded as the replacement of dry cutting and at the same time it cannot be considered as an alternative to wet machining from viewpoints of performance when applied on the hardness material. Otherwise, it was proven as the replacement for light cutting which



(a) Dry machining

(b) Wet machining



(c) Minimum quantity lubricant

Fig. 3 Chip formations for light turning operation

reduces many cutting problems coming from high consumptions of lubricant like high machining costs, environmental pollution and worker health problems.

Acknowledgements We would like to thanks UniKL MSI for the financial support for the research.

References

1. Serope, K., Steven, R.S.: Manufacturing Engineering and Technology, 6th edn. Prentice Hall (2010)
2. Steve, F.K., Arthur, R.G., Peter, S.: Technology of Machine Tools, 6th edn. McGraw-Hill Higher Education (2005)
3. Geoffrey, B., Winston, A.K.: Fundamentals of Machining and Machine Tools, 3rd edn. CRC Press, Taylor & Francis Group (2006)
4. Hassan, E.H.: Fundamentals of Machining Process—Conventional and Nonconventional Processes. CRC Press, Taylor & Francis Group (2007)

Thermal Analysis of a Cylindrical Sintered Wick Heat Pipe



Faiza Mohamed Nasir, Mohd. Zulkify Abdullah and Fairoside Idrus

Abstract The aim of this paper is to present approaches undertaken in analysing the thermal performance of a cylindrical heat pipe with copper-sintered wick. The approaches employed are the thermal resistance network, the lumped capacitance method (LCM) and two-dimensional numerical CFD simulation. The predicted variation of the evaporator temperature with different heat inputs were compared against experimental data. The accuracy of the prediction was also determined by finding the percentage difference of the calculated results with that from the experiments. All methods have shown to produce results that are in good agreement with the experimental works. The best method is the LCM, giving predictions that deviate from experimental data by as much as 3.9%, followed by the thermal resistance network and the numerical simulation with maximum percentage differences of 4.6 and 9.8%, respectively.

Keywords Heat pipe · Simulation · Superconductor · Resistance network
Lumped capacitance

Nomenclature

δ Thickness (m)
 \dot{Q} Heat input (W)
 ε Wick porosity (fraction)

F. M. Nasir (✉)
Malaysian Spanish Institute, Universiti Kuala Lumpur,
Kulim Hi-Tech Park, 09000 Kedah, Malaysia
e-mail: faiza@unikl.edu.my

F. M. Nasir · M. Z. Abdullah
Universiti Sains Malaysia, Engineering Campus,
14300 Nibong Tebal, Pulau Pinang, Malaysia
e-mail: mezul@usm.my

F. Idrus
Universiti Teknologi MARA, Kampus Permatang Pauh,
Jalan Permatang Pauh, 13500 Permatang Pauh, Pulau Pinang, Malaysia
e-mail: shidee@ppinang.uitm.edu.my

Nu	Nusselt number
μ	Dynamic viscosity (kg/m s)
ρ	Density (kg/m ³)
C	Thermal capacity (J/K)
cp	Specific heat capacity (J/kg K)
d	Diameter of the heat pipe (m)
h	Convection heat transfer coefficient (W/m ² K)
k	Thermal conductivity of material (W/m K)
L	Length of the section (m)
Pr	The Prandtl number
R	Thermal resistance (W/K)
r	Radius of the heat pipe (m)
Re	The Reynold number
T	Temperature (K)
t	Time (s)
τ	Time constant (s)

Subscripts

∞	Ambient condition
$conv$	Convection at the condenser
eff	Effective
a	Adiabatic section
c	Condenser section
e	Evaporator section
i	Inner of the heat pipe
l	Liquid in the wick
o	Outer of the heat pipe
p	Heat pipe wall
w	Wick
p, c	Pipe wall at the condenser
p, e	Pipe wall at the evaporator
tot	Overall
w, c	Liquid-wick combination at the condenser
w, e	Liquid-wick combination at the evaporator

1 Introduction

Heat pipes, which makes use of phase-change heat transfer, are widely used in many industrial applications [1]. They have been regarded as thermal superconductors [2, 3] as their effective thermal conductivity can be up to 90 times greater

than that of a copper bar with the same size [4]. This attractive characteristic along with other advantages, such as being lightweight, compact, no power supply requirement [5], have low thermal resistance [6] and flexible geometry [7, 8], have made them gaining attention in recent years.

A heat pipe consists of two main sections; the evaporator and the condenser. The evaporator section of the pipe is partially filled with a working fluid, which can be water, methanol, acetone, or even refrigerants. When the surface of the evaporator is in contact with a heat source, the working fluid inside will be vaporized. Due to the higher vapor pressure of the working fluid at the evaporator compared to that in the condenser, the vapor then flows rapidly from the evaporator to the condenser. Once the vapor reaches the condenser section, it will undergo condensation heat transfer as the outer surface of the condenser is exposed to either air flow or water flow. Subsequently, the vapor becomes liquid and it is transported back to the evaporator either by capillary force using a wick or by the gravity-induced effect [9].

There are many types of heat pipes, with the common ones being the conventional or straight heat pipes, thermosiphons, loop heat pipes (LHPs), pulsating or oscillating heat pipes and flat plate heat pipes (FPHPs). Their internal surface may or may not have wicks. Wicks are a porous structure that assists in the transportation of the liquid from the condenser back to the evaporator, by providing extra surface area to exert the capillary pressure on the liquid phase of the working fluid. Wicks can be in the form of sintered metal powder, groove or mesh. They are required for the heat pipes that functions on capillary action, such as LHPs, straight heat pipes and FPHPs. Thermosiphons, which work on the effect of gravity, and PHP, which works on capillary pressure and pressure difference, may not require wicks.

Numerous experimental and modelling works have been conducted to study the performance of wicked heat pipes [10–12], thermosiphons [13–16], LHPs [17–19], PHPs [20–22] and FPHPs [5, 23–25] under varying operating parameters. Nookaraju et al. [10] performed experimental and numerical simulation works to compare the performance of thermosiphons, sintered wick and groove wick heat pipes at varying heat inputs. They found that the sintered-wick heat pipe is the most efficient system, with thermosiphons the least. Khalili and Shafii [11] introduced an innovative type of sintered wick heat pipes that were tested against a conventional cylindrical sintered wick heat pipe, experimentally and numerically. Parametric studies were conducted by varying the heat pipe filling ratios and orientations. Their findings indicate that the best filling ratio is 20% for both heat pipes.

Approaches employed in modelling of the behaviour of heat pipes under transient and steady-state conditions are by developing and using analytical models [26–29], numerical simulations [10, 11, 20, 30, 31] and mathematical modelling [24, 32–36]. Simple analytical models such as that of Faghri and Harley [29] is easy to use and could be the tool that would provide quick and immediate solutions. Analytical models are usually developed using the concept of thermal resistance network and/or lumped parameter. Numerical simulation, although it provides comprehensive and accurate results, requires a considerable amount of effort and time to be set-up, coded and run, particularly for 3D studies that involve multiphase

interactions. A simulation of a heat pipe can be made simple by assuming that it is behaving as a solid pipe with high thermal conductivity or as a superconductor [16, 23, 37, 38]. This approach does not take into account the complex interaction between the liquid flow, vapor flow and the wick. Another simple technique in simulating the heat pipe is by creating multi-fluid zones in the computational domain [39]. This technique would produce a better axial temperature distribution, but it requires proper set-up of the appropriate boundary conditions. Conducting multiphase (2D or 3D) simulations could be very complex and complicated, but the results are accurate and comprehensive. The majority of numerical simulations of heat pipes are employing multiphase algorithm solutions, which could be volume-of-fraction (VOF), mixture models, Eulerian models or evaporation-condensation models [13, 15, 20, 31, 40–42].

The purpose of this work is to evaluate and validate the usage of the simple analytical models and numerical simulation in describing the behaviour of a sintered wick heat pipe. The calculated or simulated results of the evaporator temperature are compared with experimental data.

2 Methodology

Three approaches of the heat pipe analysis were undertaken; namely the thermal resistance network analysis, the transient lumped capacitance method (LCM) and a two-dimensional numerical simulation. The experimental data used in this work is obtained from the works of Idrus et al. [43]. Their experimental results were used as the benchmark for assessing the accuracy and reliability of the three analyses undertaken. The geometrical properties of the heat pipe are shown in Table 1. The heat pipe contains wicks in the form of copper-sintered powder with the approximate porosity of 50%.

In the experimental work, a test rig has been developed and the schematic diagram of the experimental setup is shown in Fig. 1. The working fluid in the heat pipe is water with an approximate filling ratio of 10%. Cartridge heaters were used as the heat source to the evaporator section in the range of 40–100 W. The condenser section was exposed to the circulating water via a water jacket. The surface

Table 1 Geometrical properties of the heat pipe

Property	Value (mm)
Outer diameter, d_o	10
Inner diameter, d_i	9
Evaporator length, L_e	66.5
Adiabatic length, L_a	175
Condenser length, L_c	58.5
Wick thickness, w	0.7
Pipe thickness, p	0.5

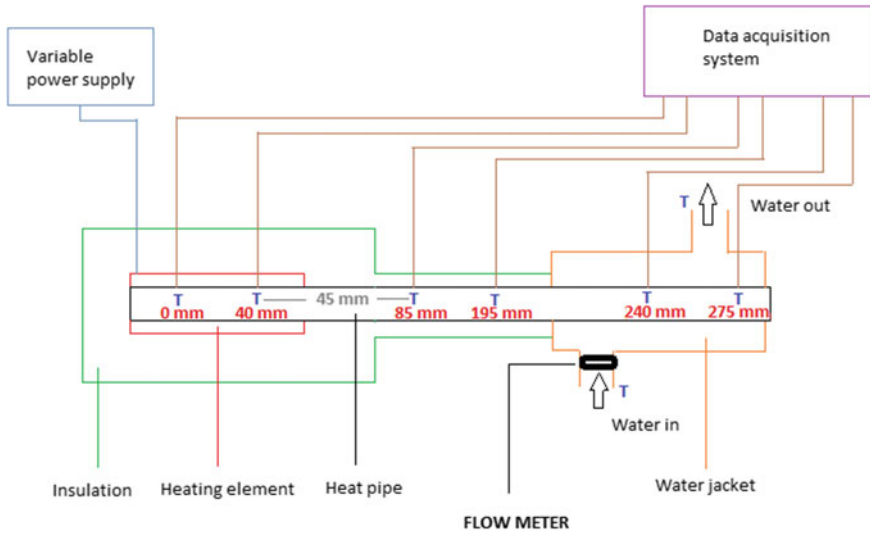


Fig. 1 Schematic of the experimental set-up

Table 2 Thermophysical properties of the heat pipe, wick and water

Property	Heat pipe and wick	Water
Density, ρ (kg/m ³)	8800	1000
Specific heat capacity, c_p (J/kg K)	420	4178
Thermal conductivity, k (W/m K)	401	0.615
Viscosity, μ (kg/m s)	–	0.798×10^{-3}

temperatures of the heat pipe during the experiments were measured by thermocouples attached over its surface. Heat losses to the surroundings were minimized by covering the heat pipe with thermal insulation. The duration of each of the experiments conducted for varying heating power is 1800 s. The thermophysical properties of water, copper pipe and the wick structure are given in Table 2.

2.1 Thermal Resistance Network Modelling

The temperature distribution of the heat pipe under steady-state condition can be approximated by utilizing an analogous electrothermal network [44, 45]. The overall thermal resistance of a cylindrical heat pipe can be calculated from:

$$R_{tot} = R_{p,e} + R_{w,e} + R_{w,c} + R_{p,c} \quad (1)$$

where:

$$R_{p,e} = \frac{\ln\left(\frac{d_o}{d_i}\right)}{2\pi L_e k_p} \quad (2)$$

$$R_{w,e} = \frac{\ln\left(\frac{d_o}{d_i}\right)}{2\pi L_e k_{eff}} \quad (3)$$

$$R_{w,c} = \frac{\ln\left(\frac{d_p}{d_i}\right)}{2\pi L_c k_{eff}} \quad (4)$$

$$R_{p,c} = \frac{\ln\left(\frac{d_o}{d_i}\right)}{2\pi L_c k_p} \quad (5)$$

The effective thermal conductivity of the liquid-wick combination of the sintered wick heat pipe can be determined from the following equation:

$$k_{eff} = \frac{k_w \left[2 + \frac{k_l}{k_w} - 2\varepsilon \left(1 - \frac{k_l}{k_w} \right) \right]}{2 + \frac{k_l}{k_w} + \varepsilon \left(1 - \frac{k_l}{k_w} \right)} \quad (6)$$

In most cases, the liquid-vapor interface resistances and the axial vapor resistance can be neglected [44]. Hence they were not accounted for in this analysis. The condenser in this analysis is exposed to external forced convection by water, thus the convection thermal resistance must be included in the analysis.

$$R_{conv} = \frac{1}{h\pi d_o L_c} \quad (7)$$

The heat transfer coefficient, h , can be determined using the Churchill and Bernstein correlation for the Nusselt number, Nu .

$$Nu = \frac{hd_o}{k_l} = 0.3 + \frac{0.62Re^{\frac{1}{2}}Pr^{\frac{1}{3}}}{\left[1 + \left(\frac{0.4}{Pr} \right)^{\frac{2}{3}} \right]^{\frac{1}{4}}} \quad (8)$$

Once the heat transfer coefficient is known, the evaporator temperature can be calculated from:

$$\dot{Q} = \frac{T_e - T_\infty}{R_{tot} + R_{conv}} \quad (9)$$

2.2 Lumped Capacitance Method (LCM)

This is a transient analysis that assumes isothermal conditions of the heat pipe as described by Faghri and Harley [29]. Their solution of Case 2 is relevant to this work where the heat input to the evaporator is constant and the condenser ambient temperature satisfies the following conditions:

$$T_{\infty,c} = \begin{cases} T_{\infty,c1} & t < 0 \\ T_{\infty,c2} & t \geq 0 \end{cases} \quad (10)$$

The exact solution for the general lumped capacitance equation is:

$$T(t) = T_{\infty,c1} + \dot{Q}R_{conv} + (T_{\infty,c2} - T_{\infty,c1}) \left(1 - e^{-\frac{t}{\tau}}\right) \quad (11)$$

where the time constant, τ , is

$$\tau = C_{tot}R_{conv} = (\rho c_p)_{eff} V_{tot} R_{conv} \quad (12)$$

Neglecting the thermal capacity of the vapor phase as the mass of the vapor is relatively small compared to that of the pipe wall and the working fluid, the overall thermal capacity of the heat pipe is represented by its effective thermal capacity. This thermal heat capacity accounts for both the liquid and the wick structure.

$$(\rho c_p) = \varepsilon(\rho c_p)_l + (1 - \varepsilon)(\rho c_p)_w \quad (13)$$

The temperature of the heat pipe at the end of the experiment, where $t = 1800$ s can be determined from Eq. (11).

2.3 Simulation Solid Conduction

Using the assumption of the heat pipe behaving as a superconductor, CFD two-dimensional simulations were conducted using FluentTM. The 2D model consists of 93,588 cartesian grids. The computational domain consists of a solid zone; representing the heat pipe and a fluid zone; representing the circulating water flow cooling the condenser. The outer pipe wall is divided into three regions with different boundary conditions. The outer surface of the evaporator region is

subjected to a heat flux boundary condition. The heat flux corresponds to the varying heat input of 40–100 W is imposed on the evaporator surface. The condenser is exposed to a convective boundary condition. The middle of the heat pipe, an adiabatic zone, is subjected to a zero heat flux boundary conditions. The water inlet velocity is set to 0.1 m/s with an initial temperature of 295 K. The initial temperature of the heat pipe is set to 309 K, similar with the initial temperature of the heat pipe during the experiments.

In order to simulate the conduction of the heat pipe, its thermal conductivity must be defined. As a heat pipe is not a purely solid material, its equivalent or effective thermal conductivity must be determined. This thermal conductivity is neither related to the thermal conductivity of the liquid-saturated wick nor the thermal conductivity of the pipe material [46] and there is no analytical expression that could be used to determine its value. Hence, in this work, simulation results of the heat pipe exposed to a heat flux of 9570 W/m^2 (40 W) is matched to the corresponding experimental work, which would yield the equivalent thermal conductivity of the heat pipe. This value then is used in subsequent cases of varying heat flux to obtain the evaporator temperature at the end of the time step.

Unsteady state calculations with a time step of 1800 s were performed for all cases of varying heat flux. The numerical calculations were conducted using a combination of the SIMPLE algorithm for pressure-velocity coupling and second-order upwind calculation scheme.

3 Results and Discussion

In this work, the results of the calculated evaporator temperature of a sintered wick heat pipe were compared with that obtained from experimental works. Three methods of analysis were employed for the purpose of the calculation. The comparison is illustrated in Fig. 2. As observed in the figure, all three methods predict evaporator temperatures that are in good agreement with the experimental results.

Using the thermal resistance network analysis, the heat pipe thermal resistance under steady-state conditions is 0.9461 K/W, with the predicted convection heat transfer coefficient of $580 \text{ W/m}^2 \text{ K}$. The resulted evaporator temperatures at different heat inputs differ by as much as 4.6% from the experimental values. The percentage difference of the calculated results with that of the experimental works is shown in Fig. 3. This small difference indicates that the experiments conducted on the heat pipe have reached steady-state conditions such that a simplistic thermal resistance network is capable of accurate prediction of the evaporator temperature.

In the lumped capacitance method, the variation of the heat pipe's temperature with time may be predicted, by assuming isothermal condition. Hence, using this method, spatial temperature distributions could not be obtained. From Fig. 2, the evaporator temperature at $t = 1800 \text{ s}$ determined using the LCM is in excellent agreement with the experimental data, with a maximum percentage difference of 3.9%.

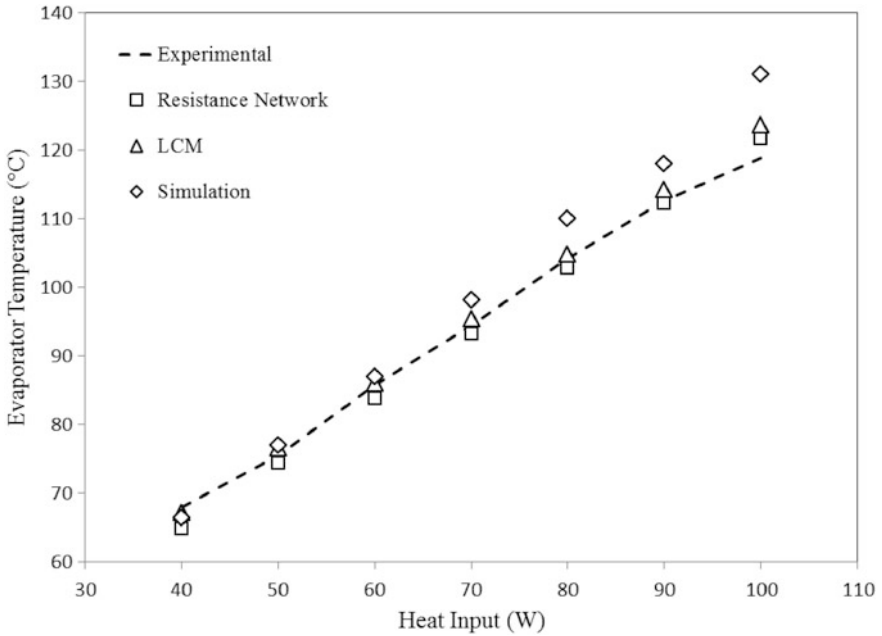


Fig. 2 Evaporator temperature at different heat inputs

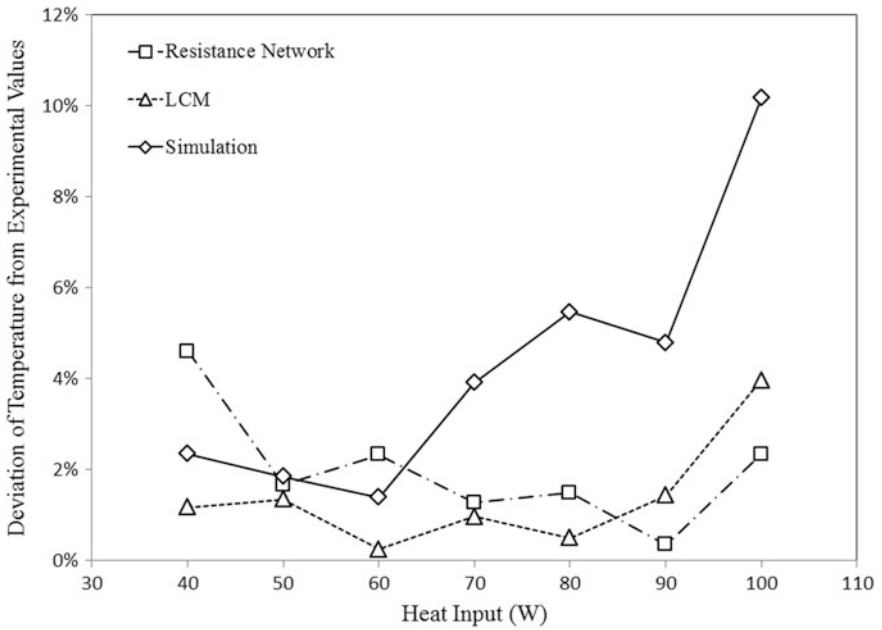


Fig. 3 Percentage difference of calculated evaporator temperature with the experimental values

Table 3 Percentage difference of calculated evaporator temperature with the experimental values

Analysis method	Average (%)	Standard deviation (%)
Resistance network	2.008	1.329
Lumped capacitance	1.383	1.186
Simulation	4.205	2.885

Numerical simulation of the heat pipe yielded results of the evaporator temperature that are less accurate than those produced by the thermal resistance network analysis and LCM. At a heat input of less than 70 W, the temperature deviates in the range of 1.4–2.4% from the experimental data. At higher heat input, a greater deviation is observed, nearly 10% for 100 W. Studies have shown that the equivalent thermal conductivity of the heat pipe varies with the heat input and it decreases when the heat pipe has reached its optimal limit [26]. Idrus et al. [43] conclude that their heat pipe optimal limit is at 70 W, hence at above this heating power, a decrease in the equivalent thermal conductivity of the heat pipe must be accounted for.

The accuracy of the results obtained by the three methods is measured by the percentage difference of the calculated temperature with the experimentally obtained temperature. Figure 3 shows the variation of the percentage difference with heat input, whilst Table 3 shows the average and the standard deviation of the percentage difference. It is found that LCM achieves the best accuracy with the lowest average percentage difference of 1.383%, followed by the thermal resistance network analysis with an average of 2%. Thus, it is demonstrated that simple analytical solutions are capable of predicting the temperature of the heat pipe exposed to varying heat input. However, with these simple solutions or analyses, one could not obtain the variation of temperature with time and space accurately. The task could only be accomplished by the complex numerical simulation that would consume resources (effort and computing). Using 2D simulation with the assumption of the heat pipe as superconductor produces results that differ from the experimental ones by as much as 10%.

4 Conclusions

Thermal analysis of a heat pipe with copper-sintered wick has been conducted by employing three approaches; the thermal resistance network, the lumped capacitance method and the two-dimensional numerical simulation. The predicted variation of the evaporator temperature with different heat inputs was compared against experimental data. The accuracy of the prediction was also determined by determining the percentage difference of the calculated results with that from the experiments. All methods have shown to produce results that are in good agreement

with the experimental works. The best method is the LCM, giving predictions that deviate by as much as 3.9%, followed by the thermal resistance network and the numerical simulation with maximum percentage difference of 4.6 and 9.8% respectively. However, the simplistic nature of the equations in the previous two methods prevents the determination of the axial temperature distribution, as well as the variation of evaporator temperature and condenser temperature with time. Using 2D numerical simulation by assuming the heat pipe as a superconductor provides results that agree reasonably well with the experimental data, for a heat input below 70 W. The simple analytical models such as the thermal resistance network and the LCM provide a quick prediction of the evaporator temperature and they are useful when the axial temperature distribution is not required. However, when accurate axial and temporal temperature distributions are of importance, numerical simulations must be used.

References

1. Tu, S.-T., Zhang, H., Zhou, W.-W.: Corrosion failures of high temperature heat pipes. *Eng. Fail. Anal.* **6**, 363–370 (1999). [https://doi.org/10.1016/S1350-6307\(98\)00057-0](https://doi.org/10.1016/S1350-6307(98)00057-0)
2. Ting, C., Chen, C.: Analyzing the heat transfer property of heat pipe influenced by integrated cooling apparatus. *Chin. J. Eng.* **2014**, 1–10 (2014)
3. Yang, X., Yan, Y.Y., Mullen, D.: Recent developments of lightweight, high performance heat pipes. *Appl. Therm. Eng.* **33–34**, 1–14 (2012). <https://doi.org/10.1016/j.applthermaleng.2011.09.006>
4. Faghri, A.: Heat pipes: review, opportunities and challenges. *Front. Heat Pipes* **5** (2014) <https://doi.org/10.5098/fhp.5.1>
5. Nandy, P., Ariantara, B., Pamungkas, R.A.: Experimental investigation on performance of lithium-ion battery thermal management system using flat plate loop heat pipe for electric vehicle application. *Appl. Therm. Eng.* **9**, 1616–1620 (2016). <https://doi.org/10.1016/j.applthermaleng.2016.01.123>
6. Murashko, K., Pyrhönen, J., Laurila, L.: Optimization of the passive thermal control system of a lithium-ion battery with heat pipes embedded in an aluminum plate. In: 2013 15th European Conference on Power Electronics and Applications, EPE 2013, pp. 1–10 (2013)
7. Tran, T.-H., Harmand, S., Desmet, B., Filangi, S.: Experimental investigation on the feasibility of heat pipe cooling for HEV/EV lithium-ion battery. *Appl. Therm. Eng.* **63**, 551–558 (2014). <https://doi.org/10.1016/j.applthermaleng.2013.11.048>
8. Zhao, R., Gu, J., Liu, J.: An experimental study of heat pipe thermal management system with wet cooling method for lithium ion batteries. *J. Power Sources* **273**, 1089–1097 (2015). <https://doi.org/10.1016/j.jpowsour.2014.10.007>
9. Chan, C.W., Siqueiros, E., Ling-Chin, J., et al.: Heat utilisation technologies: a critical review of heat pipes. *Renew. Sustain. Energy Rev.* **50**, 615–627 (2015). <https://doi.org/10.1016/j.rser.2015.05.028>
10. Nookaraju, B.C., Rao, P.S.V.K., Nagasarada, S.: Experimental and numerical analysis of thermal performance in heat pipes. *Proc. Eng.* **127**, 800–808 (2015). <https://doi.org/10.1016/j.proeng.2015.11.415>
11. Khalili, M., Shafii, M.B.: Experimental and numerical investigation of the thermal performance of a novel sintered-wick heat pipe. *Appl. Therm. Eng.* **94**, 59–75 (2016). <https://doi.org/10.1016/j.applthermaleng.2015.10.120>

12. Chnookaraju, B., Kurmarao, P.S.V., Sarada, S.N.: Thermal analysis of gravity effected sintered wick heat pipe. *Mater. Today Proc.* **2**, 2179–2187 (2015). <https://doi.org/10.1016/j.matpr.2015.07.230>
13. Jouhara, H., Fadhl, B., Wrobel, L.C.: Three-dimensional CFD simulation of geyser boiling in a two-phase closed thermosyphon. *Int. J. Hydrogen Energy* **44**, 1–14 (2016). <https://doi.org/10.1016/j.ijhydene.2016.02.038>
14. Sukchana, T., Pratinthong, N.: A two-phase closed thermosyphon with an adiabatic section using a flexible hose and R-134a filling. *Exp. Therm. Fluid Sci.* **77**, 317–326 (2016). <https://doi.org/10.1016/j.expthermflusci.2016.04.027>
15. Fadhl, B., Wrobel, L.C., Jouhara, H.: CFD modelling of a two-phase closed thermosyphon charged with R134a and R404a. *Appl. Therm. Eng.* **78**, 482–490 (2015). <https://doi.org/10.1016/j.applthermaleng.2014.12.062>
16. Mroue, H., Ramos, J.B., Wrobel, L.C., Jouhara, H.: Experimental and numerical investigation of an air-to-water heat pipe-based heat exchanger. *Appl. Therm. Eng.* **78**, 339–350 (2015). <https://doi.org/10.1016/j.applthermaleng.2015.01.005>
17. Esarte, J., Bernardini, A., Blanco, J.M., Sancibrian, R.: Optimizing the design for a two-phase cooling loop heat pipe: part A: numerical model, validation and application to a case study. *Appl. Therm. Eng.* **99**, 892–904 (2016). <https://doi.org/10.1016/j.applthermaleng.2016.01.150>
18. Nishikawara, M., Nagano, H.: Parametric experiments on a miniature loop heat pipe with PTFE wicks. *Int. J. Therm. Sci.* **85**, 29–39 (2014). <https://doi.org/10.1016/j.ijthermalsci.2014.05.016>
19. Wu, S.C., Wang, D., Chen, Y.M.: Investigating the effect of double-layer wick thickness ratio on heat transfer performance of loop heat pipe. *Int. J. Therm. Sci.* **86**, 292–298 (2014). <https://doi.org/10.1016/j.ijthermalsci.2014.07.014>
20. Pouryoussefi, S.M., Zhang, Y.: Numerical investigation of chaotic flow in a 2D closed-loop pulsating heat pipe. *Appl. Therm. Eng.* **98**, 617–627 (2016). <https://doi.org/10.1016/j.applthermaleng.2015.12.097>
21. Marni, M., Manno, V., Filippeschi, S., Marengo, M.: Thermal instability of a closed loop pulsating heat pipe: combined effect of orientation and filling ratio. *Exp. Therm. Fluid Sci.* **59**, 222–229 (2014). <https://doi.org/10.1016/j.expthermflusci.2014.04.009>
22. Naik, R., Varadarajan, V., Pundarika, G., Narasimha, K.R.: Experimental investigation and performance evaluation of a closed loop pulsating heat pipe. *J. Appl. Fluid Mech.* **6**, 267–275 (2013). <https://doi.org/10.4028/www.scientific.net/AMM.592-594.1554>
23. Cheng, P.J., Lin, D.T.W., Liu, W.M., et al.: The study of an innovative heat removal model of the aluminum-acetone flat plate heat pipe on high power leds. *Trans. Can Soc. Mech. Eng.* **39**, 739–748 (2015)
24. Oro, M.V., Bazzo, E.: Flat heat pipes for potential application in fuel cell cooling. *Appl. Therm. Eng.* **90**, 848–857 (2015). <https://doi.org/10.1016/j.applthermaleng.2015.07.055>
25. Chen, J.S., Chou, J.H.: Cooling performance of flat plate heat pipes with different liquid filling ratios. *Int. J. Heat Mass Transf.* **77**, 874–882 (2014). <https://doi.org/10.1016/j.jheatmasstransfer.2014.06.029>
26. Solomon, A.B., Sekar, M., Yang, S.H.: Analytical expression for thermal conductivity of heat pipe. *Appl. Therm. Eng.* **100**, 462–467 (2016). <https://doi.org/10.1063/1.3386464>
27. Ferrandi, C., Iorizzo, F., Marni, M., et al.: Lumped parameter model of sintered heat pipe: Transient numerical analysis and validation. *Appl. Therm. Eng.* **50**, 1280–1290 (2013). <https://doi.org/10.1016/j.applthermaleng.2012.07.022>
28. Kumar, V., Gangacharyulu, D., Tathgir, R.G.: Heat transfer studies of a heat pipe. *Heat Transf. Eng.* **28**, 954–965 (2007). <https://doi.org/10.1080/01457630701421810>
29. Faghri, A., Harley, C.: Transient lumped heat pipe analyses. *Heat Recover. Syst. CHP* **14**, 351–363 (1994). [https://doi.org/10.1016/0890-4332\(94\)90039-6](https://doi.org/10.1016/0890-4332(94)90039-6)
30. Liu, F., Lan, F., Chen, J.: Dynamic thermal characteristics of heat pipe via segmented thermal resistance model for electric vehicle battery cooling. *J. Power Sources* **321**, 57–70 (2016). <https://doi.org/10.1016/j.jpowsour.2016.04.108>

31. Mahdavi, M., Qiu, S.: Mathematical modeling and analysis of steady state performance of a heat pipe network. *Appl. Therm. Eng.* **91**, 556–573 (2015). <https://doi.org/10.1016/j.applthermaleng.2015.08.017>
32. Zhang, P., Wang, B., Shi, W., et al.: Modeling and performance analysis of a two-phase thermosyphon loop with partially/fully liquid-filled downcomer. *Int. J. Refrig.* **58**, 172–185 (2015). <https://doi.org/10.1016/j.ijrefrig.2015.06.014>
33. Tsai, T.-E., Wu, G.-W., Chang, C.-C., et al.: Dynamic test method for determining the thermal performances of heat pipes. *Int. J. Heat Mass Transf.* **53**, 4567–4578 (2010). <https://doi.org/10.1016/j.ijheatmasstransfer.2010.06.037>
34. Mistry, P.R., Thakkar, F.M., De, S., DasGupta, S.: Experimental validation of a two-dimensional model of the transient and steady-state characteristics of a wicked heat pipe. *Exp. Heat Transf.* **23**, 333–348 (2010). <https://doi.org/10.1080/08916150903564804>
35. Ismail, K.A.R., Zanardit, M.A.: A steady-state model for heat pipes of cross-sections. *Appl. Therm. Eng.* **16**, 753–767 (1996)
36. Tournier, J.-M., El-Genk, M.S.: A heat pipe transient analysis model. *Int. J. Heat Mass Transf.* **37**, 753–762 (1994). [https://doi.org/10.1016/0017-9310\(94\)90113-9](https://doi.org/10.1016/0017-9310(94)90113-9)
37. Elnaggar, M.H.A., Abdullah, M.Z., Munusamy, S.R.R.: Experimental and numerical studies of finned L-shape heat pipe for notebook-PC cooling. *IEEE Trans. Compon. Packag. Manuf. Technol.* **3**, 978–988 (2013). <https://doi.org/10.1109/TCPMT.2013.2245944>
38. Annamalai, S., Ramalingam, V.: Experimental investigation and CFD analysis of a air cooled condenser heat pipe. *Therm. Sci.* **15**, 759–772 (2011). <https://doi.org/10.2298/TSCI100331023A>
39. Huminic, G., Huminic, A.: CFD study of the heat pipes with water-nanoparticles mixture. In: *EASC 4th European Automotive Simulation Conference* (2009)
40. Lin, Z., Wang, S., Shirakashi, R., Winston Zhang, L.: Simulation of a miniature oscillating heat pipe in bottom heating mode using CFD with unsteady modeling. *Int. J. Heat Mass Transf.* **57**, 642–656 (2013). <https://doi.org/10.1016/j.ijheatmasstransfer.2012.09.007>
41. Alizadehdakheel, A., Rahimi, M., Alsairafi, A.A.: CFD modeling of flow and heat transfer in a thermosyphon. *Int. Commun. Heat Mass Transf.* **37**, 312–318 (2010). <https://doi.org/10.1016/j.icheatmasstransfer.2009.09.002>
42. Legierski, J., Wiecek, B., de Mey, G.: Measurements and simulations of transient characteristics of heat pipes. *Microelectron. Reliab.* **46**, 109–115 (2006). <https://doi.org/10.1016/j.microrel.2005.06.003>
43. Idrus, F., Mohamad, N., Zailani, R., et al.: Thermal performance of a cylindrical heat pipe for different heat inputs and inclination angles. *Appl. Mech. Mater.* **661**, 148–153 (2014). <https://doi.org/10.4028/www.scientific.net/AMM.661.148>
44. Peterson, G.P.: *An Introduction to Heat Pipes; Modelling, Testing, and Applications*. Wiley, New York (1994)
45. Chi, S.: *Heat Pipe Theory and Practice: A Sourcebook* (Series in Thermal and Fluids Engineering). McGraw-Hill Inc., USA (1976)
46. El-Nasr, A.A., El-Haggar, S.M.: Effective thermal conductivity of heat pipes. *Heat Mass Transf.* **32**, 97–101 (1996). <https://doi.org/10.1007/s002310050097>

Three Point Bending Analysis on the Side Impact Beam of a Perodua Kancil



Fazidah Saad, Zainal Nazri Mohd Yusuf, Zulkarnain Abdul Latiff
and Norhisham Ismail

Abstract FMVSS 214 (“Side Impact Protection”) that introduced in 1970 by the National Highway Traffic Safety Administration (NHTSA) specifies performance requirements for the protection of occupants in side impact crashes, in order to reduce the risk of serious and fatal injury to occupants. With FMVSS 214, every car was installed with a side impact beam which was a passive safety device inside the door. Usually steel is used as the material for the side impact beam but it has disadvantages of having heavy weight. The objective of this study is to analyse the side impact beam of a Perodua Kancil with different material that could replace steel due to its heavy weight by using three point bending analysis. In this study, the side impact beam was analyzed under three point bending with a crash load due to different types of materials, i.e. steel, stainless steel and an aluminium alloy. A finite element model of the side impact beam from the Perodua Kancil was created and analyzed by the finite element analysis software ANSYS. The result from the finite element simulation shows that one of the suggested materials, i.e. the aluminium alloy, gives better result to deflect and resist the impact force.

Keywords Side impact beam · Three point bending analysis

F. Saad (✉) · Z. N. M. Yusuf · Z. A. Latiff · N. Ismail
Malaysian Spanish Institute, Universiti Kuala Lumpur,
Kulim Hi-Tech Park, 09000 Kedah, Malaysia
e-mail: fazidah@unikl.edu.my

Z. N. M. Yusuf
e-mail: zainalnazri@unikl.edu.my

Z. A. Latiff
e-mail: zulkarnain@unikl.edu.my

1 Introduction

Side impact accidents have been listed as one of the dangerous accidents and have caused more fatalities and severe injuries compare to the front impact accidents. Njuguna has cited the McNeill and Haberl statement in their journal that global accident statistics show that side impacts account for approximately 30% of all impacts and 35% of total fatalities (source: German In Depth Accident Study-GIDAS, National Automotive Sampling System-NASS & BMW accident database) [1]. As a result, FMVSS 214 (“Side Impact Protection”) that was introduced in 1970 by the National Highway Traffic Safety Administration (NHTSA) specifies performance requirements for the protection of occupants in side impact crashes, in order to reduce the risk of serious and fatal injury to occupants. With FMVSS 214, every car was installed with the side impact beam which was a passive safety device inside the door. Since then many research has been done to develop countermeasures to the side impact events whether new material study, structure and design optimization, and usage of new technologies due to some limitation on the beam such as the beam’s weight is heavy and the side event that happens is too close to the occupant.

Side impact collisions can cause grave injuries. Often called “T-bone” or “broadside” collisions, side impact accidents occur when the side of a vehicle is impacted. It can be impacted by the front or rear of another vehicle or in some cases a fixed object. Vehicle damage is often severe and drivers or passengers on the impacted side of the vehicle usually sustain far worse injuries than they would in another type of crashes. Side impact also requires more attention because there is considerably less crash zone for absorbing impact energy in the side of the car compared to the front and rear structure and seatbelts also have limited effectiveness in side-impact crashes. So, the protection for the side impact crashes relies on a reinforced compartment structure and on the inside of the compartment, especially the door panels because the door absorbs some of the energy and the rest of it is transmitted through the side impact beams to the safety cell surrounding the passengers, thus reducing the risk of the door intruding into the cabin.

A side impact beam is a passive device that is installed at most car’s door for the safety purpose which will protect the driver and passengers from side collision by absorbing the impact energy before it reaches the passengers. The side impact beam is included inside the Federal Motor Vehicle Safety Standard (FMVSS) 214, “Side Impact Protection” as one of the most important safety regulation that was issued by NHTSA that has become effective at January 1, 1973 [2]. Before that, during the 1960s the motor vehicle manufacturers has tested many methods to reduce the impact of the door compartment when a collision occurs. From that the installation of the horizontal beam inside the door was discovered. The installation of a side impact beam has improved the car’s test scores at which the side structure intrusion from impact in crash tests was greatly reduced. There are many factors that can affected the performance of the beam during collision such as the material, design, structure and installed location [3]. Currently most of the vehicles are using steel as

the side impact beam [3]. The steel beam is good to absorb impact but due to its heavy weight, there is still some room for improvement to replace the material in order to reduce the weight but not jeopardize the material's strength.

A crash test is a form of destructive testing that was done in order to ensure safe design standards in crashworthiness and crash compatibility for various modes of transportation systems and components. One of the major causes of injury in a side impact is the lateral impact on the occupant by the door interior. There are two types of crash tests that can be done to study the side impact collision:

1. One of the most important crash configurations for side impact is the car to car side impact as shown in Fig. 1. The European New Car Assessment Programme (Euro NCAP) simulates this type of crash by having a mobile deformable barrier (MDB) impacting the driver's door at 50 km/h [4]. The injury protection is assessed by a side impact test dummy, in the driver's seat. Although it is difficult to judge the level of protection provided from the extent of intrusion, control of how the car side intrudes is important. The programme Euro NCAP has seen large improvements in side impact performance.
2. Many of these injuries occur when one car runs into the side of another or into a fixed narrow object such as a tree or pole and to study this event, the pole test was performed as shown in Fig. 2. Side impact head or curtain airbags help to protect the head and upper torso. In the test, the car tested travelled sideways at 29 kph (18 mph) into a rigid pole [4]. The pole is relatively narrow, so there is severe penetration into the side of the car. In an impact without the head

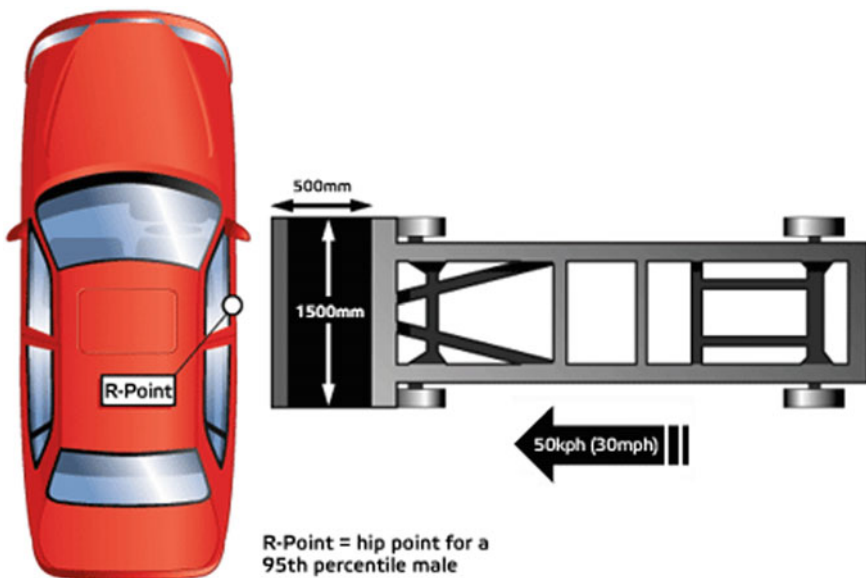


Fig. 1 Car to car side impact test

protecting airbag, a driver's head could hit the pole with sufficient force to cause a fatal head injury. A side impact airbag with head protection makes this kind of crash survivable despite the severity.

2 Methodology

The primary objective of this project was to determine the effect of the three points bending deformation on the selected materials at which the dynamic impact force was applied to the beam. Firstly, the Perodua Kancil beam was modelled by using a CAD software. Then the three point bending analysis was simulate using the finite element analysis software ANSYS by using three different materials which is steel, stainless steel and an aluminium alloy. From the finite element analysis, the beam was analyzed for the directional deformation, equivalent elastic strain, and equivalent stress. Results from the simulation show the deflection of the beam and the results were compared between the three materials. This study only focused on the front door or driver's door beam and the beam was simulated with a dynamic crash test and the three point bending behaviours were observed. The best material has been selected for the side impact beam. The weight and material properties for the side impact beam with different materials is as shown in Table 1 [5].

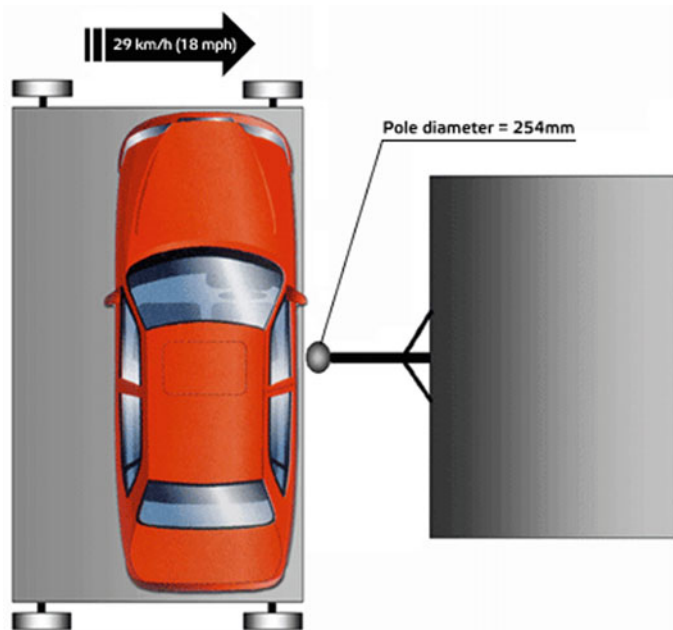


Fig. 2 Pole impact test [3]

Table 1 Weight and material properties of the impact beam

	Steel	Aluminium alloy	Stainless steel
Weight (kg)	1.246	0.677	0.835
Density (kg/m ³)	7850	2700	7740
Specific heat (J/kg.°C)	434	996	480
Young’s modulus (Pa)	2.00 e11	6.39 e10	2.00 e11
Poisson’s ratio	0.3	0.33	0.3
Yield strength (Pa)	2.50 e8	2.78 e8	3.1 e8

3 Results and Discussion

The result for this study was achieved throughout the completion of three point bending simulation under side impact beam condition.

a. Directional Deformation

The results from the directional deformation analysis are tabulated in a graph as shown in Fig. 3. It can be seen from the graph that the aluminium alloy has the highest value and this indicates that it can absorb and deflect the impact better than other materials.

b. Equivalent Elastic Strain

The results from the equivalent elastic strain analysis are tabulated in a graph as shown in Fig. 4. From the graph, the aluminium alloy has the highest value and this also indicates that it can withstand the impact better than other materials.

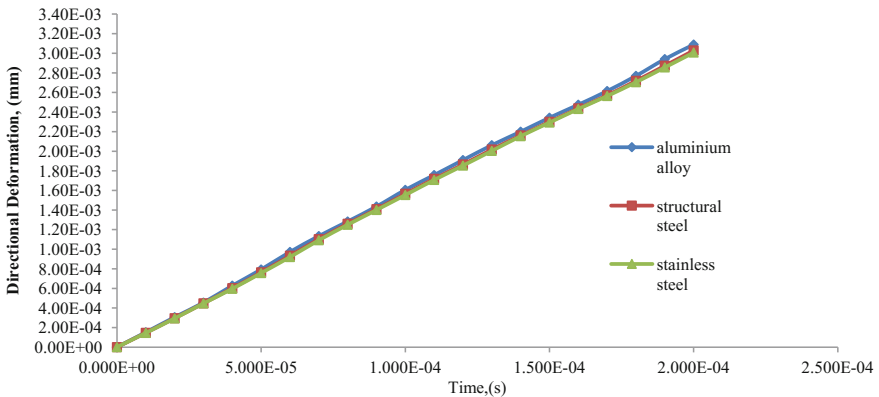


Fig. 3 Graph of directional deformation versus time

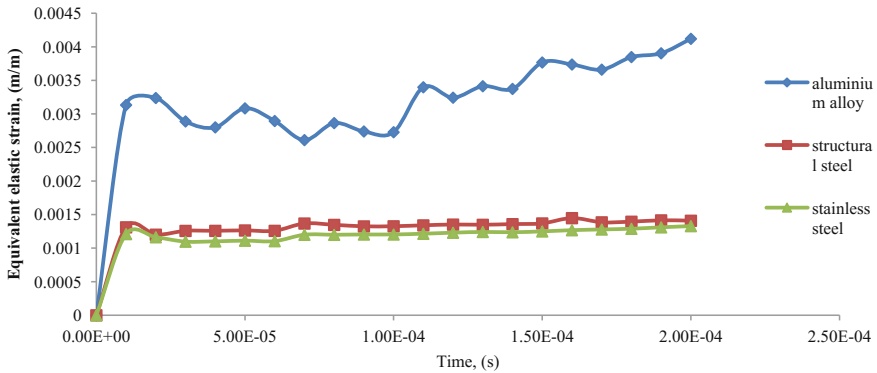


Fig. 4 Graph of equivalent elastic strain versus time

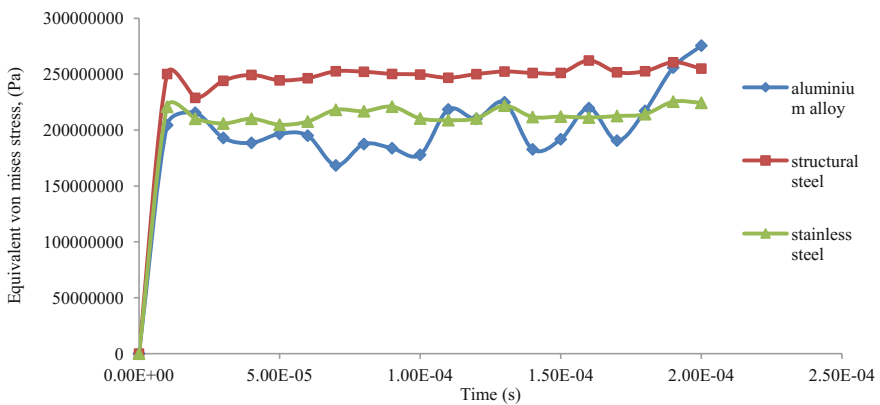


Fig. 5 Graph of equivalent von mises stress versus time

c. Equivalent Von Mises Stress

The results from the Von Mises Stress analysis are tabulated in a graph as shown in Fig. 5. From the graph, steel is having the highest value of stress if compared to other materials but the aluminium alloy has the highest value at the end of the impact and this indicates that it can also withstand the impact.

4 Conclusion

The main objective of this study is to determine the effect of the three point bending on the selected materials at which the dynamic impact force was applied to the beam with the aim to replace steel with a lighter material. Two proposed materials

had been analysed which is stainless steel and an aluminium alloy. Both of them are having a weight reduction of about 33% for stainless steel and 46% for the aluminium alloy. The beam was simulated in a crash test or impact test by using different materials and from the result, the aluminium alloys is the most suitable material because it has the highest value of directional deformation and equivalent elastic strain that can absorb and deflect the impact force much better.

Acknowledgements The authors would like to thank the Universiti Kuala Lumpur Malaysian Spanish Institute for the support for this research.

References

1. Njuguna, J.: The application of energy absorbing structures on side impact protection systems. *Int. J. Comp. Appl. Technol. (IJCAT)* **40**(4), 280–287 (2011)
2. Kahane, C.J.: An Evaluation of Side Structure Improvements in Response to Federal Motor Vehicle Safety Standard 214, vol. **214**, pp. 5–8 (1982)
3. Lim, T.S., Lee, D.G.: Mechanically fastened composite side-door impact beams for passenger cars designed for shear-out failure modes. *Compos. Struct.* **56**, 211–221 (2002)
4. Car to Car Side Impact & Pole Side Impact.: Euro NCAP—For safer cars crash test safety rating. <http://www.euroncap.com/home.aspx> (2014). Assessed 18 Feb 2014
5. Cheon, S.S., Lee, D.G., Jeong, K.S.: Composite side-door impact beams for passenger cars. *Compos. Struct.* **38**, 229–239 (1997)

Time Optimization Implementation in Conventional Lathe Machining Operations



Jumázulhisham Abdul Shukor, Syed Ahmad Faiz Syed Mohd and Mozaimi Mohamad

Abstract A study of time optimization in conventional lathe machining operations of the higher technical learning institutions in Malaysia was performed. This is to ensure that the students may complete a project within 30 contact hours. Based on previous experiences, almost 50% projects may not be able to completed on time. Time optimization is a process to increase productivity of machinists while reducing wastes. Three objectives were identified in this study, focused to identify time waste, simulate and suggest methods of the improvement. A few quantitative methods to identify the problem, i.e. the experimenting samples method, simulate and verification were used. As a result, time taken for machinist's movement, inspections and storage were improved and this contributes to the highest improvement. Hence, the idle time has been minimized. The enhancement of standard operating procedure, audio-visual learning and layout design in the study played significant roles in completing the study. The movement and storage times were suggested for enhancement to reduces the issue of productivity.

Keywords Conventional lathe machining · Time improvement
Process flow · Kaizen · Productivity

J. Abdul Shukor (✉) · S. A. F. S. Mohd · M. Mohamad
Malaysian Spanish Institute, Universiti Kuala Lumpur,
Kulim Hi-Tech Park, 09000 Kulim, Kedah, Malaysia
e-mail: azulhisham@unikl.edu.my

S. A. F. S. Mohd
e-mail: syedahmadfaiz@unikl.edu.my

M. Mohamad
e-mail: mohamadmozaimi@gmail.com

1 Introduction

The study of time optimization of conventional machining (lathe) was chosen to enhance the hands-on activity for technical students in a selected university. This study was not only conducted to see time optimization but also reflects to the productivity and efficiency [1] when waste and unnecessary operations were removed. This proves an action of continuous improvement [2, 3, 11] made in enhancing teaching and learning processes.

The aims of this study are to identify time waste in the fabrication of parts in conventional lathe machining processes, to perform a simulation of improvement through selected quality tools and finally, to recommend an improvement plan as part of a continuous improvement in teaching and learning process to improve productivity and efficiency.

Initially, the conventional lathe machining process performed by technical students would takes approximately 30 h within 5 weeks. However, it does not consider students experience, public holidays and campus activities which required these students to take part. This task was carried out by students with various backgrounds including technical and non-technical beforehand.

Figure 1 shows the technical drawing of a conventional lathe project to be performed. Based on the drawing, students were instructed to perform facing, turning, tapering, grooving and knurling operations. The time was taken to observe how much time was taken and wasted during the students performing their task and to suggest an improvement method for user machining operation.

The concept of Kaizen reduces wastes and solves problems with minimum costs and technologies [3, 4]. A Kaizen implementation was applied to identify the bottleneck operation and to improve the operation time. The study identified time of operations, movements of the operator, time of inspection, delays, and storage time. Through this investigation the researcher can identify the number of time consumed to be considered for improvement. Hence, it eliminates waste, waiting time and transportation. [5]. Finally, it increases the productivity of the operation.

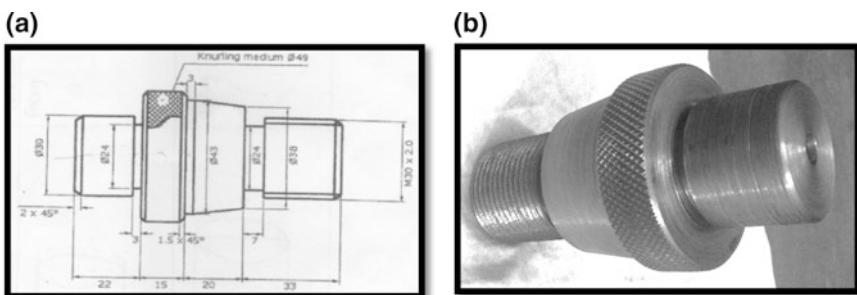


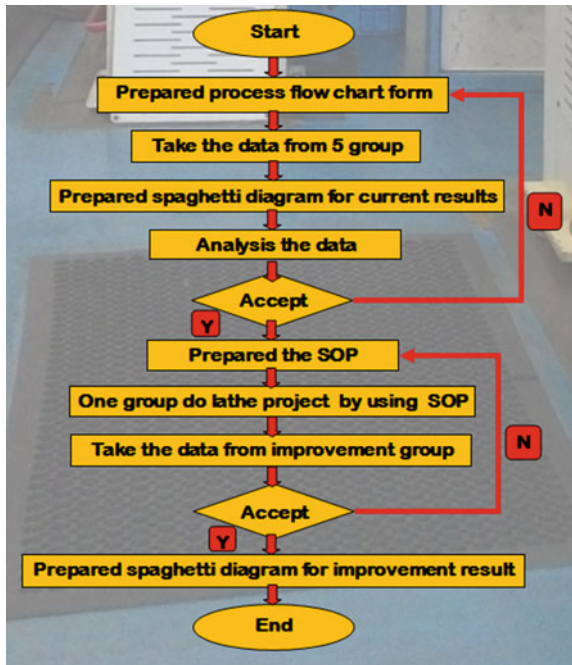
Fig. 1 a Lathe project drawing. b Finished product

The right methods of analysis were carried out to identify the problem, select the correct method, run the simulation, value added method and verification were conducted in this study.

Several traditional quality tools were identified including QCC7 tools [6] Plan-Do-Check-Act cycle [12] or plan do check adjust (PDCA), Process Flow Chart, Critical Path Method (CPM), Program Evaluation and Review Technique (PERT), Six Sigma [12], and Spaghetti Diagram. These tools and techniques were very practical to be applied in a change or improvement of systems [6, 11]. These tools also the good methods in investigating the root cause of problems and to find solutions to remove or minimize them [13]. However, not all of these analyses were used in this study.

Figure 2 shows the overview of the study where 5 samples which were representing a population of 50 students were taken for the data gathering. It interpreted the confidence level of the study. The groups were selected under consideration of their background of previous studies and experiences including those form technical and vocational background and others.

Fig. 2 The overall flow of the study



1.1 Flow Process Chart

Flow process chart or path process chart was used in this study. It is a technique to trace the path taken by the operator and interrelationship including the process of work [8] in completion the task given.

It helps in setting out the sequence of the flow of a product or a procedure by recording all events under review using appropriate process chart symbols. It covers symbols for operation, inspection, storage, delay and transportation [10]. Step in development of process flow consists of planning, implementation, verification and recommendation process. There are a few items required including the work piece, tools, machine, drawing, stop watch etc. To implement the process flow, it requires the operation, inspection, transportation, delay and storage to be considered.

The flow process was then translated in a time study form where each operation from 5 samples were simultaneously taken. Then the researchers have identified any critical operations to be improvised.

1.2 Spaghetti Diagram

A method that uses a continuous line to trace the path and distance travelled of a particular object or person throughout a process. It is most commonly illustrated on a floor map diagram that contains the entire process you are process to evaluated and been considered in this study [7, 9]. The purpose of this Lean Six Sigma tool has exposed inefficient process layouts, unnecessary travel distances between process steps and overall process waste [7].

In this study, the Spaghetti Diagram was divided into 2 phases; initial operation and improvement operation. The results were used for comparison purposes. This reveals the real data of improvement made.

1.3 Standard Operation Procedure (SOP)

Standard Operating Procedure (SOP) was developed to guide the user in an appropriate and systematic way of performing machining operations. It leads to waste reduction in terms of time in movement and delay. Below is a procedure to reduce time waste:

- Check the condition of lathe machine and tools (i.e. safety, coolant level before start the machining operation, amount of tools availability).
- Take all the necessary tools for the process from the tool center.
- Prepare progress report writing at the end of the day.
- Delegate tasks among the group members (if any):

- Workpiece, tool, machine settings.
- Verify the current work operation and the next operation preparation 5 min before the current operation ends.

1.4 Relocate the Tool Centre in Optimizing Support Staff and Machinist Function

The decision of relocating the Tool Centre nearer to the machining operation was made and seen its function on its purpose was made. The exercise was made to optimize staff function as store personnel and to assist an inexperienced machinist during machining operation. The frequency of the machinist to obtain tools, equipment and accessories for the machining operation in a day was not regular. The relocation of the Tool Centre near to the machine has optimize the function of the support staff requirement for the whole workshop.

2 Results and Discussion

Table 1 below is the initial process of data collection of conventional lathe operations. From the initial data collected, delay was recorded as the highest readings followed by machining operation and others.

The idle time obtained showed that the time waste contributed due to tool settings, watching other machinist operation and sharpening of High Speed Steel (HSS) cutting tools were the highest contribution.

A SOP was designed to assists the machinist in the development of machining operations. The SOP shows the detail of process steps for the development of the task. In addition, a video presentation assists the processes in advanced. This is to ensure that the machinist understands the process beforehand.

An improvement of the distance of Tool Centre was also made to reduce the distance of the machinist to take and return tools, accessories and others. This reduces a total length of almost 20 m each time the machinist deals with the Tool Centre.

Table 1 Time taken to identify area of improvement (minutes)

Operation	Initial (min)
Machining	325.9
Movement	14.96
Inspection	39.47
Delay	516.56
Storage	19.98

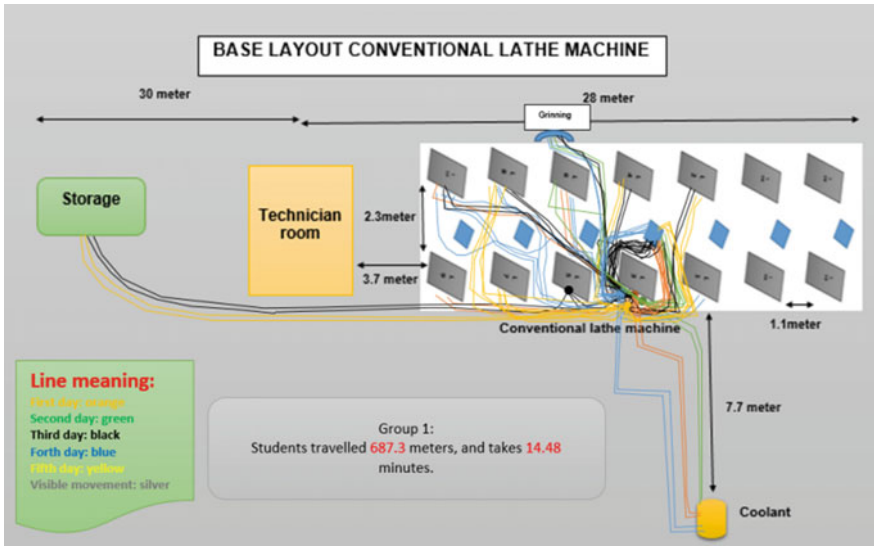


Fig. 3 Spaghetti diagram of conventional lathe operation before improvement been made

Figure 3 shows the spaghetti diagram of conventional lathe operation in an early stage of the study. An average of 30 h of operation time was spent to complete the lathe project. The machinist travelled approximately 687.3 m, and it takes 14.48 min to and from the Tool Centre.

Figure 4 shows the spaghetti diagram for the improvement made later. It takes 18 h which is equivalent to 3 days to complete the task. The machinist requires to travel only 206.6 m and it takes overall 3.33 min in completion of the task. The results of improvement by simulations is gathered in Table 2 and shows a huge difference before and after improvement. 5 activities in machining operations were identified. Idle time including delay contributed by delay has been reduced by 61%. Even though the time of movement reduces by 12 min, it gives significant improvement to the study. It gives the highest percentage of improvement with 411%.

A total of 339 min or nearly 6 h of overall improvement was made for this study. This is because SOP, video presentation and layout improvement contribute to the productivity enhancement.

Figure 5 shows the time improved by using SOP. The operation time was improved by 108.61 min. The movement, inspection and storage of time were enhanced to 12.026, 9.86 and 14.02 min, respectively. Meanwhile, the most time saver displayed in the delay of 196.24 min. This shows SOP helps in the process of fabrication. The total time was improved to 14 h in completing the lathe project.

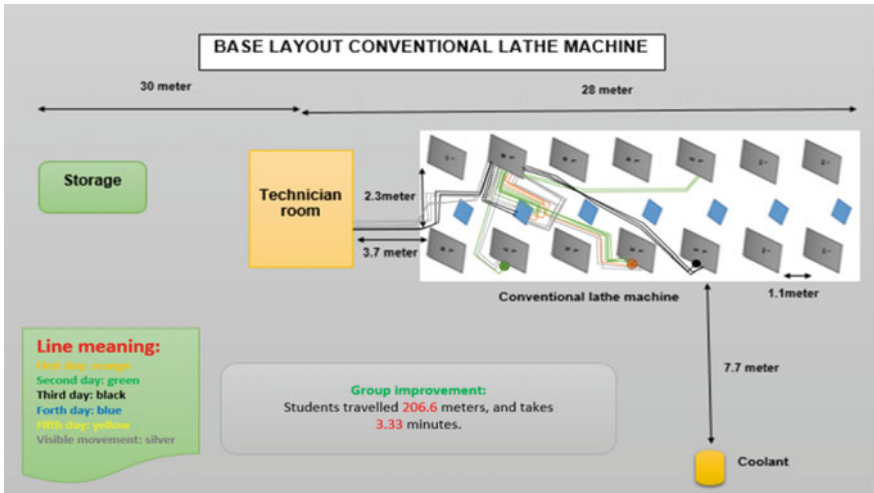


Fig. 4 Spaghetti diagram for group improvement

Table 2 Time comparisons before and after the improvement being made

Operation	Before	Improvement	Time improve (min)	%
Machining	325.9	217.29	108.61	50
Movement	14.96	2.93	12.03	411
Inspection	39.47	29.61	9.86	33
Delay	516.56	320.32	196.24	61
Storage	19.89	7	12.89	184
Minutes	916.78	577.15	339.63	
Hours	15.28	9.62	5.66	

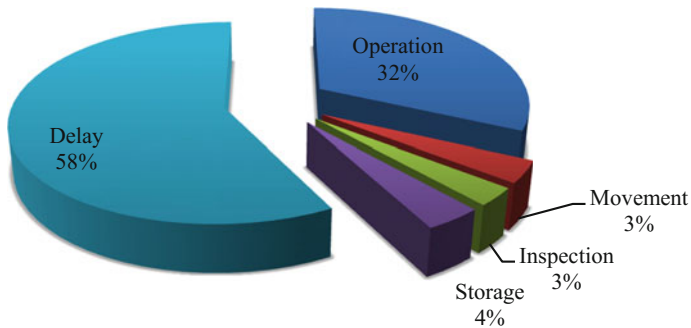


Fig. 5 Percentage distribution in total time improvement made from this study

3 Conclusion

Finally, the objective of this project was successfully achieved. Work procedures and the redesigning process [4] improved student's time in completing the lathe project. Video presentation of each process in the lathe project also assists users in understanding conventional lathe's operation by his/her own initiative. Through the video presentation, we managed to ensure that the students understood the process of the lathe project. This increases students' confidence during the machining operation. The research recommended to use the automated layout design program (ALDEP) and the Witness Simulation software in the next study which are more reliable and time effective. Overall equipment effectiveness (OEE) can also be applied to identify its affection and simulate for the real application for mass production.

Acknowledgements Thanks to the UniKL MSI Conventional Machining technicians who allow researchers to conduct the study for the sake of improvement in teaching and learning process.

References

1. Dimitrov, D., Saxer, M.: Productivity improvement in tooling manufacture through high speed 5 axis machining. In: 5th CIRP Conference on High Performance Cutting 2012, pp. 277–282 (2012)
2. Singh, J., Singh, H.: Continuous improvement approach: state-of-art review and future implications. *Int. J. Lean Six Sigma* **3**(2), 88–111 (2012)
3. Thessaloniki: Kaizen definition and principles in brief: a concept tools for employees improvement. Retrieve from www.michailolidis.gr on 11 Jan 2016 (2006)
4. Iberahim, H., Mazlinda, H., Marhainie, H.D., Hidayah, A.N.: Determines the sustainable continuous improvement practices in mail processing service operation. *Procedia Soc. Behav. Sci.* **219**, 330–337 (2015)
5. Jamaludin, K.R., Haron, H.N.: Nurturing Lean Manufacturing Concepts in the Industrial Engineering Subject at the Undergraduate Level. Proceedings of the Regional Conference on Engineering Education. Dec 12–13, 2005, Johor, Malaysia (2005)
6. Magar, V.M., Shinde, V.B.: Application of 7 quality control (7QC) tools for continuous improvement of manufacturing process. *Int. J. Eng. Res. Gen. Sci.* **2**(4), 364–371 (2014)
7. Allen, T.T.: Introduction to Engineering Statistics and Lean Sigma: Statistical Quality Control and Design of Experiments and Systems, p. 128. Springer, Berlin (2010). ISBN 978-1-84882-999-2. Retrieved 17 Feb 2011
8. Magu, P., et al.: Path process chart—a technique for conducting time and motion study. *Procedia Manuf.* **3**, 6475–6482 (2015)
9. Environmental Modeling Center: NCEP Medium-Range Ensemble Forecast (MREF) System Spaghetti Diagrams. National Oceanic and Atmospheric Administration. Retrieved 2011-02-17 (2003-08-21)
10. Graham, B.B.: Detail process charting: speaking the language of process, Online-Ausg. edn., p. 2. Wiley, Hoboken, N.J. (2004)

11. Johansson, P.E.C.: Current state of standardized work in automotive industry in Sweden. *Procedia CIRP* **7**, 151–156 (2013)
12. Kabir, M.E., Bobby, M.M.I., Lutfi, M.: Productivity improvement by using six-sigma. *Int. J. Eng. Technol.* **3**(12), 1056–1084 (2013)
13. Jirasuktasert, P., Garza-Reyes, J.A., Kumar, V., Lim, M.K.: A six sigma and DMAIC application for the reduction of defects in a rubber gloves manufacturing process. *Int. J. Lean Six Sigma* **5**(1), 2–21 (2014)